Modifying fluorescence of single quantum emitters: single dye molecules and SiO_2 nanoparticles in a tunable subwavelength microcavity

Dissertation

der Mathematisch-Naturwissenschaftlichen Fakultät

der Eberhard Karls Universität Tübingen

zur Erlangung des Grades eines

Doktors der Naturwissenschaften

(Dr. rer. nat.)

vorgelegt von

Dipl.-Phys. Alexey Chizhik

aus Sankt-Petersburg

Tübingen

2011

Tag der mündlichen Qualifikation:	24.05.2011
Dekan:	Prof. Dr. Wolfgang Rosenstiel
1. Berichterstatter:	Prof. Dr. Alfred J. Meixner
2. Berichterstatter:	Prof. Dr. Dines Christen
3. Berichterstatter:	Prof. Dr. Markus Sauer

Table of Contents

Abstract

In this thesis we study controlled modification of the radiative transition rate and fluorescence spectrum of a single dye molecule and SiO_2 nanoparticle (NP) by embedding it within a tunable planar microcavity with subwavelength spacing. We develop a theoretical model and find excellent agreement between theoretical prediction and experimental results. Whereas fluorescence of single dye molecules in glass-air confinement (i.e., in free space) is fairly well known, the details of optical properties of individual SiO_2 NPs are still unclear. Therefore, a part of this thesis is dedicated to investigation of their photoluminescence in free space. In introduction of the thesis we present a tunable microcavity construction, which has been used for the measurements.

In chapter 1, we present a review of different microresonator structures and how they can be used in future device applications in modern analytical methods by tailoring the optical properties of single quantum emitters. The main emphasis is on the tunable $\lambda/2$ Fabry-Perot type microresonator which we used to obtain the results presented in this chapter. By varying the mirror distance the local mode structure of the electromagnetic field is altered and thus the radiative coupling of fluorescent single quantum emitters embedded inside the resonator to that field is changed, too. As a result a modification of the optical properties of these quantum emitters can be observed. We present experimental as well as theoretical results illustrating this effect.

In chapter 2, we present experimental and theoretical results on changing the fluorescence emission spectrum of a single molecule by embedding it within a tunable planar microcavity with subwavelength spacing. The cavity length is changed with nanometer precision by using a piezoelectric actuator. By varying its length, the local mode structure of the electromagnetic field is changed together with the radiative coupling of the emitting molecule to the field. Because mode structure and coupling are both frequency dependent, this leads to a renormalization of the emission spectrum of the molecule. We develop a

theoretical model for these spectral changes and find excellent agreement between theoretical prediction and experimental results.

In chapter 3, using a tunable optical micro-resonator with subwavelength spacing, we demonstrate controlled modulation of the radiative transition rate of a single molecule, which is measured by monitoring its fluorescence lifetime. Variation of the cavity length changes the local mode structure of the electromagnetic field, which modifies the radiative coupling of an emitting molecule to that field. By comparing the experimental data with a theoretical model, we extract both the pure radiative transition rate as well as the quantum yield of individual molecules. We observe a broad scattering of quantum yield values from molecule to molecule, which reflects the strong variation of the local interaction of the observed molecules with their host environment.

In chapter 4, we present experimental results on changing the ratio of detected on- and off-axis emission of dye molecules embedded in the microcavity.

In chapter 5, we show details of single SiO_2 NPs synthesis. Silicon nanocrystals (Si NCs) were synthesized by CO_2 laser pyrolysis of SiH_4. The fresh silicon nanopowder was oxidized in water to obtain SiO_2 nanoparticles (NPs) exhibiting strong red-orange photoluminescence.

In chapter 6, we present new results on single SiO_2 NPs study. Samples of SiO_2 NPs embedded in low concentration in a thin polymer layer were prepared by spin-coating a dedicated solution on glass cover slides. The spectral analysis of single SiO_2 NPs revealed double-peak spectra consisting of a narrow zero-phonon line and a broader phonon band being associated with the excitation of longitudinal optical phonons in the SiO_2 NP.

In chapter 7, we study single Si NCs and SiO_2 NPs using confocal laser scanning microscopy with the goal to compare both kinds of NPs and to determine to what extent quantum confinement or surface-related defect centers are responsible for the strong fluorescence of Si NCs. The single particle spectra of Si NCs and SiO_2 NPs are composed of a zero-phonon line and one or two phonon bands, which are associated with longitudinal optical phonons in SiO_2, and reveal in every detail an amazing similarity. Both systems reflect the same dynamical behavior (blinking

and bleaching). Spectrally resolved fluorescence decay measurements yield the important result that the direct and the phonon-assisted recombination processes occur on the same nanosecond timescale (~4 ns). These experimental observations suggest that the photoluminescence of the Si NCs observed in this study is governed by defect luminescence.

In chapter 8, we discuss details of fluorescence dynamics of single SiO_2 NPs and single Si NCs. A redistribution of energy of defect states caused by charge fluctuations in the surrounding of the embedded NP is investigated.

In chapter 9, using a tunable optical subwavelength microcavity, we demonstrate controlled modification of the electron-phonon coupling in a single SiO_2 nanoparticle. By varying the distance between the cavity mirrors we change the electromagnetic field mode structure around a single nanoparticle, which results in modification of probability of electron-phonon coupling in the particle. Experimentally, we demonstrate redistribution of the photoluminescence spectrum between zero-phonon and phonon-assisted bands and modification of excited state lifetime of the same individual SiO_2 particle measured at different cavity lengths. Mono-exponential character of the single-particle decay curves shows that zero phonon, phonon- and double phonon-assisted transitions occur from the same energy level but possess different transition probabilities, which are related to the probability of electron-phonon coupling.

Zusammenfassung

In dieser Arbeit untersuchen wir die kontrollierte Änderung der Strahlungsübergangsrate und des Fluoreszenzspektrums eines einzelnen Farbstoffmoleküls und SiO_2-Nanopartikels (NP) durch Einbetten in eine durchstimmbare plane Mikrokavität mit Subwellenlängenabstand. Wir haben ein theoretisches Modell entwickelt und finden hervorragende Übereinstimmungen zwischen theoretischen Voraussagen und experimentellen Ergebnissen. Während die Fluoreszenz einzelner Farbstoffmoleküle in Glas-Luft-Grenzfläche (d.h. im freien Raum) sehr gut bekannt ist, sind die Einzelheiten der optischen Eigenschaften individueller SiO_2-NP immer noch unklar. Daher widmet sich ein Teil dieser Arbeit der Untersuchung ihrer Fotolumineszenz im freien Raum. Einleitend präsentieren wir die Konstruktion der durchstimmbaren Mikrokavität, die für die Messungen verwendet wurde.

In Kapitel 1 geben wir eine Übersicht über die verschiedenen Mikroresonatorstrukturen und wie sie in zukünftigen Bauteilen Verwendung in modernen Analysemethoden finden können, indem die optischen Eigenschaften einzelner Quantenemitter konfektioniert werden. Die Betonung liegt dabei auf dem durchstimmbaren $\lambda/2$ Fabry-Perot-Mikroresonator, den wir verwendet haben um die in diesem Kapitel präsentierten Ergebnisse zu erhalten. Durch Variation des Spiegelabstandes ändert sich die lokale Modenstruktur des elektromagnetischen Feldes und dadurch auch die Strahlungskopplung der fluoreszierenden einzelnen Quantenemitter, die im Resonator eingebettet sind. Resultierend kann eine Modifizierung der optischen Eigenschaften dieser Quantenemitter beobachtet werden. Zur Erläuterung des Effekts präsentieren wir sowohl experimentelle als auch theoretische Ergebnisse.

In Kapitel 2 präsentieren wir experimentelle und theoretische Ergebnisse bezüglich der Veränderung des Fluoreszenzemissionsspektrums eines einzelnen Moleküls indem es in eine durchstimmbare plane Mikrokavität mit Subwellenlängenabstand eingebettet wird. Die Kavitätslänge wird mit Piezostellern mit Nanometerpräzision verändert. Durch Variation der Länge

verändert sich die lokale Modenstruktur des elektromagnetischen Feldes zusammen mit der Strahlenkopplung des emittierenden Moleküls zum Feld. Weil Modenstruktur und kopplung beide Frequenzabhängig sind, führt dies zur Renormalisierung des Emissionsspektrums des Moleküls. Wir entwickeln ein theoretisches Model für die spektralen Änderungen und finden hervorragende Übereinstimmungen zwischen theoretischen Voraussagen und experimentellen Ergebnissen.

In Kapitel 3 benutzen wir einen durchstimmbaren optischen Mikroresonator mit Subwellenlängenabstand und demonstrieren damit die kontrollierte Modulation der Strahlungsübergangsrate eines einzelnen Moleküls, die durch Beobachtung der Fluoreszenzlebenszeiten gemessen wird. Veränderung der Kavitätslänge führt zur Änderung der lokalen Modenstruktur des elektromagnetischen Feldes, die die Strahlungskopplung eines emittierenden Moleküls zu dem Feld modifiziert. Beim Vergleich der experimentellen Daten mit einem theoretischen Modell bestimmen wir beides, die reine Strahlungsübergangrate, sowie die Quantenausbeute individueller Moleküle. Wir beobachten eine breite Fächerung der Quantenausbeuten von Molekül zu Molekül, was die starke Variation der lokalen Wechselwirkung der beobachteten Moleküle mit deren Umgebung wiederspiegelt.

In Kapitel 4 präsentieren wir experimentelle Ergebnisse bei Veränderung des Verhältnisses der detektierten Emission aus longitudinaler und transversaler Richtung von Fluoreszenzmolekülen eingebettet in der Mikrokavität.

In Kapitel 5 zeigen wir Details der Synthese einzelner SiO_2-NP. Siliziumnanokristalle (Si-NC) wurden mit Hilfe der CO_2-Laserpyrolyse von SiH_4 hergestellt. Das frische Siliziumnanopulver wurde in Wasser oxidiert um SiO_2-NP mit starker rot-orangener Fotolumineszenz zu erhalten.

In Kapitel 6 präsentieren wir neue Ergebnisse der Untersuchungen an einzelnen SiO_2-NP. Proben von SiO_2-NP eingebettet in niedrig konzentrierten dünnen Polymerschichten wurden durch Aufschleudern geeigneter Lösung auf Glas-Deckgläschen hergestellt. Die Spektrale Analyse einzelner SiO_2-NP zeigten Doppelpeaks bestehend aus einer schmalen Null-Phonon-Linie und einer breiteren

Phonon-Bande, die mit der Anregung der longitudinalen optischen Phononen in den SiO_2-NP assoziiert wurde.

In Kapitel 7 untersuchen wir einzelne Si-NC und SiO_2-NP mit konfokaler Laser-Raster-Mikroskopie mit dem Ziel die beiden Arten der NP zu vergleichen und zu bestimmen bis zu welchem Grad Quantum-Confinement oder oberflächenbezogene Defektzentren für die starke Fluoreszenz von Si-NC verantwortlich sind. Die Einzelpartikelspektren von Si-NC und SiO_2-NP setzen sich aus einer Null-Phonon-Linie und einer oder zweier Phonon-Banden zusammen, die mit LO_3-Phononen in SiO_2 assoziiert werden, und offenbaren in jeder Einzelheit eine verblüffende Ähnlichkeit. Beide Systeme zeigen dasselbe dynamische Verhalten (Blinken und Bleichen). Messungen spektral aufgelöster Fluoreszenzabklingkurven ergeben das wichtige Ergebnis, dass sowohl die direkten als auch die Phonon-unterstützten Rekombinationsprozesse innerhalb derselben Zeitskala ablaufen (~4 ns). Diese experimentellen Beobachtungen deuten darauf hin, dass die Fotolumineszenz der Si-NC, die in dieser Untersuchung beobachtet wurde, von Defektlumineszenz beherrscht wird.

In Kapitel 8 diskutieren wir Einzelheiten der Fluoreszenzdynamik einzelner SiO_2-NP und einzelner Si-NC. Eine Umverteilung der Energie der Defektzustände verursacht durch Ladungsfluktuationen in der Umgebung der eingebetteten NP wird untersucht.

In Kapitel 9 demonstrieren wir unter Verwendung einer durchstimmbaren optischen subwellenlängen Mikrokavität, kontrollierte Modifikation der Elektron-Phonon-Kopplung in einem einzelnen SiO_2-NP. Durch Variation des Abstandes zwischen den Kavitätsspiegeln verändern wir die Modenstruktur des elektromagnetischen Feldes um einen einzelnen NP, was in einer Modifizierung der Wahrscheinlichkeit der Elektron-Phonon-Kopplung im Partikel resultiert. Experimentell zeigen wir die Umverteilung der Fotolumineszenzspektren zwischen Null-Phonon und Phonon-unterstützte Banden und Modifizierung der Lebenszeiten im angeregten Zustand desselben individuellen SiO_2-NP, gemessen bei unterschiedlichen Kavitätslängen. Monoexponentieller Charakter der Abklingkurve der einzelnen Partikel zeigen, dass Null-Phonon, Phonon- und

Doppel-Phonon-unterstützte Übergänge vom selben Energieniveau auftreten, aber unterschiedliche Übergangswahrscheinlichkeiten besitzen, die mit der Wahrscheinlichkeit der Elektron-Phonon-Kopplung einhergehen.

Introduction

1. Optical microcavities

1.1. Sate of the art

Since the realization of the first laser in 1960 by Maiman [1], interest in optical resonators and their use in diverse applications, from fundamental studies to industrial manufacturing, has grown continuously. Photonic devices have followed the trend towards miniaturization witnessed in the semiconductor industries. This development has already reached a level in which one has to deal with single molecules or even atomic structures. Microresonators are a very suitable tool to control the optical properties of these quantum emitters (Figure 1) [2–5]. However, depending on the application area, today's microresonators vary much in their design – from classical configurations using distributed Bragg reflectors (DBR) or metallic mirrors via microtoroids to photonic crystal-based cavities and thus also in their properties. This diversity has its origin in the manifold photonic devices needed in future applications. By modifying the shape and the size of a resonator and changing its material composition it is already possible to generate and/or support only desired wavelengths

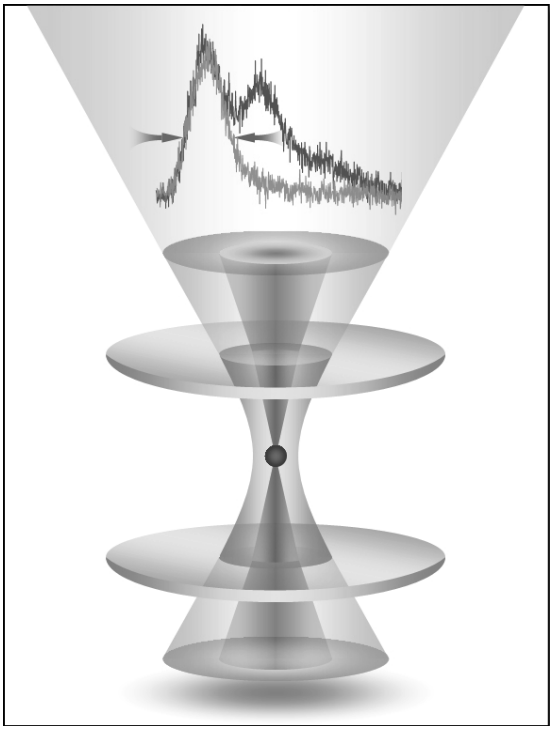

Figure 1. Scheme of a single quantum emitter embedded in the Fabry-Perot optical microcavity. Orange curve shows the narrowing of a single PI molecule fluorescence spectrum with respect to the emission in free space (blue curve).

and polarizations. This offers the potential for developing new types of photonic devices such as low-threshold microlasers, ultra-small optical filters, and switches for wavelength-division-multiplexed (WDM) networks. In particular, whispering gallery mode (WGM) lasers and photonic crystal devices are very suitable for integration in new photonic devices due to their compact size, allowing a device density of 105 cm^{-2} [5]. These key elements provide generation, guiding, coupling, switching, splitting, multiplexing, and demultiplexing of optical signals. In the recent years the progress in developing new functions of microcavites, most of them already known from their macroscopic counterparts, was enormous. Using a toroidal silica microresonator Vahala's group was able to demonstrate tunable continuous-wave third-harmonic generation at room temperature [12]. Based on a silica-on-silicon microstructure the 1550 nm pump wavelength was converted into 517 nm emission with a threshold as low as 300 μW of pump power. Using silica toroid microresonators it is also possible to generate optical frequency combs in a very efficient way as demonstrated by Del'Haye et al. [13]. These combs consist of equidistant frequencies covering a large wavelength region and therefore they are useful in precision spectroscopy, such as studies of dynamic processes in atoms [14], gas sensing [15], and molecular fingerprinting [16]. Other applications based on frequency combs include frequency metrology [17] and optical waveform synthesis for telecommunications [18, 19]. Most of the effects described above are based on the properties of the resonator itself (material, shape, Q factor etc.). Additionally, the microresonator can be used either to tailor the optical properties of single quantum emitters placed inside or it can be modified by the presence of a quantum object. The latter effect can be used in bioanalytics for label-free single molecule detection. In this case, binding of molecules to the functionalized surface of microspheres [20] or microtoroids [21] can be observed by a stepwise shift of the resonance frequency based on a thermo-optic effect. As this sensor is applicable with single molecule sensitivity it is interesting not only for biomedicine but also for pollution monitoring and security issues [22]. The 'controlling effect' of a microresonator on quantum emitters which are placed inside was described by Purcell in 1946: an emitter

within a low-loss, wavelength-scale confined structure, like a resonator, alters its spontaneous emission rate [23]. This effect is quantized by Fermi's golden rule:

$$\Gamma_{SpE} = \frac{1}{\tau_{SpE}} = \frac{2\pi}{h^2}\left|\left\langle\left|\hat{\mu}\cdot\hat{\mathrm{E}}^{+}{}_{cav}\right|\right\rangle\right|^2 \rho_{cav}(\omega) \qquad (1)$$

which states that the spontaneous emission rate depends on the density of modes (DOM) of the electromagnetic field [24]. As a result of the changed DOM inside a microresonator compared with non-confined space the spontaneous emission is either suppressed [25] or enhanced [23]. Of special interest is the latter case, which can be expressed by the Purcell factor

$$F_P = \frac{3}{4\pi^2}\left(\frac{\lambda_c}{n}\right)^3 \frac{Q}{V} \qquad (2)$$

where λ_c/n is the wavelength within the material, and Q and V are the quality factor and mode volume of the cavity, respectively. As a consequence of the enhanced (or suppressed) spontaneous emission rate the spectral characteristics of quantum emitters placed inside a microresonator are changed. For broadband emitters one has to take optical dispersion effects into account, i.e., wavelength-dependent electromagnetic coupling of the emitter to its environment. As a result the observable emission spectrum of the embedded emitter can undergo drastic changes, which are determined by frequency-selective coupling efficiencies between the emitter and available cavity modes. This effect will be discussed later in more detail for a planar metallic subwavelength microcavity. There is obviously a great variety amongst the introduced microcavities, e.g., practical differences (ease of fabrication, connectivity to waveguides, chip integration) or principal differences (free spectral range (FSR), Q factor, mode volume). However, for fundamental research on the physics of the interaction between light and matter and cavity quantum electrodynamics the classical Fabry–Perot resonator type using external mirrors is first choice as it is versatile and offers a

small mode volume. In 1983 Goy and coworkers reported on the first observation of enhanced spontaneous emission in a resonant cavity by using Rydberg atoms of sodium [26]. These types of experiments became increasingly interesting and formed the basis of the above-mentioned applications. In recent years, the investigations of single quantum emitters, such as atoms [27], ions [8], quantum dots [28], molecules [29], or single walled carbon nanotubes [30–33] in a Fabry–Perot type cavity have increased, especially driven by the quest for a single photon source for quantum communication and computing [7, 34–36].

Now we will limit the discussion to the Fabry-Perot type microresonator and present the possibility to control the optical properties of single molecules with such a device. In general, a Fabry-Perot resonator consists of two plane parallel reflecting surfaces with a distance *d* allowing multiple beam interference. The medium in between these surfaces is described by its refractive index $n(\lambda)$. For transmission through the resonator, i.e., constructive interference, the half-wavelength $\lambda/2$ has to fit an integer number of times into the cavity. More specifically the resonance condition for irradiation normal to the plane parallel mirrors is

$$m\lambda/2 = n(\lambda)d \qquad (3)$$

Such a resonator type is often characterized by its frequency spacing between adjacent resonances v_j and v_{j+1}, called free spectral range (FSR), which is defined by:

$$FSR_\nu = \Delta_\nu = \nu_{j+1} - \nu_j = c_0/2n(\nu)d \qquad (4)$$

where c_0 is the vacuum velocity of light. In the case of microresonators where *d* is comparable to $\lambda/2$ the penetration of the optical mode into the mirror has to be taken into account. Another important characteristic of a resonator is its finesse *F*, which is a measure for the number of round trips before the stored energy decays to *1/e* of its original value. The higher the reflectivity *R* of the mirrors is the

longer the photon storage time will be and, as a consequence, the sharper the transmission maxima characterized by $\delta\nu$ will become. Formally, the finesse can be written as

$$F = \frac{FSR}{\delta\nu} = \frac{\pi\left(R_1 R_2\right)^{1/4}}{1-\sqrt{R_1 R_2}}. \qquad (5)$$

Sometimes, the finesse is replaced by the quality factor Q, given by the ratio of transmission wavelength λ_0 and peak width $\delta\lambda$, i.e., $Q=\lambda_0/\delta\lambda=\nu_0/\delta\nu$. The last expression in particular reflects nicely the correlation between the energy decay in the time domain (finite photon storage time) and the peak width in the frequency domain. Depending on the reflectivity, Q values reach 50 when metal mirrors are used and up to several thousands in the case of Bragg mirrors.

Plane-parallel resonators are commonly used in microchip and microcavity lasers based on confined electronic systems in semiconductors with reduced dimensionality but not on single quantum emitters. Experimental results are mostly related to ensemble measurements [37] as these systems are promising candidates for more efficient LEDs, OLEDs, and microlasers [38–40]. However, experimental results of direct modification of the emission behavior of a single molecule in a microcavity are rare in the literature, even though microcavities are a suitable tool for manipulating the optical properties of quantum emitters. For example, strong changes in the emission and absorption spectra are predicted for a Rhodamine 6G molecule embedded within a spherical metal nanocavity [41]. Experimentally, the effect of emission changes was observed qualitatively by Steiner et al. [42] who investigated single isolated perylene dye molecules in a planar metal microcavity for different mirror spacings and hence for different electromagnetic mode structures. As a result of the fixed mirror spacings that were used in these experiments each single molecule could only be investigated at one specific resonator length.

1.2. Novelty of work

We developed a new design of a tunable optical microresonator with subwavelength spacing between its mirrors. The starting point of our work was a non-tunable optical microcavity, which consists of two metallic mirrors, glued with an optical adhesive [48]. A non-tunable cavity construction allowed Steiner and co-workers to observe modification of a single dye molecule radiative rate as well as fluorescence spectrum. However, as the mirror spacing was fixed, they could investigate a distinct molecule only for one given resonator length.

In our study, by varying the mirror separation with a nanometer precision using piezo-actuators, we can tune the cavity resonance and tailor the optical properties of an embedded molecule. Thus, for the first time we were able to actively change the local electromagnetic field structure around a single quantum emitter by changing the mirror spacing of the cavity. While it is well known from quantum electrodynamics that the spontaneous emission is not an intrinsic process but can be modified by tailoring the electromagnetic environment, the radiation rate and relaxation path of a molecule depend on the balance between the radiative and non-radiative relaxation paths. Hence, by controlling the electromagnetic environment of a single molecule we select the vibronic transition where fluorescence will mostly occur and we can tune its radiative transition and determine its fluorescence quantum yield.

Thus, we show, for the first time that the color of the fluorescence photons emitted by one single molecule can be continuously tuned by pure optical means in a microresonator. Decades ago, this was experimentally demonstrated by measuring the cavity-induced modification of the fluorescence lifetime [98]. However, only now it was shown that the emission spectrum of one and the same individual molecule can be tailored by continuously changing the mode density of the electromagnetic field in the resonator and thus its coupling with a molecule's internal quantum-mechanical states. Because this is sensitively dependent on the wavelength of the field modes, it leads to a complete restructuring of a molecule's emission spectrum as distinct wavelengths are affected differently. This opens an

exciting field for designing fluorescent emitters with adjustable spectral emission properties. This fundamental experiment could potentially applied in integrated photonics devising optical switches based on one single quantum system.

Moreover, we develop a semiclassical theoretical model for the spectral changes, and find excellent agreement between theory and experiment. Together with the well-studied changes of radiative transition rates (fluorescence or luminescence lifetime) and angular distributions of radiation, this is another important step in our understanding of the complex electromagnetic interaction of single photon emitters with an electromagnetic field structure that is tailored by the emitter's surrounding.

In the next part of the study, we modified the radiative transition rate of individual molecules by placing them into a tunable microcavity. This allowed us to extract radiative as well as nonradiative transition rates and to determine quantum yield of individual molecules, which are fundamental parameters of any quantum emitter. Average values thus obtained showed excellent agreement with the results from ensemble measurements. Moreover, we found a broad distribution of quantum yield values, whereas radiative transition rates did not change significantly from molecule to molecule. This reflects the heterogeneous local nature of the host, which determines the nonradiative relaxation of an excited molecule via interaction with the local chemical environment. Our technique can be applied to any single quantum emitter of interest, such as dye molecules, semiconductor nanoparticles, carbon nanotubes, and so forth. Thus, the tunable cavity method makes it a versatile tool for singlemolecule spectroscopy and quantum yield measurements of individual emitters.

We also study modification of single SiO_2 nanoparticles (NPs) photoluminescence when it is placed inside the tunable microcavity. Whereas fluorescence of single dye molecules in glass-air confinement (i.e., in free space) is fairly well known, the details of optical properties of individual SiO_2 NPs are still unclear. Therefore, a part of this thesis is dedicated to investigation of their photoluminescence in free space.

2. New design and characterization of a Tunable Fabry-Perot subwavelength microcavity

Here we present a new tunable subwavelength microresontaor construction. We will consider how to build and characterize such a microcavity and demonstrate that it is possible to spatially address single molecules and SiO_2 NPs in the microresonator using confocal microscopy. Moreover, we show that the spectral width of microresonator-controlled single molecule fluorescence spectra is determined by the spectral width of the measured on-axis transmission spectrum of the microresonator.

2.1. Microcavity design

The tunable microcavity construction is schematically shown in Fig. 2a and is similar to a previously built one but with no adjustable cavity length [48]. However, new design allows us to change the distance between the cavity mirrors, which opens new advances in single molecule fluorescence study. A homemade aluminum cavity holder, was used to fix two metallic mirrors together. The bottom part of the cavity consisted of a cover slide (thickness 170 μm), covered by a thin silver film (30 nm), a silicon oxide layer (30 nm, refractive index n=1.46), a polymer layer (70 nm, determined by atomic force microscope measurements (AFM); refractive index n=1.49) with dissolved dye molecules, and a second thin silicon oxide layer (8 nm, refractive index n=1.46). The bottom silicon oxide layer serves as a finite spacer between the silver metal and the dye embedding polymer. The upper silicon oxide layer prevents any interaction of embedded dye molecules with atmospheric oxygen during cavity assembly. The top part of the cavity consists of a plane-convex lens (F=150 mm), again covered with a silver layer (60 nm). Ag-layers as well as the silica spacers were fabricated by electron beam evaporation. The intermediate space between the multilayer covered coverslide and the silver layer covered lens was filled with oil (Immersol

518F, Zeiss, refractive index n=1.52) in order to achieve an optically homogeneous intra-cavity environment. The cavity length could be adjusted with piezo actuators (PSt 150/3.5×3.5/20, Piezomechanik GmbH) that move the lens toward or away from the bottom coverslide.

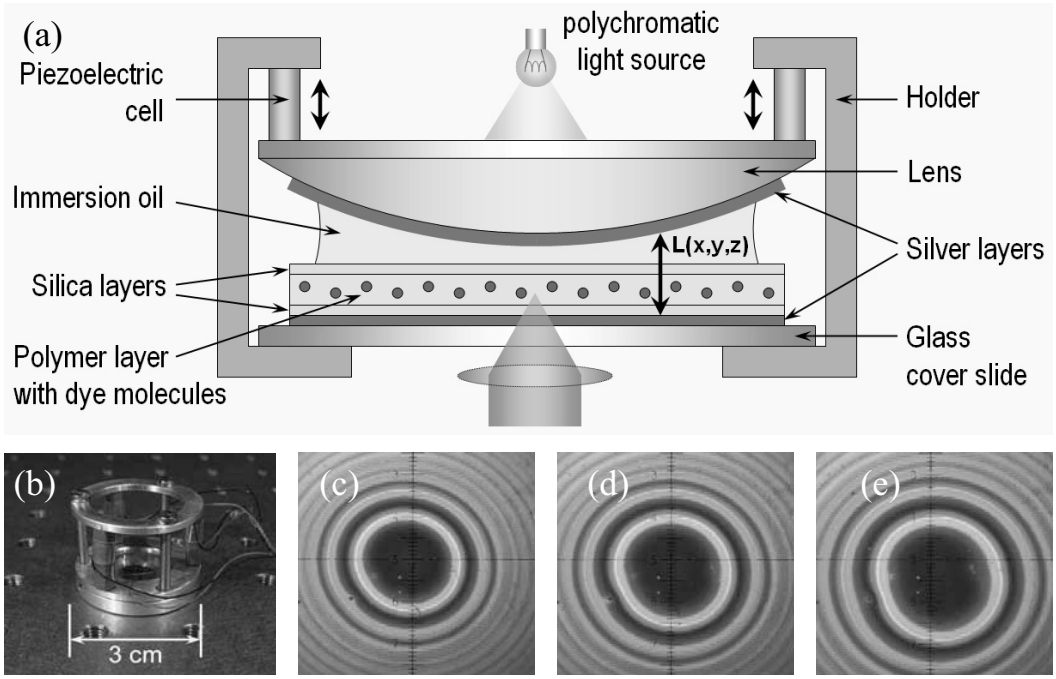

Figure 2. (a) Scheme of the experimental setup. (b) A photograph of the tunable microcavity. (c)-(e) White light transmission patterns (Newton rings) of the microcavity at different values of voltage, applied to the piezoelectric cells. The inner transmission ring satisfies the λ/2 condition for visible light. Applying a voltage to the piezoelectric elements changes the distance between the two mirrors, which results in a shift of the Newton rings.

2.2. Optical characterization of the microcavity

The spherical shape of the upper mirror allows us to control the optical quality and the tuning capability of the microresonator by observing the white light transmission pattern (Figure 2(c)-(e)). The Newton rings are a result of the different resonator lengths provided by the lens. The central region of the microcavity (i.e., the region of the minimum cavity length) remains dark, as no visible light can be transmitted anymore. The movement of the upper cavity mirror leads to the shift of the transmission pattern. The absolute cavity length

values L(x,y,z) were determined using on-axis white light transmission profiles, fitted by a Lorenzian line-shape function (Figure 4(b)). We can recalculate the local cavity length L(x,y,z) from the maximum transmission wavelength λ(x,y,z) by using the resonance condition (see [43,48,50] for more details):

$$L(x,y,z)=\left(m-\frac{\sum_i \Delta\Phi_i(d_i,\vartheta,\lambda)}{2\pi}\right)\frac{\lambda(x,y,z)}{2n_{eff}\cos\vartheta};m=1,2,3...;i=1,2. \qquad (6)$$

Here, m denotes the order of interference, $\Delta\varphi_i$ the phase change due to reflection at the respective silver mirror i = 1, 2 with thickness d_i. The effective refractive index of the intracavity medium n_{eff} was assumed to be 1.52. We use white light illumination with perpendicular incidence on the upper mirror (the angle of incidence ϑ=0) to determine the intensity maximum λ(x,y,z) of the local on-axis transmission spectrum. Moreover, the transmission profiles give the values of the cavity Q factor, characterizing the energy storage capability of the resonator. Although the average value of 45 is considerably lower than the typical one for high- and ultrahigh-Q resonators, such a cavity is well suited for our purpose allowing the clear visualization of the cavity-effect and the precise tuning of the resonance mode.

All fluorescence measurements were performed in the λ/2 region of the cavity, close to the center of the lens, where the displacement Δ(x,y) within the focal spot of our microscope objective (500 nm) results in a cavity length change ΔL of about 1 nm, which is in the order of the surface roughness of our silver mirrors. Therefore, our

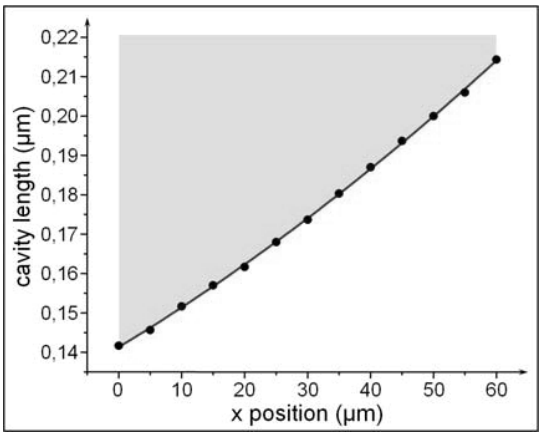

Figure 3. Variation of the cavity length L(x,y) (●) determined from a series of transmission spectra, taken across the first order interference region of the cavity. The solid line is a second-order polynomial fit.

microresonator can be considered as a plane-parallel system (Figure 3).

3. Single molecules in a tunable microcavity

3.1. Single molecule fluorescence detection

Using scanning confocal fluorescence microscopy, we were able to detect spatially isolated bright spots that originate from single molecules on resonance with the cavity mode. The fluorescence image, acquired within the λ/2 cavity range (Figure 4(c)), exhibits a cavity-controlled emission of single molecules. Those molecules, which are located in the cavity resonance mode, possess maximum emission, while the emission of those, which are out of resonance is suppressed down to the background level.

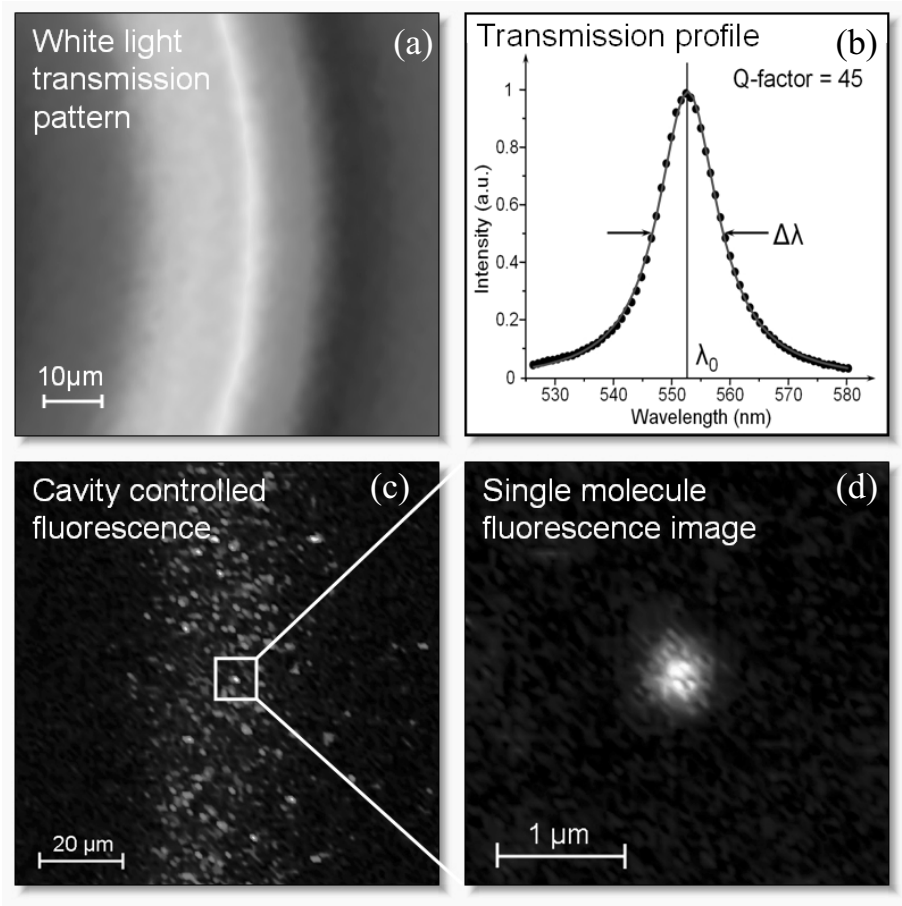

Figure 4. a) A photograph of white light transmission pattern taken from the first (λ/2) interference region. b) Microcavity white light transmission spectrum (●) fitted by a Lorenzian function (—) giving a cavity quality factor Q=45. c) Fluorescence emission image acquired from the first interference region of the cavity. The image demonstrates the on/off resonance emission distribution of single molecules. d) Fluorescence image of a single molecule emission.

Decreasing down the scanning area of the sample (Figure 4(d)) we achieve single molecule imaging level and precisely determine the (x,y) position of the molecule. Remarkably, that some of fluorescence patterns demonstrated single level photo blinking and photo bleaching behavior, proving them as single molecules.

3.2. Modification of single dye molecule fluorescence spectrum with a tunable microcavity

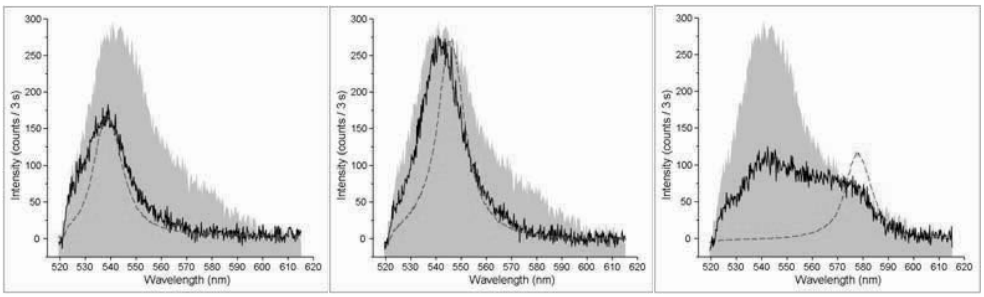

Figure 5. Measured spectra (black curves) of a single Rhodamine 6G molecule embedded in the microcavity at different cavity lengths. Red dashed curves indicate cavity white light transmission profiles, normalized to the respective emission spectrum. The grey shaded area represents the Rhodamine 6G free space spectrum.

By varying its length, the local mode structure of the electromagnetic field is changed together with the radiative coupling of the emitting molecule to the field. Because mode structure and coupling are both frequency dependent, this leads to a renormalization of the emission spectrum of the molecule. In a first experiment we demonstrate tailoring the emission spectrum of a single Rhodamine 6G dye molecule. Figure 5 shows three fluorescence spectra acquired from the same single molecule at different cavity lengths. Tuning of the cavity mode, i.e. white light transmission profile, leads to a modification of the single molecule emission spectrum shape and intensity. This phenomenon can be visualized by the scheme of the vibronic transitions shown in Figure 6. Changing the cavity mode, we actually suppress or enhance different vibronic transitions. This leads to a modification of the emission energy resulting in spectral renormalization.

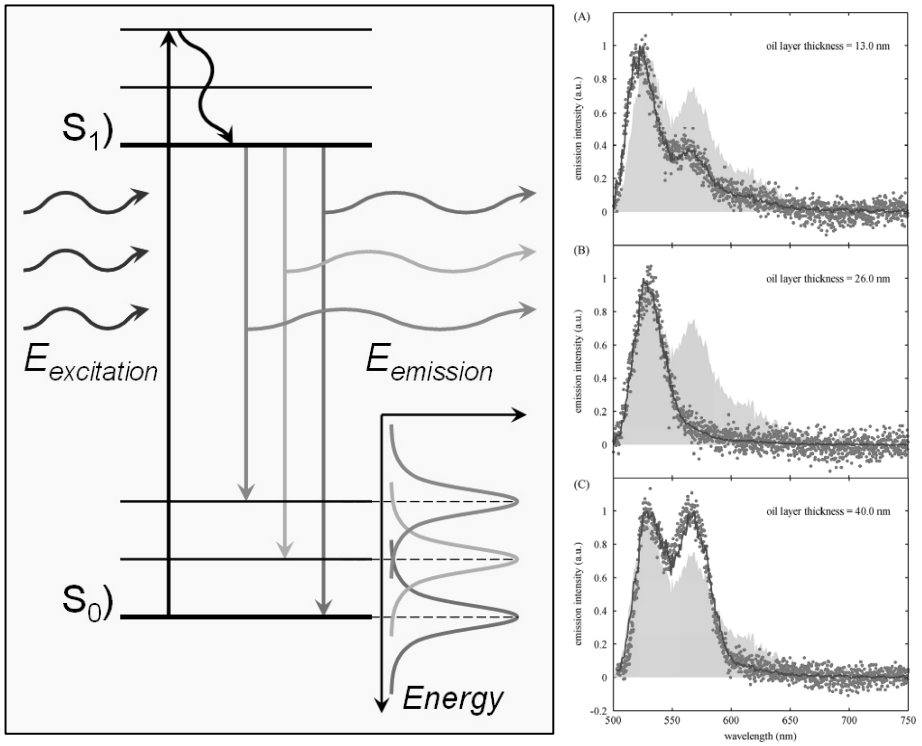

Figure 6. Left panel: general vibronic transition scheme. Lorenzian curves in the right-bottom corner schematically represent cavity white light profiles, corresponding to different vibronic transitions. **Right panel:** Measured spectra (red dots) of a single PI molecule embedded in the microcavity at various values of cavity length. The blue solid lines show the best fit of a theoretically calculated spectrum, using the free spectrum in polymer (gray shaded area) as the starting point. Fitted value of oil layer thickness is indicated in each of the plots.

In the second experiment we demonstrate modification of a fluorescence spectrum of a perylene derivative molecule embedded in the tunable cavity. Right panel in figure 6 show three spectra (red dots) of the same individual molecule, measured at different cavity lengths. Theoretical modeling of the spectrum was done within a semiclassical approach, treating the fluorescing molecule as an oscillating electric dipole emitter and solving Maxwell's equation for the given geometry of the microcavity. Blue curve shows the result of fitting the measured data and demonstrate excellent agreement between the theory and experiment. The agreement with a theoretical model based on a semiclassical approach is remarkable demonstrating its appropriateness for describing cavity-induced changes of the entire emission spectrum.

4. Probing the radiative transition of single dye molecule. Single molecule quantum yield

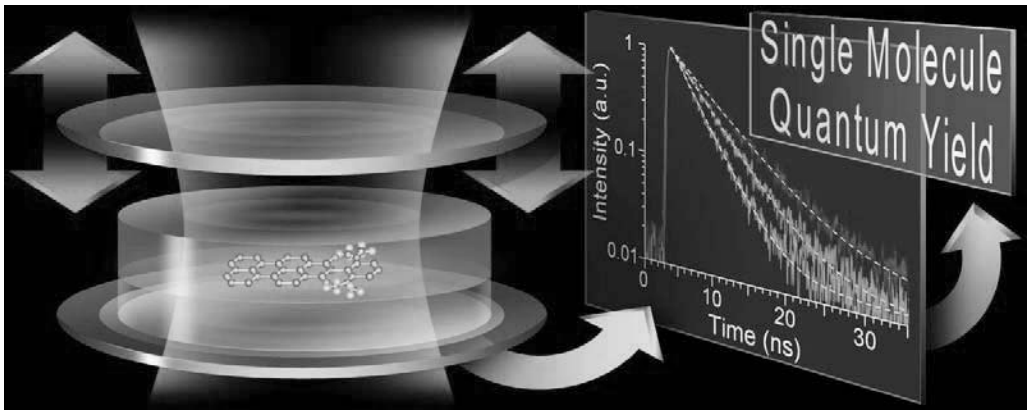

In this part of study, we demonstrate controlled modulation of the radiative transition rate of a single molecule, which is measured by monitoring its fluorescence lifetime. Variation of the cavity length changes the local mode structure of the electromagnetic field, which modifies the radiative coupling of an emitting molecule to that field. However, the radiative transition constitutes only one of the possible ways for returning from the excited to the ground state when considering molecules embedded in a condensed matter environment (e.g. solid or liquid). Due to collisions/interactions with surrounding molecules, so-called non-radiative transitions constitute a significant alternative way of de-excitation. The ratio of radiative to non-radiative transition rates is quantitatively described by the fluorescence quantum yield (QY) which is defined as the average chance to emit a photon (radiative transition) upon return from the excited to the ground state or

$$\phi = k_r / \left(k_r + k_{nr} \right) \qquad (7)$$

where k_r and k_{nr} are the radiative and non-radiative transition rates, respectively. From a spectroscopic point of view, the QY of fluorescence is the parameter which is most challenging to assess. Whereas absorption and emission spectra as

well as excited state lifetime (fluorescence lifetime) are straightforward to measure with modern measurement techniques, QY values are mostly determined in a comparative manner against a standard of known QY. Nonetheless, precise knowledge of QY is important for many practical applications such as the development of materials for organic and inorganic light emitting diodes [51], single-photon sources [52], solar cells [53], laser technology [54] or labeling in biological research [55].

The first successful estimates of the QY of fluorescent solutions had been made by Vavilov in 1924 [56] by comparing the fluorescence with scattering intensities. This approach was used, although much refined, over the following decades [57]. Only by 1978, Brannon and Magde developed a method for absolute measurements of QY via sensitive measurements of sample heating upon illumination [58]. However, extending this idea to the single-molecule level seems rather impossible due to the minute amount of heat generated by a single molecule upon non-radiative de-excitation.

Thus, when considering the QY of individual molecules, an appealing idea is to use the aforementioned sensitivity of the radiative transition to the local electromagnetic field mode density, which can be changed by placing the emitter close to a mirror or within a cavity. On the single-emitter level, this effect has been demonstrated by several authors, either by

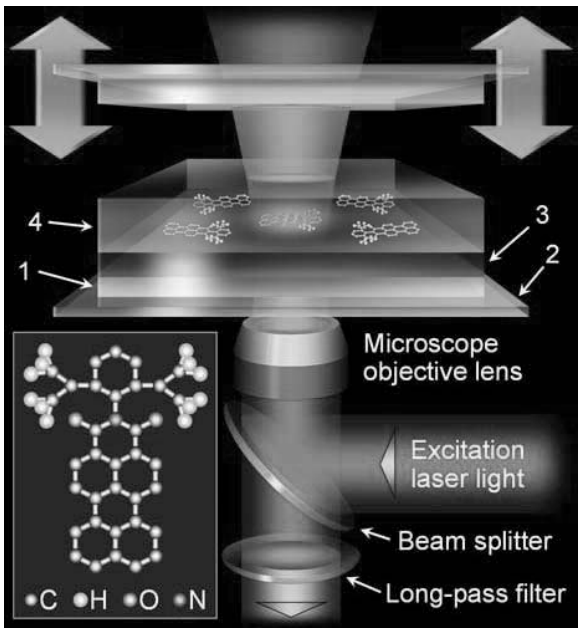

Figure 7. Scheme of the experimental setup, used for single molecule quantum yield measurements. The tunable microcavity consists of: Silver layers (1) sputtered on the glass surface (2); silica layer (3), acting as a spacer between the metallic surface and the molecules; a polymer layer (4), immobilizing molecules and protecting them from the interaction with atmospheric oxygen. The vertical position of the top mirror is adjusted with nanometer precision by piezo actuator. The inset shows a molecular structure of PI molecule.

measuring the fluorescence lifetime of an emitter in two different environments [59,60] or by placing the emitter on or close to a sharp tip [61,62]. Sandoghdar has recently extended this approach to measuring the fluorescence lifetime of a single molecule as a function of its distance to a metallic mirror [63], thus replicating Drexhage's original measurements on a single molecule level.

An even more efficient method to change the local mode density of the electromagnetic field is to place an emitter into an optical microcavity [64,65]. Furthermore, if the cavity is tunable, it becomes a powerful tool for changing the mode density and resulting radiative transition rate of an emitter in a continuous way. We have recently used such a tunable microcavity to watch, on one and the same molecule, the varying emission spectrum while changing the cavity width [66].

We present absolute measurements of the QY of individual molecules using the tunable microcavity (Figure 7). The distance between the cavity mirrors is reduced down to the range of one half of the emission wavelength, therefore there is only one resonance frequency maximum, which is tuned when the cavity length is changed. Since the mode structure and the coupling between the molecule and the resonator are both frequency dependent, variation of the cavity length leads to a modification of the radiative transition in a molecule according to Fermi's golden rule [24]. The core idea is to record the fluorescence lifetime of the same single molecule as a function of cavity width, in that way changing the radiation rate via the optical mode density in the resonator while leaving at the same time the non-radiative rate of the molecule unaffected. This information is then compared with theoretical modeling for extracting both the pure radiative transition rate and the QY for a given molecule. We observe a broad distribution of QY values from molecule to molecule, which reflects the strong variation of the local interaction of the observed molecules with their host molecules. The method is of fundamental importance wherever one is interested in investigating interactions between fluorescent emitters and surrounding host molecules, which is most sensitively reported by the non-radiative transition rate. This is different to the modification of the QY of a molecule by a plasmonic nanostructure when the

molecule must be so close to the metal that absorptive losses to the metal may even dominate the non-radiative relaxation [68,69].

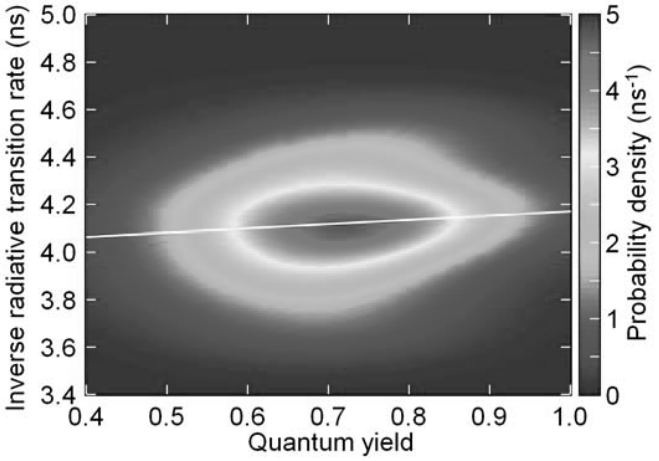

Figure 8. A probability density distribution quantum yield and inverse radiative transition rate obtained from 28 PI molecules. The distribution has its maximum at 0.72 and 4.1 ns, respectively. The solid white line represents a linear least square fit through the distribution.

We employed a bootstrap algorithm for estimating the mean square deviation of the fitted lifetime for each molecule at each cavity width [97]. Mean square deviations of the single molecule lifetime values did typically not exceed 0.1 ns. We also used a bootstrap analysis for estimating the mean square deviation of the QY and the inverse radiative transition rate as obtained by fitting theoretical curves against the experimentally determined dependencies of fluorescence lifetime on cavity width. Assuming that, for each molecule, these mean square deviation values describe the widths of a corresponding two-dimensional Gaussian distribution in QY-τ_{rad} parameter space, we superimposed these Gaussian distributions of all molecules in one plot, resulting in a probability density plot of QY versus τ_{rad} values. This plot is shown in the Figure 8. The maximum of the probability density distribution corresponds to a value 0.72 for the QY and of 4.1 ns for τ_{rad}, which is in excellent agreement with values obtained from ensemble measurements (0.75 and 4.2 ns respectively) [42]. The solid line represents a linear least square fit through the distribution. An inclination of 0.18 ns^{-1} shows that the molecule-to-molecule variation in τ_{rad} is much smaller than that of QY. This is in excellent agreement with the expectation that local variations in interaction between a fluorescent molecule and its surrounding (SiO_2, polymer) will mostly affect its non-radiative transition rate but

not so much its radiative transition rate, which is mostly determined by the coupling of the transition to the electromagnetic field.

5. Photoluminescence of SiO_2 nanoparticles in glass-air confinement*

* SiO_2 and Si nanopowder was synthesized by Torsten Schmidt, Karsten Potrick and Jana Sommerfeld (Research group of Prof. Dr. Friedrich Huisken, University of Jena)

Since the first observation of red photoluminescence (PL) from nanostructured porous silicon in 1990 [70,71] there has been increasing interest in the study of the optical properties of nanostructured silicon. While this observation was attributed to the radiative recombination of charge carriers in a quantum-confined system, other authors made defect luminescence responsible for the PL of their nanocrystalline Si samples [72,73]. Since these days, there is still ongoing discussion on whether the PL originates from intergap transitions in quantum-confined systems or whether it is due to surface defect states (see ref [74] for an early review). Very recently, in an elegant experiment, Godefroo et al. [75,76] were able to control the origin of the PL of their silicon nanocrystals (Si NCs) and to switch between quantum-confined and defect PL by hydrogen passivation and UV irradiation, respectively. Using a single size-dispersed sample of Si NCs with diameters ranging from 2.5 to 8 nm, Ledoux et al. [77] could show that the PL of naturally oxidized Si NCs produced by gas-phase condensation was governed by quantum confinement with a small deviation occurring for small Si NCs. This observation was in agreement with the study of Wolkin et al. [78] who compared the PL of hydrogen- and oxygen-passivated Si NCs with theoretical results and found that defect luminescence via oxygen-related inner-gap states becomes operative when quantum confinement causes the band gap to exceed a certain energy. The same observation has been made by Martin et al. [79] in their confocal microscopy investigation on single Si NCs. Their study is in accordance with a gradual transition of the photoluminescence from PL governed by quantum confinement for large Si NCs to defect luminescence for small Si NCs.

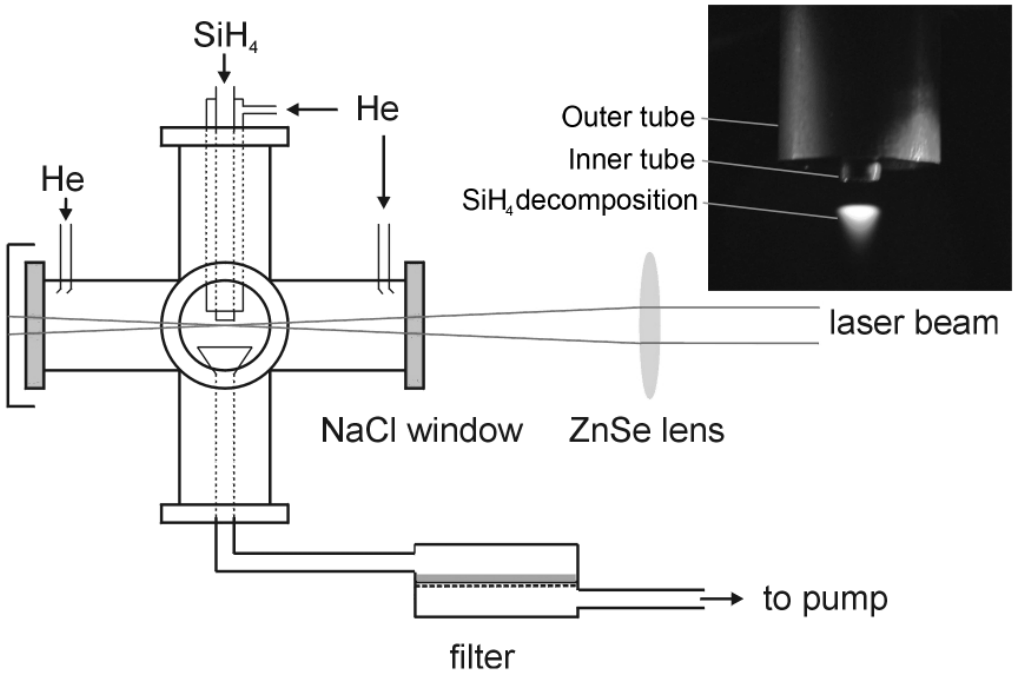

Figure 9. Schematic view of the gas flow reactor. The reactant gas SiH_4 enters through the inner tube, the confinement gas He through the outer tube. The flow of the gases is regulated by controlling independently flow velocity and concentration by means of a flow meter system. The radiation of a pulsed CO_2 laser enters and leaves the reactor through NaCl windows and is focused tightly below the inner tube perpendicular to the gas flow axis to induce the decomposition of SiH_4.
Inset: Photography of the reaction zone. The inner tube and the outer tube for admitting the reactant gas and the confinement gas, respectively. The decomposition of silane (SiH_4) induced by the CO_2 laser radiation results in a visible luminescence, appearing just 2 – 3 mm below the inner tube of the flow reactor.

The defect luminescence taking place in oxygen-passivated Si NCs originates from localized states in the SiO_2 shell surrounding the crystalline silicon core. The same states should also be operative if the entire Si core is removed, for example, by full oxidation. Hence, the question arises whether the same defect luminescence can also be observed in SiO_2 nanoparticles (SiO_2 NPs), which are prepared by intentional oxidation of Si NCs. Indeed, a few years ago, Colder et al. [80] reported on the observation of strong luminescence from hollow SiO_2 NPs that had been obtained from Si NCs by full oxidation in water.

The technique for synthesis of ultra fine silicon powder is based on laser-induced pyrolysis of the gaseous precursor silane (SiH_4). The dissociation of SiH_4

followed by gas phase condensation and subsequent formation of crystalline silicon quantum dots (Si NCs) takes place in a laser-driven gas flow reactor. For decomposition of the precursor molecules a pulsed CO_2 laser is used providing very sharp temperature gradients in the gas phase combined with reactions proceeding in a wall-less environment.

A schematic view of the flow reactor employed for synthesis of Si NCs is shown in Figure 9. The reactor is built from a standard stainless steel NW40 cross vacuum fitting. The reaction gas enters the centre of the flow reactor through a stainless-steel tube of 3 mm diameter. Coaxially arranged, in order to confine the precursor gas flow to the flow axis, helium is flushed as buffer gas through the outer tube of 12 mm diameter. The gas and reaction products are pumped by a backing pump (D16B, Typ Leybold) through a funnel-shaped tube facing the inlet tubes. The produced nanopowder is collected in a filter unit at the exit of the flow reactor.

Gas flow rates and the total pressure inside the reaction chamber and therefore concentrations and flow velocities of the precursor gas and the inert confinement gas are regulated independently by means of an appropriate flow meter system (flow regulation system Typ 647BE, MKS instruments; needle valve 248AC, MKS instruments; pressure gauge, 122A, MKS instruments).

The molecular flow emanating from the inner gas inlet is crossed perpendicularly by the focused radiation (ZnSe lens with 190.5 mm focus length) of a line-tunable CO_2 laser which enters and leaves the reactor through NaCl windows (loss by reflection ≈ 8 %). The viewing ports are continuously flushed with rare gas to prevent nanoparticles from coating the NaCl windows. The infrared laser intensity is regulated by passing the laser beam through a propylene gas cell with adjustable pressure. As pyrolysing laser a pulsed URENCO-TEA CO_2 laser (model ML 104, Uranit) was used. The working conditions for the laser are: repetition rate, 20 Hz; pulse width, 150 ns; laser emission wavelength, 10.6 µm.

During the course of the experiments, various reactor conditions have been tested. However, the following conditions have been found to be particularly favourable: SiH_4 flow rate, 15 sccm; He flow rate, 1100 sccm; pulse energy of the CO_2 laser,

45 mJ. (sccm denotes standard cubic centimeter per minute). The total pressure inside the reaction chamber was kept constant at 330 mbar. The induced decomposition of the gaseous precursor SiH_4 results in visible luminescence, appearing just 2 – 3 mm below the inner tube (see inset in figure 9).

The PL spectra of such SiO_2 nanopowder resembled very much the PL spectra known from Si NCs suggesting that there could possibly be a common origin. In the present study, we have carried out confocal microscopy experiments on individual SiO_2 NPs obtained by full oxidation of freshly synthesized Si NCs by investigating their optical response upon excitation with 473 and 488 nm laser light. The SiO_2 NPs are shown to possess a linear, randomly oriented transition dipole moment for excitation and to exhibit dynamical effects such as transition dipole moment flipping and fluorescence intermittency. The PL spectra reveal a narrow zero-phonon line and a broader phonon band that can be associated with the excitation of longitudinal optical phonons in SiO_2. These spectra are identical to those reported by Martin et al. [79] suggesting that both SiO_2 and Si single particle spectra are governed by the same mechanisms**.**

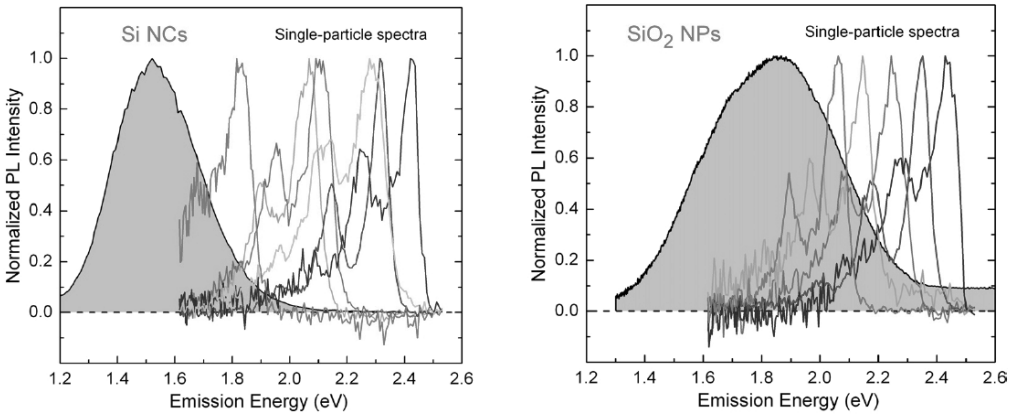

Figure 10. PL spectra of individual Si NCs (left) and SiO_2 NPs (right) are displayed in color. The broad spectra in gray are ensemble spectra taken from the Si and SiO_2 nanopowders, from which the samples for confocal microscopy were prepared.

Since more than two decades, there has been an ongoing discussion on whether the PL from nanostructured silicon originates from intergap transitions assisted by quantum confinement (QC) [70] or whether it is governed by surface related defect centers (DCs) [74]. Very recently, it was shown [75] that it is possible to

control the origin of the PL of Si NCs and to switch between quantum confinement and defect-based PL by hydrogen passivation and UV irradiation, respectively. Investigations of naturally oxidized Si NCs selected in size (2.5 – 8 nm) revealed that the PL is caused by quantum confinement, with some slight deviation occurring for small NCs (2 – 3 nm in diameter) [81]. This observation was confirmed by Wolkin et al. [78] who compared the PL of Si NCs passivated by hydrogen and oxygen with theoretical results. They concluded that defect PL via oxygen-related inner-gap states becomes dominant when quantum confinement causes the band gap to exceed a certain energy. Furthermore, Martin et al. [79] showed that the emission from Si NCs is governed by quantum confinement for the larger particles, while in smaller Si NCs defect-based luminescence is dominant. The defect PL in oxygen-passivated Si NCs originates from localized states in the SiO_2 shell surrounding the crystalline silicon core. Removing the entire Si core, for example by full oxidation, the same states should still be operative. Therefore, the question arises whether the same defect luminescence can also be observed in SiO_2 NPs which are prepared by intentional and complete oxidation of Si NCs. Strong visible luminescence observed from hollow SiO_2 NPs which had been obtained by full oxidation of Si NCs in water was reported by Colder et al. [80]. Surprisingly, the PL spectra of such SiO_2 nanopowder are very similar to the ones recorded from Si NCs, giving rise to the assumption that the origin of the PL can be attributed to the same operating mechanism, which would then obviously be related to defect PL. Thus, in spite of the extensive results on Si NCs, the origin of the emission is still under debate. The observations suggest that there is not a strict separation between quantum confinement-induced PL and defect PL but rather a gradual transition. With the purpose to shed some new light on the origin of the PL in oxidized Si NCs, we have carried out a comparative study of the optical properties of single Si NCs and single SiO_2 NPs employing confocal laser scanning microscopy.

We found evidence that the PL of single Si NCs as prepared for this study is governed by defect luminescence (Figure 10). This conclusion is based on the close resemblance of Si NC and SiO_2 NP spectra and on the short lifetimes around

4 ns, incompatible with radiative recombination of charge carriers in a quantum-confined system. These findings, however, should not be generalized since the present technique is better adapted to processes with short lifetimes and may therefore overlook PL processes with long timescale. Thus, for example, the quantum-confined nature of the PL of larger size-selected Si NCs [81] is not questioned. In the near future, efforts should be undertaken to improve the signal-to noise level in order to search for single Si NCs revealing QC PL with long lifetime.

6. Modification of photoluminescence spectrum and excited state lifetime of a single SiO_2 nanoparticle with a tunable microcavity

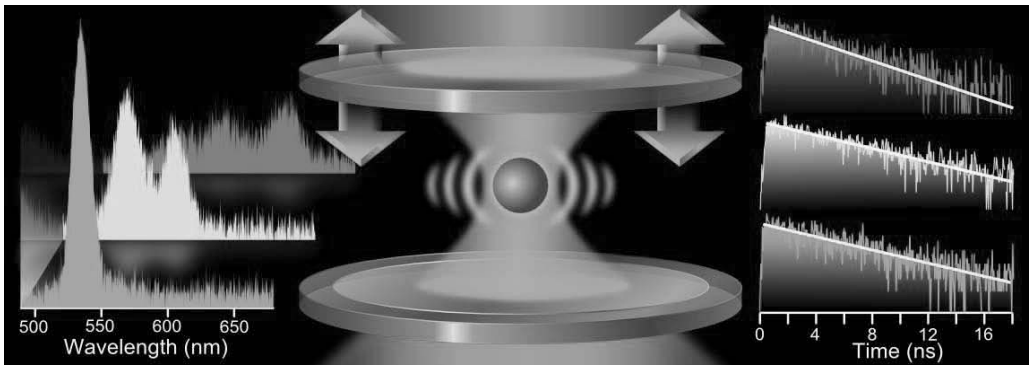

Placing a single SiO_2 nanoparticle in the tunable microcavity we carried out an experiment, which shows a complete picture of the complex electromagnetic interaction of single photon emitters with an electromagnetic field structure that is tailored by the emitter's surrounding. We demonstrate for the first time a redistribution of the PL spectrum and modification of the excited state lifetime of the same individual SiO_2 NP measured at different cavity lengths.

According to Fermi's golden rule, the density of modes of the electromagnetic field inside a cavity is changed with respect to the free space, and hence, the coupling of the dipole transition of an emitter to this field. Recently, extensive experimental studies of the cavity-controlled PL have been conducted for single quantum dots [82-86], molecules [87-89] and atoms [90].

Here we demonstrate the modification of the electron-phonon coupling in a single SiO_2 NP, embedded in a tunable subwavelength microcavity. By varying the distance between the cavity mirrors we change the electromagnetic field mode structure around the single NP, which results in a modification of the probability of electron-phonon coupling. This allows us for the first time to demonstrate a redistribution of the PL spectrum and modification of the excited state lifetime of the same individual SiO_2 NP measured at different cavity lengths. Experimentally,

we demonstrated a redistribution of the PL spectrum and modification of excited state lifetime of the same individual SiO_2 NP at different cavity lengths.

After selecting a single SiO_2 NP, we acquired PL spectra for the same particle at different cavity lengths. For each acquisition, the cavity length was adjusted in resonance with one of the spectral bands of the single particle spectrum. Since the cavity length is reduced down to the range of one half of the emission wavelength, there is only one resonator mode which overlaps with the emission spectrum of the particle. Therefore, the enclosed quantum object is forced to emit photons within a narrowed energy distribution, determined by the $\lambda/2$-resonator mode. This allows us to select those transitions, where the PL will mostly occur, which leads to a modification of the emission spectrum of a single SiO_2 NP. In total, we collected spectra for 14 particles. Figure 11 shows three spectra (red curves) of the same individual SiO_2 NP, recorded at different cavity lengths. The spectra exhibit a clear modification upon tuning the local cavity mode. In particular, Figure 11(a) demonstrates an enhancement of the zero-phonon band, while the phonon-assisted transitions are inhibited. Adjusting the cavity mode in resonance with the spectral bands, originating from phonon-assisted transitions results in their enhancement and suppression of the zero-phonon band. It should be noted, that the redistribution of the spectrum is exclusively determined by the coupling of the SiO_2 NP to the cavity mode, while plasmonic effects do not play a significant role, since the particles are separated from the surface of the bottom mirror with a spacer layer.

For better comparison of the measured single particle spectra and a free space spectrum, the latter was shifted along the wavelength axis to fit the maxima of the cavity-controlled spectra. The position of the single SiO_2 NP PL spectrum in free space depends not only on the type of the defect, but also on its local environment in the SiO_2 structure, which can vary from one particle to another. Therefore, as has been recently observed [91], the single SiO_2 NP PL exhibits a spectral shift, individual for each particle. The free space spectrum was arbitrarily normalized to obtain an equal area for the zero-phonon line with the spectrum shown in Figure 11(a).

Moreover, all measured decay curves could be well fitted by a single-exponential function, which proves that zero-phonon, phonon- and double phonon-assisted transitions occur from the same energy level but possess different transition probabilities, which are related to the probability of electron-phonon coupling.

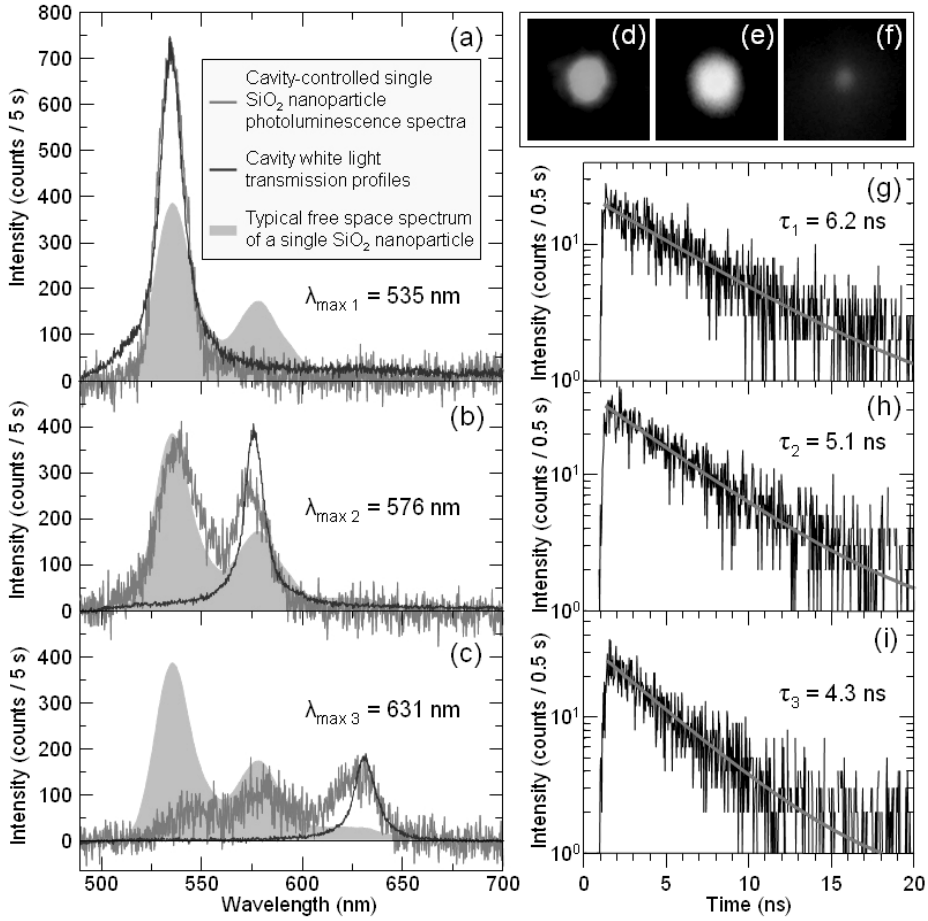

Figure 11. (a)-(c): Measured photoluminescence spectra (red curve) of a single SiO_2 nanoparticle placed inside the micro-resonator at different cavity lengths. The blue curve shows the cavity white light transmission profile, normalized to the respective emission spectrum. The grey shaded area represents a typical photoluminescence spectrum of a free space single SiO_2 nanoparticle, shifted along the wavelength axis to fit the position of the cavity-controlled spectra. (d)-(f): Photographs of the emission of the SiO_2 particle ensemble at respective cavity lengths taken through the eyepiece of the microscope. (g)-(i): Transients of the same single SiO_2 nanoparticle inside the micro-resonator as was used for recording the spectra measured at the. The decay curves (g)-(i) were acquired at the same cavity lengths, which were selected for measurements of single particle spectra shown in figures (a)-(c), respectively. All transients were fitted using a single-exponential decay function (red curves).

Modification of the electron-phonon coupling can be used for applications, where the control of the electron-phonon coupling is required, e.g. phonon-assisted chemical reactions [92,93], electron-defect scattering in plasmonic nanostructures [94] or in recombination processes where the assistance of a phonon modifies the rate of the electron-hole recombination [95]. Modification of single-particle PL spectrum can be considered as a new step toward a single SiO_2 particle tunable laser, which can become an alternative way towards silicon optoelectronics [96]. Combining the crystalline silicon, which possesses the exceptional electronic properties but is a poor light emitter due to an indirect band structure, with SiO_2 structure can allow for converting the electronic signal from silicon chip to the light and back.

References:

[1] Maiman, T.H. *Nature* **1960**, *187 (4736)*, 493.

[2] Yokoyama, H., Ujihara, K. (1995) Spontaneous emission and laser oscillation in microcavities. CRC, Boca Raton, FL.

[3] Chang, R.K., Campillo, A.J. (1996) Optical processes in microcavities. World Scientific, Singapore.

[4] Vahala, K.J. *Nature* **2003,** *424*, 839–846.

[5] Benson, T.M., Boriskina, S.V., Sewell, P., Vukovic, A., Greedy, S.C., Nosich, A.I. (2006) Micro-optical resonators for microlasers and integrated optoelectronics. Frontiers in planar lightwave circuit technology, vol 216. Springer, Berlin, 39–70.

[6] Gerard, J.M., Barrier, D., Marzin, J.Y., Kuszelewicz, R., Manin, L., Costard, E., Thierry-Mieg, V., Rivera, T. *Appl. Phys. Lett.* **1996**, *69*, 449.

[7] Kimble, H.J. *Nature* **2008**, *453*, 1023.

[8] Lipson, M., Chen, T., Chen, K., Duan, X., Kimerling, L.C. *Mat. Sci. Eng. B* **2001**, *81*, 36–39.

[9] Henze, R. et al. (2006) Quantum optics with microresonators. https://www.physik.hu-berlin.de/nano/forschung-en/mr. Accessed 7 July 2009

[10] MHM Salleh (2009) Label free biosensors. http://www.gla.ac.uk/departments/electronicsandelectricalengineering/research/bioelectronics/researchareas/nanophotonics/. Accessed 7 July 2009

[11] EFONGA (2006) http://www.efonga.org/images/microsfera.jpg. Accessed 7 July 2009.

[12] Carmon, T., Vahala, K.J. *Nature Physics* **2007**, *3*,430.

[13] Del'Haye, P., Schliesser, A., Arcizet, O., Wilken, T., Holzwarth, R., Kippenberg, T.J. *Nature* **2007**, *450*, 1214.

[14] Marian, A., Stowe, M.C., Lawall, J.R., Felinto, D., Ye, J. *Science* **2004**, *306*, 2063.

[15] Thorpe, M.J., Moll, K.D., Jones, R.J., Safdi, B., Ye, J. *Science* **2006**, *311*, 1595.

[16] Diddams, S.A., Hollberg, L., Mbele, V. *Nature* **2007**, *445*, 627.

[17] Diddams S.A., Jones D.J., Ye J., Cundiff S.T., Hall J.L., Ranka J.K., Windeler, R.S., Holzwarth, R., Udem, T., Hänsch, T.W. *Phys. Rev. Lett.* **2000**, *84*, 5102.

[18] Weiner, A.M. Rev. *Sci. Instr.* **2000**, *71*, 1929.

[19] Ye, J. *Nature Photon.* **2007**, *1*, 447.

[20] Vollmer, F., Braun, D., Libchaber, A., Khoshsima, M., Teraoka, I., Arnold, S. *Appl. Phys. Lett.* **2002**, 80 (21), 4057

[21] Armani, A.M., Kulkarni, R.P., Fraser, S.E., Flagan, R.C., Vahala, K.J. *Science* **2007**, *317*, 783.

[22] Loncar, M. *Nature Photon.* **2007**, *1*, 565.

[23] Purcell, E.M. *Phys. Rev.* **1946**, *69*, 681.

[24] Fermi, E. *Rev. Mod. Phys.* **1932**, *4*, 87

[25] Kleppner, D. *Phys. Rev. Lett.* **1981**, *47*, 233–236.

[26] Goy, P., Raimond, J.M., Gross, M., Haroche S. *Phys. Rev. Lett.* **1983**, *50*, 1903

[27] Ye, J., Vernooy, D.W., Kimble, H.J. *Phys. Rev. Lett.* **1999**, *83*, 4987

[28] Bennett, A.J., Unitt, D.C., See, P., Shields, A.J., Atkinson, P., Cooper, K., Ritchie, D.A. *Appl. Phys. Lett.* **2005**, *86*, 181102

[29] Steiner, M., Korlacki, R., Hartschuh, A., Meixner, A.J. *Appl. Phys. Lett.* **2007**, *90*, 183122.

[30] Korlacki, R., Steiner, M., Qian, H.H., Hartschuh, A., Meixner, A.J. *Chem. Phys. Chem.* **2007**, *8*, 1049.

[31] Steiner, M., Qian, H., Hartschuh, A., Meixner, A.J. *Nano Lett.* **2007**, *7*, 2239–2242.

[32] Xia, F., Steiner, M., Lin, Y.-M., Avouris, P. *Nature Nanotechnol.* **2008**, *3*, 609–613.

[33] Steiner, M., Xia, F., Qian, H., Lin, Y.-M., Hartschuh, A., Meixner, A.J., Avouris, P. *Proc. SPIE* **2008**, 7037,703713

[34] Moerner, W.E. *New. J. Phys.* **2004**, *60*, 88.

[35] Lounis, B., Orrit, M. *Rep. Prog. Phys.* **2005**, *68*, 1129–1179.

[36] Ye, J., Kimble, H.J., Katori, H. *Science* **2008**, *320*, 1734.

[37] Begon, C., Rigneault, H., Jonsson, P., Rarity J.G. *Single Molecules* **2000**, 1, 207.

[38] Hou, L., Hou, G., Mo, Y., Peng, J., Cao, Y. *Appl. Phys. Lett.* **2005**, *87*, 243504.

[39] Langner, M., Gehlhaar, R., Schriever, C., Frob, H., Lyssenko, V.G., Leo, K. *Appl. Phys. Lett.* **2007**, *91*, 181119.

[40] Langner, M., Gehlhaar, R., Hintschich, S.I., Frob, H., Wendrock, H., Lyssenko, V.G., Leo K. *Opt. Quant. Electr.* **2008**, 40, 403–409

[41] Enderlein, J. *Phys. Chem. Chem. Phys.* **2002**, *4*, 2780.

[42] Steiner, M., Schleifenbaum, F., Stupperich, C., Failla, A.V., Hartschuh, A., Meixner, A.J. *Chem. Phys. Chem.* **2005**, *6*, 2190.

[43] Schleifenbaum, F., Elgass, K., Steiner, M., Enderlein, J., Peter, S., Meixner, A. J., *Proc. SPIE* **2009**, *7185*, 718504.

[44] Lukosz, W., *J. Opt. Soc. Am.* **1979**, *69*, 1495.

[45] Lieberherr, M., Fattinger, C., and Lukosz, W., *Surf. Sci.* **1987**, *189*, 954.

[46] Stefani, F.D., Vasilev, K., Bocchio, N., Stoyanova, N., and Kreiter, M., *Phys. Rev. Lett.* **2005**, *94*, 023005.

[47] Enderlein, J., *Phys. Chem. Chem. Phys.* **2002**, *4*, 2780.

[48] Steiner, M., Schleifenbaum, F., Stupperich, C., Failla, A.V., Hartschuh, A., and Meixner, A.J., *Chem. Phys. Chem.* **2005**, *6*, 2190.

[49] Chizhik, A.I., Enderlein, J., Schleifenbaum, F., Gutbrod, R., Chizhik, A.M., Khoptyar, D. and Meixner, A.J., *Phys. Rev. Lett.* **2009**, *102*, 073002.

[50] Steiner, M., Failla, A.V., Hartschuh, A., Schleifenbaum F., Stupperich C. and Meixner, A.J., *New J. Phys.* **2008**, *10*, 123017.

[51] Reineke, S.; Lindner, F.; Schwartz, G.; Seidler, N.; Walzer, K.; Lüssem, B.; Leo, K. *Nature* **2009**, *459*, 234-238.

[52] Lounis, B.; Moerner, W. E. *Nature* **2000**, *407*, 491-493.

[53] Thompson, B. C.; Frechet, J. M. J. *Angew. Chem. Int. Ed.* **2008**, *47*, 58-77.

[54] Tessler, N. *Adv. Mat.* **1999**, *11*, 363-370.

[55] Medintz, I. L.; Uyeda, H.; Goldman, E. R.; Mattoussi, H. *Nature Mat.* **2005**, *4*, 435-446.

[56] Vavilov, S. I. *Z. Phys.* **1924**, *22*, 266.

[57] Demas, J. N.; Crosby, G. A. *J. Phys Chem.* **1971,** *75*, 991-1024.

[58] Brannon, E. H.; Magde, D. *J. Phys. Chem.* **1978**, *82*, 705-709.

[59] Macklin, J.; Trautman, J.; Harris, T.; Brus, L. *Science* **1996**, *272*, 255-258.

[60] Brokmann, X.; Coolen, L.; Dahan, M.; Hermier, J. P. *Phys. Rev. Lett.* **2004**, *93*, 107403-1-4.

[61] Ambrose, W.P.; Goodwin, P. M.; Martin, J.C.; Keller, R. A. *Science* **1994**, *265*, 364-367.

[62] Trabesinger, W.; Kramer, A.; Kreiter, M.; Hecht, B.; Wild, U.P. *Appl. Phys. Lett.* **2002**, *81*, 2118-2120.

[63] Buchler, B. C.; Kalkbrenner, T.; Hettich, C.; Sandoghdar, V. *Phys. Rev. Lett.* **2005**, *95*, 063003-1-4.

[64] Vahala, K. J. *Nature* **2003**, *424*, 839-846.

[65] Steiner, M.; Schleifenbaum, F.; Stupperich, C.; Failla, A. V.; Hartschuh, A.; Meixner, A. J. *Chem. Phys. Chem.* **2005**, *6*, 2190-2196.

[66] Chizhik, A. I.; Schleifenbaum, F.; Gutbrod, R.; Chizhik, A. M.; Khoptyar, D.; Meixner, A. J.; Enderlein, J. *Phys. Rev. Lett.* **2009**, *102*, 073002-1-4.

[67] Dulkeith, E.; Morteani, A. C.; Niedereichholz, T.; Klar, T. A.; Feldmann, J.; Levi, S. A.; van Veggel, F. C. J. M.; Reinhoudt, D. N.; Möller, M.; Gittins, D. I. *Phys. Rev. Lett.* **2002**, *89*, 203002-1-4.

[68] Anger, P.; Bharadwaj, P.; Novotny, L. *Phys. Rev. Lett.* **2006**, *96*, 113002-1-4.

[69] Kinkhabwala, A.; Yu, Z.; Fan, S.; Avlasevich, Y.; Müllen, K.; Moerner, W. E. *Nature Photon.* **2009**, *3*, 654-657.

[70] Canham, L. T. *Appl. Phys. Lett.* **1990**, *57*, 1046.

[71] Lehmann, V.; Go¨sele, U. *Appl. Phys. Lett.* **1991**, *58*, 856.

[72] Prokes, S. M. *Appl. Phys. Lett.* **1993**, *62*, 3244.

[73] Kanemitsu, Y.; Okamoto, S.; Otobe, M.; Ota, S. *Phys. Re*V. *B* **1997**, *55*, R7375.

[74] Cullis, A. G.; Canham, L. T.; Calcott, P. D. J. *J. Appl. Phys.* **1997**, *82*, 909.

[75] Godefroo, S.; Hayne, M.; Jivanescu, M.; Stesmans, A.; Zacharias, M.; Lebedev, O. I.; Van Tendeloo, G.; Moshchalkov, V. V. *Nat. Nanotechnol.* **2008**, *3*, 174.

[76] Gösele, U. *Nat. Nanotechnol.* **2008**, *3*, 134.

[77] Ledoux, G.; Gong, J.; Huisken, F.; Guillois, O.; Reynaud, C. *Appl. Phys. Lett.* **2002**, *80*, 4834.

[78] Wolkin, M. V.; Jorne, J.; Fauchet, P. M.; Allan, G.; Delerue, C. *Phys. Rev. Lett.* **1999**, *82*, 197.

[79] Martin, J.; Cichos, F.; Huisken, F.; von Borczyskowski, Chr. *Nano Lett.* **2008**, *8*, 656.

[80] Colder, A.; Huisken, F.; Trave, E.; Ledoux, G.; Guillois, O.; Reynaud, C.; Hofmeister, H.; Pippel, E. *Nanotechnology* **2004**, *15*, L1.

[81] G. Ledoux, J. Gong, F. Huisken, O. Guillois, and C. Reynaud, *Appl. Phys. Lett.* **2002**, *80*, 4834-4836 .

[82] Santori, C.; Fattal, D.; Vuckovic, J.; Solomon, G.S.; Yamamoto, Y. *Nature* **2002**, *419*, 594-597.

[83] Englund, D.; Fattal, D.; Waks, E.; Solomon, G.; Zhang, B.; Nakaoka, T.; Arakawa, T.; Yamamoto, Y.; Vuckovic, J. *Phys. Rev. Lett.* **2005**, *95*, 0139041-4.

[84] Amans, D.; Callard, S.; Gagnaire, A.; Joseph, J.; Ledoux, G.; Huisken, F. *Mater. Sci. Eng., B* **2003,** *101*, 305-308.

[85] Amans, D.; Callard, S.; Gagnaire, A, Joseph, J.; Huisken, F.; Ledoux, G. *J. Appl. Phys.* **2004**, *95*, 5010-5013.

[86] Kazes M.; Lewis, D. Y.; Ebenstein, Y.; Mokari, T.; Banin U. *Adv. Mater.* **2002,** *14*, 317-321.

[87] Steiner, M.; Schleifenbaum, F.; Stupperich, C.; Failla, A.V.; Hartschuh, A.; Meixner, A.J. *Chem. Phys. Chem.* **2005,** *6*, 2190.

[88] Chizhik, A.; Schleifenbaum, F.; Gutbrod, R.; Chizhik, A.; Khoptyar, D.; Meixner, A.J. *Phys. Rev. Lett.* **2009**, *102*, 073002-1.

[89] Baer, S.; Chizhik, A.; Gutbrod, R.; Schleifenbaum, F.; Chizhik, A.; Meixner, A.J. *Anal. Bioanal. Chem.* **2010**, *396*, 3.

[90] Aoki, T.; Dayan, B.; Wilcut, E.; Bowen, W.P.; Parkins, A.S.; Kippenberg, T. J.; Vahala, K.J.; Kimble, H.J. *Nature* **2006**, *443*, 671-674.

[91] Chizhik, A.M.; Chizhik, A.I.; Gutbrod, R.; Meixner, A.J.; Schmidt, T.; Sommerfeld, J.; Huisken, F. *Nano Lett.* **2009**, *9*, 3239.

[92] Liu, C.-S.; Hernandez, R.; Schuster, G.B. *JACS* **2004**, *126*, 2877-2884.

[93] Killelea, D.R.; Campbell, V.L.; Shuman, N. S.; Utz A. L. *Science* **2008**, *319*, 790-793.

[94] Link S.; El-Sayed, M. A.; *J. Phys. Chem. B* **1999**, *103*, 8410-8426.

[95] Alivisatos, A.P. *J. Phys. Chem.* **1996**, *100*, 13226-13239.

[96] Ball, P. *Nature* **2001,** *409*, 974-976.

[97] Efron, B. *Ann. Statt.* **1979**, *7*, 1-26.

[98] Drexhage, K. H. *Prog. Opt.* **1974**, *12*, 163.

Chapter 1

Microcavities: tailoring the optical properties of single quantum emitters

In this chapter, we present a general review of different microresonator structures and how they can be used in future device applications in modern analytical methods by tailoring the optical properties of single quantum emitters. The main emphasis is on the tunable λ/2-Fabry–Perot-type microresonator which we used to obtain the results presented in this article. By varying the mirror distance the local mode structure of the electromagnetic field is altered and thus the radiative coupling of fluorescent single quantum emitters embedded inside the resonator to that field is changed, too. As a result a modification of the optical properties of these quantum emitters can be observed. We present experimental as well as theoretical results illustrating this effect. Furthermore, the developed resonator can be used to determine the longitudinal position of embedded emitters with an accuracy of λ/60 by analyzing the excitation patterns of nano-sized fluorescent polymer spheres after excitation with a radially polarized doughnut mode laser beam. Finally, we will apply this
resonator to a biological system and demonstrate the modification of Förster resonant energy transfer (FRET) efficiency by inhibiting the excited state energy transfer from the donor to the acceptor chromophore of a single DsRed protein.

This chapter is based on:

Bär S., Chizhik, A.I., Gutbrod, R., Schleifenbaum, F., Chizhik, A.M., Meixner, A.J. "Microcavities: tailoring the optical properties of single quantum emitters" *Anal. Bioanal. Chem.* **2010**, *396*, 3-14.

Anal Bioanal Chem (2010) 396:3–14
DOI 10.1007/s00216-009-3227-5

REVIEW

Microcavities: tailoring the optical properties of single quantum emitters

Sebastian Bär · Alexey Chizhik · Raphael Gutbrod · Frank Schleifenbaum · Anna Chizhik · Alfred J. Meixner

Received: 30 July 2009 / Revised: 1 October 2009 / Accepted: 7 October 2009 / Published online: 12 November 2009

Abstract We present a general review of different microresonator structures and how they can be used in future device applications in modern analytical methods by tailoring the optical properties of single quantum emitters. The main emphasis is on the tunable $\lambda/2$-Fabry–Perot-type microresonator which we used to obtain the results presented in this article. By varying the mirror distance the local mode structure of the electromagnetic field is altered and thus the radiative coupling of fluorescent single quantum emitters embedded inside the resonator to that field is changed, too. As a result a modification of the optical properties of these quantum emitters can be observed. We present experimental as well as theoretical results illustrating this effect. Furthermore, the developed resonator can be used to determine the longitudinal position of embedded emitters with an accuracy of $\lambda/60$ by analyzing the excitation patterns of nano-sized fluorescent polymer spheres after excitation with a radially polarized doughnut mode laser beam. Finally, we will apply this resonator to a biological system and demonstrate the modification of Förster resonant energy transfer (FRET) efficiency by inhibiting the excited state energy transfer from the donor to the acceptor chromophore of a single DsRed protein.

Keywords Microresonator · Single molecule spectroscopy · Confocal microscopy · Autofluorescent proteins · Higher-order laser modes · FRET

S. Bär (✉) · A. Chizhik · R. Gutbrod · F. Schleifenbaum · A. Chizhik · A. J. Meixner (✉)
Institute of Physical and Theoretical Chemistry,
Eberhard Karls University,
72076 Tübingen, Germany
e-mail: sebastian.baer@uni-tuebingen.de
e-mail: alfred.meixner@uni-tuebingen.de

Introduction

Since the realization of the first laser in 1960 by Maiman [1], interest in optical resonators and their use in diverse applications, from fundamental studies to industrial manufacturing, has grown continuously. Photonic devices have followed the trend towards miniaturization witnessed in the semiconductor industries. This development has already reached a level in which one has to deal with single molecules or even atomic structures. Microresonators are a very suitable tool to control the optical properties of these quantum emitters (see, e.g., [2–5] and citations therein). However, depending on the application area, today's microresonators vary much in their design—from classical configurations using distributed Bragg reflectors (DBR) or metallic mirrors via microtoroids to photonic crystal-based cavities—and thus also in their properties. A detailed summary can be found elsewhere [4, 5], and Fig. 1 shows different types of microresonators. This diversity has its origin in the manifold photonic devices needed in future applications. By modifying the shape and the size of a resonator and changing its material composition it is already possible to generate and/or support only desired wavelengths and polarizations. This offers the potential for developing new types of photonic devices such as low-threshold microlasers, ultra-small optical filters, and switches for wavelength-division-multiplexed (WDM) networks. In particular, whispering gallery mode (WGM) lasers and photonic crystal devices are very suitable for integration in new photonic devices due to their compact size, allowing a device density of 10^5 cm^{-2} [5]. These key elements provide generation, guiding, coupling, switching, splitting, multiplexing, and demultiplexing of optical signals.

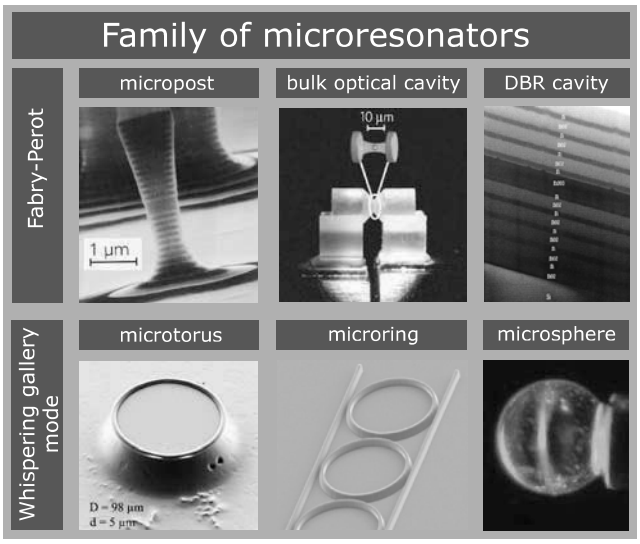

Fig. 1 Different types of microresonators. Fabry–Perot-type resonators: micropost (reprinted from [6] with permission from the American Institute of Physics, copyright 1996), bulk optical cavity (adapted from [7] with permission from Macmillan Publishers, copyright 2008), and distributed Bragg reflector (DBR cavity) (reprinted from [8] with permission from Elsevier, copyright 2001). Whispering gallery mode resonators: microtorus [9], microring [10], and microsphere [11]

In the last couple of years the progress in developing new functions of microcavites, most of them already known from their macroscopic counterparts, was enormous. Using a toroidal silica microresonator Vahala's group was able to demonstrate tunable continuous-wave third-harmonic generation at room temperature [12]. Based on a silica-on-silicon microstructure the 1,550-nm pump wavelength was converted into 517-nm emission with a threshold as low as 300 μW of pump power. Using silica toroid microresonators it is also possible to generate optical frequency combs in a very efficient way as demonstrated by Del'Haye et al. [13]. These combs consist of equidistant frequencies covering a large wavelength region and therefore they are useful in precision spectroscopy, such as studies of dynamic processes in atoms [14], gas sensing [15], and molecular fingerprinting [16]. Other applications based on frequency combs include frequency metrology [17] and optical waveform synthesis for telecommunications [18, 19].

Most of the effects described above are based on the properties of the resonator itself (material, shape, Q factor etc.). Additionally, the microresonator can be used either to tailor the optical properties of single quantum emitters placed inside or it can be modified by the presence of a quantum object. The latter effect can be used in bioanalytics for label-free single molecule detection. In this case, binding of molecules to the functionalized surface of microspheres [20] or microtoroids [21] can be observed by a stepwise shift of the resonance frequency based on a thermo-optic effect. As this sensor is applicable with single molecule sensitivity it is interesting not only for biomedicine but also for pollution monitoring and security issues [22].

The 'controlling effect' of a microresonator on quantum emitters which are placed inside was described by Purcell in 1946: an emitter within a low-loss, wavelength-scale confined structure, like a resonator, alters its spontaneous emission rate [23]. This effect is quantized by Fermi's golden rule, which states that the spontaneous emission rate depends on the density of modes (DOM) of the electromagnetic field [24]. As a result of the changed DOM inside a microresonator compared with non-confined space the spontaneous emission is either suppressed [25] or enhanced [23]. Of special interest is the latter case, which can be expressed by the Purcell factor

$$F_P = \frac{3}{4\pi^2}\left(\frac{\lambda_c}{n}\right)^3 \frac{Q}{V} \tag{1}$$

where λ_c/n is the wavelength within the material, and Q and V are the quality factor and mode volume of the cavity, respectively. As a consequence of the enhanced (or suppressed) spontaneous emission rate the spectral characteristics of quantum emitters placed inside a microresonator are changed. For broadband emitters one has to take optical dispersion effects into account, i.e., wavelength-dependent electromagnetic coupling of the emitter to its environment. As a result the observable emission spectrum of the embedded emitter can undergo drastic changes, which are determined by frequency-selective coupling efficiencies between the emitter and available cavity modes. This effect will be discussed later in more detail for a planar metallic subwavelength microcavity.

There is obviously a great variety amongst the introduced microcavities, e.g., practical differences (ease of fabrication, connectivity to waveguides, chip integration) or principal differences (free spectral range (FSR), Q factor, mode volume). However, for fundamental research on the physics of the interaction between light and matter and cavity quantum electrodynamics the classical Fabry–Perot resonator type using external mirrors is first choice as it is versatile and offers a small mode volume. In 1983 Goy and coworkers reported on the first observation of enhanced spontaneous emission in a resonant cavity by using Rydberg atoms of sodium [26]. These types of experiments became increasingly interesting and formed the basis of the above-mentioned applications. In recent years, the investigations of single quantum emitters, such as atoms [27], ions [8], quantum dots [28], molecules [29], or single-walled carbon nanotubes [30–33], in a Fabry–Perot-type cavity have increased, especially driven by the quest for a single photon source for quantum communication and computing [7, 34–36].

Microresonators for single molecule detection and spectroscopy

Of course, the given introduction can only provide limited insight into the large field of microresonators. Thus, we will limit the discussion to the Fabry–Perot-type microresonator and present the possibility to control the optical properties of single molecules with such a device. In general, a Fabry–Perot resonator consists of two plane parallel reflecting surfaces with a distance d allowing multiple beam interference. The medium in between these surfaces is described by its refractive index $n(\lambda)$. For transmission through the resonator, i.e., constructive interference, the half-wavelength $\lambda/2$ has to fit an integer number of times into the cavity. More specifically the resonance condition for irradiation normal to the plane parallel mirrors is

$$m\lambda/2 = n(\lambda)d. \tag{2}$$

Such a resonator type is often characterized by its frequency spacing between adjacent resonances ν_j and ν_{j+1}, called free spectral range (FSR), which is defined by

$$\mathrm{FSR}_\nu = \Delta_\nu = \nu_{j+1} - \nu_j = \frac{c_0}{2n(\nu)d} \tag{3}$$

where c_0 is the vacuum velocity of light. In the case of microresonators where d is comparable to $\lambda/2$ the penetration of the optical mode into the mirror has to be taken into account. Another important characteristic of a resonator is its finesse F, which is a measure for the number of round trips before the stored energy decays to $1/e$ of its original value. The higher the reflectivity R of the mirrors is the longer the photon storage time will be and, as a consequence, the sharper the transmission maxima characterized by $\delta\nu$ will become. Formally, the finesse can be written as

$$F = \frac{\mathrm{FSR}}{\delta\nu} = \frac{\pi(R_1R_2)^{1/4}}{1-\sqrt{R_1R_2}}. \tag{4}$$

Sometimes, the finesse is replaced by the quality factor Q, given by the ratio of transmission wavelength λ_0 and peak width $\delta\lambda$, i.e., $Q=\lambda_0/\delta\lambda=\nu_0/\delta\nu$. The last expression in particular reflects nicely the correlation between the energy decay in the time domain (finite photon storage time) and the peak width in the frequency domain. Depending on the reflectivity, Q values reach 50 when metal mirrors are used and up to several thousands in the case of Bragg mirrors.

Plane-parallel resonators are commonly used in microchip and microcavity lasers based on confined electronic systems in semiconductors with reduced dimensionality but not on single quantum emitters. Experimental results are mostly related to ensemble measurements [37] as these systems are promising candidates for more efficient LEDs, OLEDS, and microlasers [38–40]. However, experimental results of direct modification of the emission behavior of a single molecule in a microcavity are rare in the literature, even though microcavities are a suitable tool for manipulating the optical properties of quantum emitters. For example, strong changes in the emission and absorption spectra are predicted for a Rhodamine 6G molecule embedded within a spherical metal nanocavity [41]. Experimentally, the effect of emission changes was observed qualitatively by Steiner et al. [42] who investigated single isolated perylene dye molecules in a planar metal microcavity for different mirror spacings and hence for different electromagnetic mode structures. As a result of the fixed mirror spacings that were used in these experiments each single molecule could only be investigated at one specific resonator length. By developing this design further into a resonator with tunable mirror spacing we were able to actively change the optical properties such as the emission rate and emission spectrum of a single molecule, as presented by Chizhik et al. for the first time [43]. Thus, we will present at first a detailed view of our resonator design and the principle of its function, followed by a brief description of the experimental setup. Then we will focus on the resonators' effect on the emission of different single quantum emitters (i.e., single molecules, fluorescent spheres) placed inside the cavity, where we could not only manipulate the emission behavior of these emitters, but also determine their exact position and orientation inside the cavity by using a radially polarized doughnut-mode laser beam. With respect to the application potential of this type of microresonator, our first experiments on FRET studies of the DsRed protein system [44] and biomolecules in a liquid environment [45] are presented.

Experimental

The microresonator setup presented here is an advancement of the non-tunable cavity used in previous experiments [42]. This tunable Fabry–Perot-type microresonator consists of two silver mirrors, as shown in Fig. 2 together with a simplified sketch of the confocal microscope setup. The isolated, single quantum emitters under investigation are embedded in a polymer matrix and placed between these two mirrors. The polymer matrix prevents clustering of the molecules and allows one to easily investigate single species. In addition, this polymer matrix immobilizes the molecules to avoid translational and rotational motions during measurements. To ensure efficient excitation and emission through the bottom mirror it consists only of a 30-nm silver layer resulting in a transmission of this mirror of approx. 25%.

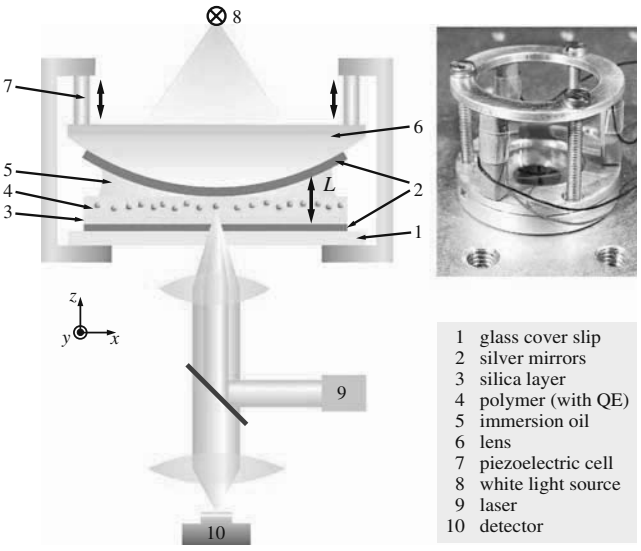

Fig. 2 Schematic of the microresonator and the simplified confocal microscope setup

In contrast, the top mirror deposited on the curved surface of a plano-convex 150-mm-focal-distance lens has a thickness of 60 nm, offering a higher reflectivity of approx. 95% (calculation of the transmission and reflection coefficients can be found elsewhere [46]). These Ag layers as well as the silica spacers (cf. Fig. 2) were fabricated by electron beam evaporation (EBV). The bottom SiO_2 spacer layer prevents interaction between the quantum emitters (e.g., dye molecules) and the silver to avoid quenching effects. Varying the thickness of these silica layers allows us also to place the molecules in a defined distance from the bottom mirror, which is important for orientation and position determination (see Sect. Orientation and position of single quantum emitters). Optionally, another silica layer can be deposited on top of the dye–polymer film, which serves as the active medium, to minimize oxidation processes of the molecules. To provide an optical homogeneous intracavity medium, but being flexible enough to allow tuning of the cavity length, a refractive-index-matching liquid fills the remaining space between the multilayered cover slip and the upper mirror.

The active dye-doped polymer layer was fabricated by spin coating a subnanomolar solution of either Rhodamine 6G or the perylene derivative *N*-(2,6-diisopropylphenyl) perylene-3,4-dicarboximide (PI) in poly(methyl methacrylate) (PMMA) dissolved in dichloromethane. Using an atomic force microscope (AFM) the resulting layer thickness was determined to be around 70 nm. To obtain a reference spectrum of the polymer-embedded molecules, a single molecule sample was prepared by spin coating the same polymer–dye–dichloromethane mixture onto a pure glass cover slip. This reference sample will be referred to as the ‘free space sample’.

The whole resonator construction is installed in a homemade aluminum holder. Tuning of the cavity length is achieved via piezoelectric elements mounted at the plane side of the lens. The resonator is then characterized by white-light transmission measurements to monitor the optical quality and the tuning capability (Fig. 3a). The observed Newton rings are a result of the different resonator lengths provided by the lens, i.e., where for a certain wavelength the resonance condition is fulfilled. The central region of the microcavity remains dark, as no visible light can be transmitted below the $\lambda/2$ regime. In turn, the first visible rings indicate exactly the $\lambda/2$ condition. A horizontal displacement of the resonator of 500 nm leads to a resonator length change of the order of 0.5 nm [42], which is of the order of the surface roughness of our silver mirrors as determined by atomic force microscope measurements. Hence, the microcavity can be considered as planar within the focal-spot diameter of the microscope. Applying a voltage to the piezoelectric elements results in an increased diameter of the Newton rings, which shows that the resonator length can be reversibly tuned with nanometer accuracy. Recording the on-axis transmission spectrum of the microcavity (details can be found elsewhere [42]), we obtain a resonator Q factor of 45 (see also Fig. 3b). Even though this value is not very high, it is sufficient for our purpose to modify the emission properties of single quantum emitters.

The following optical measurements on the quantum emitters were performed using an inverted confocal microscope equipped with a high-numerical-aperture objective lens. An argon-ion laser as well as an optically pumped semiconductor laser, both operating at λ=488 nm, served as excitation sources for the fluorescence spectra. Both the reflected excitation light and the fluorescence from the quantum emitters are collected with the same objective lens and after removing the excitation light the remaining fluorescence is focused onto the detector. The detection unit was either a spectrograph equipped with a CCD camera for fluorescence measurements or an avalanche photodiode for sample imaging. Confocal images are produced by raster scanning the sample through the focal spot of the microscope objective. An example is shown in Fig. 3c and d, where one can see an image of the cavity-controlled emission (i.e., emission occurs only in a ring where the resonance condition for the molecular fluorescence is fulfilled) and an image of a single PI molecule, respectively. Both patterns are acquired using a Gaussian excitation beam.

For determination of the three-dimensional orientation of the single molecules as well as for the position measurements of fluorescent beads in the resonator, a radially polarized doughnut-mode laser beam (RPDB) served as excitation source. This mode is generated from the

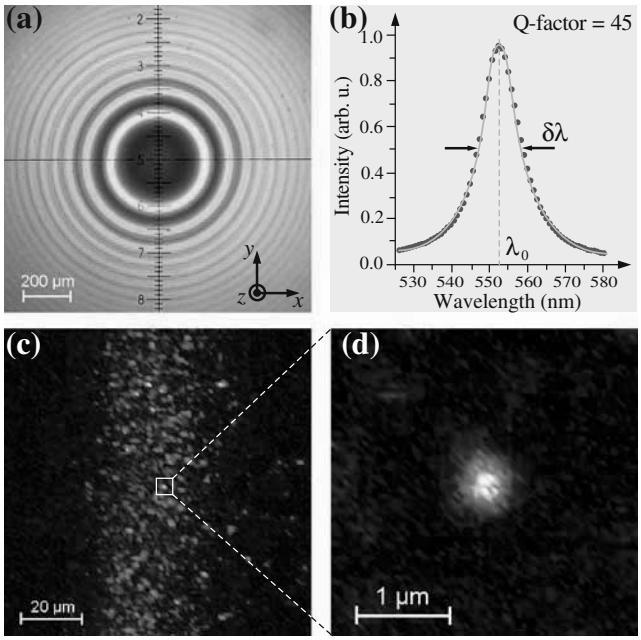

Fig. 3 Cavity characterization: **a** Newton rings, **b** transmission spectrum fitted by a Lorentzian function (*solid line*) giving a cavity Q factor of 45, **c** cavity-controlled emission, **d** single molecule fluorescence

Gaussian beam output of the argon-ion laser according to the method described by Dorn et al. [47] using a polarization converter. A pinhole is used to remove higher spatial frequencies before the beam is expanded to fit in the back aperture of the objective lens. The collimated beam is reflected by a non-polarizing beam-splitter cube and focused onto the sample by the microscope objective.

Results and discussion

Single molecules in a microresonator

For single molecule measurements dye solutions were diluted to 10^{-9} M. However, the final molecular density on the substrate depends also on experimental factors like polymer concentration and rotational speed during the spin-coating process. Thus, to ensure that only one single molecule is located in the focal spot intensity–time traces were collected (not presented here). These intensity trajectories prove very clearly the single step blinking behavior as expected from a single quantum emitter. Once a single molecule was selected, it was possible to alter its emission characteristic by varying the resonator length as can be seen by changes in the fluorescence spectra.

Three representative spectra of a single Rhodamine 6G molecule are shown in Fig. 4a. The observed changes in the fluorescence behavior can be explained by a redistribution of the energy within the different vibronic transitions due to the variations of the resonator mode. Depending on the resonator lengths a certain transition is preferred, i.e., enhanced spontaneous emission rate, while the other transitions are efficiently suppressed. This effect is nicely represented by the four photographs of the emission of an ensemble of PI molecules taken through the eyepiece of the microscope at different resonator lengths. As can be seen in the free space spectrum in Fig. 4b the fluorescence of PI covers a broad spectral range between 500 and 650 nm. Embedded in a resonator, the molecules are forced to emit in a narrow energy distribution allowing the change of emission color from deep green through yellow and orange to red. To exclude

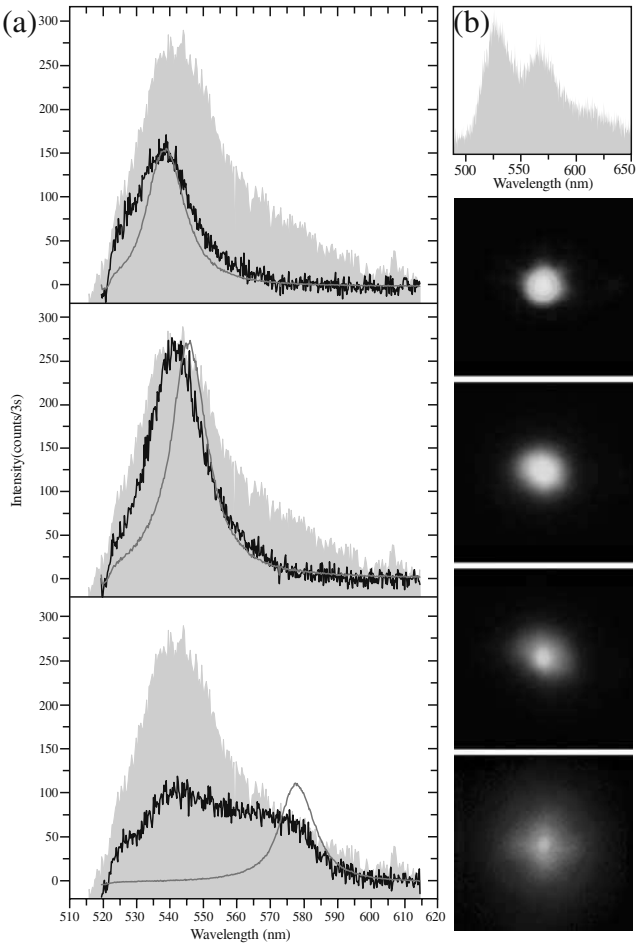

Fig. 4 **a** Cavity-induced changes in the spectral emission characteristics of a single Rhodamine 6G (R6G)molecule. Measured spectra (*black line*) of a single molecule embedded in the microcavity at various values of cavity length. The *red lines* show the white-light transmission profile of the cavity, normalized to the respective emission spectrum, while the *gray shaded area* represents the free space spectrum of a single R6G molecule. **b** Free space fluorescence spectrum of a PI molecule covering a broad spectral range from 500 to 650 nm and four color photographs of the emission of a PI molecule ensemble at different resonator lengths taken through the eyepiece of the microscope

that these emission changes are due to reorientation or movement of the molecules, polarization measurements were performed.

One would expect a modified emission spectrum which is limited to the transmission profile of the microresonator. However, this picture applies only for emission along the resonator axis. For off-axis emission this condition becomes loose, allowing blue-shifted emission with respect to the resonator wavelength. As a high-numerical-aperture objective is used for efficient light collection, this off-axis emission is also collected giving rise to the spectra presented here (clearly visible in the third R6G spectrum in Fig. 4a). While a direct suppression of the off-axis emission is not possible with a Fabry–Perot-type microresonator structure—as this would require a three-dimensional confinement, e.g., photonic crystal structure—the detection of the off-axis emission can be easily suppressed by either choosing an objective with a low numerical aperture or a pinhole in the detection path to cut out the off-axis emission [48].

We have shown that using a tunable subwavelength microresonator one is able to tailor the optical properties of single quantum emitters, i.e., modify the spontaneous emission rate and in turn the spectral shape of emission of one distinct molecule [43].

However, if one really wants to control single quantum emitters, or at least select those which are most suitable, knowledge about the quantum emitters' three-dimensional transition dipole moment orientation and position would be required. As already described in the Experimental section, this task can be solved by using a radially polarized doughnut mode.

Orientation and position of single quantum emitters

The technique of creating higher-order laser modes is well known and was described in the Experimental section. A confocal image of a single quantum emitter will provide the information of its three-dimensional dipole moment orientation in space when an RPDB is used for excitation. Here we briefly present the basic idea and describe first results using this technique, while detailed information can be found elsewhere [49, 50].

An RPDB possesses an electrical field distribution in the focus with components oriented in-plane and in the longitudinal direction (cf. Fig. 5a). As the fluorescence rate R_f of a molecule depends on the projection of the excitation dipole moment $\boldsymbol{\mu}_{exc}$ on the electric field strengths $\mathbf{E}_0$ according to $R_f \propto |\boldsymbol{\mu}_{exc}\mathbf{E}_0|^2$, the obtained excitation patterns have shapes ranging from disk-like and double-lobe patterns, depending on the three-dimensional orientation of the molecule. As can be seen from the calculations presented in Fig. 5b, a double-lobe pattern arises from a

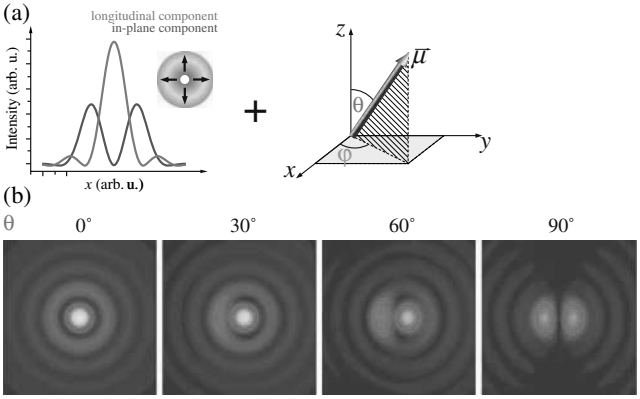

Fig. 5 Interaction of an RPDB with a dipole of a quantum emitter and the calculated resulting patterns for different θ angles (φ=90°=const.). In the *upper left picture* the intensity distribution of the longitudinal and the in-plane component of the RPDB in the focal plane are shown

dipole in the focal plane and changes to a disk-like pattern for a dipole oriented perpendicular to this plane. Based on this consideration confocal images of single molecules are now compared with this theoretical prediction and their orientation can be determined (see Fig. 6).

The presented examples show polymer-embedded PI molecules in a non-confined sample. For determining the orientation inside a microresonator this technique is so far only valid if the position of the emitters is known, e.g., when the molecules are spin-coated on a silica spacer of certain thickness (see Fig. 2). This is due to the different electromagnetic field distribution inside a cavity as compared with free space [51]. First experiments with molecules placed at defined positions indicate that their orientation can be determined inside a resonator. Thus, we tried—in addition to the orientation—to identify the exact longitudinal (i.e., along the optical axis) position of the quantum emitter in a cavity.

In general, it is far more challenging to determine the longitudinal position of a molecule than the lateral one [50,

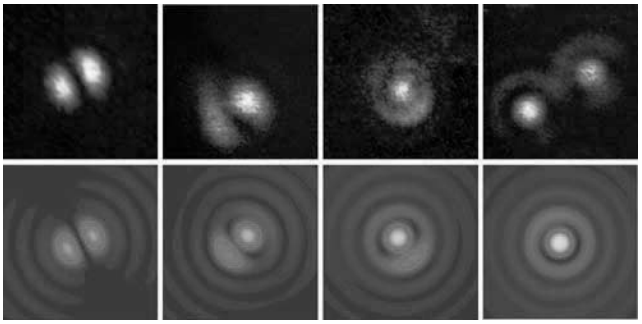

Fig. 6 Experimental (*upper row*) and the corresponding calculated (*lower row*) excitation patterns of five PI molecules resulting from illumination with an RPDM. The corresponding θ/φ angles are: 85°/320°, 60°/45°, 40°/210°, 15°/25°, where φ=0° is in the *x*-direction (cf. Fig. 5)

52, 53], as the focal spot of a lens is at least three times longer than wide due to technical limitations of the numerical aperture of the microscope objective [54].

First experiments have been carried out with polymer spheres of 20 nm in diameter, which contain a large number of fluorescent molecules (approx. 200). As a result these spheres have no preferred dipole orientation and act as isotropic emitters. In turn, a variation in the excitation pattern could only arise due to a changed electromagnetic field for different resonator lengths. This effect was observed for fluorescent spheres in a non-tunable cavity, where the excitation pattern changed from a ring structure to a disk-like structure during raster scanning of the sample, i.e., for changing the cavity length [55]. Using now a tunable resonator as a tool to change the local electric field, we were able to determine the longitudinal position of a single bead with an accuracy of ±2 nm by analyzing the excitation patterns from an RPDB. To illustrate this in more detail, Fig. 7b–d presents the excitation patterns for a specific bead at three different resonator lengths and the corresponding field intensity distribution. For comparison, the field intensity distribution for the non-confined case, i.e., without mirrors, is also presented (see Fig. 7a). The insets in the experimentally recorded patterns display the corresponding calculated cross sections for a constant particle distance of 50 nm from the bottom resonator mirror. A detailed description of the calculation procedure is reported elsewhere [55]. In brief, the resonator structure suppresses the in-plane field components close to the mirror surfaces as well as the longitudinal field components in the central region of the resonator (in comparison with the free space distribution, cf. Fig. 7a). Obviously, the excitation pattern depends strongly on the relative position of the emitter inside the resonator (the absolute position was fixed). For short resonator lengths the bead is located close to the resonator center, resulting in a doughnut-shaped pattern (Fig. 7b), whereas for increased cavity lengths the relative position moves closer to the bottom mirror and thus changes the excitation pattern to a circular spot (Fig. 7d).

As even small variations in the resonator lengths result in significantly different excitation patterns, this effect can be used to determine precisely the longitudinal position of the emitter between the two mirrors. This is demonstrated in Fig. 8, where a line cross section through the experimental pattern (c) in Fig. 7 is fitted by the calculated line profile. In this case, also using the other patterns, the bead position was determined to 48±2 nm. To prove the sensitivity of this method for longitudinal position identification the dashed lines in Fig. 8 represent a deviation of only ±5 nm from the optimum position, which implies a longitudinal resolution better than $\lambda/60$.

Modifying FRET of the autofluorescent protein DsRed by using a microresonator

Another interesting application of microresonators is the study of the interaction between two adjacent dye molecules via a non-radiative dipole–dipole coupling [56]. This type of near-field energy transfer—fluorescent resonance energy transfer (FRET)—plays an important role in light-induced processes in biology and life sciences, especially for the interactions of individual chromophores in a multi-chromophoric system [57–63]. For biological FRET systems the modification of the local photonic mode density inside a resonator structure provides the opportunity to

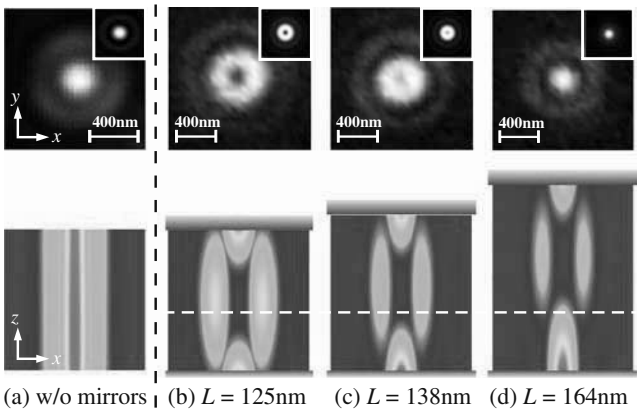

Fig. 7 Electromagnetic field distribution along the optical axis (*lower row*) and corresponding excitation pattern of a single fluorescent sphere perpendicular to the optical axis (*upper row*) for **a** non-confined case without mirrors and **b**–**d** different resonator lengths. The *insets* show the calculated excitation pattern in comparison with the measured patterns

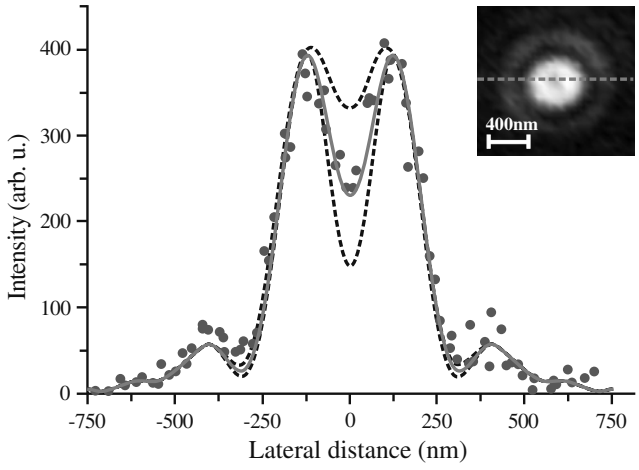

Fig. 8 Line section (*dots*) through the measured excitation pattern shown in Fig. 7c. The fit of the theoretical line section (*red solid curve*) results in this case in a bead position of 50 nm above the lower mirror. The sensitivity of the fit is indicated by the *dotted curves*, which are calculated for a deviation of ±5 nm from the optimum position

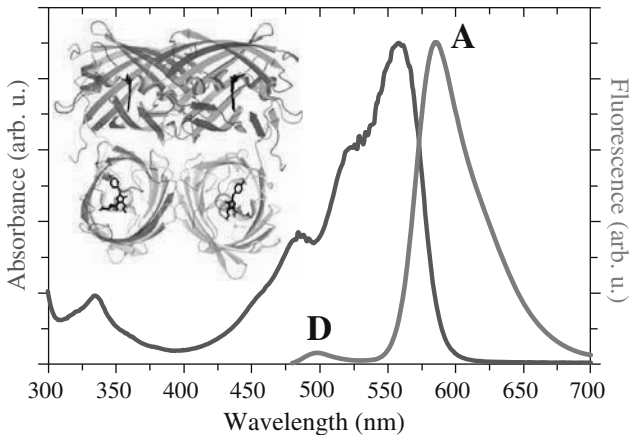

Fig. 9 Absorbance (*blue*) and fluorescence (*red*) spectra of the red fluorescent protein DsRed. The labels *D* and *A* indicate the fluorescence contribution of the donor and acceptor, respectively. The *inset* displays the tetrameric structure of DsRed

control the transfer of excited state energy between the chromophoric subunits without changing their physiological environment or their chemical composition. For studying dipole–dipole coupling of a rigidly coupled multichromophoric system in a confined structure, the red autofluorescent protein DsRed was placed in the $\lambda/2$ Fabry–Perot microresonator (see Fig. 2). The free space optical properties of DsRed, i.e., absorption and emission (see Fig. 9), are determined by its structural composition and geometry. The native tetrameric structure consists of four barrel-shaped subunits, each of them formed by 11 β sheets. These subunits can host either a green- or a red-emitting chromophore with equal probability [64–66] (cf. inset in Fig. 9). However, as two chromophoric subunits are dipole-coupled with a FRET efficiency of up to 95% [64, 65], excitation of the donor in the blue spectral region will result primarily in red fluorescence of the acceptor. This can be seen in the fluorescence spectrum displayed in Fig. 9. While the small peak around 505 nm can be assigned to the green fluorescent chromophore (D, donor) the main contribution with a maximum at 580 nm can be associated with the red-emitting chromophor (A, acceptor).

In the following we demonstrate that it is possible to disentangle the two chromophoric units of DsRed in a microresonator solely by optical means without destroying the composition of the tetrameric protein complex. For this purpose a 50-nm thin layer of poly(vinyl alcohol) PVA doped with DsRed was placed between the two mirrors of the microresonator. In the confocal image of Fig. 10a we observe a spatial intensity distribution consisting of sections of two concentric rings. This image was recorded in the first white-light interference ring (i.e., $\lambda/2$ condition for visible light). The lower part of Fig. 10a shows how the cavity transmission maximum increases from 400 to

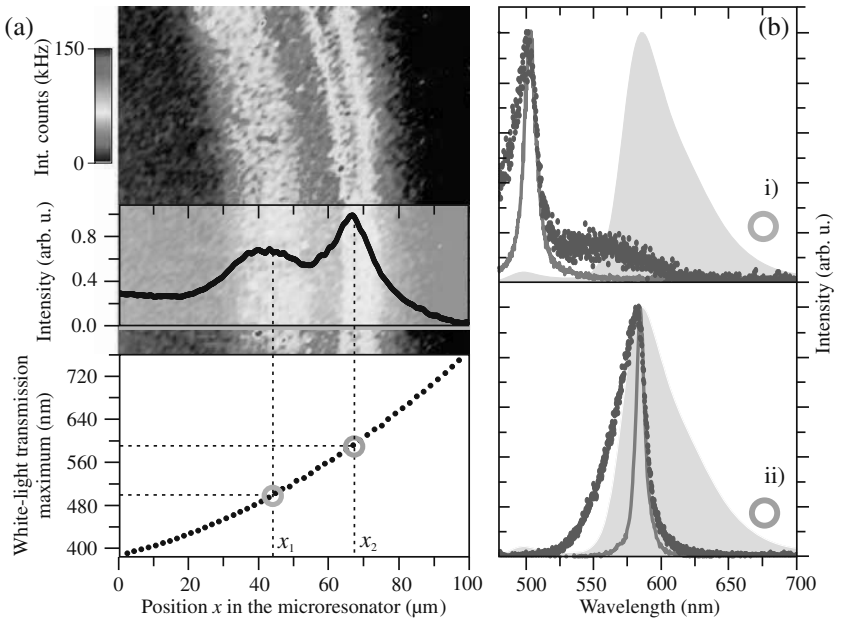

Fig. 10 **a** Confocal microscopy image showing the spatial intensity distribution of the microresonator-controlled DsRed fluorescence. The separated sections of two concentric rings represent the intensity maxima associated with either resonant green (around x=40 μm) or red fluorescent chromophores (around x=70 μm). The cross section of the integrated fluorescence intensity (*black solid line*) recorded along the *blue line* is correlated with the intensity maximum $\lambda(x,y)$ of the measured local on-axis transmission spectrum (*circles*) of the microresonator. **b** Microresonator-controlled DsRed fluorescence spectra measured at specific microresonator positions indicated by colored rings in Fig. 10a referring to the green (*i*) and red chromophore (*ii*). The corresponding local on-axis transmission spectra are plotted as a reference (*red*). Additionally a free space spectrum of DsRed is shown as reference (*gray shaded area*)

760 nm along a line scan (blue line) in the confocal image. Spectra recorded from the maximum of the inner ring (marked by a green circle) and from the maximum of the outer ring (orange circle) show that the inner ring originates from the donor luminescence and the outer ring from the acceptor luminescence. As can be seen from the on-axis transmission spectra (red curves in Fig. 10b) both intensity maxima occur where the local resonance wavelength of the microresonator coincides either with the donor (D) or acceptor (A) of the free space spectrum (cf. Fig. 9). In addition, the confined structure leads to a relative enhancement of the green fluorescence by a factor of 15 as compared with free space. The results presented in Fig. 10 clearly show that for a resonator length corresponding to the green emission of the donor, the fluorescence at 505 nm dominates the spectrum while the non-resonant red fluorescence is strongly suppressed. In turn, choosing a resonator length corresponding to the red emission of the acceptor the fluorescence at 580 nm is dominant due to radiative coupling of the acceptor to the local cavity modes. Deviations of the fluoresecence spectra from the microresonator transmission function (red curves in Fig. 10b) result from off-axis emission.

The key to microresonator-controlled fluorescence lies in the influence of local photonic mode density $\rho_{\mathrm{cav}}(\omega)$ on the spontaneous emission rate $\Gamma_{\mathrm{sp.em.}}$ of individual emitters, which is described by Fermi's golden rule [25]:

$$\Gamma_{\mathrm{sp.em.}} = \frac{1}{\tau_{\mathrm{sp.em.}}} = \frac{2\pi}{h}|1\mu \cdot \mathbf{E}_{\mathrm{cav}}|^2 \rho_{\mathrm{cav}}(\omega)$$

Here, $\boldsymbol{\mu}$ is the dipole moment of the emitter and the surrounding electric field given by its vector $\mathbf{E}_{\mathrm{cav}}$. The emission rate is inversely proportional to the fluorescence lifetime and, consequently, modifications of the chromophore lifetimes $\tau_{\mathrm{cav}}^{\mathrm{D}}$ and $\tau_{\mathrm{cav}}^{\mathrm{A}}$ alter the FRET efficiency in DsRed due to $E_{ET} = 1 - \frac{\tau_{DA}}{\tau_D}$. Here, τ_{DA} is the lifetime of the donor in the presence of an acceptor where energy transfer can take place and τ_{D} is the lifetime of the donor in the absence of an acceptor ($\tau_{\mathrm{DA}} < \tau_{\mathrm{D}} = \text{const.}$). Indeed, fluorescence lifetime measurements of DsRed in a microresonator show that the ratio of the donor and acceptor lifetimes $\tau_{\mathrm{cav}}^{\mathrm{A}}/\tau_{\mathrm{cav}}^{\mathrm{D}}$ depends sensitively on the effective resonator lengths L and reaches a maximum value of 4.5 (7.5 times higher than free space) at L=115 nm [44]. The mirror separation of 115 nm corresponds to a local resonance wavelength of 510 nm, which is close to the wavelength of maximum donor emission at 505 nm. At this resonator length the donor lifetime is shortened while the acceptor fluorescence is off-resonant and its spontaneous emission process is strongly suppressed. Furthermore, we found that the resonator-controlled emission intensity ratio between donor and acceptor $I_{\mathrm{D}}/I_{\mathrm{A}}$ depends not only on the resonator length, but also on the excitation power P_{exc}. While for free space samples of DsRed the energy transfer efficiency is nearly independent of the excitation power and equals 0.93—in good agreement with literature [65], the FRET efficiency for systems enclosed in a microresonator with mirror spacings of 115 nm drops to 0.1–0.5 and depends on the excitation power. This can be explained by the saturation of the acceptor due to its longer excited state lifetime and thus the non-radiative transfer from the donor to the acceptor is reduced. As a consequence the donor emission intensity increases as a function of the pumping rate. Following a rate equation model, where $D=D_0+D_1=$ const. and $A=A_0+A_1=$const. are the population numbers of the ground state (0) and the excited state (1) of the respective chromophores, the power- and resonance-dependent energy transfer efficiency E_{ET} can be expressed as [44]:

$$E(P_{exc}, L) = \frac{I_A}{I_{\mathrm{D}} + I_{\mathrm{A}}} = \frac{P_{\mathrm{exc}}.\sigma_{\mathrm{D}}.D.k_t.A}{k_t.A.D.P_{\mathrm{exc}}.\sigma_D + (P_{\mathrm{exc}}.\sigma_D + \Phi_{\mathrm{D}}(L) + k_t)(k_t + \Phi_A(L))}.$$

Here, $\Phi_{\mathrm{D,A}}(L) = k_{r;\mathrm{D,A}}(L)/\left(k_{r;\mathrm{D,A}}(L) + k_{\mathrm{nr;D,A}}\right)$ represent the fluorescence quantum yield of the donor and the acceptor, respectively, which depend on the mirror spacing L of the microresonator. k_t denotes the energy transfer rate from the donor to the acceptor and is a near-field effect. σ_{D} is the absorption cross section of the donor. In summary, the enhanced fluorescence lifetime of the acceptor effectively forms a bottleneck for the transfer of excited state energy from donor to acceptor chromophores. This results in an inhibition of the excited state energy transfer from donor to acceptor which can be tuned over a wide range of energy transfer efficiencies from 0.1 to 0.97. Thus, optical microresonators are promising for controlling energy transfer processes between dipole-coupled emitters.

While the results presented in the previous section dealt with ensemble measurements we will address single protein and FRET control in the following. Figure 11 displays two fluorescence spectra of single DsRed proteins at different resonator lengths. Depending on the effective mirror distance L, either the green fluorescence band associated with the resonant donor (for L around 115 nm, see Fig. 11a) or the red fluorescence band of the resonant acceptor (L around 140 nm, see Fig. 11b) can be observed. This is in good agreement with the ensemble results presented in the previous section (cf. Fig. 10).

However, as the chromophoric composition and mutual orientation as well as the transfer efficiency will vary for each single DsRed protein [64, 67], the optical confinement of a resonator will affect each individual protein differently. This drawback from an experimental point of view can be overcome when a large number of single

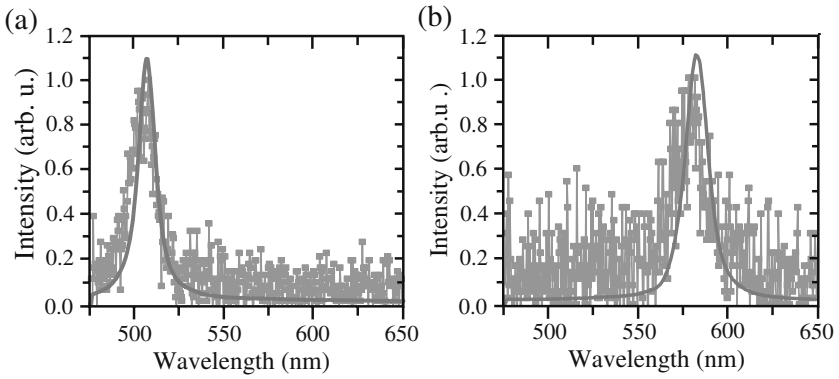

Fig. 11 Microresonator-modified fluorescence spectra of single DsRed proteins. If, as shown in **a**, the resonator length is tuned to be on resonance with the green-emitting donor chromophore at 505 nm only the green fluorescence is present. When the resonance wavelength of the resonator is centered at 580 nm (**b**), it is on resonance with the red-emitting chromophore and thus only the red fluorescence is visible. The corresponding local on-axis transmission spectra of the microresonator are shown as *solid red lines*

proteins are investigated. Then the statistical weight should clearly favor the observation of the green fluorescent donor chromophores in DsRed proteins (for L being tuned to that wavelength). Thus, we have investigated the emission behavior of 257 single proteins in the microresonator and for reference 339 single DsRed entities in free space. The resulting histograms for the occurrence of the spectral peak position in the fluorescence are shown in Fig. 12a and b for proteins embedded in the resonator and in free space, respectively. As a result, 83% of the investigated proteins inside the resonator structure show green fluorescence for a cavity length below 140 nm, which is nearly 14 times higher as compared with the green emission in free space, where only 6% of the investigated tetramers exhibit the green emission. This result demonstrates clearly that an optical microresonator can be used as a powerful tool to investigate donor chromophores in single, isolated FRET-pairs without structural modifications of the chromophoric subunits.

Summary and conclusion

We presented in this review article the use of microresonators for fundamental studies as well as for applications. The main emphasis was the introduction of a $\lambda/2$ microresonator, which is reversibly tunable with nanometer precision across the entire visible spectral range. This resonator allows us not only to modify the spectral characteristics of single quantum emitters but to control them by choosing a specific resonator length and results either in enhancement or inhibition of the spontaneous emission rate compared with the free, non-confined space. The experimental results are in good agreement with a theoretical model based on a semi-classical approach which describes very well the transition rates of the embedded molecules and the angular distribution of the radiation as well as the resonator-induced changes of the entire emission spectrum.

Furthermore, the tunable microresonator allows us to determine the longitudinal position of a single quantum emitter embedded in a transparent dielectric medium with an accuracy of $\lambda/60$ by analyzing fluorescence images from excitation with a radially polarized doughnut mode as a function of the mirror spacing.

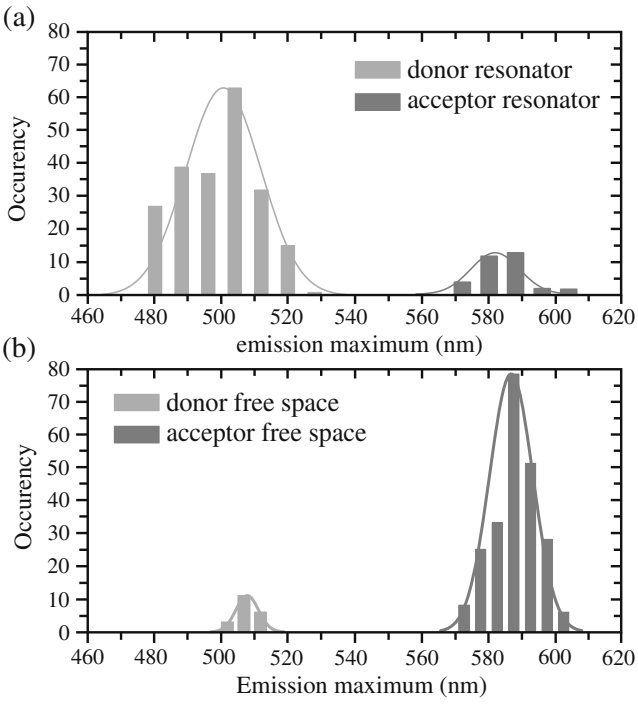

Fig. 12 The histograms display the occurrence of spectral peak positions in the emissions from single DsRed proteins inside the microresonator (**a**) and in free space (**b**)

Finally, we were able to control the FRET efficiency in single bichromophoric DsRed proteins via tuning the spectral mode density of the resonator.

Acknowledgements The authors would like to thank Dr. Mathias Steiner, Dr. Dmitry Khoptyar, and Prof. Dr. Jorg Enderlein. We gratefully acknowledge financial support from the "Kom-petenznetz Funktionelle Nanostrukturen" of the Landesstiftung Baden-Württemberg, the European Commission through the Human Potential Program (Marie-Curie Research Training Network NANOMATCH, contract MRTN-CT-2006-035884), and the Deutsche Forschungsgemeinschaft DFG (ME 1600/6-1,2). We also thank Coherent GmbH Germany for providing a Sapphire™ 488-20 OPS laser. The WSxM software from Nanotec [68] was partly used for scan image processing.

References

1. Maiman TH (1960) Stimulated optical radiation in ruby. Nature 187(4736):493
2. Yokoyama H, Ujihara K (1995) Spontaneous emission and laser oscillation in microcavities. CRC, Boca Raton, FL
3. Chang RK, Campillo AJ (1996) Optical processes in microcavities. World Scientific, Singapore
4. Vahala KJ (2003) Optical microcavities. Nature 424:839–846
5. Benson TM, Boriskina SV, Sewell P, Vukovic A, Greedy SC, Nosich AI (2006) Micro-optical resonators for microlasers and integrated optoelectronics. Frontiers in planar lightwave circuit technology, vol 216. Springer, Berlin, pp 39–70
6. Gerard JM, Barrier D, Marzin J Y, Kuszelewicz R, Manin L, Costard E, Thierry-Mieg V, Rivera T (1996) Quantum boxes as active probes for photonic microstructures: the pillar microcavity case. Appl Phys Lett 69:449
7. Kimble HJ (2008) The quantum internet. Nature 453:1023
8. Lipson M, Chen T, Chen K, Duan X, Kimerling LC (2001) Erbium in Si-based light confining structures. Mat Sci Eng B 81:36–39
9. Henze R et al (2006) Quantum optics with microresonators. https://www.physik.hu-berlin.de/nano/forschung-en/mr. Accessed 7 July 2009
10. MHM Salleh(2009) Label free biosensors. http://www.gla.ac.uk/departments/electronicsandelectricalengineering/research/bioelectronics/researchareas/nanophotonics/. Accessed 7 July 2009
11. EFONGA (2006) http://www.efonga.org/images/microsfera.jpg. Accessed 7 July 2009
12. Carmon T, Vahala KJ (2007) Visible continous emission from a silics microphotonic device by third-harmonic generation. Nature Physics 3:430
13. Del'Haye P, Schliesser A, Arcizet O, Wilken T, Holzwarth R, Kippenberg TJ (2007) Optical frequency comb generation from a monolithic microresonator. Nature 450:1214
14. Marian A, Stowe MC, Lawall JR, Felinto D, Ye J (2004) United time-frequency spectroscopy for dynamics and global structure. Science 306:2063
15. Thorpe MJ, Moll KD, Jones RJ, Safdi B, Ye J (2006) Broadband cavity ringdown spectroscopy for sensitive and rapid molecular detection. Science 311:1595
16. Diddams SA, Hollberg L, Mbele V (2007) Molecular fingerprinting with the resolved modes of a femtosecond laser frequency comb. Nature 445:627
17. Diddams SA, Jones DJ, Ye J, Cundiff ST, Hall JL, Ranka JK, Windeler RS, Holzwarth R, Udem T, Hänsch TW (2000) Direct link between microwave and optical frequencies with a 300 THz femtosecond laser comb. Phys Rev Lett 84:5102
18. Weiner AM (2000) Femtosecond pulse shaping using spatial light modulators. Rev Sci Instr 71:1929
19. Ye J (2007) Optical metrology: everything under control. Nature Photonics 1:447
20. Vollmer F, Braun D, Libchaber A, Khoshsima M, Teraoka I, Arnold S (2002) Protein detection by optical shift of a resonant microcavity. Appl Phys Lett 80(21):4057
21. Armani AM, Kulkarni RP, Fraser SE, Flagan RC, Vahala KJ (2007) Label-free, single-molecule detection with optical microcavities. Science 317:783
22. Loncar M (2007) Molecular sensors—cavities lead the way. Nature Photonics 1:565
23. Purcell EM (1946) Spontaneous emission probabilities at radio frequencies. Phys Rev 69:681
24. Fermi E (1932) Quantum theory of radiation. Rev Mod Phys 4:87
25. Kleppner D (1981) Inhibited spontaneous emission. Phys Rev Lett 47:233–236
26. Goy P, Raimond JM, Gross M, Haroche S (1983) Observation of cavity-enhanced single-atom spontaneous emission. Phys Rev Lett 50:1903
27. Ye J, Vernooy DW, Kimble HJ (1999) Trapping of single atoms in cavity QED. Phys Rev Lett 83:4987
28. Bennett AJ, Unitt DC, See P, Shields AJ, Atkinson P, Cooper K, Ritchie DA (2005) Microcavity single photon-emitting diode. Appl Phys Lett 86:181102
29. Steiner M, Korlacki R, Hartschuh A, Meixner AJ (2007) Highly efficient, tunable single photon source based on single molecules. Appl Phys Lett 90:183122
30. Korlacki R, Steiner M, Qian HH, Hartschuh A, Meixner AJ (2007) Optical Fourier transform spectroscopy of single-walled carbon nanotubes and single molecules. ChemPhysChem 8:1049
31. Steiner M, Qian H, Hartschuh A, Meixner AJ (2007) Controlling nonequilibrium phonon populations in single-walled carbon nanotubes. Nano Lett 7:2239–2242
32. Xia F, Steiner M, Lin Y-M, Avouris P (2008) A microcavity-controlled, current-driven, on-chip nanotube emitter at infrared wavelengths. Nat Nanotechnol 3:609–613
33. Steiner M, Xia F, Qian H, Lin Y-M, Hartschuh A, Meixner AJ, Avouris P (2008) Carbon nanotubes and optical confinement: controlling light emission in nanophotonic devices. Proc SPIE 7037:703713
34. Moerner WE (2004) Single-photon sources based on single molecules in solids. New J Phys 60:88
35. Lounis B, Orrit M (2005) Single-photon sources. Rep Prog Phys 68:1129–1179
36. Ye J, Kimble HJ, Katori H (2008) Quantum state engineering and precision metrology using state-insensitive light traps. Science 320:1734
37. Begon C, Rigneault H, Jonsson P, Rarity JG (2000) Spontaneous emission control with planar dielectric structures: an asset for ultrasensitive fluorescence analysis. Single Molecules 1:207
38. Hou L, Hou G, Mo Y, Peng J, Cao Y (2005) All-organic flexible polymer microcavity light-emitting diodes using 3M reflective multilayer polymer mirrors. Appl Phys Lett 87:243504
39. Langner M, Gehlhaar R, Schriever C, Frob H, Lyssenko VG, Leo K (2007) Strong optical confinement and multimode emission of organic photonic dots. Appl Phys Lett 91:181119
40. Langner M, Gehlhaar R, Hintschich SI, Frob H, Wendrock H, Lyssenko VG, Leo K (2008) Optical modes in wavelength-sized organic microcavity structures. Opt Quant Electr 40:403–409
41. Enderlein J (2002) Spectral properties of a fluorescing molecule within a spherical metallic nanocavity. Phys Chem Chem Phys 4:2780
42. Steiner M, Schleifenbaum F, Stupperich C, Failla AV, Hartschuh A, Meixner AJ (2005) Microcavity-controlled single-molecule fluorescence. Chem Phys Chem 6:2190

43. Chizhik A, Schleifenbaum F, Gutbrod R, Chizhik A, Khoptyar D, Meixner AJ (2009) Tuning the fluorescence emission spectra of a single molecule with a variable optical subwavelength metal microcavity. Phys Rev Let 102:073002
44. Schleifenbaum F, Elgass K, Steiner M, Enderlein J, Peter S, Meixner AJ (2009) Optical microresonator modifies the efficiency of the fluorescence resonance energy transfer in the autofluorescent protein DsRed. Proc SPIE 7185:718504
45. Schleifenbaum F (2008) Energy transfer in the fluorescent protein DsRed in confined optical fields. Rhombos-Verlag, Berlin
46. Steiner M, Failla AV, Hartschuh A, Schleifenbaum F, Stupperich C, Meixner AJ (2008) Controlling molecular broadband-emission by optical confinement. New J Phys 10:123017
47. Dorn R, Quabis S, Leuchs G (2003) Sharper focus for a radially polarized light beam. Phys Rev Lett 91:233901
48. Chizhik A, Gutbrod R, Chizhik A, Bär S, Meixner AJ (2009) Controlling the optical properties by optical confinement in a tunable microcavity. Proc SPIE 7396:73960F. doi:10.1117/12.825278
49. Novotny L, Beversluis MR, Youngworth KS, Brown TG (2001) Longitudinal field modes probed by single molecules. Phys Rev Lett 86:5251
50. Novotny L, Hecht B (2006) Principles of nanooptics. Cambridge University Press, Cambridge
51. Gutbrod R, Chizhik A, Chizhik A, Khoptyar D, Meixner AJ (2009) Longitudinal localization of a fluorescent bead in a tunable microcavity with an accuracy of λ/60. Opt Lett 34:629
52. Hell SW (2007) Far-field optical nanoscopy. Science 316:1153
53. Hell SW (2003) Toward fluorescence nanoscopy. Nat Biotechnol 21:1347
54. Born M, Wolf E (1999) Principles of optics. Cambridge University Press, Cambridge
55. Khoptyar D, Gutbrod R, Chizhik A, Enderlein J, Schleifenbaum F, Steiner M, Meixner AJ (2008) Tight focusing of laser beams in a λ/2-microcavity. Optics Express 16(13):9907–9917
56. Barnes WL, Andrew P (1999) Energy transfer under control. Nature 400:505
57. Baird G, Zacharias D, Tsien R (2000) Biochemistry, mutagenesis, and oligomerization of dsRed, a red fluorescent protein from coral. Proc Natl Acad Sci USA 97:11984–11989
58. Blum C, Subramaniam V, Schleifenbaum F, Stracke F, Angres B, Terskikh A, Meixner AJ (2002) Single molecule fluorescence spectroscopy of mutants of the Discosoma red fluorescent protein DsRed. Chem Phys Lett 362:355–361
59. Yarbrough D, Wachter RM, Kallio K, Matz MV, Remington SJ (2001) Refined crystal structure of DsRed, a red fluorescent protein from coral, at 2.0-A resolution. Proc Natl Acad Sci USA 98:462–467
60. Bonsma S, Purchase R, Jezowski S, Gallus J, Knz F, Vlker S (2005) Green and red fluorescent proteins: photo- and thermally induced dynamics probed by site-selective spectroscopy and hole burning. Chem Phys Chem 6:838–849
61. Bowen B, Woodbury N (2003) Single-molecule fluorescence lifetime and anisotropy measurements of the red fluorescent protein, DsRed, in solution. Photochem Photobiol 77:362–369
62. Hofkens J, Cotlet M, Vosch T, Tinnefeld P, Weston KD, Ego C, Grimsdale A, Mllen K, Beljonne D, Brdas JL, Jordens S, Schweitzer G, Sauer M, De Schryver FC (2003) Revealing competitive Förster-type resonance energy-transfer pathways in single bichromophoric molecules. Proc Natl Acad Sci USA 100:13146–13151
63. Terskikh A, Fradkov A, Ermakova G, Zaraisky A, Tan P, Kajava AV, Zhao X, Lukyanov S, Matz M, Kim S, Weissman I, Siebert P (2000) Fluorescent timer: protein that changes color with time. Science 290:1585–1588
64. Schleifenbaum F, Elgass K, Blum C, Subramaniam V, Meixner AJ (2008) New insights into the photophysics of DsRed by combined spectral and time domain spectroscopy on single proteins. J Phys Chem B 112:7669
65. Garcia-Parajo MF, Koopman M, v Dijk EMHP, Subramaniam V, v Hulst NF (2001) The nature of fluorescence emission in the red fluorescent protein DsRed, revealed by single-molecule detection. Proc Natl Acad Sci USA 98:14392
66. Gross LA, Baird GS, Hoffman RC, Baldridge KK, Tsien RY (2000) The structure of the chromophore within DsRed, a red fluorescent protein from coral. Proc Natl Acad Sci USA 97:11990
67. Cotlet M, Hofkens J, Habuchi S, Dirix G, Guyse Mv, Michiels J, Vanderleyden J, Schryver FCd (2001) Identification of different emitting species in the red fluroescent protein DsRed by means of ensemble and single-molecule spectroscopy. Proc Natl Acad Sci USA 98:14398–14403
68. Horcas I, Fernández R, Gómez-Rodríguez JM, Colchero J, Gómez-Herrero J, Baro AM (2007) WSXM: a software for scanning probe microscopy and a tool for nanotechnology. Rev Sci Instrum 78:013705

Chapter 2

Tuning the fluorescence emission spectra of a single molecule with a variable optical subwavelength metal microcavity

In this chapter, we present experimental and theoretical results on changing the fluorescence emission spectrum of a single molecule by embedding it within a tunable planar microcavity with subwavelength spacing. The cavity length is changed with nanometer precision by using a piezoelectric actuator. By varying its length, the local mode structure of the electromagnetic field is changed together with the radiative coupling of the emitting molecule to the field. Because mode structure and coupling are both frequency dependent, this leads to a renormalization of the emission spectrum of the molecule. We develop a theoretical model for these spectral changes and find excellent agreement between theoretical prediction and experimental results.

This chapter is based on:

Chizhik, A.I., Schleifenbaum, F., Gutbrod, R., Chizhik, A.M., Khoptyar, D., Meixner, A.J., Enderlein, J. “Tuning the Fluorescence Emission Spectra of a Single Molecule with a Variable Optical Sub-wavelength Metal Microcavity" *Phys. Rev. Lett.* **2009**, *102,* 073002-1-4.

Tuning the Fluorescence Emission Spectra of a Single Molecule with a Variable Optical Subwavelength Metal Microcavity

Alexey Chizhik, Frank Schleifenbaum, Raphael Gutbrod, Anna Chizhik, Dmitry Khoptyar,* and Alfred J. Meixner†
Institute of Physical and Theoretical Chemistry, Eberhard Karls University, 72076 Tübingen, Germany

Jörg Enderlein‡
III. Institute of Physics, Georg August University, 37077 Göttingen, Germany
(Received 21 October 2008; published 18 February 2009)

We present experimental and theoretical results on changing the fluorescence emission spectrum of a single molecule by embedding it within a tunable planar microcavity with subwavelength spacing. The cavity length is changed with nanometer precision by using a piezoelectric actuator. By varying its length, the local mode structure of the electromagnetic field is changed together with the radiative coupling of the emitting molecule to the field. Because mode structure and coupling are both frequency dependent, this leads to a renormalization of the emission spectrum of the molecule. We develop a theoretical model for these spectral changes and find excellent agreement between theoretical prediction and experimental results.

DOI: 10.1103/PhysRevLett.102.073002 PACS numbers: 37.30.+i, 32.50.+d, 33.50.Dq, 42.50.Pq

As was first noted by Purcell more then 60 years ago [1], placing an emitter within a confined geometry alters its emission properties, in particular, the rate of spontaneous emission is increased. This can be easily understood within a Fermi's golden rule approach to the emission of an electric dipole within the given geometry: The density of modes of the electromagnetic field inside a cavity is changed with respect to free space, and hence the coupling of the dipole transition of an emitting molecule to this field. The first extensive experimental studies of the changes in spontaneous emission rates of molecules in front of a metal mirror were conducted by Kuhn and Drexhage (see Ref. [2]), and a comprehensive semiclassical model for these experiments was developed by Chance, Prock and Silbey [3]. Lukosz and coworkers conducted extensive studies of the changes in the angular distribution of radiation of fluorescent molecules close to a metallic mirror or dielectric interfaces [4,5]. Later, all of these results had been confirmed also on a single molecule level, see Ref. [6] and citations therein. Remarkably, little attention has been paid to the changes in the *emission spectrum* of a fluorescent dye as induced by the changes of the local electromagnetic field structure. This is partially due to the fact that when observing molecules with narrow emission bands, optical dispersion of the molecule's environment is rather weak, so that the *wavelength dependence* of the changes in the radiative transition rate by its environment is negligible. However, if a molecule displays a broad emission spectrum, one can no longer neglect optical dispersion effects, and strong shape changes of a molecule's emission spectrum are expected. This is due to the fact that the optical dispersion of a molecule's environment leads to a wavelength-dependent electromagnetic coupling of the emitter to its environment, which results in a renormalization of the observable emission spectrum of the embedded molecule. For example, strong changes in the emission and absorption spectra have been predicted for a Rhodamine6G molecule embedded within a spherical metal nanocavity [7].

Experimentally, this effect has been observed qualitatively by Steiner *et al.* [8] who investigated single isolated perylene dye molecules in a planar metal microcavity for different mirror spacings and hence for different electromagnetic mode structures. However, as the mirror spacing was fixed, they could investigate a distinct molecule only for one given resonator length. In the present Letter, we report on changing the emission spectrum of a single fluorescent molecule embedded in a tunable microcavity. Thus, for the first time we were able to actively change the local electromagnetic field structure around a molecule by changing the mirror spacing of the cavity. In doing that, one selects the vibronic transition where fluorescence will mostly occur. Moreover, we develop a semiclassical theoretical model for these spectral changes, and find excellent agreement between theory and experiment. Together with the well-studied changes of radiative transition rates (fluorescence or luminescence lifetime) and angular distributions of radiation, this is another important step in our understanding of the complex electromagnetic interaction of single photon emitters with an electromagnetic field structure that is tailored by the emitter's surrounding.

The experimental setup is depicted in Fig. 1(a) and is similar to a previously built microcavity but with no adjustable cavity length [8]. A homemade aluminum cavity holder was used to hold the multilayer cavity. The bottom part of the cavity consisted of a coverslip (thickness 170 μm), covered by a thin silver film (47 nm), a silicon oxide layer (30 nm, refractive index $n = 1.46$), a polymer layer (70 nm, refractive index $n = 1.49$) with dissolved dye molecules, and a second thin silicon oxide layer (8 nm,

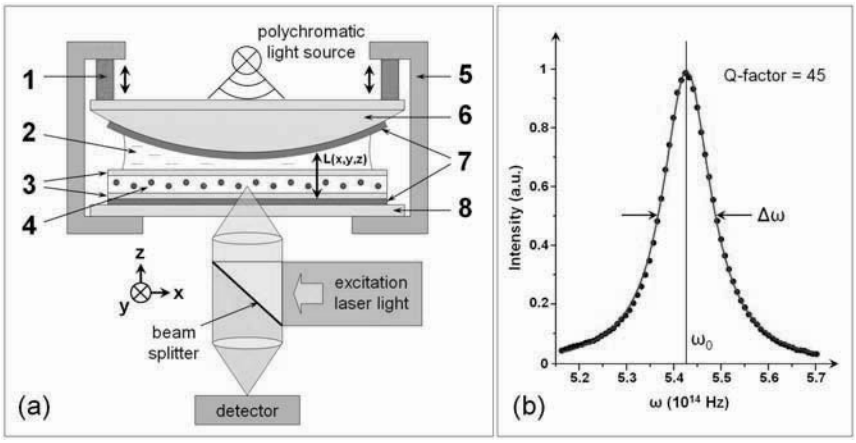

FIG. 1 (color online). (a) Scheme of the experimental setup. The tunable microcavity consists of: 1. Piezoelectric cell, 2. Immersion oil, 3. Silica layers, 4. Polymer (PMMA) layer with PI molecules, 5. Aluminum holder, 6. Lens, 7. Silver layers, 8. Glass coverslide. For more details see main text. (b) Microcavity transmission spectrum fitted by a Lorentzian function (full line) giving a cavity Q-factor = 45.

refractive index $n = 1.46$). The bottom silicon oxide layer serves as a finite spacer between the silver metal and the dye embedding polymer. The upper silicon oxide layer prevents any interaction of embedded dye molecules with atmospheric oxygen during cavity assembly. The top part of the cavity consists of a plane-convex lens ($F = 150$ mm), again covered with a silver layer (94 nm). The intermediate space between the multilayer covered coverslip and the multilayer covered lens was filled with oil (Immersol 518F, Zeiss, refractive index $n = 1.52$). The cavity length could be adjusted with piezo actuators (PSt $150/3.5 \times 3.5/20$, Piezomechanik GmbH) that move the lens toward or away from the bottom coverslip. Silver and oxide layers were made using an evaporation technique reported elsewhere [8]. Absolute thickness values were determined afterward by fitting a transmission spectrum that was recorded using a collimated white light source [see Fig. 1(b)]. Although the resonance peak in the emission spectrum depends on the absolute value of cavity length, the peak width is only determined by the thickness of the various layers (mostly the silver film thickness values). All subsequent fluorescence spectrum measurements were performed close to the center of the lens, where the formed cavity can be considered to be a plane-parallel system.

The dye doped polymer layer was fabricated by spin coating a subnanomolar solution of the perylene derivative *N*-(2,6-diisopropylphenyl)-perylene-3,4-dicarboxymide (abbreviated by PI) in 2% poly(methyl methacrylate) (PMMA) dissolved in dichloromethane. The resulting layer thickness was determined to be around 70 nm by an atomic force microscope (AFM). To obtain a reference spectrum of the PMMA-embedded molecules, a free space sample was prepared by spin coating a thick layer of the same polymer-dye-dichloromethane mixture onto a pure glass coverslip.

All optical measurements were performed using an inverted confocal microscope (based on an Axiovert 135 TV, Zeiss) equipped with a high-numerical-aperture objective [Planeoflex 100/(numerical aperture) = 1.3, Zeiss]. An argon-ion laser (60X-200, American Laser Corporation) at $\lambda = 488$ nm served as excitation source for the fluorescence spectrum measurements. Back-scattered excitation light was blocked with a long-pass filter (Semrock Razor Edge LP02-488RU-25). Fluorescence spectra were acquired with a spectrograph (SpectraPro 300i, Acton Research) in combination with a CCD camera (LNCCD-1340/100-EB/1, Princeton Instruments). For each spectral measurement, the cavity length was adjusted via a defined voltage applied to the piezo actuator. The measurement of each spectrum lasted only three seconds, to prevent premature bleaching, and to reduce the effects of piezo drifting and potential spectral jumps of the molecule (see also below).

Theoretical modeling of the spectrum was done within a semiclassical approach, treating the fluorescing molecule as an oscillating electric dipole emitter and solving Maxwell's equation for the given geometry of the microcavity, see, e.g., Ref. [9] and citations therein. Let us first consider a purely monochromatic emitter. For such an emitter, the electric field amplitude $\vec{E}(\vec{r})$ at position $\vec{r}$ of a free electric dipole emitter within a homogeneous polymer environment is represented by a plane wave expansion (Weyl representation [10]) as

$$\vec{E}(\vec{r}) = \frac{ik^2}{2\pi\epsilon} \int \frac{d\vec{q}}{w} [\vec{\kappa}_p(\vec{\kappa}_p \cdot \vec{p}) + \vec{\kappa}_s(\vec{\kappa}_s \cdot \vec{p})] e^{i\vec{q}\cdot\vec{\rho} + iw|z|}, \tag{1}$$

where $k = \sqrt{q^2 + w^2}$ is the modulus of the wave vector in polymer, $\vec{q}$ and w being its horizontal (two-dimensional vector parallel to cavity interfaces) and vertical (orthogonal to cavity interfaces) components, respectively; ϵ is the dielectric constant of the polymer, which is equal to the square of its refractive index n; and $\vec{p}$ is the amplitude vector of the oscillating dipole. The vector $\vec{\rho}$ is the projection of the position vector $\vec{r}$ onto a plane parallel to the cavity interfaces, and z its projection onto a line orthogonal to these interfaces. Furthermore, it is assumed that the emitter is positioned at coordinates $\vec{r} = (0, 0, 0)$. The unit vectors $\vec{\kappa}_p$ and $\vec{\kappa}_p$ correspond to the p-wave and s-wave contributions (with respect to the cavity interfaces) of the

corresponding plane wave component and are explicitly given by

$$\vec{\kappa}_p = \frac{1}{k}(-w\vec{q}, q), \qquad \vec{\kappa}_s = (\vec{e}_z \times \vec{q}, 0), \tag{2}$$

where $\vec{e}_z$ is the unit vector along the z direction. For modeling the electromagnetic interaction between the emitter and the cavity, one solves Maxwell's equation of the whole cavity system separately for each plane wave component in representation Eq. (1) as source. This is done in a straightforward way by using Fresnel's relations for a planar multilayered system and yields a plane wave representation of the electric field amplitude within each layer of the cavity and in both half-spaces outside the cavity. These representations have the form

$$\vec{E}_j(\vec{r}) = \frac{ik_j^2}{2\pi\epsilon_j}\int \frac{d\vec{q}}{w_j}[\vec{\kappa}_{p,j}(\vec{\kappa}_{p,j}\cdot\vec{p}) + \vec{\kappa}_s(\vec{\kappa}_s\cdot\vec{p})] \cdot e^{i\vec{q}\cdot\vec{\rho}}\cdot[a_j(q)e^{iw_jz} + b_j(q)e^{-iw_jz}], \tag{3}$$

where the ϵ_j, $k_j = \sqrt{q^2 + w_j^2}$, w_j, and $\vec{\kappa}_{p,j}$ correspond now to the jth layer of the system, and the a_j and b_j are the q-dependent coefficients of the plane wave modes traveling toward $+z$ and $-z$, respectively. For the half-space bordering the cavity along the $+z$ direction, there will be no b coefficient, and for the half-space bordering the cavity along the $-z$ direction, there will be no a coefficient (only outgoing waves are admitted).

Knowing the full electric field amplitudes in all layers, two important quantities can be calculated: the total power S_{tot} of emission, and the angular distribution of radiation (ADR) in the half-space toward the light-collecting objective. The total power of emission is found by integrating the positive or negative z component of the Poynting vector $\vec{P} = (c/8\pi)\text{Re}(\vec{E}\times\vec{B}^*)$ over both interfaces of the polymer layer containing the emitting molecule, where the positive sign is chosen for the interface toward the $+z$ direction, and the negative sign for the interface toward the $-z$ direction. The magnetic field amplitude $\vec{B}$ which enters the expression of the Poynting vector is found from Eq. (1) and Eq. (3) using the magnetic induction law from Maxwell's equations. Within the semiclassical interpretation, the total power of emission S_{tot} is proportional to the radiative transition rate of the molecule from its excited to its ground state (at the considered wavelength).

The ADR in the half-space bordering the cavity toward the $-z$ direction (toward the objective) can be found when taking into account that each outgoing plane wave component in the plane wave representation of Eq. (3) is connected with an energy flux proportional to $n_g|b_g|^2$ along the direction $(\vec{q}, -w_g)$, where the subscript g refers now to that half space (glass), and n_g is the corresponding refractive index. Integrating this ADR over the solid angle of light collection of the objective yields a number proportional to the light detection efficiency, C_{det}, of the measurement system for a fluorescent molecule with the given position, orientation, and at the considered wavelength.

The cavity-renormalized spectrum is obtained by calculating $S_{\text{tot}}(\lambda)$ and $C_{\text{det}}(\lambda)$ as functions of the emission wavelength λ. The optical dispersion of the cavity's material, in particular the silver layer, can be taken into account by using the wavelength-dependent refractive index of all materials in the calculations. For the actual cavity considered here, we kept the refractive index values of all dielectrics constant at their values given above, but approximated the wavelength-dependent complex-valued refractive index of silver by a Brendel-Borman model [11]. Knowing both functions $S_{\text{tot}}(\lambda)$ and $C_{\text{det}}(\lambda)$, and the free emission spectrum $F_0(\lambda)$ of the dye in an infinite and pure polymer environment, the emission spectrum $F(\lambda)$ of the dye within the cavity is now obtained (up to a constant factor) by

$$F(\lambda) \propto F_0(\lambda)\frac{C_{\text{det}}(\lambda)S_{\text{tot}}(\lambda)}{\int S_{\text{tot}}(\lambda')d\lambda'}, \tag{4}$$

where $S_{\text{tot}}(\lambda)/\int S_{\text{tot}}(\lambda')d\lambda'$ is proportional to the cavity-induced change of the radiative transition at wavelength λ, and C_{det} is proportional to the probability of detecting a photon at that wavelength.

When fitting experimentally measured spectra, one has two intrinsic unknown fit parameters: the exact position of the molecule within the polymer layer, i.e., its distance from the bottom interface of the polymer layer (interface toward the objective), and its orientation, i.e., inclination toward the z axis. Furthermore, the precise length of the cavity is also not exactly known. Each spectral measurement was done ca. 5 min after adjusting the piezo actuator to a new position. However, there were no means to absolutely measure the cavity length with nanometer resolution, and we observed furthermore a slow (over couple of minutes) drift of the cavity length (due to mechanical relaxation and creeping), which could be seen as a slow shape change of the emission spectrum with time. Thus, the cavity length, i.e., the thickness of the oil layer between the polymer-covering silicon oxide layer and the silver layer on the lens, was used as a third fit parameter. Finally, it was realized that an excellent agreement between calculated and experimentally measured spectra could only be achieved when also taking into account an additional spectral shift of the molecule's emission as commonly observed for single molecule spectra [12].

After selecting a single molecule, we measured several emission spectra for the same molecule at different values of the cavity length. Three prominent spectra are presented in Fig. 2. The figures also show best fits of the calculated spectra to the data. In these fits, the fit parameters, position and orientation of the molecule, were kept constant for all spectra (global fitting). We checked by polarization measurements that there is no reorientation of the molecule and the position of the molecule is fixed. In contrast, cavity length (i.e., oil layer thickness) and spectral shift were allowed to vary from spectrum to spectrum. The calcula-

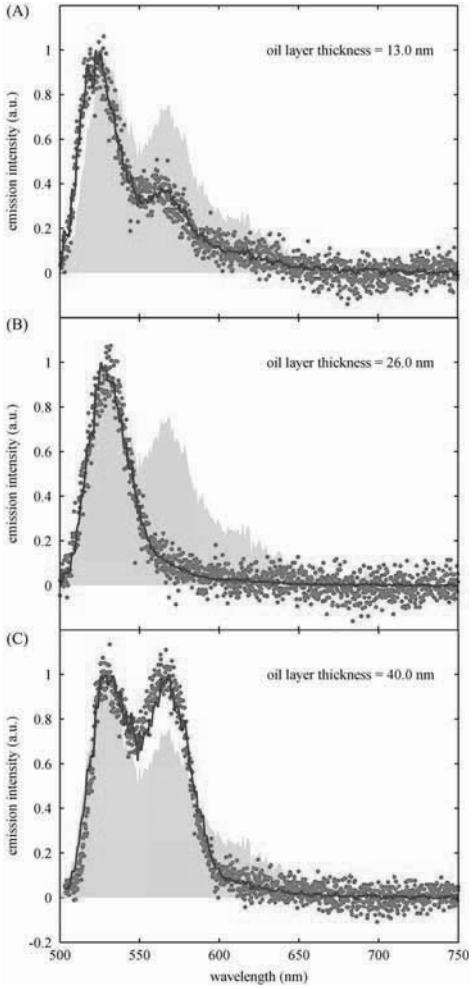

FIG. 2 (color online). Measured spectra (red dots) of a single molecule embedded in the microcavity at various values of cavity length. The blue solid lines show the best fit of a theoretically calculated spectrum, using the free spectrum in polymer (gray shaded area) as the starting point [F_0 in Eq. (4)]. Fitted value of oil layer thickness is indicated in each of the plots. The determined spectral shifts are, from top to bottom, -2 nm, -5 nm, and -14 nm. For better comparison with the free spectrum, the measured and fitted spectra are shown shifted by the opposite of these values toward the red spectral region.

tions showed that the observed molecule was close to the upper polymer interface (toward the oil) and had a nearly vertical orientation. Because of the special electric field configuration of the focused laser light inside the cavity [13], such dipoles are efficiently excited. The obtained values of spectral shift between -2 nm and -14 nm are common when observing single perylene emission spectra, and similar values have been reported before [14]. To quantify fit quality, we calculated the covariance between measured and fitted spectra and found covariance values of better than 0.9. In total, we measured spectra for more than 30 molecules and always found similar excellent agreement between measured and fitted spectra. The reason for the success of the semiclassical model is that we observe molecules that are rather far away from the metal surfaces so that fluorescence quenching is still moderate and nonlocal plasmonic effects (which are not accounted for in our model) do not play a significant role.

In summary the experimental results show that, by tuning the cavity length, one can significantly change the emission spectrum of an individual molecule, and control the ratio of distinct vibronic transition probabilities. The agreement with a theoretical model based on a semiclassical approach is remarkable demonstrating its appropriateness not only for calculating transition rates and ADRs (as was done before) but also for describing cavity-induced changes of the entire emission spectrum.

The authors thank Kirstin Elgass, Sébastien Peter, and Mathias Steiner for fruitful discussions and valuable technical support, and Tyler Arbour for his linguistic advice. Financial support by the European Commission (Marie-Curie Research Training Network NANOMATCH, Contract No. MRTN-CT-2006-035884), the ''Kompetenznetz Funktionelle Nanostrukturen Baden-Württemberg'' and by the Deutsche Forschungsgesellschaft (project EN 297/12-1) is gratefully acknowledged.

*Present address: Department of Physics, Lund University, SE-22100 Lund, Sweden.
†alfred.meixner@uni-tuebingen.de
‡enderlein@physik3.gwdg.de;
A significant part of the work was done by JE during his stay with Tübingen University.

[1] E. M. Purcell, Phys. Rev. **69**, 681 (1947).
[2] K. Drexhage, Prog. Opt. **XII**, 165 (1974).
[3] R. Chance, A. Prock, and R. Silbey, Adv. Chem. Phys. **37**, 1 (1978).
[4] W. Lukosz, J. Opt. Soc. Am. **69**, 1495 (1979).
[5] M. Lieberherr, C. Fattinger, and W. Lukosz, Surf. Sci. **189–190**, 954 (1987).
[6] F. D. Stefani, K. Vasilev, N. Bocchio, N. Stoyanova, and M. Kreiter, Phys. Rev. Lett. **94**, 023005 (2005).
[7] J. Enderlein, Phys. Chem. Chem. Phys. **4**, 2780 (2002).
[8] M. Steiner, F. Schleifenbaum, C. Stupperich, A. V. Failla, A. Hartschuh, and A. J. Meixner, Chem. Phys. Chem. **6**, 2190 (2005).
[9] J. Enderlein and T. Ruckstuhl, Opt. Express **13**, 8855 (2005).
[10] C. Girard and A. Dereux, Phys. Rev. B **49**, 11 344 (1994).
[11] A. D. Rakić, A. B. Djurišić, J. M. Elazar, and M. L. Majewski, Appl. Opt. **37**, 5271 (1998).
[12] H. P. Lu and X. S. Xie, Nature (London) **385**, 143 (1997).
[13] D. Khoptyar, R. Gutbrod, A. Chizhik, J. Enderlein, F. Schleifenbaum, M. Steiner, and A. J. Meixner, Opt. Express **16**, 9907 (2008).
[14] F. Stracke, C. Blum, S. Becker, K. Müllen, and A. Meixner, Chem. Phys. Chem. **6**, 1242 (2005).

Chapter 3

Probing the radiative transition of single molecules with a tunable microresonator

In this chapter, using a tunable optical microresonator with subwavelength spacing, we demonstrate controlled modulation of the radiative transition rate of a single molecule, which is measured by monitoring its fluorescence lifetime. Variation of the cavity length changes the local mode structure of the electromagnetic field, which modifies the radiative coupling of an emitting molecule to that field. By comparing the experimental data with a theoretical model, we extract both the pure radiative transition rate as well as the quantum yield of individual molecules. We observe a broad scattering of quantum yield values from molecule to molecule, which reflects the strong variation of the local interaction of the observed molecules with their host environment.

This chapter is based on:

Chizhik, A.I., Chizhik, A.M., Khoptyar, D., Bär, S., Meixner, A.J., Enderlein, J. "Probing the radiative transition of single molecules with a tunable microresonator" *Nano Lett.* **2011** published online.

NANO LETTERS

LETTER

pubs.acs.org/NanoLett

Probing the Radiative Transition of Single Molecules with a Tunable Microresonator

Alexey I. Chizhik,[†] Anna M. Chizhik,[†] Dmitry Khoptyar,[†] Sebastian Bär,[†] Alfred J. Meixner,[*,†] and Jörg Enderlein[*,‡]

[†]Institute of Physical and Theoretical Chemistry, Eberhard Karls University, 72076 Tübingen, Germany

[‡]III. Institute of Physics—Biophysics, Georg August University, 37077 Göttingen, Germany

Supporting Information

ABSTRACT: Using a tunable optical microresonator with subwavelength spacing, we demonstrate controlled modulation of the radiative transition rate of a single molecule, which is measured by monitoring its fluorescence lifetime. Variation of the cavity length changes the local mode structure of the electromagnetic field, which modifies the radiative coupling of an emitting molecule to that field. By comparing the experimental data with a theoretical model, we extract both the pure radiative transition rate as well as the quantum yield of individual molecules. We observe a broad scattering of quantum yield values from molecule to molecule, which reflects the strong variation of the local interaction of the observed molecules with their host environment.

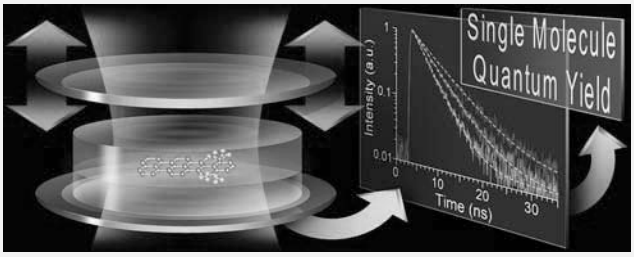

KEYWORDS: Confocal microscopy, microcavity, nanooptics, quantum yield, radiative rate, single molecule

One of the fascinating aspects of single molecule fluorescence spectroscopy is that it allows for studying discrete transitions between an electronically excited and the ground state in an individual quantum-mechanical system. This becomes even more fascinating by the option to change the physics of that transition by placing a molecule into a cavity. As E. M. Purcell already pointed out in his seminal contribution to the meeting of the American Physical Society in 1946,[1] the cavity will change the coupling of the intramolecular transition to the vacuum electromagnetic field, thus leading to an acceleration of the radiative transition in a molecule. This has been confirmed in bulk by measuring the fluorescence lifetime as function of the molecules' distance to a metallic mirror.[2] A thorough theoretical description of these measurements had been developed by Chance et al.[3] using a semiclassical approach based on Fermi's Golden Rule.[4] However, the radiative transition constitutes only one of the possible ways for returning from the excited to the ground state when considering molecules embedded in a condensed matter environment (e.g., solid or liquid). Because of collisions/interactions with surrounding molecules, so-called nonradiative transitions constitute a significant alternative way of de-excitation. The ratio of radiative to nonradiative transition rates is quantitatively described by the fluorescence quantum yield (QY) that is defined as the average chance to emit a photon (radiative transition) upon return from the excited to the ground state or

$$\phi = \frac{k_r}{k_r + k_{nr}} \qquad (1)$$

where k_r and k_{nr} are the radiative and nonradiative transition rates, respectively.

From a spectroscopic point of view, the QY of fluorescence is the parameter that is most challenging to assess. Whereas absorption and emission spectra as well as excited state lifetime (fluorescence lifetime) are straightforward to measure with modern measurement techniques, QY values are mostly determined in a comparative manner against a standard of known QY. Nonetheless, precise knowledge of QY is important for many practical applications such as the development of materials for organic and inorganic light emitting diodes,[5] single-photon sources,[6] solar cells,[7] laser technology,[8] or labeling in biological research.[9]

The first successful estimates of the QY of fluorescent solutions had been made by Vavilov in 1924[10] by comparing the fluorescence with scattering intensities. This approach was used, although much refined, over the following decades.[11] Only by 1978, Brannon and Magde developed a method for absolute measurements of QY via sensitive measurements of sample heating upon illumination.[12] However, extending this idea to the single-molecule level seems rather impossible due to the minute amount of heat generated by a single molecule upon nonradiative de-excitation.

Thus, when considering the QY of individual molecules, an appealing idea is to use the aforementioned sensitivity of the

Received: January 19, 2011
Revised: February 21, 2011
Published: March 16, 2011

radiative transition to the local electromagnetic field mode density, which can be changed by placing the emitter close to a mirror or within a cavity. On the single-emitter level, this effect has been demonstrated by several authors, either by measuring the fluorescence lifetime of an emitter in two different environments[13,14] or by placing the emitter on or close to a sharp tip.[15,16] Sandoghdar has recently extended this approach to measuring the fluorescence lifetime of a single molecule as a function of its distance to a metallic mirror,[17] thus replicating Drexhage's original measurements on a single molecule level.

An even more efficient method to change the local mode density of the electromagnetic field is to place an emitter into an optical microcavity.[18,19] Furthermore, if the cavity is tunable, it becomes a powerful tool for changing the mode density and resulting radiative transition rate of an emitter in a continuous way. We have recently used such a tunable microcavity to watch, on one and the same molecule, the varying emission spectrum while changing the cavity width.[20]

Here, we present absolute measurements of the QY of individual molecules using the tunable microcavity. The distance between the cavity mirrors is reduced down to the range of one-half of the emission wavelength, therefore there is only one resonance frequency maximum, which is tuned when the cavity length is changed. Since the mode structure and the coupling between the molecule and the resonator are both frequency dependent, variation of the cavity length leads to a modification of the radiative transition in a molecule according to Fermi's golden rule.[4] The core idea is to record the fluorescence lifetime of the same single molecule as a function of cavity width, in that way changing the radiation rate via the optical mode density in the resonator while leaving at the same time the nonradiative rate of the molecule unaffected. This information is then compared with theoretical modeling for extracting both the pure radiative transition rate and the QY for a given molecule. We observe a broad distribution of QY values from molecule to molecule, which reflects the strong variation of the local interaction of the observed molecules with their host molecules. The method is of fundamental importance wherever one is interested in investigating interactions between fluorescent emitters and surrounding host molecules, which is most sensitively reported by the nonradiative transition rate. This is different to the modification of the QY of a molecule by a plasmonic nanostructure when the molecule must be so close to the metal that absorptive losses to the metal may even dominate the nonradiative relaxation.[21−23]

Figure 1 depicts a schematic of the experimental setup with the tunable microcavity. The cavity mirrors are made by placing thin silver layers (50 nm bottom and 100 nm top) on a glass substrate (see Supporting Information for further details). The bottom semitransparent silver mirror is covered with a 30 nm SiO_2 layer that acts as a spacer between sample molecules and the silver surface. A droplet of a highly diluted solution of fluorescent PI molecules (a perylene derivative; a molecular structure is shown in the inset of Figure 1) was spin coated onto the SiO_2 surface (rotation speed 1000 r/min), resulting in a sparse distribution of molecules across the surface. The molecules were covered with a 70 nm layer of poly(methyl methacrylate) (PMMA) for fixation by spin coating a 1% polymer solution dissolved in dichlormethane (see Supporting Information). Between the top of the polymer layer and the top cavity mirror was air. The cavity height was adjusted with a piezo actuator and the width value was determined by measuring the white light transmission spectrum (see 19 and Supporting Information).

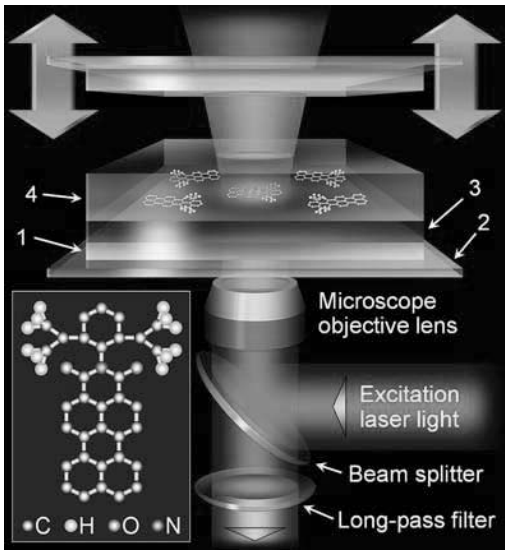

Figure 1. Scheme of the experimental setup. The tunable microcavity consists of the following: silver layers (1) sputtered on the glass surface (2); silica layer (3), acting as a spacer between the metallic surface and the molecules; a polymer layer (4), immobilizing molecules and protecting them from the interaction with atmospheric oxygen. The vertical position of the top mirror is adjusted with nanometer precision by piezo actuator. The inset shows a molecular structure of PI molecule.

An important issue when aiming at an accurate QY determination of single molecules is to have precise knowledge of their position and orientation within the cavity. Both information determine the electromagnetic field mode density that is sensed by a molecule. In our experiment, a molecule's position is given by the position of the SiO_2 surface. However, determining its orientation is more challenging. For that purpose, we scanned molecules with a focused laser beam having higher-order beam modes and thus exhibiting a well-defined three-dimensional polarization geometry of light within the focus. The higher-order beam modes were prepared from a Gaussian beam of an Ar^+-laser (λ_{exc} = 488 nm) by using a laser-mode conversion system (see refs 24−28 and Supporting Information). We have successfully applied this method in the past for probing single molecules orientations inside the cavity.[29,30] Our measurements show that all observed molecules have a dipole orientation parallel to the SiO_2 surface, which can be explained by the fact that the aromatic perylene ring system lays flat down on the surface upon spin coating and subsequent solvent evaporation.

The lifetime measurements within the microcavity were performed with a home-built confocal scanning microscope with a fluorescence lifetime imaging extension (see Supporting Information).

After selecting a single molecule, we acquired fluorescence decay curves for the same molecule at different cavity lengths. Before each lifetime measurement, the cavity width was adjusted by applying a defined voltage to the piezo-actuator and determined by measuring a cavity white-light transmission spectrum with a wide-field transmission microscope. The measured single-molecule fluorescence decays could be well fitted by single-exponential decay functions, yielding the excited state lifetimes of the observed molecules. In total, we collected data for 28 molecules. Figure 2 shows the result of the measured fluorescence lifetime values (red dots) as a function of cavity width (measured

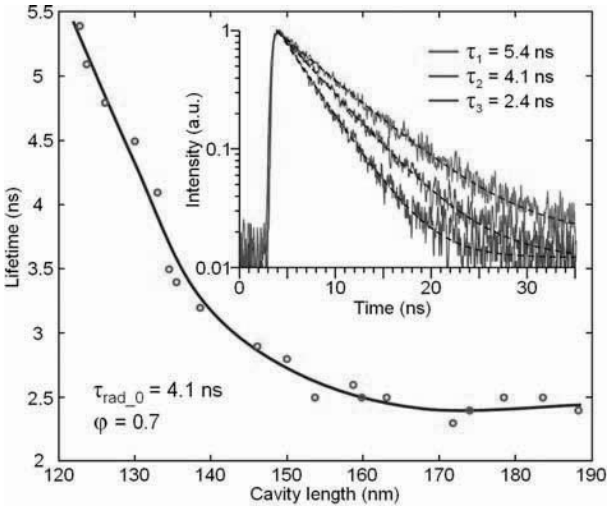

Figure 2. Cavity-controlled fluorescence lifetimes of a single horizontally oriented molecule (red dots) measured at different values of mirror spacing. The solid curve shows the best fit to the experimental data, giving values of $\varphi = 0.7$ and $\tau_{rad\_0} = 4.1$ ns for the single molecule fluorescence quantum yield and the inverse radiative transition rate, respectively. Inset shows fluorescence decays of the single molecule inside the microresonator acquired at the following three different cavity lengths: 123 (red curve), 133 (green curve), and 174 (blue curve) nm. All transients were fitted using monoexponential decay functions (dashed lines).

via maximum of transmission spectrum). The dependence exhibits a strong decrease of the lifetime value with decreasing cavity width, which is due to the gradual shift of SM emitter position toward the center of the cavity where stronger coupling to optical modes occurs.[20] The blue curve shows a theoretical fit as calculated using the theory of Chance et al.[3] and the full information about the cavity's structure and geometry, as well as the molecules' position, orientation, and emission spectrum (for modeling details, see Supporting Information). There are only two free parameters when fitting the theoretical curve against the measurement, the inverse radiative transition rate (τ_{rad_0}), and the QY. For the shown measurement, the best fit to the experimental data yields values of 0.7 for QY and 4.1 ns for τ_{rad_0}.

We employed a bootstrap algorithm for estimating the mean square deviation of the fitted lifetime for each molecule at each cavity width.[31] Mean square deviations of the single molecule lifetime values did typically not exceed 0.1 ns. We also used a bootstrap analysis for estimating the mean square deviation of the QY and the inverse radiative transition rate as obtained by fitting theoretical curves against the experimentally determined dependencies of fluorescence lifetime on cavity width. Assuming that, for each molecule, these mean square deviation values describe the widths of a corresponding two-dimensional Gaussian distribution in QY$-\tau_{rad}$ parameter space, we superimposed these Gaussian distributions of all molecules in one plot, resulting in a probability density plot of QY versus τ_{rad} values. This plot is shown in the Figure 3. The maximum of the probability density distribution corresponds to a value 0.72 for the QY and of 4.1 ns for τ_{rad}, which is in excellent agreement with values obtained from ensemble measurements (0.75 and 4.2 ns, respectively).[19] The solid line represents a linear least-squares fit through the distribution. An inclination of 0.18 ns^{-1} shows that the molecule-to-molecule variation in τ_{rad} is much smaller than that of QY. This is in excellent agreement with the expectation that local

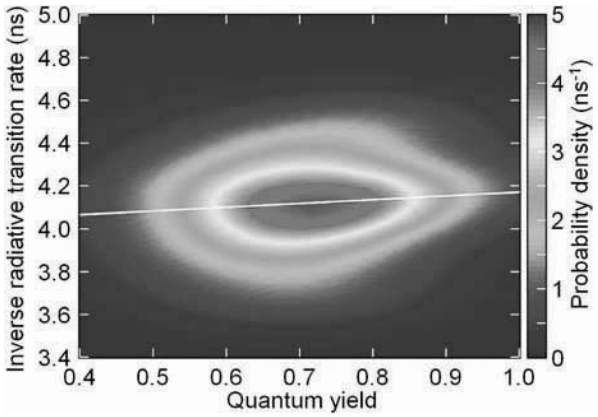

Figure 3. A probability density distribution quantum yield and inverse radiative transition rate obtained from 28 molecules. The distribution has its maximum at 0.72 and 4.1 ns, respectively. The solid white line represents a linear least-squares fit through the distribution.

variations in interaction between a fluorescent molecule and its surrounding (SiO_2, polymer) will mostly affect its nonradiative transition rate but not so much its radiative transition rate, which is mostly determined by the coupling of the transition to the electromagnetic field.

In summary, tuning of the radiative transition rate of individual molecules by placing them into a microcavity of changing width has been demonstrated. This allowed us to extract radiative as well as nonradiative transition rates and to determine QY of individual molecules, which are fundamental parameters of any quantum emitter. Average values thus obtained showed excellent agreement with the results from ensemble measurements. Moreover, we found a broad distribution of QY values, whereas radiative transition rates did not change significantly from molecule to molecule. This reflects the heterogeneous local nature of the host, which determines the nonradiative relaxation of an excited molecule via interaction with the local chemical environment. Our technique can be applied to any single quantum emitter of interest, such as dye molecules, semiconductor nanoparticles, carbon nanotubes, and so forth. Thus, the tunable cavity method makes it a versatile tool for single molecule spectroscopy and QY measurements of individual emitters.

■ ASSOCIATED CONTENT

Supporting Information. Details on preparation of cavity, controlling the cavity geometry, polymer solution and spin-coating, determining molecular orientation, lifetime measurement, and lifetime modeling. This material is available free of charge via the Internet at http://pubs.acs.org.

■ AUTHOR INFORMATION

Corresponding Author

*E-mail: (A.J.M.) alfred.meixner@uni-tuebingen.de; (J.E.) enderlein@physik3.gwdg.de.

■ ACKNOWLEDGMENT

Financial support by the Forschungsschwerpunktprogramm Baden-Württemberg and from the European Commission through the Human Potential Program (Marie-Curie Research

Training Network NANOMATCH, Contract No. MRTN-CT-2006-035884) is acknowledged.

REFERENCES

(1) Purcell, E. M. *Phys. Rev.* **1946**, *69*, 681.
(2) Drexhage, K. H. *Prog. Opt.* **1974**, *12*, 163.
(3) Chance, R. R.; Prock, A.; Silbey, R. *Adv. Chem. Phys.* **1978**, *37*, 1–65.
(4) Fermi, E. *Rev. Mod. Phys.* **1932**, *4*, 87.
(5) Reineke, S.; Lindner, F.; Schwartz, G.; Seidler, N.; Walzer, K.; Lüssem, B.; Leo, K. *Nature* **2009**, *459*, 234–238.
(6) Lounis, B.; Moerner, W. E. *Nature* **2000**, *407*, 491–493.
(7) Thompson, B. C.; Frechet, J. M. J. *Angew. Chem., Int. Ed.* **2008**, *47*, 58–77.
(8) Tessler, N. *Adv. Mater.* **1999**, *11*, 363–370.
(9) Medintz, I. L.; Uyeda, H.; Goldman, E. R.; Mattoussi, H. *Nat. Mater.* **2005**, *4*, 435–446.
(10) Vavilov, S. I. *Z. Phys.* **1924**, *22*, 266.
(11) Demas, J. N.; Crosby, G. A. *J. Phys. Chem.* **1971**, *75*, 991–1024.
(12) Brannon, E. H.; Magde, D. *J. Phys. Chem.* **1978**, *82*, 705–709.
(13) Macklin, J.; Trautman, J.; Harris, T.; Brus, L. *Science* **1996**, *272*, 255–258.
(14) Brokmann, X.; Coolen, L.; Dahan, M.; Hermier, J. P. *Phys. Rev. Lett.* **2004**, *93*, No. 107403.
(15) Ambrose, W. P.; Goodwin, P. M.; Martin, J. C.; Keller, R. A. *Science* **1994**, *265*, 364–367.
(16) Trabesinger, W.; Kramer, A.; Kreiter, M.; Hecht, B.; Wild, U. P. *Appl. Phys. Lett.* **2002**, *81*, 2118–2120.
(17) Buchler, B. C.; Kalkbrenner, T.; Hettich, C.; Sandoghdar, V. *Phys. Rev. Lett.* **2005**, *95*, No. 063003.
(18) Vahala, K. J. *Nature* **2003**, *424*, 839–846.
(19) Steiner, M.; Schleifenbaum, F.; Stupperich, C.; Failla, A. V.; Hartschuh, A.; Meixner, A. J. *Chem. Phys. Chem.* **2005**, *6*, 2190–2196.
(20) Chizhik, A.; Schleifenbaum, F.; Gutbrod, R.; Chizhik, A.; Khoptyar, D.; Meixner, A. J.; Enderlein, J. *Phys. Rev. Lett.* **2009**, *102*, No. 073002.
(21) Dulkeith, E.; Morteani, A. C.; Niedereichholz, T.; Klar, T. A.; Feldmann, J.; Levi, S. A.; van Veggel, F. C. J. M.; Reinhoudt, D. N.; Möller, M.; Gittins, D. I. *Phys. Rev. Lett.* **2002**, *89*, No. 203002.
(22) Anger, P.; Bharadwaj, P.; Novotny, L. *Phys. Rev. Lett.* **2006**, *96*, No. 113002.
(23) Kinkhabwala, A.; Yu, Z.; Fan, S.; Avlasevich, Y.; Müllen, K.; Moerner, W. E. *Nat. Photonics* **2009**, *3*, 654–657.
(24) Chizhik, A. M.; Jäger, R.; Chizhik, A. I.; Bär, S.; Mack, H.-G.; Sackrow, M.; Stanciu, C.; Lyubimtsev, A.; Hanack, M.; Meixner, A. J. *Phys. Chem. Chem. Phys.* **2011**, *13*, 1722–1733.
(25) Dorn, R.; Quabis, S.; Leuchs, G. *Phys. Rev. Lett.* **2003**, *91*, No. 233901.
(26) Novotny, L.; Beversluis, M. R.; Youngworth, K. S.; Brown, T. G. *Phys. Rev. Lett.* **2001**, *86*, 5251–5254.
(27) Chizhik, A. M.; Chizhik, A. I.; Gutbrod, R.; Meixner, A. J.; Schmidt, T.; Sommerfeld, J.; Huisken, F. *Nano Lett.* **2009**, *9*, 3239–3244.
(28) Chizhik, A. I.; Chizhik, A. M.; Khoptyar, D.; Bär, S.; Meixner, A. J. *Nano Lett.* **2011**, *11*, 1131–1135.
(29) Gutbrod, R.; Khoptyar, D.; Steiner, M.; Chizhik, A. M.; Chizhik, A. I.; Bär, S.; Meixner, A. J. *Nano Lett.* **2010**, *10*, 504–508.
(30) Bär, S.; Chizhik, A.; Gutbrod, R.; Schleifenbaum, F.; Chizhik, A.; Meixner, A. J. *Anal. Bioanal. Chem.* **2010**, *396*, 3–14.
(31) Efron, B. *Ann. Stat.* **1979**, *7*, 1–26.

Supporting information

Preparation of cavity

The bottom silver mirror and silica layer were prepared by vapor deposition onto commercially available and cleaned microscope glass coverslides (thickness 170 µm) using an electron beam source (EB3, Edwards) under high-vacuum conditions (≈ 10^{-6} mbar). The top silver layer was prepared by vapor deposition of silver on the surface of a plan-convex lens (focal length of 150 mm) under the same conditions. Film thickness was monitored during vapor deposition using an oscillating quartz unit (FTM7, Edwards) and verified by atomic force microscopy (AFM) measurements. The mirrors were fixed in a home-built aluminum holder, equipped with the piezo actuators (PSt 150/3.5×3.5/20, Piezomechanik GmbH) for adjusting cavity height.

Controlling the cavity geometry

The spherical shape of the upper mirror allows us to control the optical quality and the tuning capability of the micro-resonator by imaging the cavity white-light transmission patterns, see Fig. S1(a). The Newton rings are a result of the different resonator lengths due to the curved surface of the top mirror. The central region of the micro-cavity (i.e., the region of minimum cavity length) remains dark, as no visible light is transmitted there. Moving of the upper cavity mirror leads to a shift of the transmission pattern.

The absolute values L of cavity length, see Fig. S1(b), were determined using on-axis white light transmission profiles acquired with a spectrograph (SpectraPro 300i, Acton Research) in combination with a CCD camera (LNCCD-1340/100-EB/1, Princeton Instruments) and fitted by a Lorentzian line-shape function (see e.g. [1] for further details). We calculate the local cavity length (in particular thickness of air layer) by comparing the measured spectrum with a calculated spectrum using standard transfer-matrix method for plane waves passing through a stratified medium [2].

All fluorescence measurements were performed in the λ/2 region of the cavity, close to the center of the lens, where the horizontal displacement within the focal spot of our microscope objective (500 nm) results in a cavity length change ΔL of about 1 nm, which is of the order of the surface roughness of our silver mirrors. Therefore, our micro-resonator can be considered as a plane-parallel system.

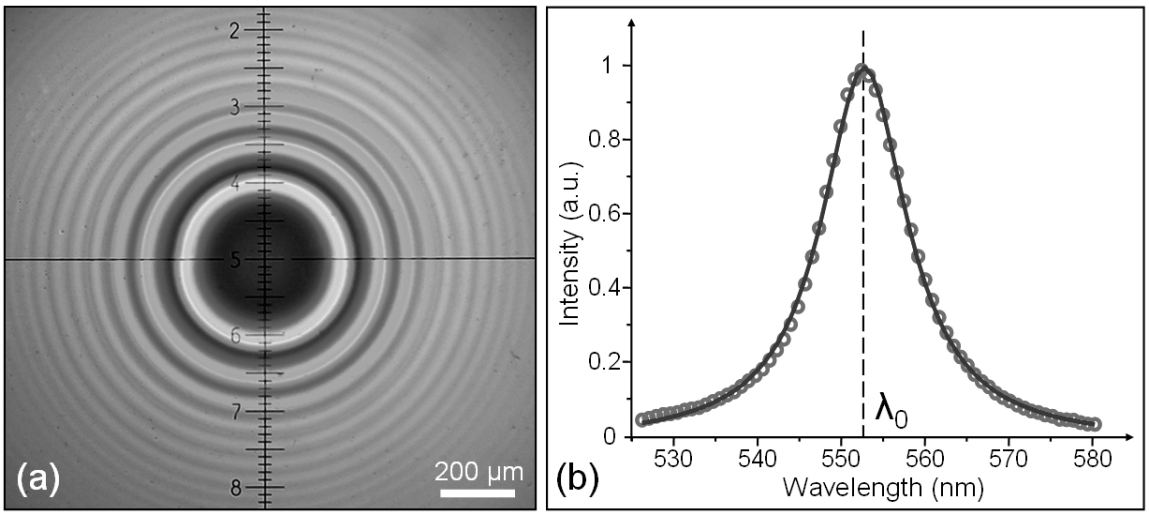

Figure S1. (a) White light transmission patterns (Newton rings) of the micro-cavity. The inner transmission ring shows the first order of interference. (b) Micro-cavity white light transmission spectrum (○) fitted by a Lorentzian function (–).

Polymer solution and spin-coating

A 10 µl droplet of a 10^{-10} M solution of the perylene derivative N-(2,6-diisopropylphenyl)-perylene-3,4-dicarboxymid (abbreviated by PI in the following) in dichloromethane was spin-coated on the surface of the silica layer at a rotation speed of 1000 rpm. After evaporation of the solvent, spatially separated molecules were covered with a layer of poly(methyl-methacrylate) (PMMA, [C5O2H8]*n*). A droplet (10 µl) of a 1% polymer solution in dichloromethane was spin-coated at rotation speed of 8000 rpm to deposit a 70 nm thick polymer film as was subsequently determined by AFM.

Determining molecular orientation

To investigate the three-dimensional orientation of the molecules' transition dipole moment, we equipped a home-built confocal microscope with a mode conversion optical line as schematically shown in Fig. S2(a) [3-8]. The key element of that system is the mode converter, consisting of four λ/2 plates glued together as shown in Fig. S2(a). When a linearly polarized Gaussian laser beam passes the mode converter, a radially polarized beam is created. A pinhole is used to remove higher spatial frequencies. The collimated beam is reflected by a non-polarizing beam-splitter and focused onto the sample with the microscope objective lens (numerical aperture N.A. = 1.25). The radially polarized laser beam (RPLB) has a field distribution containing both longitudinal and in-plane components in the focal region, see Fig. S2(b) [3, 4, 8-10]. The strong difference between the distributions of the longitudinal and the in-plane components of the electric field vector within the focus leads to a strong orientation dependence of the fluorescence image pattern of a single emitter [8, 10, 11]. This makes the RPLB ideally suited to determine the three-dimensional orientation of the three-dimensional orientation of single molecules. Vertically oriented molecules display a spot in the center of the focal area as the result of excitation by only the longitudinal component of the field, while horizontally oriented molecules can be excited only by the in-plane components, thus exhibiting two lobes with a dark gap in between (see [8, 10, 11] for further details). In the latter case, the transition dipole moment of the molecule is oriented along a line that connects the maxima of the two lobes. Tilted positions of a molecule show an intermediate image shape, thus allowing for a precise determination of their three-dimensional orientation with an accuracy up to 5° [7]. Fig. S2(c) shows an experimental image of a single PI molecule investigated during our study. The best theoretical fit of the pattern as shown in Fig. S2(d) reveals that the molecule is oriented horizontally, along the dashed line.

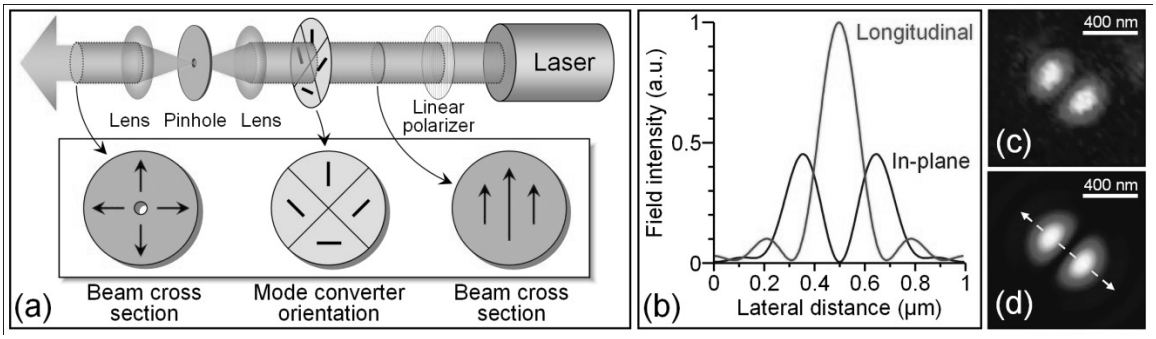

Figure S2. (a) Scheme of the mode-conversion optical line according to Dorn et al. [4]. (b) Excitation field in-plane and longitudinal components intensity distribution within the focal spot of the microscope objective in the case of the radially polarized laser beam. The distribution is calculated for the case of a 1.25 numerical aperture objective and an excitation wavelength of λ_{exc} = 488 nm. (c) Fluorescence image of a single PI molecule, excited with a radially polarized laser beam. (d) Simulated excitation pattern, showing the best theoretical

fit to the experimental image in (c). The dashed line indicates the orientation of the single molecule transition dipole moment which is parallel to the sample surface.

Lifetime measurement

Fluorescence lifetime measurements were performed with a home-built confocal scanning microscope based on a Zeiss Axiovert 135 TV with fluorescence lifetime imaging extension (Picoharp 300, Picoquant GmbH, Berlin, Germany). Laser focusing and fluorescence light detection were done with the same objective (Plan-Neofluar, 100×/N.A. = 1.25 oil immersion, Zeiss). Excitation light and fluorescence light were separated by a dichroic beam splitter (Zeiss FT500). For sample scanning, a feedback-controlled sample stage (PI, E-710.3CD) with nanometer positioning precision was employed. Fluorescence excitation was done with the light of a 473 nm pulsed diode laser (LDH-P-C-470, Picoquant GmbH, Berlin, Germany). Within the detection path, a steep edge filter (LP02-473RU-25 Semrock) was used to block back-reflected or elastically scattered light. Collected fluorescence was focused onto the active area of a spectrally integrating avalanche photo diode (APD) (SPCM 200, Perkin Elmer). Data acquisition was accomplished with a commercially available software package (SymPhoTime, Picoquant GmbH, Berlin, Germany). Fluorescence decay curves were fitted using a mono-exponential function, $A \exp(-t/\tau + B)$, convoluted with the instrument response function, which was recorded under comparable experimental conditions. All fluorescence transients were recorded with an integration time of five seconds.

Lifetime modeling

The lifetime calculation of a fluorescing molecule within the cavity proceeds in several steps. Let us consider the general case of a single molecule with inclination angle β towards the vertical axis (optical axis) immobilized on the surface of the SiO_2 layer (see. Fig. S3).

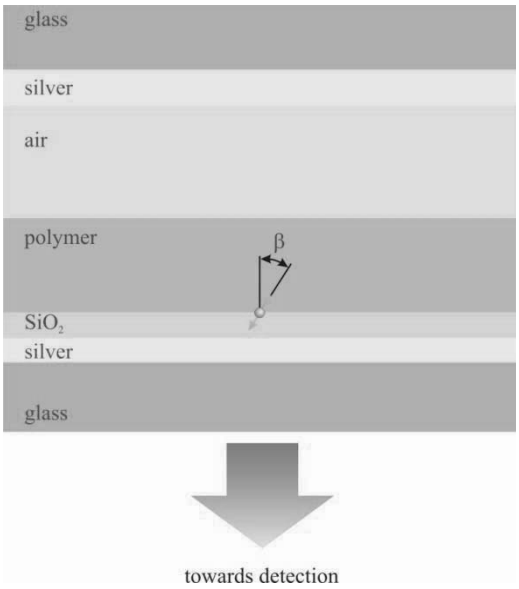

Figure S3. General schematic of a molecule within the micro-cavity.

The molecule is assumed to be a perfect electric dipole emitter. Starting point of all calculations is Weyl's plane-wave representation of the electric field of a monochromatic oscillating electric dipole with oscillation frequency ν embedded in a homogeneous space with refractive index n_{poly} :

$$\mathbf{E}_D = \frac{ik_0^2}{2\pi}\int\frac{d\mathbf{q}}{|w_\pm|}\left[\boldsymbol{\kappa}_{p\pm}\left(\boldsymbol{\kappa}_{p\pm}\cdot\mathbf{p}\right)+\boldsymbol{\kappa}_s\left(\boldsymbol{\kappa}_s\cdot\mathbf{p}\right)\right]\exp\left(i\mathbf{q}\cdot\boldsymbol{\rho}+iw_\pm z\right) \tag{S1}$$

where k_0 is the vacuum wave number, $k_0 = 2\pi/\lambda_0 = 2\pi\nu/c$ (c being the vacuum speed of light); $\mathbf{q}$ and w are the transversal and axial components of the wave vector in the polymer layer, $\mathbf{k}_\pm = (\mathbf{q}, w_\pm) = (q_x, q_y, w_\pm)$, so that one has the relationship $w_\pm = \pm\sqrt{n_{poly}^2 k_0^2 - q^2}$; $\boldsymbol{\kappa}_{p\pm}$ and $\boldsymbol{\kappa}_s$ are unit polarization vectors for the *p*- and *s*-polarized component of a plane wave traveling along $\mathbf{k}$. In particular, we have

$$\boldsymbol{\kappa}_{p\pm} = \frac{1}{k}\left(-\frac{w_\pm q_x}{q}, -\frac{w_\pm q_y}{q}, q\right) \tag{S2}$$

and

$$\boldsymbol{\kappa}_s = \frac{1}{q}\left(-q_y, q_x, 0\right) \tag{S3}$$

where k and q denote the lengths of the vectors $\mathbf{k}$ and $\mathbf{q}$, respectively (see. Fig. S4).

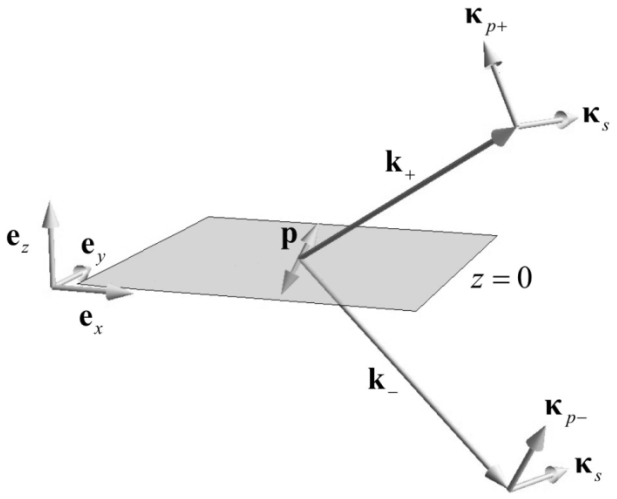

Figure S4. Visualization of geometry and vectors in the Weyl representation of electric dipole emission. The emitting dipole sits in the plane $z = 0$, the unit vector $\boldsymbol{\kappa}_s$ is co-planar with this plane.

In all the above equations, the plus and minus subscripts refer to plane waves traveling along the positive or negative *z*-direction, respectively. Using this plane wave representation, it is straightforward to find the electric field on the inner surfaces (oriented towards cavity) of the silver mirrors by solving, for each plane wave component as input, Maxwell's equation in the presence of the planar cavity [12,13,14]. The electric field amplitude is found to have the general structure

$$\mathbf{E}_\pm = \frac{ik_0^2}{2\pi}\int\frac{d\mathbf{q}}{|w_\pm|}\left[t_{p\pm}(q)\boldsymbol{\kappa}_{p\pm}\left(\boldsymbol{\kappa}_{p\pm}\cdot\mathbf{p}\right)+t_{s\pm}(q)\boldsymbol{\kappa}_s\left(\boldsymbol{\kappa}_s\cdot\mathbf{p}\right)\right]\exp\left(i\mathbf{q}\cdot\boldsymbol{\rho}+iw'_\pm z\right) \tag{S4}$$

where the plus and minus subscript refer to the inner surfaces of the top and bottom mirror of the cavity. The $t_{p\pm}$ and $t_{s\pm}$ are *q*-dependent coefficients, and the $w'_\pm$ are the vertical component of the wave vector in the media adjacent to the top and bottom silver layer, respectively, thus in our case $w'_+ = \sqrt{n_{air}^2 k_0^2 - q^2}$ and $w'_- = \sqrt{n_{\mathrm{SiO_2}}^2 k_0^2 - q^2}$. It is important to note that the functions $t_{p\pm}$ and $t_{s\pm}$ are also wavelength-dependent and have to be calculated separately for

each wavelength of the emission spectrum $F_0(\lambda)$ of the fluorescent molecule. In all the calculations, it has also to be taken into account that the dielectric properties of metals are strongly wavelength-dependent [15].
Knowing the electric field amplitudes on the metal surfaces, the total emission power of the dipole is then calculated as the time-averaged integral of the scalar product of the Poynting vector with a unit vector perpendicular to the surface and directed outwards from the cavity:

$$S(\beta,\lambda) = \frac{c}{8\pi} \iint dxdy \,\mathrm{Re}\left[\mathbf{e}_z \cdot \left(\mathbf{E}_+ \times \mathbf{B}_+^* - \mathbf{E}_- \times \mathbf{B}_-^*\right)\right] \tag{S5}$$

where a star superscript denotes complex conjugation, and the $\mathbf{B}_\pm$ are the magnetic field amplitudes which are given by a similar plane wave representation as the electric field amplitudes, namely

$$\mathbf{B}_\pm = \frac{ik_0^2}{2\pi} \int \frac{d\mathbf{q}}{|w_\pm|} \mathbf{n}_\pm \times \left[t_{p\pm}(q)\boldsymbol{\kappa}_{p\pm}\left(\boldsymbol{\kappa}_{p\pm}\cdot\mathbf{p}\right) + t_{s\pm}(q)\boldsymbol{\kappa}_s\left(\boldsymbol{\kappa}_s\cdot\mathbf{p}\right)\right]\exp\left(i\mathbf{q}\cdot\boldsymbol{\rho} + iw'_\pm z\right). \tag{S6}$$

Here, the $\mathbf{n}_\pm$ are vectors collinear with the wave vectors $\mathbf{k}'_\pm = (\mathbf{q}, w'_\pm)$ but having a length equal to the refractive index of the layer adjacent to the corresponding silver surface (SiO_2 for bottom surface, air for top surface).
The core assumption of the semi-classical approach as developed by Chance, Prock and Silbey is that the radiative transition rate, k_{rad}, is proportional to the total power of emission as calculated above, i.e. Eq.(S5) times the dye's spectrum $F_0(\lambda)$ integrated over all emission wavelengths:

$$k_{rad} \propto \int F_0(\lambda) S_{tot}(\beta,\lambda) d\lambda \tag{S7}$$

The proportionality constant can be easily found by requiring that k_{rad} becomes equal to the rate of a dipole in a homogenous polymer space when no cavity is present.
All the above consideration refer only to the radiative transition rate of a fluorescent molecule. For molecules with a quantum yield of fluorescence ϕ smaller than one, the observable fluorescence lifetime is given by

$$\tau = \left(k_{rad} + k_{nr}\right)^{-1}. \tag{S8}$$

Thus, in the presence of the cavity one finds

$$\tau^{-1} = \frac{k_{rad} + k_{nr}}{k_{rad,0} + k_{nr}} \tau_0^{-1} = \frac{k_{rad}}{k_{rad,0}}\phi + 1 - \phi \tag{S9}$$

where the subscript 0 refers to the situation with no cavity (pure polymer), and the ratio $k_{rad}/k_{rad,0}$ is calculated as described above. Because the k_{rad} strongly depends on dipole orientation β, it is crucial to have *a apriori* knowledge of this parameter. In the case of our experiments, β was determined to be close to 90° for all observed molecules. Thus, when fitting the measured curve of fluorescence lifetime τ against cavity size, we have only two free fit parameters: the free radiative rate $k_{rad,0}$, and the fluorescence quantum yield ϕ, which can be uniquely extracted from the fit (ϕ determines the vertical offset of the τ^{-1} versus cavity-size curve, and $\phi/k_{rad,0}$ its modulation amplitude).

Modification of the cavity mode

The distance between the mirrors of our tunable cavity is reduced down to the range of one half of the emission wavelength, therefore there is only one resonance frequency maximum, which is tuned when the cavity length is changed (Figure S5) [16]. Since the mode structure and the coupling between the molecule and the resonator are both frequency dependent, a

variation of the cavity length leads to a modification of the radiative transition in a molecule according to Fermi's golden rule [17].

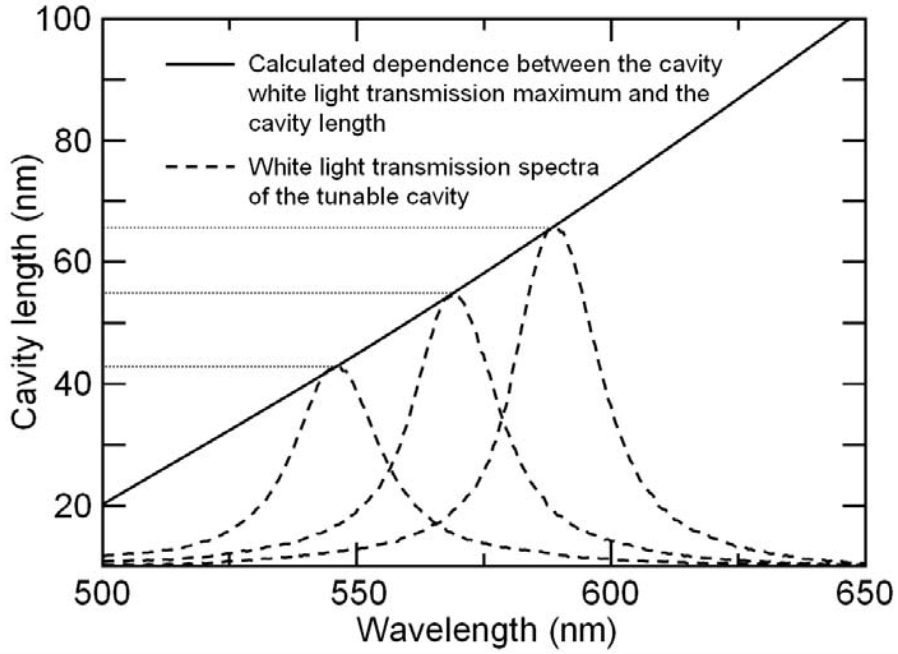

Figure S5. Modification of the tunable cavity white light transmission spectrum upon changing the cavity length.

Let us derive the mode density along the cavity axis. The mode density in the cavity is proportional to the optical transmittance through the cavity $T(\nu)$ [18,19]:

$$\rho(\nu) = KT(\nu), \qquad \text{(S10)}$$

where K is a constant. The value of this constant will be determined by a normalization condition. The transmission through a Fabry-Perot cavity can be represented in the following form [18]:

$$T = \frac{T_1 T_2}{1 + R_1 R_2 - 2\sqrt{R_1 R_2}\cos 2\phi}, \qquad \text{(S11)}$$

where ϕ is the phase change of the optical wave for a single pass between the two reflectors, T_1 and T_2 are transmittances through the two cavity mirrors and R_1 and R_2 are the respective reflectivities. Rewriting Equation (11) in terms of frequency, one obtains:

$$T(\lambda) = \frac{T_1 T_2}{1 + R_1 R_2 - 2\sqrt{R_1 R_2}\cos\left(4\pi n L_c \nu / c\right)}. \qquad \text{(S12)}$$

where L_c is the length of the cavity, ν is the frequency of light, n is the refractive index of the medium and c is the velocity of light in vacuum. The transmittance has maxima when the resonance condition $2L_c = m\lambda_1$, m=1, 2, 3, … is fulfilled. For our resonator m=1, $2L_c = \lambda_1$ and $\nu_1 = c/2L_c$. At the transmission maximum the Lorenzian approximation can be obtained by expanding the cosine term in Equation (12) into a power series using $\cos(x) \approx 1 - x^2/2$. This gives:

$$T(\nu)=\frac{T_1T_2}{\sqrt{R_1R_2}\left(4\pi nL_c/c\right)^2}\frac{1}{\frac{\left(1-\sqrt{R_1R_2}\right)^2}{\sqrt{R_1R_2}\left(4\pi nL_c/c\right)^2}+\left(\nu_1-\nu\right)^2}. \quad \text{(S13)}$$

Integrating $\rho(\nu)$ over all frequencies ν and the cavity lengths L yields a single optical mode, that is,

$$\int_0^{L_c}\int_{-\infty}^{\infty}\rho(\nu)d\nu dL=1. \quad \text{(S14)}$$

The lower and the upper limit of the frequency integration can be chosen to be $\pm\infty$ since the Lorenzian approximation of Equation (13) has only one maximum at $\nu=\nu_1$. Equations (10), (13) and (14) give:

$$\int_0^{L_c}\int_{-\infty}^{\infty}K\frac{T_1T_2}{\sqrt{R_1R_2}\left(4\pi nL_c/c\right)^2}\frac{1}{\frac{\left(1-\sqrt{R_1R_2}\right)^2}{\sqrt{R_1R_2}\left(4\pi nL_c/c\right)^2}+\nu^2}d\nu dL=1 \quad \text{(S15)}$$

Using the definite integral $\int_{-\infty}^{\infty}\left(a^2+x^2\right)^{-1}dx=\pi/a$, where $a=\left(1-\sqrt{R_1R_2}\right)/\left(\left(R_1R_2\right)^{1/4}\left(4\pi nL_c/c\right)\right)$ we come to the following:

$$\int_0^{L_c}K\frac{T_1T_2}{\sqrt{R_1R_2}\left(4\pi nL_c/c\right)^2}\frac{\pi}{\frac{1-\sqrt{R_1R_2}}{\left(R_1R_2\right)^{1/4}\left(4\pi nL_c/c\right)}}dL=1, \quad \text{(S16)}$$

which can be rewritten as:

$$\int_0^{L_c}K\frac{T_1T_2}{4nL_c}\frac{c}{\left(R_1R_2\right)^{1/4}\left(1-\sqrt{R_1R_2}\right)}dL=1 \quad . \quad \text{(S17)}$$

Integration gives:

$$K\frac{c}{4n}\frac{T_1T_2}{\left(R_1R_2\right)^{1/4}\left(1-\sqrt{R_1R_2}\right)}=1. \quad \text{(S18)}$$

This gives us the value for K:

$$K=\frac{\left(R_1R_2\right)^{1/4}}{T_1T_2}\frac{4n}{c}\left(1-\sqrt{R_1R_2}\right). \quad \text{(S19)}$$

With equation (10), the optical mode density of a one-dimensional cavity for emission along the cavity axis is given by:

$$\rho(\lambda) = \frac{(R_1 R_2)^{1/4}}{T_1 T_2} \frac{4n}{c} \left(1 - \sqrt{R_1 R_2}\right) T(\lambda). \qquad \text{(S20)}$$

References

[1] Chizhik A. I.; Schleifenbaum, F.; Gutbrod, R.; Chizhik, A. M.; Khoptyar, D.; Meixner, A. J.; Enderlein, J. *Phys. Rev. Lett.* **2009**, *102*, 073002-1-4.

[2] Born, M.; Wolf, E. *Principles of optics: electromagnetic theory of propagation, interference and diffraction of light.* Pergamon Press, Oxford, 1964.

[3] Novotny, L.; Beversluis, M. R.; Youngworth, K. S.; Brown, T. G. *Phys. Rev. Lett.* **2001**, *86*, 5251-5254.

[4] Dorn, R.; Quabis, S.; Leuchs, G. *Phys. Rev. Lett.*, **2003**, *91*, 233901-1-4.

[5] Failla, A. V.; Qian, H.; Qian, H.; Hartschuh, A.; Meixner, A. J. *Nano Lett.* **2006**, *6* , 1374-1378.

[6] Gutbrod, R.; Chizhik, A. I.; Chizhik, A. M.; Khoptyar, D.; Meixner, A. J. *Opt. Lett.* **2009**, *34*, 629-631.

[7] Gutbrod, R.; Khoptyar, D.; Steiner, M.; Chizhik, A. M.; Chizhik, A. I.; Bär, S.; Meixner, A. J. *Nano Lett.* **2010**, *10*, 504-508.

[8] Bär, S.; Chizhik, A. I.; Gutbrod, R.; Schleifenbaum, F.; Chizhik, A. M.; Meixner, A. J. *Anal. Bioanal. Chem.* **2010**, *396*, 3-14.

[9] Khoptyar, D.; Gutbrod, R.; Chizhik, A.; Enderlein, J.; Schleifenbaum, F.; Steiner, M.; Meixner, A. J. Opt. Express **2008**, *16(13)*, 9907-9917.

[10] Chizhik, A. M.; Schmidt, T.; Chizhik, A. I.; Huisken, F.; Meixner, A. J. *Proc. SPIE* **2009**, *7393*, 739305-1-11.

[11] Chizhik, A. M.; Chizhik, A. I.; Gutbrod, R.; Meixner, A. J.; Schmidt, T.; Sommerfeld, J.; Huisken, F.; *Nano Lett.* **2009**, *9*, 3239-3244.

[12] Enderlein, J.; Ruckstuhl, T.; Seeger, S. *Appl. Opt.* **1999**, *38*, 724-732.

[13] Enderlein, J.; Ruckstuhl, T. *Opt. Express* **2005**, *13*, 8855-8865.

[14] Enderlein, J. *Biophys. J.* **2000**, *78*, 2151-2158.

[15] Rakić, A. D.; Djurišić, A. B.; Elazar, J. M.; Majewski, M. L. *Appl. Opt.* **1998**, *37*, 5271-5283.

[16] Steiner, M.; Schleifenbaum, F.; Stupperich, C.; Failla, A. V.; Hartschuh, A.; Meixner, A. J. *Chem. Phys. Chem.* **2005**, *6*, 2190-2196.

[17] Fermi, E. *Rev. Mod. Phys.* **1932**, *4*, 87.

[18] Wilmsen, C.; Temkin, H.; Coldren, L.A. *Vertical-cavity surface-emitting lasers: design, fabrication, characterization, and applications. Cambridge University Press*. Cambridge, 1999.

[19] Chang, R. K; Campillo, A. J. *Optical processes in microcavities*. World Scientific Publishing Co. Pte. Ltd., Singapore, 1996.

Chapter 4

Controlling the optical properties of single molecules by optical confinement in a tunable microcavity

In this chapter, we present experimental results on changing the fluorescence spectrum of a single molecule by embedding it within a tunable optical microresonator with subwavelength spacing. The cavity length is reversibly changed across the entire visible range with nanometer precision by using a piezoelectric actuator. By varying its length, the local mode structure of the electromagnetic field is changed together with the radiative coupling of the emitting molecule to the field. Since mode structure and coupling are both frequency dependent, this leads to a renormalization of the emission spectrum of the molecule.

This chapter is based on:

Chizhik, A.I., Gutbrod, R., Chizhik, A.M., Bär, S., Meixner, A.J. "Controlling the optical properties of single molecules by optical confinement in a tunable microcavity" *Proc. SPIE* **2009**, 7396, 73960F. doi:10.1117/12.825278.

Controlling the optical properties of single molecules by optical confinement in a tunable microcavity

Alexey Chizhik, Raphael Gutbrod, Anna Chizhik, Sebastian Baer, Alfred Meixner.

Institute of Physical and Theoretical Chemistry, University of Tuebingen,
Auf der Morgenstelle 8, 72076 Tuebingen, Germany
E-mail: alfred.meixner@uni-tuebingen.de

ABSTRACT

We present experimental results on changing the fluorescence spectrum of a single molecule by embedding it within a tunable optical microresonator with subwavelength spacing. The cavity length is reversibly changed across the entire visible range with nanometer precision by using a piezoelectric actuator. By varying its length, the local mode structure of the electromagnetic field is changed together with the radiative coupling of the emitting molecule to the field. Since mode structure and coupling are both frequency dependent, this leads to a renormalization of the emission spectrum of the molecule. Moreover, we use doughnut laser modes in the tunable microcavity to determine the longitudinal position of an isotropic emitter. By analyzing the excitation patterns resulting from the illumination of a single fluorescent bead in the focus of a radially polarized doughnut mode laser beam we can determine the longitudinal position of this bead in the microcavity with an accuracy of a few nanometers.

Keywords: tunable microcavity, single molecule spectroscopy, single molecule microscopy, fluorescence microscopy, confocal microscopy, longitudinal localization of the emitter, doughnut laser modes.

INTRODUCTION

It was first noted by Purcell more then 60 years ago [1], that placing an emitter within a confined geometry alters its emission properties, in particular, the rate of spontaneous emission is increased. This can be easily understood within a Fermi's golden rule approach to the emission of an electric dipole within the given geometry: The density of modes of the electromagnetic field inside a cavity is changed with respect to free space, and hence the coupling of the dipole transition of an emitting molecule to this field. The first extensive experimental studies of the changes in spontaneous emission rates of molecules in front of a metal mirror were conducted by Kuhn and Drexhage [2]. Lukosz and coworkers performed extensive studies of the changes in the angular distribution of fluorescent molecules radiation close to a metallic mirror or dielectric interfaces [4,5]. Later, all of these results had been confirmed also on a single molecule level, see Ref. [6] and citations therein. Remarkably, little attention has been paid to the changes in the emission spectrum of a fluorescent dye as induced by the changes of the local electromagnetic field structure. This is partially due to the fact that when observing molecules with narrow emission bands, optical dispersion of the molecule's environment is rather weak, so that the wavelength dependence of the changes in the radiative transition rate by its environment is negligible. However, if a molecule displays a broad emission spectrum, one can no longer neglect optical dispersion effects, and strong shape changes of a molecule's emission spectrum are expected. This is due to the fact that the optical dispersion of a molecule's environment leads to a wavelength-dependent electromagnetic coupling of the emitter to its environment, which results in a renormalization of the observable emission spectrum of the embedded molecule. For example, strong changes in the emission and absorption spectra have been predicted for a Rhodamine 6G molecule embedded within a spherical metal nanocavity [7]. Experimentally, this effect has been observed qualitatively by Steiner et al. [8] who investigated single isolated perylene dye molecules in a planar metal microcavity for different mirror

Physical Chemistry of Interfaces and Nanomaterials VIII, edited by Oliver L. A. Monti, Oleg V. Prezhdo,
Proc. of SPIE Vol. 7396, 73960F · © 2009 SPIE · CCC code: 0277-786X/09/$18 · doi: 10.1117/12.825278

spacings and hence for different electromagnetic mode structures. However, as the mirror spacing was fixed, they could investigate a distinct molecule only for one given resonator length.
Just recently we demonstrated a new tunable microcavity design allowing us to actively change the local electromagnetic field structure around a molecule by changing the mirror spacing of the cavity, thus changing the emission spectrum of a single fluorescent molecule embedded in a tunable microcavity [9]. In doing that, one selects the vibronic transition where fluorescence will mostly occur. Here we expand the overview of the microcavity controlled single molecule emission, focusing on broader variety of the cavity physics aspects.
The exact localization of a quantum emitter in a transparent dielectric medium is an important task in applications of precision confocal microscopy. Therefore we use a planar metallic subwavelength microcavity that can be reversibly tuned across the entire visible range, with the transparent medium between the cavity mirrors. According to diffraction theory [11] the resolution of a light microscope is related to the size of its focal spot. Although there are extensive methods to determine the lateral position of a quantum emitter with nanometer accuracy, it is difficult to determine the longitudinal (i.e., along the optical axis) position of the quantum emitter [12–15]. This is related to the fact that the focal spot of a lens is at least three to four times as long as it is wide owing to technical limitations of the numerical aperture [11]. One concept to overcome this limitation is to combine the aperture of two opposing lenses, as it is used for example in 4PI-fluorescence microscopy [16,17]. We present here a method to determine the longitudinal position of a fluorescent bead using the excitation in a microcavity with a radially polarized doughnut-mode laser beam. This beam provides an intracavity excitation field that is strongly dependent on the longitudinal position [18] and can be used for a precise determination of the emitter position. The microcavity is formed by two silver mirrors enclosing a transparent dielectric medium and allows for reversible tuning of the cavity resonances on the same lateral position. This offers the possibility to determine the longitudinal position of a deliberately chosen single quantum emitter in the microcavity with an accuracy of a few nanometers [19].

EXPERIMENTAL SECTON

Tunable microcavity design and characterization.

The tunable microcavity construction is schematically shown in Fig. 1a and is similar to a previously built one but with no adjustable cavity length [8]. A homemade aluminum cavity holder was used to hold the cavity. The bottom part of the cavity consisted of a coverslide (thickness 170 μm), covered by a thin silver film (30 nm), a silicon oxide layer (30 nm, refractive index n=1.46), a polymer layer (70 nm, determined by atomic force microscope measurements (AFM); refractive index n=1.49) with dissolved dye molecules, and a second thin silicon oxide layer (8 nm, refractive index n=1.46). The bottom silicon oxide layer serves as a finite spacer between the silver metal and the dye embedding polymer. The upper silicon oxide layer prevents any interaction of embedded dye molecules with atmospheric oxygen during cavity assembly. The top part of the cavity consists of a plane-convex lens (F=150 mm), again covered with a silver layer (60 nm). Ag-layers as well as the silica spacers were fabricated by electron beam evaporation (EBV). The intermediate space between the multilayer covered coverslide and the silver layer covered lens was filled with oil (Immersol 518F, Zeiss, refractive index n=1.52) in order to achieve an optically homogeneous intra-cavity environment. The cavity length could be adjusted with piezo actuators (PSt 150/3.5×3.5/20, Piezomechanik GmbH) that move the lens toward or away from the bottom coverslide.
The spherical shape of the upper mirror allows us to control the optical quality and the tuning capability of the microresonator by observing the white light transmission pattern (Fig. 1b). The Newton rings are a result of the different resonator lengths provided by the lens. The central region of the microcavity (i.e., the region of the minimum cavity length) remains dark, as no visible light can be transmitted anymore. The movement of the upper cavity mirror leads to the shift of the transmission pattern. The absolute cavity length values L(x,y,z) were determined using on-axis white light transmission profiles, fitted by a Lorenzian line-shape function (Fig. 2a). We can recalculate the local cavity length L(x,y,z) from the maximum transmission wavelength λ(x,y,z) by using the resonance condition (see [3,8,10] for more details):

$$L(x,y,z)=\left(m-\frac{\sum_i \Delta\Phi_i(d_i,\vartheta,\lambda)}{2\pi}\right)\frac{\lambda(x,y,z)}{2n_{eff}\cos\vartheta};m=1,2,3...;i=1,2. \quad (1)$$

Here, m denotes the order of interference, $\Delta\varphi_i$ the phase change due to reflection at the respective silver mirror i = 1, 2 with thickness d_i. The effective refractive index of the intracavity medium n_{eff} was assumed to be 1.52. We use white light illumination with perpendicular incidence on the upper mirror (the angle of incidence ϑ=0) to determine the intensity maximum λ(x,y,z) of the local on-axis transmission spectrum. Moreover, the transmission profiles give the values of the cavity Q factor, characterizing the energy storage capability of the resonator. Although the average value of 45 is considerably lower than the typical one for high- and ultrahigh-Q resonators, such a cavity is well suited for our purpose allowing the clear visualization of the cavity-effect and the precise tuning of the resonance mode.

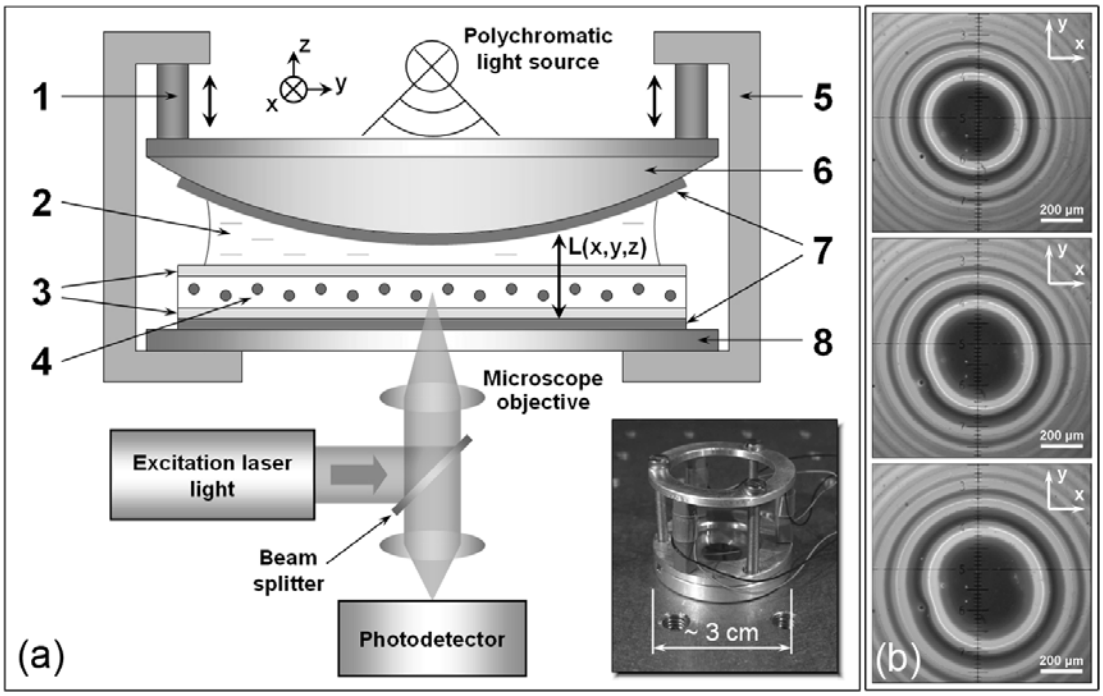

Figure 1. a) Scheme of the experimental setup. The tunable microcavity consists of: 1. Piezoelectric cell, 2. Immersion oil, 3. Silica layers, 4. Polymer (PMMA) layer with dye molecules, 5. Aluminum holder, 6. Lens, 7. Silver layers, 8. Glass coverslide. Inset: A photograph of the tunable microcavity. b) White light transmission patterns (Newton rings) of the microcavity at different values of voltage, applied to the piezoelectric cells. The inner transmission ring satisfies the λ/2 condition for visible light. Applying a voltage to the piezoelectric elements changes the distance between the two mirrors, which results in a shift of the Newton rings.

All fluorescence measurements were performed in the λ/2 region of the cavity, close to the center of the lens, where the displacement Δ(x,y) within the focal spot of our microscope objective (500 nm) results in a cavity length change ΔL of about 1 nm, which is in the order of the surface roughness of our silver mirrors. Hence, our microresonator can be considered as a plane-parallel system (Fig. 2b).

The fluorescence image, acquired within the λ/2 cavity range (Fig. 2d and c), exhibits a cavity-controlled emission of single molecules. Molecules, which are located in the cavity resonance mode, possess maximum emission, while the

emission of those ones, which are out of resonance is surpressed down to the background level. Decreasing down the scanning area of the sample (Fig. 2e) we achieve single molecule imaging level and precisely determine the (x,y) position of the molecule. Remarkably, that some of fluorescence patterns demonstrated single level photo blinking and photo bleaching behavior, proving them as single molecules.

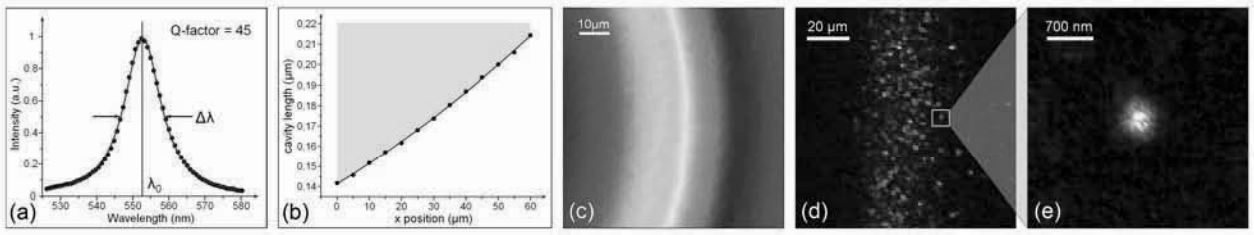

Figure 2. a) Microcavity white light transmission spectrum (●) fitted by a Lorenzian function (—) giving a cavity quality factor Q=45. b) Variation of the cavity length L(x,y) (●) determined from a series of transmission spectra, taken across the first order interference region of the cavity. The solid line is a second-order polynomial fit. c) A photograph of white light transmission pattern taken from the first (λ/2) interference region. d) Fluorescence emission image acquired from the first interference region of the cavity. The image demonstrates the on/off resonance emission distribution of single molecules. e) Fluorescence image of a single molecule emission.

Experimental setup

The following optical measurements on the quantum emitters were performed using an inverted confocal microscope equipped with a high numerical (abbreviated by NA) aperture immersion oil objective (Zeiss, 100×, N/A=1.25). An argon-ion laser operated at 514 nm or 488 nm served as an excitation source for the measurements of fluorescence spectra and longitudinal position of the emitter, respectively. Both the reflected excitation light and the fluorescence from the quantum emitters are collected with the same objective and after removing the excitation light with a filter focused on the detector. The detection unit was either a spectrograph equipped with a CCD camera for fluorescence measurements or an avalanche photodiode (APD) for imaging the sample. These confocal images are produced by raster scanning the sample through the focal spot of the microscope objective.
The dye doped polymer layer was fabricated by spin coating a subnanomolar solution of the perylene derivative (abbreviated by PI) or Rhodamine 6G in 1% poly(methyl methacrylate) (PMMA) dissolved in dichloromethane. All values denoted as free space in this work refer to molecular fluorescence emission in a microcavity of the same type as that reported in the experimental section, but without silver mirrors.
For the position measurements of fluorescent beads (Invitrogen, Nile red, 20 nm diameter) in the resonator, a radially polarized doughnut-mode laser beam (RPDB) served as excitation source. This mode is generated from the Gaussian beam output of the argon-ion laser using a mode converter, consisting of four λ/2 plates glued together according to the method described elsewhere [20,21]. A pinhole is used to remove higher spatial frequencies before the beam is expanded to fit in our objective back aperture. The collimated beam is reflected by a non-polarizing beam splitter cube and focused onto the sample with the microscope objective.

RESULTS AND DISCUSSIONS

Tuning the fluorescence emission spectra of a single molecule.

The tunable microresonator allows us to control and moreover, tune the emission properties of a single quantum emitter. Here we demonstrate new results of tailoring the emission spectrum of a single Rhodamine 6G dye molecule. Being embedded in the cavity a molecule is forced to emit within the cavity mode. Figure 3a shows three fluorescence spectra acquired from the same single molecule at different cavity lengths. Tuning of the cavity mode, i.e. white light

transmission profile, leads to a modification of the single molecule emission spectrum shape and intensity. This phenomenon can be visualized by the scheme of the vibronic transitions shown in Figure 3b. Changing the cavity mode, we actually suppress or enhance different vibronic transitions. This leads to a modification of the emission energy resulting in spectral renormalization. Figure 3c shows five photographs of PI molecules ensemble emission taken from the eyepiece of the microscope at different cavity lengths. Covering a relatively broad spectral range between 500 and 650 nm in free space, the molecules are forced to emit within a narrowed energy distribution in the cavity. Thus we observe transmission from deep green through yellow and orange to red emission.

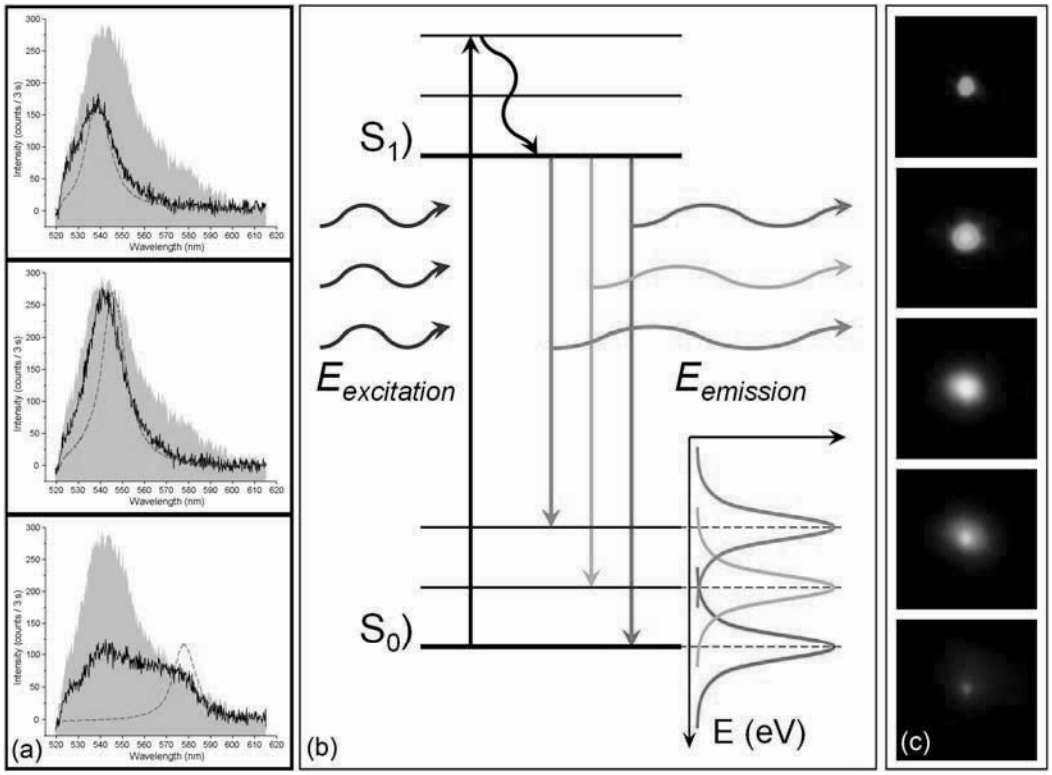

Figure 3. a) Measured spectra (black curves) of a single Rhodamine 6G molecule embedded in the microcavity at different cavity lengths. Red dashed curves indicate cavity white light transmission profiles, normalized to the respective emission spectrum. The grey shaded area represents the Rhodamine 6G free space spectrum. b) General vibronic transition scheme. Lorenzian curves in the right-bottom corner schematically represent cavity white light profiles, corresponding to different vibronic transitions. c) Photographs of PI molecules ensemble emission taken from the eyepiece of the microscope at different cavity lengths.

While the cavity modification of the molecules emission is strongly pronounced at the "red" side of the spectrum, the "blue" side reveals off-axis emission (Fig. 3a). Using a high NA microscope objective we actually collect a large angular emission distribution, hence acquiring significant part of the off-resonance emission. This allows us to acquire maximum information about the spatial distribution of the intra-cavity emission of the molecule. At the same time the detection of the off-axis signal can be enhanced or suppressed by experimental means. Simply using low NA objective we can significantly eliminate this effect. Another, usually more convenient and flexible tool is a pinhole, placed in front of the photo detector (Fig. 4a) and cutting out the external part of the beam, i.e. off-axis emission. Figure 4b shows an example of significant suppressing the off-axis emission of PI molecules ensemble in the cavity (fluorescence of PI molecules in the microresonator is extensively described in [8-10]) by cutting out the external part of the beam with a 200 µm pinhole. Still exhibiting off-resonance emission, the spectra demonstrates strong narrowing at the blue side in contrast to the red,

on-resonance part, which becomes dominant. Varying the diameter of the pinhole one can modify the degree of the off-resonance signal detection suppression. Thus selecting mainly on-axis emission one can approach to such a promising application as single-emitter tunable photon sources, quantum information processing or lab on a chip technology.

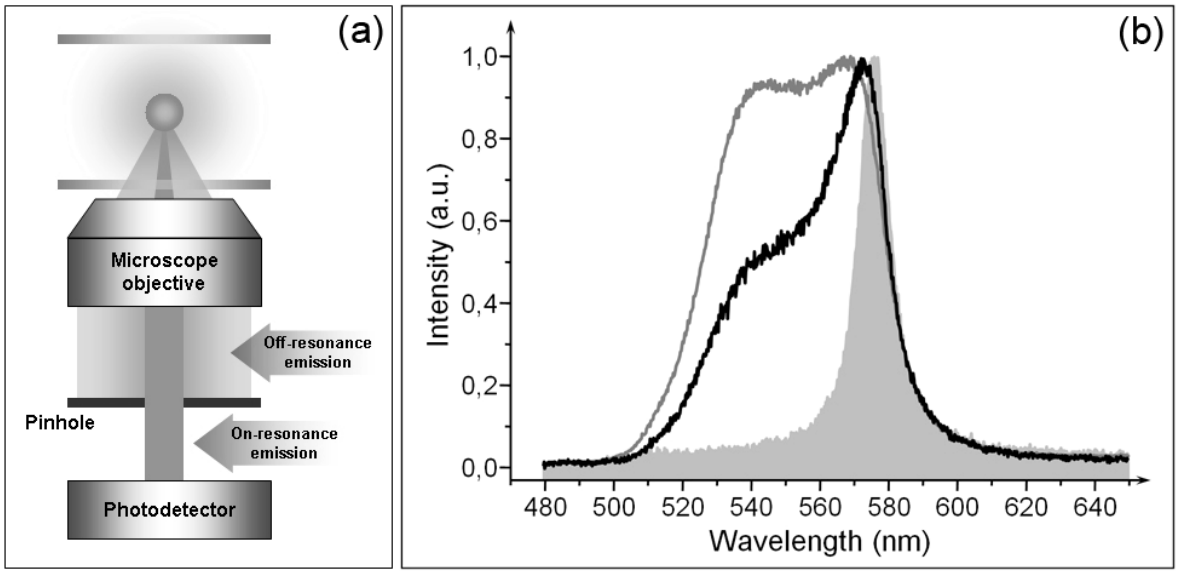

Figure 4. a) Scheme of cutting out the off-resonance emission with a pinhole. b) Normalized fluorescence spectra of PI molecules ensemble in microcavity. Grey curve – without a pinhole in front of the photo detector, black curve – with 200 μm pinhole. Grey shaded area represents cavity white light transmission profile.

Longitudinal localization of a fluorescent bead in a tunable microcavity.

Using the combination of the tunable microcavity and a radially polarized doughnut-mode laser beam as an excitation source we are able to determine the longitudinal position of an isotropic emitter inside the cavity with nanometer accuracy. Figures 5a–5c present characteristic excitation patterns for a distinct single bead situated inside the first transmission ring of the microcavity using a RPDB at three different resonator lengths (shown in the figures). The insets show the (x,y) cross sections for a focused RPDB and are calculated for a constant particle distance of 50 nm from the bottom cavity mirror. A detailed description of the calculation procedure is found in [18]. In brief, the microcavity changes the excitation field distribution with respect to the free space (non-confined) focus by suppressing the longitudinal field components in the center region of the resonator and the in-plane field components close to the mirrors. The calculated (x,z) cross sections (Figs. 5d–5f) for the respective resonator lengths (given in the figures) are shown beneath the corresponding experimental excitation patterns. The bead is situated close to the center for the short resonator length, which results in a doughnut like excitation pattern (Figs. 5a and 5d). When the resonator length increases, the relative position of the bead moves away from the center of the microcavity. Consequently, the excitation pattern changes its shape from a doughnut (Fig. 5a) to a circular spot (Fig. 5c). Hence even small changes of the resonator length lead to drastically different excitation patterns of the emitter.

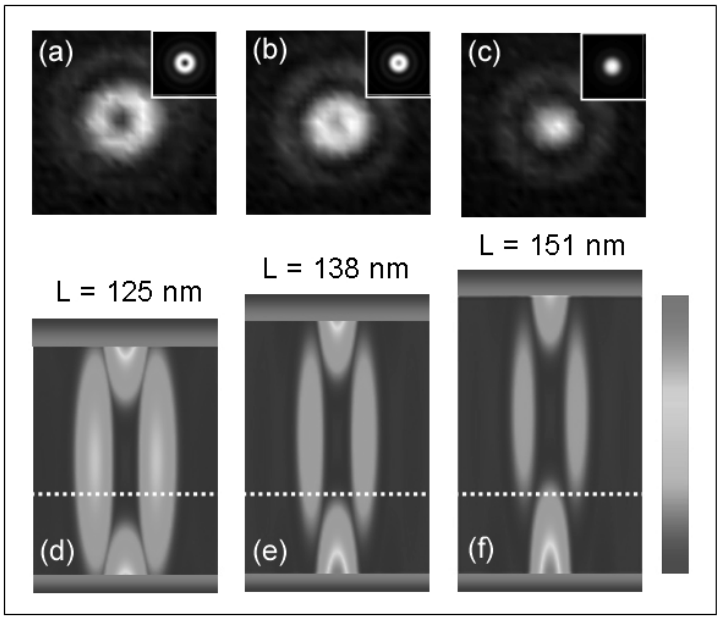

Fig. 5. Excitation patterns resulting from illumination with a RPDB for the same single fluorescent bead (a)–(c) in the λ/2 microcavity tuned to different resonator lengths shown in (d)–(f); the insets show the respective calculated patterns. The experimental data represents cross sections through the excitation field intensity distribution in the plane perpendicular to the optical axis (the size of the image is 1,5×1,5 μm). Panels (d)–(f) show the calculated field intensity distributions along the optical axis for the same resonator lengths as for the respective experimental patterns in (a)–(c). The white horizontal line indicates the position of the bead.

Notably, this can be used for a precise determination of the longitudinal emitter position inside the intracavity medium. In Fig. 6 we show line sections through the experimental patterns for the same bead as in Fig. 5 fitted by the respective theoretical line profiles, with the amplitude and longitudinal bead position as the only free parameters for a given resonator length. Importantly, comparing the three fits we find an average bead position of 48 nm with a variation of ±2 nm, which is below λ/60. The sensitivity of the line shape to the bead position is illustrated by the dotted curves, which are calculated for a deviation of ±5 nm from the optimum position. This clearly shows that we can determine the longitudinal position of the bead with an accuracy of a few nanometers.

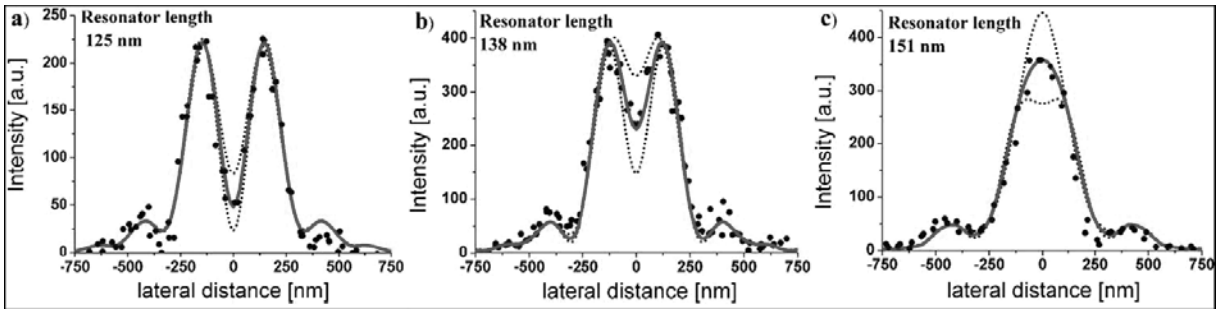

Fig. 6. Line sections (dots) through the respective measured excitation pattern shown in Fig. 5. The fit of the theoretical line sections (solid curves) results in a bead position of (a) 46, (b) 49, and (c) 50 nm above the lower mirror. The sensitivity of the fit is indicated by the dotted curves, which are calculated for a deviation of ±5 nm from the optimum position.

CONCLUSIONS

In summary, we presented a new tunable sub-wavelength microcavity design, allowing us to actively change the local electromagnetic field structure around a molecule by changing the mirror spacing of the cavity. Experimental results showed that, by tuning the cavity length, one can significantly change the emission spectrum of an individual molecule, and control the ratio of distinct vibronic transition probabilities. The fluorescence of an ensemble of molecules allowed us to visualize spectral modulation determined by the cavity mode. Moreover, suppressing the off-resonance emission detection we demonstrated flexible narrowing of the fluorescence spectrum and domination of on-resonance emission. Thus, we showed the capability of further development of the tunable microcavity towards the applications in the lab on a chip technology.
In addition, we presented a new approach to determine the longitudinal position of a quantum emitter in a transparent dielectric medium. By analyzing the excitation patterns resulting from the illumination of a single fluorescent bead with radially polarized doughnut-mode laser beams, we can determine the longitudinal emitter position in the intra-cavity medium with an accuracy of $\lambda/60$.

ACKNOWLEDGEMENT

Financial support by the European Commission (Marie-Curie Research Training Network NANOMATCH, Contract No. MRTN-CT-2006-035884), the „Kompetenznetz Funktionelle Nanostrukturen Baden-Wuerttemberg“ and by the Deutsche Forschungsgesellschaft (project EN 297/12-1) is gratefully acknowledged.

REFERENCES

[1] Purcell, E.M., “Spontaneous emission probabilities at radio frequencies”, Phys. Rev. 69, 681 (1946).
[2] Drexhage, K.H., “Interaction of light with monomolecular dye layers”, Prog. Opt. XII, 163 (1974).
[3] Schleifenbaum, F., Elgass, K., Steiner, M., Enderlein, J., Peter, S., Meixner, A. J., “Optical microresonator modifies the efficiency of the fluorescence resonance energy transfer in the autofluorescent protein DsRed”, Proc. SPIE 7185, 718504 (2009).
[4] Lukosz, W., “Light-emission by magnetic and electric dipoles close to a plane dielectric interface .3. radiation-patterns of dipoles with arbitrary orientation”, J. Opt. Soc. Am., 69, 1495 (1979).
[5] Lieberherr, M., Fattinger, C., and Lukosz, W., “Optical-environment-dependent effects on the fluorescence of submonomolecular dye layers on interfaces”, Surf. Sci., 189, 954 (1987).
[6] Stefani, F.D., Vasilev, K., Bocchio, N., Stoyanova, N., and Kreiter, M., “Surface-plasmon-mediated single-molecule fluorescence through a thin metallic film”, Phys. Rev. Lett. 94, 023005 (2005).
[7] Enderlein, J., “Spectral properties of a fluorescing molecule within a spherical metallic nanocavity”, Phys. Chem. Chem. Phys. 4, 2780 (2002).
[8] Steiner, M., Schleifenbaum, F., Stupperich, C., Failla, A.V., Hartschuh, A., and Meixner, A.J., “Microcavity-controlled single-molecule fluorescence”, Chem. Phys. Chem. 6, 2190 (2005).
[9] Chizhik, A.I., Enderlein, J., Schleifenbaum, F., Gutbrod, R., Chizhik, A.M., Khoptyar, D. and Meixner, A.J., “Tuning the Fluorescence Emission Spectra of a Single Molecule with a variable Optical Subwavelength Metal Microcavity”, Phys. Rev. Lett., 102, 073002 (2009).
[10] Steiner, M., Failla, A.V., Hartschuh, A., Schleifenbaum F., Stupperich C. and Meixner, A.J., “Controlling molecular broadband-emission by optical confinement”, New J. Phys. 10, 123017 (2008).
[11] Born, M., Wolf, E., Bhatia A.B., [Principles of Optics], Cambridge Univ. Press, Cambridge, (1999).
[12] Novotny L. and Hecht, B., [Principles of Nanooptics], Cambridge Univ. Press, Cambridge, (2006).
[13] Hell, S.W. and Wichmann, J., “Breaking the diffraction resolution limit by stimulated-emission - stimulated-emission-depletion fluorescence microscopy”, Opt. Lett. 19(11), 780-782 (1994).
[14] Hell, S.W., “Far-field optical nanoscopy”, Science 316(5828), 1153-1158 (2007).

[15] Hell, S.W., “Toward fluorescence nanoscopy”, Nat. Biotechnol. 21(11), 1347-1355 (2003).
[16] Schrader, M. and Hell, S.W., “4Pi-confocal images with axial superresolution”, J. Microsc. 183, 189-193 (1996).
[17] Nagorni, M. and Hell, S.W., “Coherent use of opposing lenses for axial resolution increase in fluorescence microscopy. I. Comparative study of concepts”, J. Opt. Soc. Am. A 18(1), 36-48 (2001).
[18] Khoptyar, D., Gutbrod, R., Chizhik, A., Enderlein, J., Schleifenbaum, F., Steiner, M., and Meixner, A.J., “Tight focusing of laser beams in a λ/2-microcavity”, Opt. Express 16 (13), 9907-9917 (2008).
[19] Gutbrod, R., Chizhik, A., Chizhik, A., Khoptyar, D. and Meixner, A.J., “Longitudinal localization of a fluorescent bead in a tunable microcavity with an accuracy of λ/60”, Opt. Lett. 34(5), 629-631 (2009).
[20] R. Dorn, S. Quabis, and G. Leuchs, “Sharper focus for a radially polarized light beam”, Phys. Rev. Lett. 91 (23), 233901 (2003).
[21] Novotny, L., Beversluis, M.R., Youngworth, K.S., Brown T.G., “Longitudinal field modes probed by single molecules”, Phys. Rev. Lett., 86 (23), 5251-5254 (2001).

Chapter 5

Confocal microscopy and spectroscopy of defect photoluminescence in single SiO_2 nanoparticles

In this chapter, we show details of single SiO_2 NPs synthesis. Silicon nanocrystals (Si NCs) were synthesized by CO_2 laser pyrolysis of SiH_4. The fresh silicon nanopowder was oxidized in water to obtain SiO_2 nanoparticles (NPs) exhibiting strong red-orange photoluminescence.

This chapter is based on:

Chizhik, A.M., Schmidt, T., Chizhik, A.I., Huisken, F., Meixner, A.J. "Confocal microscopy and spectroscopy of defect photoluminescence in single SiO_2 nanoparticles" *Proc. SPIE* **2009**, *7393*, 739305. doi:10.1117/12.825288.

Confocal microscopy and spectroscopy of defect photoluminescence in single SiO_2 nanoparticles.

Anna M. Chizhik[1], Torsten Schmidt[2], Alexey I. Chizhik[1], Friedrich Huisken[2], Alfred Meixner[1].

[1]Institute of Physical and Theoretical Chemistry, University of Tübingen, Auf der Morgenstelle 8, D-72076 Tübingen, Germany.
[2]Laboratory Astrophysics Group of the Max Planck Institute for Astronomy at the Institute of Solid State Physics, University of Jena, Helmholtzweg 3, D-07743 Jena, Germany.
E-mail: alfred.meixner@uni-tuebingen.de

ABSTRACT

We present new results on single SiO_2 nanoparticles (SiO_2 NPs). NPs were obtained by full oxidation in water of silicon nanocrystals synthesized by CO_2 laser pyrolysis of SiH_4. Samples of SiO_2 NPs embedded in low concentration in a thin polymer layer were prepared by spin-coating a dedicated solution on quartz cover slides. Using focused higher order laser modes, we determine the three-dimensional orientation of the nanoparticles' transition dipole moment (TDM). The SiO_2 NPs were found to possess a quite stable and randomly oriented TDM. However, characteristic dynamical effects featuring single NPs such as fluorescence intermittency and TDM flipping could also be observed. Photoluminescence (PL) spectroscopy of single SiO_2 NPs revealed spectra with a double-peak structure consisting of a narrow zero-phonon line and a broader phonon band. The phonon band can be attributed to longitudinal optical phonons excited in the SiO_2 network.

Keywords: single nanoparticle spectroscopy, single nanoparticle microscopy, nanomaterials, silica nanoparticles, silicon nanoparticles, fluorescence microscopy, confocal microscopy, doughnut laser modes, higher order laser modes

INTRODUCTION

Since more than two decades there is an ongoing discussion on whether the photoluminescence (PL) from nanostructured silicon originates from intergap transitions in quantum confined systems [1,2] or whether it is due to surface defect states [3-5]. Very recently it was shown [6,7] that it is possible to control the origin of the PL of silicon nanocrystals (Si NCs) and to switch between quantum confinement and defect-based PL by hydrogen passivation and UV irradiation, respectively. Investigation of naturally oxidized Si NCs selected in size (2.5 to 8 nm) revealed that the PL is caused by quantum confinement, with slight deviation occurring for small NCs (2 to 3 nm in diameter) [8]. This observation was confirmed by Wolkin et al. [9] comparing the PL of Si NCs passivated with hydrogen and oxygen with theoretical results. He concluded that defect PL via oxygen-related inner-gap states becomes dominant when quantum confinement causes the band gap to exceed a certain energy. Furthermore, Martin et al. [10] showed that the emission from Si NCs is ruled by quantum confinement for large particles, while small Si NCs revealed that defect-based luminescence is dominating. The defect PL in oxygen-passivated Si NCs originates from localized states in the SiO_2 shell surrounding the crystalline silicon core. Removing the entire Si core, for example by full oxidation, the same states should also be operative. Therefore, the question arises whether the same defect luminescence can also be observed in SiO_2 NPs which are prepared by intentional oxidation of Si NCs. Strong visible luminescence observed from hollow SiO_2 NPs which had been obtained by full oxidation of Si NCs in water was reported by Colder et al. [11]. Surprisingly, the PL spectra of such SiO_2 nanopowder show a very similar shape to that ones recorded from Si NCs. This gives reason to assume that the origin of the PL can be referred to the same operating mechanism, obviously related to defect PL. Thus, in spite of the extensive results on Si NCs, the origin of the emission is still under debate. Apparently, the border between quantum confinement and defect PL is diffuse, especially for small Si NCs.

Nanophotonic Materials VI, edited by Stefano Cabrini, Taleb Mokari, Proc. of SPIE Vol. 7393, 739305 · © 2009 SPIE · CCC code: 0277-786X/09/$18 · doi: 10.1117/12.825288

In the present study, experiments on single SiO_2 NPs obtained by full oxidation of Si NCs were carried out. On the one hand confocal microscopy in combination with higher-order laser modes revealed that the SiO_2 NPs posses a linear, randomly oriented transition dipole moment (TDM) for excitation and exhibit dynamical effects such as TDM flipping and fluorescence intermittency. On the other hand PL spectra obtained by confocal PL spectroscopy show a narrow zero-phonon line and a broader phonon band. The phonon band can be referred to the excitation of longitudinal optical phonons in the silica network.

EXPERIMENTAL SECTION

Laser-driven flow reactor for synthesis of Si nanopowder

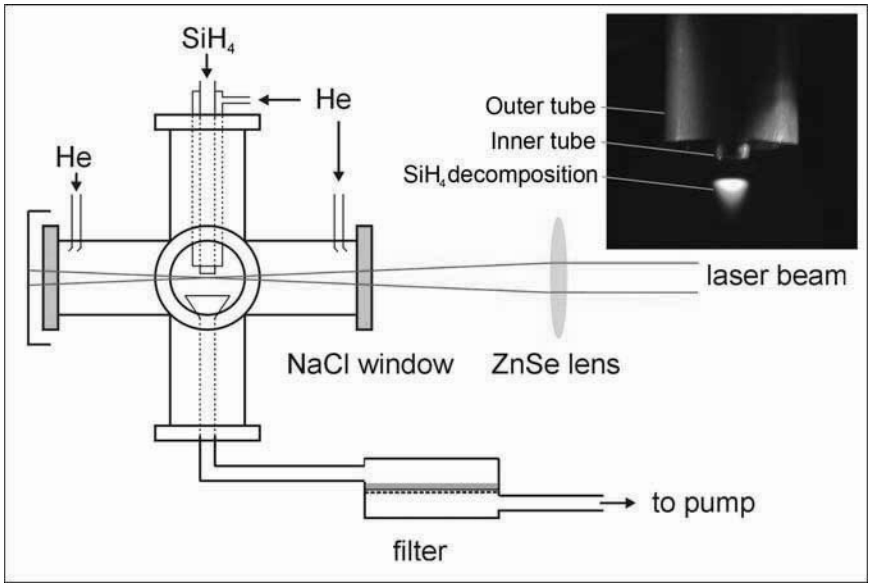

Figure 1. Schematic view of the gas flow reactor. The reactant gas SiH_4 enters through the inner tube, the confinement gas He through the outer tube. The flow of the gases is regulated by controlling independently flow velocity and concentration by means of a flow meter system. The radiation of a pulsed CO_2 laser enters and leaves the reactor through NaCl windows and is focused tightly below the inner tube perpendicular to the gas flow axis to induce the decomposition of SiH_4.
Inset: Photography of the reaction zone. The inner tube and the outer tube for admitting the reactant gas and the confinement gas, respectively. The decomposition of silane (SiH_4) induced by the CO_2 laser radiation results in a visible luminescence, appearing just 2 – 3 mm below the inner tube of the flow reactor.

The technique for synthesis of ultra fine silicon powder is based on laser-induced pyrolysis of the gaseous precursor silane (SiH_4). The dissociation of SiH_4 followed by gas phase condensation and subsequent formation of crystalline silicon quantum dots (Si NCs) takes place in a laser-driven gas flow reactor. For decomposition of the precursor molecules a pulsed CO_2 laser is used providing very sharp temperature gradients in the gas phase combined with reactions proceeding in a wall-less environment.
A schematic view of the flow reactor employed for synthesis of Si NCs is shown in figure 1. The reactor is built from a standard stainless steel NW40 cross vacuum fitting. The reaction gas enters the centre of the flow reactor through a stainless-steel tube of 3 mm diameter. Coaxially arranged, in order to confine the precursor gas flow to the flow axis, helium is flushed as buffer gas through the outer tube of 12 mm diameter. The gas and reaction products are pumped by a backing pump (D16B, Typ Leybold) through a funnel-shaped tube facing the inlet tubes. The produced nanopowder is collected in a filter unit at the exit of the flow reactor.

Gas flow rates and the total pressure inside the reaction chamber and therefore concentrations and flow velocities of the precursor gas and the inert confinement gas are regulated independently by means of an appropriate flow meter system (flow regulation system Typ 647BE, MKS instruments; needle valve 248AC, MKS instruments; pressure gauge, 122A, MKS instruments).
The molecular flow emanating from the inner gas inlet is crossed perpendicularly by the focused radiation (ZnSe lens with 190.5 mm focus length) of a line-tunable CO_2 laser which enters and leaves the reactor through NaCl windows (loss by reflection ≈ 8 %). The viewing ports are continuously flushed with rare gas to prevent nanoparticles from coating the NaCl windows. The infrared laser intensity is regulated by passing the laser beam through a propylene gas cell with adjustable pressure (not shown in figure 1). As pyrolysing laser a pulsed URENCO-TEA CO_2 laser (model ML 104, Uranit) was used. The working conditions for the laser are: repetition rate, 20 Hz; pulse width, 150 ns; laser emission wavelength, 10.6 μm.
During the course of the experiments, various reactor conditions have been tested. However, the following conditions have been found to be particularly favourable: SiH_4 flow rate, 15 sccm; He flow rate, 1100 sccm; pulse energy of the CO_2 laser, 45 mJ. (sccm denotes standard cubic centimeter per minute). The total pressure inside the reaction chamber was kept constant at 330 mbar. The induced decomposition of the gaseous precursor SiH_4 results in visible luminescence, appearing just 2 – 3 mm below the inner tube (see inset in figure 1).

Synthesis of SiO_2 NPs

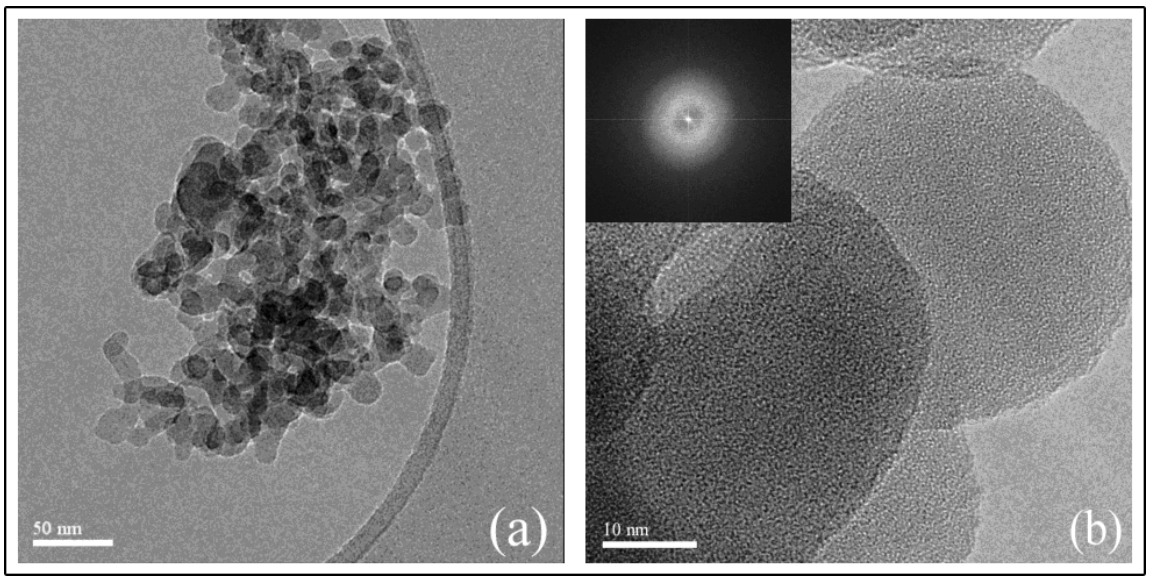

Figure 2: The micrograph images (a) and (b) of silica nanoparticles reveal the complete amorphous structure of the nanoparticles. The inset in picture (b) is the FFT of the HRTEM image shown in (b). The FFT image clearly indicates absence of crystallinity in the oxidized nanopowder.

Amorphous SiO_2 NPs were prepared according to the recipe of Colder et al. [11]. Si NCs (~10 mg), freshly prepared by laser-induced pyrolysis [12,13], collected on a filter paper in the exhaust line of the flow reactor were dispersed in 1 ml doubly distilled water applying ultrasonic treatment for 10 min. The beige viscous solution was stored at room temperature for several days without any further treatment until the yellowish color had turned to a transparent appearance, a clear indication for complete oxidation of the crystalline Si NPs to amorphous SiO_2 NPs. Finally, to evaporate the water, the vessel containing the nanoparticles solution was heated in a simple non-evacuated oven at 95°C.

The residue at the bottom of the vial is a white powder exhibiting strong red-orange PL under the illumination of a laboratory UV lamp ($\lambda = 254$ nm).
High-resolution transmission electron microscopy (HRTEM) images, shown in figure 2, reveal the complete amorphous structure of the as-synthesized silica nanopowder. Also electron energy loss spectroscopy (EELS) as well as x-ray diffraction (XRD) measurements confirmed these observations. Sometimes the as-prepared powder contains hollow SiO_2 NPs as reported by Colder et al. [11]. For hollow SiO_2 NPs of spherical shape outer diameters are between 9 and 18 nm. The shell thickness is about 4 nm. In the present study, the SiO_2 NPs are mostly solid with an average size of 21 nm. To record the (ensemble) PL spectrum of the SiO_2 nanopowder a mini-spectrometer (Ocean Optics, model QE 65000) was applied. For excitation the 4th harmonic ($\lambda = 266$ nm) of a pulsed Nd:YAG laser with 5 ns pulse width was used.

Sample preparation for confocal microscopy

For investigation of single SiO_2 NPs in glass-polymer-air confinement, the particles were embedded in very low concentration into a thin polymer film. For preparing samples containing SiO_2 NPs a small amount of the processed silica nanopowder was dispersed in toluene and then mixed with the polymer poly(methyl methacrylate) (PMMA, $[C_5O_2H_8]_n$) or polystyrene (PS, $[C_8H_8]_n$). Then the droplet (10 µl) of the mixture was spin-coated onto a clean quartz cover slide surface (thickness 170 µm). The thickness of the polymer film of about 50-60 nm was determined by atomic force microscopy (AFM) measurements. The two polymers (PMMA and PS) were used to clarify the influence of a polar (PMMA) and a non-polar (PS) matrix on the properties of SiO_2 NPs. To exclude contamination by impurities (e.g. dye molecules) a droplet of the polymer without dissolved particles was spin-coated onto a quartz cover slide and investigated spectroscopically.

Confocal microscopy setup

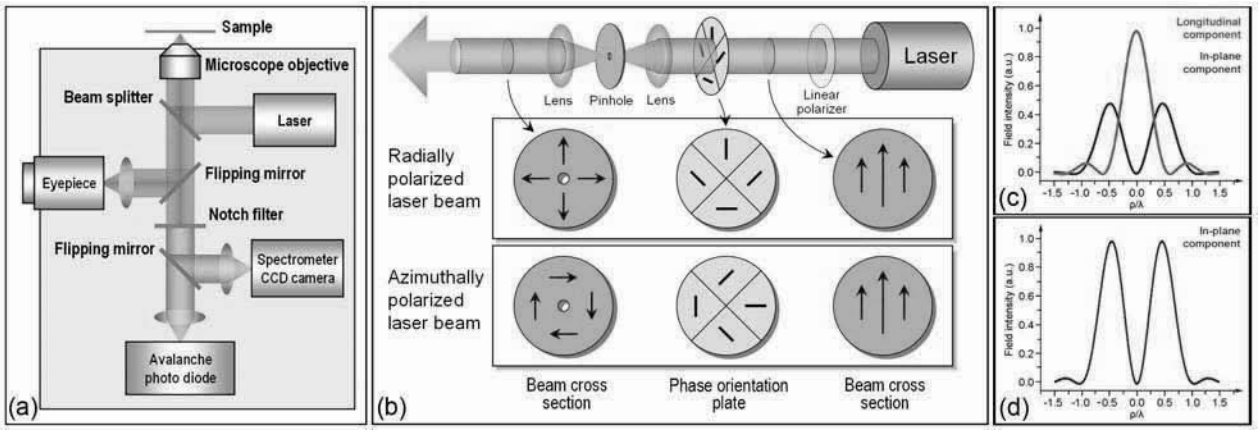

Figure 3. (a) Scheme of the home-built confocal microscope setup. (b) Scheme of the mode converter according to Dorn et al. [15]. Excitation field intensity distribution within the focal spot of the microscope objective: (c) in the case of radially polarized laser beam; (d) in the case of azimuthally polarized laser beam.

Two slightly different confocal microscope setups were used in the present study. The common scheme is shown in figure 3(a). The optical measurements were performed with a modified inverted confocal microscope (Zeiss Axiovert 135 TV) using a high-numerical aperture oil immersion objective (Zeiss Plan Neofluar, 100/NA = 1.3). The term inverted refers to the fact that the polymer film with the SiO_2 NPs was on the opposite side of the cover slide with respect to the objective. An ultrafast laser system (Picoquant, model LDH-P-C470) operating at $\lambda = 473$ nm (2.62 eV) and providing pulses at a repetition rate of 10 MHz with a width of 300 ps served as excitation source for the

measurements of fluorescence spectra. In order to discriminate against the stray light from the laser, the setup was equipped with a long-wave pass filter having its 50% transmission value at 510 nm. Fluorescence spectra were acquired with a spectrograph (Acton Research SpectraPro 300i) equipped with a CCD camera (Princeton Instruments, model LNCCD-1340/100-EB/1).
To investigate the three-dimensional orientation of the nanoparticles' TDM, we used a similar home-built confocal microscope setup additionally equipped with a mode conversion optical line for generation of radially and azimuthally polarized laser beams [14-17]. The nanoparticles were excited at λ = 488 nm (2.54 eV) in the diffraction limited laser focus of the NA = 1.25 immersion oil objective. The typical image size was 100 × 100 pixels distributed over 2 × 2 or 5 × 5 μm. For each pixel, the signal was integrated over 5 ms, resulting in a acquisition time of 50 s. Monodirectional scanning process doubles this time to the value of 100 s for one fluorescence image. Recording a series of images, the next scan was started immediately after the previous had finished.

Laser polarization conversion technique

The measurements of the nanoparticles TDM orientation were performed using radially and azimuthally polarized laser beams (RPLB and APLB respectively) [14-17]. Figure 3(b) schematically shows an optical line for the conversion of the linearly polarized Gaussian beam into a doughnut mode laser beam. A key element of the system is a mode converter consisting of four $\lambda/2$ plates glued together as shown in the scheme. Passing the linearly polarized Gaussian beam through the mode converter we create either a radial or an azimuthal polarization of the laser beam. Moreover, transition from one type of polarization to another and back can be done simply by reorientation of the mode converter as shown on the scheme. A pinhole is used to remove higher spatial frequencies before the beam is expanded to fit in our objective back aperture. The collimated beam is reflected by a non-polarizing beam-splitter cube and focused onto the sample with the microscope objective.
Figures 3(c) and (d) show the field intensity distribution within the focal spot of the RPLB and the APLB respectively demonstrating a key difference between the modes. The RPLB possesses both in-plane and longitudinal component of the field, while the APLB only the in-plane component, however more intensive than in the case of the radial polarization.

RESULTS AND DISCUSSION

Transition dipole moment of single SiO_2 NPs (three-dimensional orientation)

In contrast to a focused Gaussian laser beam, a focused RPLB allows us to excite emitters possessing any orientation of the TDM due to the presence of both in-plane and longitudinal field components. A strong difference between the distributions of the longitudinal and the in-plane components within the focus of the RPLB leads to significant variations of the fluorescence image shape of a single emitter at different orientation. Figures 4(d)-(g) demonstrate four calculated excitation patterns of a single quantum emitter, possessing a one-dimensional TDM oriented according to the scheme shown in figure 4(c). Thus, vertically oriented TDM is depicted as a spot in the center of the focal area in the result of excitation only by the longitudinal component of the field, while horizontally oriented TDM can be excited only by the in-plane component, exhibiting two lobes with dark gap in between (coffee bean shape of the image). In the latter case the TDM is oriented along the line, connecting the maxima of the coffee bean lobes. Reorientation of the TDM within the horizontal plane (i.e. variation of the angle φ) leads to the turn of the image to respective angle. Tilted positions of the TDM (variation of the angle θ) show different intermediate shapes of the image, allowing precise determination of the three-dimensional TDM orientation with an accuracy up to 5°.
Figure 4(a) shows an experimental fluorescence image of two single SiO_2 NPs possessing a one-dimensional TDM. Particle (1) reveals nearly vertical orientation of the TDM (see calculated pattern in figure 4(d)). Particle (2) demonstrates a coffee bean shape and significantly lower intensity than in the previous case. This is caused by higher intensity of the longitudinal component of the excitation field. The shape of particle (2) reveals nearly horizontal orientation of the NP TDM ($\varphi \approx 100°$; $\theta \approx 90°$ see figure 4(g)).

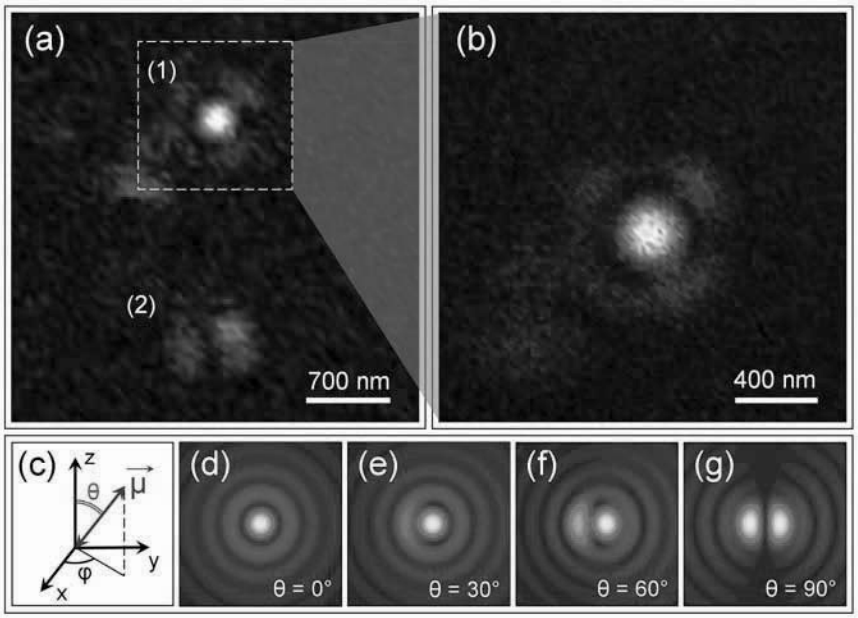

Figure 4. (a) Fluorescence image of two single SiO_2 NPs (PMMA matrix) excited with a radially polarized laser beam revealing different three-dimensional orientation of TDM. (b) High resolution fluorescence image of particle (1) allowing precise determination of the three-dimensional orientation of the TDM. (c) Scheme of the coordinate system, used for determination of the three-dimensional orientation of the TDM. (d)-(f) Examples of simulated emission patterns of four orientations of TDM after excitation with radially polarized laser beam (all four images are calculated considering φ=90°).

An extensive number of measurements (more than 200 images) provides a statistically significant evidence for the presence of a one-dimensional TDM in contrast to a two-dimensional TDM observed in some quantum-confined systems [18]. Moreover, we found that there is no preferred direction with respect to the substrate surface suggesting that the TDMs are randomly oriented. This is not surprising if one keeps in mind that the NPs are embedded in a ~50 nm thick polymer matrix which keeps them far away from the substrate. Although the diffraction-limited focal spot of the microscope objective is much larger than the size of the nanoparticle, the LBPC technique allows us to distinguish emission from single nanoparticle and ensemble, acquiring just one fluorescence image. Emission of agglomerated nanoparticles excited with RPLB typically exhibits a spot resulting from the overlapping of single nanoparticle images and hence, is strongly different from the image of an individual emitter.

Although the APLB contains only the in-plane field component, the mode is suitable for single nanoparticle imaging in two-dimensional space. Horizontally oriented TDM is depicted as a coffee-bean shape, possessing higher intensity than in the case of radial polarization. Declination of the TDM from the horizontal orientation will not change the shape of the image but leads to decrease of the intensity of the coffee bean, while TDM oriented exactly perpendicular to the sample surface can not be seen at all.

Figure 5(a)-(d) shows a series of images of a single SiO_2 NP in PMMA excited with APLB, acquired one after another. The images demonstrate one-dimensional TDM, which remains constant during the whole acquisition time of four images (~ 400 s). In the case of APLB TDM orientation of the emitter is codirectional with the dark gap, separating the lobes of the coffee bean (figure 5(a)). Figures 5(b) and (c) reveal blinking process, clearly proving that we deal with a single quantum emitter. After sudden bleaching depicted in figure 5(d) the particle didn't show PL anymore.

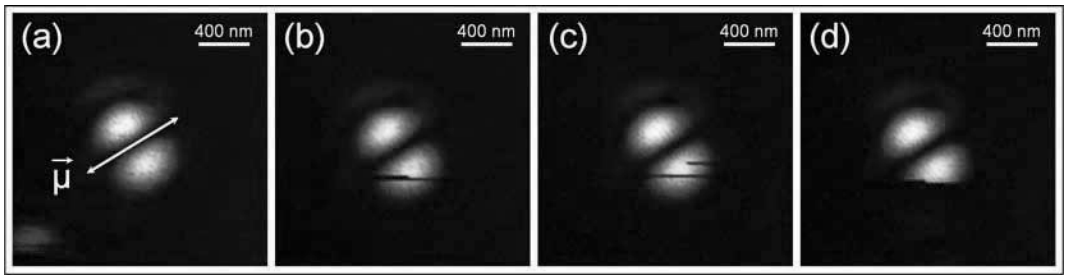

Figure 5. (a)-(d) A series of consecutive fluorescence images of a single SiO_2 NP (PMMA matrix) excited with an azimuthally polarized laser beam. The arrow in image (a) indicates the orientation of the SiO_2 NP TDM. Image (b) and (c) shows blinking of the particle, while the sudden disappearance of PL in image (d) reveals bleaching.

After having presented results on SiO_2 NPs embedded in a thin PMMA polymer layer, we turn to polystyrene (PS) as matrix material. At first, we would like to state that, in PS, dynamical effects seem more likely to occur than in PMMA. An example is given in Figure 6(a)-(d) which shows a series of images taken one after the other, all showing the same section of 4.3×4.3 μm containing essentially one SiO_2 NP exhibiting relatively strong photoluminescence and 4 NPs of lower intensity. The sample was excited with azimuthally polarized laser beam, and the time between two consecutive samplings of the same area was 100 s. Following the images from (a) to (d), we observe a bright coffee bean in the center of each image. Image (b) shows fluorescence intermittency (blinking) of the NP manifested by the sudden quenching of the PL being active for at least 12 s. In image (c), the same NP appears bright again. Another interesting dynamical effect is demonstrated by the fainter coffee bean marked by the dashed circle. Comparing image (a) and (d), we observe a flipping of the orientation of the TDM, while images (b) and (c) demonstrate intermediate states without a definite stable TDM orientation. Moreover, image (c) also reveals sudden blinking of the NP.
However, it should be mentioned that such dynamic effects as fluorescence intermittency and flipping of the TDM were observed quite rarely. These phenomena can be explained by a redistribution of defect states caused by charge fluctuations in the surrounding of the NP. TDM flipping results from the fact that another defect has become energetically more favorable to be accessed. As usual, fluorescence intermittency can be explained by electron trapping and non-radiative charge carrier recombination at the hole. As already mentioned, we have found that dynamical effects are more likely to occur when the SiO_2 NPs are embedded in the non-polar PS matrix. In contrast to this, defects involved in the excitation and emission process seem locally and energetically more stable if the NPs are surrounded by the polar PMMA matrix. This is ascribed to the oxygen atoms surrounding the NPs and giving rise to a stronger fixation or localization of the defects. The stabilized situation is also reflected by the better contrast of the fluorescence images.

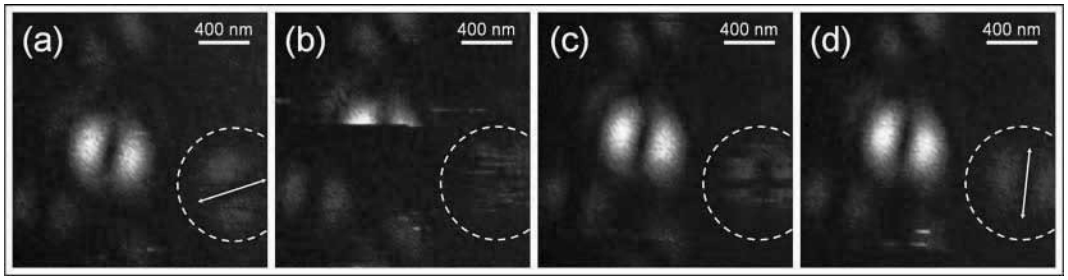

Figure 6. Images of SiO_2 NPs embedded in a polystyrene matrix and excited with an azimuthally polarized laser beam. The images (a) to (d) show the same image section of a series of pictures recorded one after the other every 100 s. The following dynamical processes are observed: Image (b) reveals fluorescence intermittency of the brighter NP (blinking). Blinking is also observed for the fainter NP (marked by the dashed circle) in image (c). In addition, sudden flipping of the TDM of the fainter NP is observed as can be seen by comparing images (a) and (d), while images (b) and (c) show intermediate unstable conditions of the TDM.

Photoluminescence spectroscopy of single SiO_2 NPs

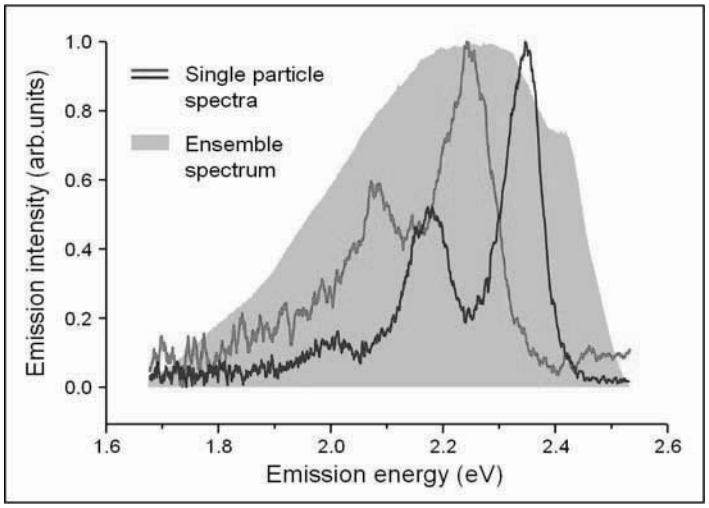

Figure 7. Two PL spectra of individual SiO_2 nanoparticles embedded in PMMA (blue curve) and PS (red curve). Before plotting, the experimental data has been subjected to averaging over five data points. The grey shaded area represents the PL spectrum obtained from an ensemble of SiO_2 NPs. For acquiring the ensemble spectrum the same high resolution confocal microscope was used, which can lead to a certain narrowing of the spectrum.

We have measured PL spectra of various individual SiO_2 nanoparticles embedded both in PMMA and PS polymer matrices. The PL spectra recorded as a function of wavelength, $I_{PL}(\lambda)$, were transformed to energy spectra, $I_{PL}(E)$, taking into account the proper Jacobian and dividing the intensities by $dE/d\lambda$. Figure 7 shows two examples of single particle spectra representing the energy range, where most of the single NP spectra were observed. PL spectra acquired from NPs embedded in a PS matrix typically exhibit lower signal to noise ratios and broader bands than in the case of PMMA as matrix material. The ensemble PL spectrum (grey shaded area), as well as some of the single NP spectra (not shown in figure 7) seem to be truncated at short wavelengths (respectively high energy). This is caused by the long-wave pass filter that we had to use, in order to block the straylight from the excitation laser. The ensemble spectrum, as expected, is much broader than the spectra of the single NPs and covers the same energy range. Essentially one has to notice, that the ensemble measurements were performed using the same high resolution confocal microscope as it was used for single NPs spectra acquisition. The narrow area of the microscope objective focal spot (~ 500 nm) leads to a localized character of the sample excitation. This may result in a certain narrowing of the spectral band recorded from the ensemble sample.
The PL spectra of single SiO_2 NPs were found to have, besides a narrow zero-phonon line, one or even two satellite peaks on the lower-energy side. The separation between the peaks is on the average 160 meV but may vary from 140 to 180 meV. This energy separation comes very close to the energy of the longitudinal optical mode (LO_3) of SiO_2 at 156 meV [19]. As a result, the satellite peaks can be assigned to the excitation of one or two LO_3 phonon quanta in the SiO_2 NP being excited simultaneously with the radiative recombination of the charge carriers. Apparently, there is a strong coupling between the electronic transition and a collective vibration in the SiO_2 NP due to a sudden relaxation mechanism involving charges. Similar phonon couplings have been reported for other nanosized systems, for example CdSe NCs [20] and Si NCs [21]. Very recently, Martin et al. [10] observed strong electron-phonon coupling in single Si NCs involving LO_3 phonons in the surrounding SiO_2 shell. Interestingly, the spectra of Martin et al. are almost identical to the ones presented here. We will postpone the discussion of this amazing similarity to the end of this paragraph.
Comparing PL spectra of SiO_2 in PMMA with those obtained in PS, it is found that, in general, the quality of the SiO_2/PMMA spectra is higher. This is explained with the stronger fixation of the luminescent centers due to the presence of the polar ester groups in the PMMA matrix. The enhanced dynamics in PS are most likely related to a flipping of the loosely bound phenyl groups which are known to be responsible for considerable spectral dynamics and heterogeneity in

single molecule spectroscopy [22]. As another point, we have observed that the spectra of SiO_2 NPs in PS appeared more often truncated than the ones in PMMA. This can also be explained with the presence of oxygen in PMMA. Due to the interaction between the defect state and the oxygen in the matrix, the energy of the defect state is lowered, thus giving rise to a red shift for the NPs embedded in PMMA compared to those in PS. Another explanation could be that a certain type of defect associated with higher energy is passivated by the presence of oxygen in PMMA while this is not the case in PS.

Now we would like to discuss the origin of the PL observed in the present study. According to the work of Glinka et al. [23], a broad PL band in the green extending from 1.8 to 2.8 eV (in our case the band is cut at near 2.45 eV by the long-pass filter, protecting the photo detector from the reflected laser light) with maximum at 2.35 eV, which has been observed for thermally untreated SiO_2 NPs with diameters of 7 and 15 nm, can be attributed to hydrogen-related species (≡Si–H and ≡Si–OH) on the surface of the nanoparticles. This broad band measured in ensemble spectra is an inhomogeneous composition of many different species each contributing with a slightly different energy mimicking small differences in the local environment of the defect. In single particle spectroscopy, this inhomogeneity is removed, and we can observe sharp zero-phonon lines characteristic for each individual NP.

As already mentioned, the fluorescence spectra of single SiO_2 NPs presented in figure 7 are amazingly similar to the single particle spectra of Si NCs measured by Martin et al. [10]. This similarity refers to the entire shape of the PL spectra including the splitting into zero-phonon line and phonon band and the energy range in which single particle spectra could be recorded. Since the Si NCs are surrounded by a l-2 nm thick layer of amorphous SiO_2 [24] it could be possible that the PL observed in both systems (SiO_2 NPs and Si NCs) with single particle spectroscopy have the same origin.

CONCLUSIONS

In conclusion, the work performed in single SiO_2 NPs microscopy and spectroscopy has significantly improved our understanding of defect PL. Imaging of single NPs using focused higher order laser modes revealed new details of origin and dynamics of the SiO_2 NPs TDM. In particular, the fluorescence images clearly revealed presence of one-dimensional TDM, which was stable for most of the NPs. However, such dynamic effects as fluorescence intermittency and flipping of the TDM were rarely observed.

The spectra reveal a strong zero-phonon line and two peaks attributed to phonon bands associated with the excitation of one or two quanta of vibrations in the SiO_2 network. To obtain more detailed information on this interesting issue, dedicated studies, including spectrally resolved lifetime measurements on single particles, will be carried out in the near future. Finally, we would like to emphasize that the luminescent SiO_2 NPs, presented in this study, will be attractive candidates for fluorescence labeling and local heating centers in biological and medical applications. Moreover, the results described in this work contribute to further single nanoparticle studies of core-shell systems [25], which are of a great interest from the point of view of tunable light emitters on the single molecule level [26].

ACKNOWLEDGMENT

This work was carried out within the European cooperation NANOLUM. F. H. and T. S. are grateful for support by the Max Planck Society and the European Commission (Specific Targeted Project: BONSAI, Contract No. LSHB-CT-2006-037639). Financial support by the Forschungsschwerpunktprogramm Baden-Württemberg and from the European Commission through the Human Potential Program (Marie-Curie Research Training Network NANOMATCH, Contract No. MRTN-CT-2006-035884) is acknowledged. We thank Sebastian Bär, Raphael Gutbrod and Holger Hintz for fruitful discussions. WSxM software from nanotech [27] was used for image processing.

REFERENCES

[1] Canham, L. T., “Silicon quantum wire array fabrication by electrochemical and chemical dissolution of wafers”, Appl. Phys. Lett. 57, 1046-1048 (1990).

[2] Lehmann, V., Gösele, U., “Porous silicon formation: A quantum wire effect”, Appl. Phys. Lett. 58, 856-858 (1991).

[3] Prokes, S. M. “Light emission in thermally oxidized porous silicon: Evidence for oxide related luminescence”, Appl. Phys. Lett. 62, 3244-3246 (1993).
[4] Kanemitsu, Y., Okamoto, S., Otobe, M., Ota, S., “Photoluminescence mechanism in surface-oxidized silicon nanocrystals”, Phys. Rev. B 55, R7375-R7378 (1997).
[5] Cullis, A. G., Canham, L. T., Calcott, P. D. J., “The structural and luminescence properties of porous silicon”, J. Appl. Phys. 82, 909-965 (1997).
[6] Godefroo, S., Hayne, M., Jivanescu, M., Stesmans, M., Zacharias, M., Lebedev, O. I., van Tendeloo, G., Moshchalkov, V. V., “Classification and control of the origin of photoluminescence from Si nanocrystals”, Nature Nanotech. 3, 174-178 (2008).
[7] Gösele, U., “Shedding new light on silicon”, Nature Nanotech. 3, 134-135 (2008).
[8] Ledoux, G., Gong, J., Huisken, F., Guillois, O., Reynaud, C., “Photoluminescence of sizeseparated silicon nanocrystals: confirmation of quantum confinement”, Appl. Phys. Lett. 80, 4834-4836 (2002).
[9] Wolkin, M. V., Jorne, J., Fauchet, P. M., Allan, G., Delerue, C., “Electronic states and luminescence in porous silicon quantum dots: the role of oxygen”, Phys. Rev. Lett. 82, 197-200 (1999).
[10] Martin, J., Cichos, F., Huisken, F., von Borczyskowski, C., “Electron-phonon coupling and localization of excitons in single silicon nanocrystals”, Nano Lett. 8, 656-660 (2008).
[11] Colder, A., Huisken, F., Trave, E., Ledoux, G., Guillois, O., Reynaud, C., Hofmeister, H., Pippel, E., “Strong visible photoluminescence from hollow silica nanoparticles”, Nanotechnology 15, L1-L4 (2004).
[12] Huisken, F., Hofmeister, H., Kohn, B., Laguna, M. A., Paillard, V., “Laser production and deposition of light-emitting silicon nanoparticles”, Appl. Surf. Sci. 154-155, 305-313 (2000).
[13] Huisken, F., Ledoux, G., Guillois, O., Reynaud, C., “Light-emitting silicon nanocrystals from laser pyrolysis”, Adv. Mater. 14, 1861-1865 (2002).
[14] Novotny, L., Beversluis, M. R., Youngworth, K. S., Brown, T. G., “Longitudinal field modes probed by single molecules”, Phys. Rev. Lett. 86, 5251-5254 (2001).
[15] Dorn, R., Quabis, S., Leuchs, G., “Sharper focus for a radially polarized light beam”, Phys. Rev. Lett. 91, 233901 (2003).
[16] Gutbrod, R., Chizhik, A., Chizhik, A., Khoptyar, D., Meixner, A. J., “Longitudinal localization of a fluorescent bead in a tunable microcavity with an accuracy of λ/60”, Opt. Letters 34, 629-631 (2009).
[17] Failla, A.V., Qian H., Qian H., Hartschuh A., Meixner A.J., “Orientational imaging of subwavelength au particles with higher order laser modes” Nano Lett. 6 (7), 1374-1378 (2006).
[18] Empedocles, S. A., Neuhauser, R., Bawendi, M. G., “Three-dimensional orientation measurements of symmetric single chromophores using polarization microscopy”, Nature 339, 126-129 (1999).
[19] Gourbilleau, F., Portier, X., Ternon, C., Voivenel, P., Madelon, R., Rizk, R., “Si-rich/SiO_2 nanostructured multilayers by reactive magnetron sputtering”, Appl. Phys. Lett. 78, 3058-3060 (2001).
[20] Empedocles, S. A., Neuhauser, R., Shimizu, K., Bawendi, M. G., “Photoluminescence from single semiconductor nanostructures”, Adv. Mater. 11, 1243-1256 (1999).
[21] Kovalev, D., Heckler, H., Ben-Chorin, M., Polisski, G., Schwartzkopff, M., Koch, F., “Breakdown of the k-conservation rule in Si nanocrystals”, Phys. Rev. Lett. 81, 2803-2806 (1998).
[22] Stracke, F., Blum, C., Becker, S., Mullen, K., Meixner, A. J. “Two and multilevel spectral switching of single molecules in polystyrene at room temperature”, Chem. Phys. 300, 153-164 (2004).
[23] Glinka, Y. D., Lin, S.-H., Chen, Y.-T., “The photoluminescence from hydrogen-related species in composites of SiO_2 nanoparticles”, Appl. Phys. Lett. 75, 778-780 (1999).
[24] Hofmeister, H., Huisken, F., Kohn, B., “Lattice contraction in nanosized silicon particles produced by laser pyrolysis of silane”, Europ. Phys. J. D 9, 137-140 (1999).
[25] Ma, L. B., Schmidt, T., Guillois, O., Huisken, F., “Evolution of photoluminescence properties of $Si_{1-x}Ge_x$ nanocrystals synthesized by laser-induced pyrolysis”, Appl. Phys. Lett. 95, 013115 (2009).
[26] Chizhik, A.I., Enderlein, J., Schleifenbaum, F., Gutbrod, R., Chizhik, A.M., Khoptyar, D. and Meixner, A.J., “Tuning the fluorescence emission spectra of a single molecule with a variable optical subwavelength metal microcavity”, Phys. Rev. Lett. 102, 073002 (2009).

[27] Horcas, I., Fernandez, R., Gomez-Rodrigez, J.M., Colchero, J., Gomez-Herrero, J., Baro, A.M., "WSXM: A software for scanning probe microscopy and a tool for nanotechnology", Rev. Sci. Instrum. 78, 013705-013708 (2007).

Chapter 6

Imaging and spectroscopy of defect luminescence and electron-phonon coupling in single SiO_2 nanoparticles

In this chapter, we present new results on single SiO_2 NPs study. Samples of SiO_2 NPs embedded in low concentration in a thin polymer layer were prepared by spin-coating a dedicated solution on glass cover slides. The spectral analysis of single SiO_2 NPs revealed double-peak spectra consisting of a narrow zero-phonon line and a broader phonon band being associated with the excitation of longitudinal optical phonons in the SiO_2 NP.

This chapter is based on:

Chizhik, A.M., Chizhik, A.I., Gutbrod, R., Meixner, A.J., Schmidt, T., Sommerfeld, J., Huisken, F. "Imaging and Spectroscopy of Defect Luminescence and Electron-Phonon Coupling in Single SiO_2 Nanoparticles" *Nano Lett.* **2009**, *9*, 3239-3244.

NANO LETTERS

2009
Vol. 9, No. 9
3239-3244

Imaging and Spectroscopy of Defect Luminescence and Electron−Phonon Coupling in Single SiO_2 Nanoparticles

Anna M. Chizhik,[†] Alexey I. Chizhik,[†] Raphael Gutbrod,[†] Alfred Johann Meixner,*[,†] Torsten Schmidt,[‡] Jana Sommerfeld,[‡] and Friedrich Huisken*[,‡]

Institute of Physical and Theoretical Chemistry, University of Tübingen, Auf der Morgenstelle 8, D-72076 Tübingen, Germany, and Laboratory Astrophysics Group of the Max Planck Institute for Astronomy at the Institute of Solid State Physics, University of Jena, Helmholtzweg 3, D-07743 Jena, Germany

Received May 12, 2009; Revised Manuscript Received July 2, 2009

ABSTRACT

Silicon nanocrystals were synthesized by CO_2 laser pyrolysis of SiH_4. The fresh silicon nanopowder was oxidized in water to obtain SiO_2 nanoparticles (NPs) exhibiting strong red-orange photoluminescence. Samples of SiO_2 NPs embedded in low concentration in a thin polymer layer were prepared by spin-coating a dedicated solution on quartz cover slides. Using an argon ion laser at 488 nm with higher-order laser modes (azimuthally and radially polarized doughnut modes) for excitation, the three-dimensional orientation of the nanoparticles' transition dipole moment was investigated in a confocal microscope. The linear transition dipole moment was found to be rather stable and randomly oriented. However, dynamical effects such as fluorescence intermittency and transition dipole moment flipping could also be observed. The spectral analysis of single SiO_2 NPs revealed double-peak spectra consisting of a narrow zero-phonon line and a broader phonon band being associated with the excitation of longitudinal optical phonons in the SiO_2 NP.

Since the first observation of red photoluminescence (PL) from nanostructured porous silicon in 1990,[1,2] there has been increasing interest in the study of the optical properties of nanostructured silicon. While this observation was attributed to the radiative recombination of charge carriers in a quantum-confined system, other authors made defect luminescence responsible for the PL of their nanocrystalline Si samples.[3,4] Since these days, there is still ongoing discussion on whether the PL originates from intergap transitions in quantum-confined systems or whether it is due to surface defect states (see ref 5 for an early review). Very recently, in an elegant experiment, Godefroo et al.[6,7] were able to control the origin of the PL of their Si NCs and to switch between quantum-confined and defect PL by hydrogen passivation and UV irradiation, respectively.

Using a single size-dispersed sample of silicon nanocrystals (Si NCs) with diameters ranging from 2.5 to 8 nm, Ledoux et al.[8] could show that the PL of naturally oxidized Si NCs produced by gas-phase condensation was governed by quantum confinement with a small deviation occurring for small Si NCs. This observation was in agreement with the study of Wolkin et al.[9] who compared the PL of hydrogen- and oxygen-passivated Si NCs with theoretical results and found that defect luminescence via oxygen-related inner-gap states becomes operative when quantum confinement causes the band gap to exceed a certain energy. The same observation has been made by Martin et al.[10] in their confocal microscopy investigation on single Si NCs. Their study is in accordance with a gradual transition of the photoluminescence from PL governed by quantum confinement for large Si NCs to defect luminescence for small Si NCs.

The defect luminescence taking place in oxygen-passivated Si NCs originates from localized states in the SiO_2 shell surrounding the crystalline silicon core. The same states should also be operative if the entire Si core is removed, for example, by full oxidation. Hence, the question arises whether the same defect luminescence can also be observed in SiO_2 nanoparticles (SiO_2 NPs), which are prepared by intentional oxidation of Si NCs. Indeed, a few years ago, Colder et al.[11] reported on the observation of strong luminescence from hollow SiO_2 NPs that had been obtained from Si NCs by full oxidation in water. The PL spectra of such SiO_2 nanopowder resembled very much the PL spectra known from Si NCs suggesting that there could possibly be a common origin.

* To whom correspondence should be addressed. E-mail: (A.J.M.) alfred.meixner@ipc.uni-tuebingen.de; (F.H.) friedrich.huisken@uni-jena.de.
[†] University of Tübingen.
[‡] University of Jena.

10.1021/nl901509k CCC: $40.75
Published on Web 08/04/2009

In the present study, we have carried out confocal microscopy experiments on individual SiO_2 NPs obtained by full oxidation of freshly synthesized Si NCs by investigating their optical response upon excitation with 473 and 488 nm laser light. The SiO_2 NPs are shown to possess a linear, randomly oriented transition dipole moment for excitation and to exhibit dynamical effects such as transition dipole moment flipping and fluorescence intermittency. The PL spectra reveal a narrow zero-phonon line and a broader phonon band that can be associated with the excitation of longitudinal optical phonons in SiO_2. These spectra are identical to those reported by Martin et al.[10] suggesting that both SiO_2 and Si single particle spectra are governed by the same mechanisms.

Single Particle Imaging. In order to obtain detailed information on the origin and the properties of the defect luminescence of SiO_2 NPs and to reveal possible similarities with the recently published single-particle spectroscopy of Si NCs surrounded by a SiO_2 shell,[10] we have investigated the PL of single SiO_2 NPs employing an inverted confocal microscope. At first, we have concentrated on single-particle imaging and the visualization of the transition dipole moment using tightly focused higher-order laser modes.

The excitation of a single SiO_2 NP by scanning it through the focal region of an azimuthally polarized laser beam with doughnut-shaped intensity profile gives rise to an image consisting of two nearby bright spots of elliptical shape resembling a "coffee bean".[12−15] This situation is displayed in the upper image (a) of Figure 1. The projection of the transition dipole moment on the substrate is oriented along the dark gap between the two halfs of the coffee bean. Out-of-plane orientations of the dipole moment lead to a weaker intensity of the coffee bean image, while dipole moments oriented exactly perpendicular to the surface cannot be seen at all. Weaker images are also obtained if the PL activity of the SiO_2 NP is smaller. A small asymmetry of the coffee beans is caused by a small asymmetry of the excitation laser beam.

Radially polarized laser beams are ideally suited to determine the three-dimensional orientation of the transition dipole moment as they have a field distribution containing both a longitudinal and transversal component[12−15] in the focal region of a high numerical aperture (NA) objective lens. Note that for SiO_2 NPs with a component of their transition dipole moment parallel to the substrate the coffee beans are oriented perpendicularly to the ones that are seen with azimuthally polarized laser beam. This fact is demonstrated by the SiO_2 NP shown in the right halfs of Figure 1a,b. Figure 1b shows the same sample area as Figure 1a and therefore the same SiO_2 NPs but now with radial mode excitation. As a result, the coffee bean is rotated by 90°. The image of the other particle shown in the left half of Figure 1b has a peculiar shape. It can be explained by the mixing of two images, one being produced by the longitudinal component of the electric field vector (giving rise to a centrosymmetric spot) and the other being due to the transversal component of the electric field (giving rise to a coffee bean rotated by 90° with respect to the one imaged in Figure 1a).

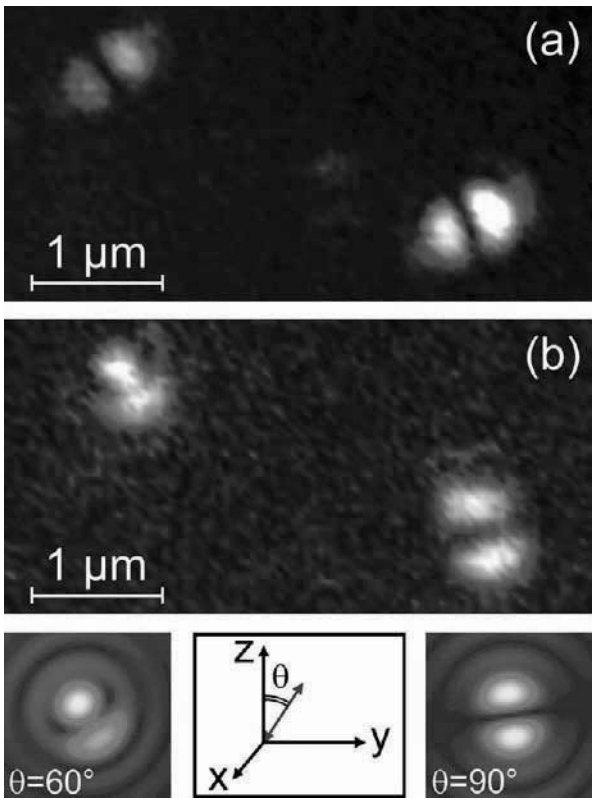

Figure 1. SiO_2 NPs in PMMA observed with an excitation wavelength of 488 nm. The upper panel (a) shows two NPs excited with the azimuthal mode (maximum intensity: 614 counts per pixel in 5 ms). Image (b) presenting the same NPs has been obtained with the radial mode (maximum intensity: 176 counts per pixel in 5 ms). The bottom panel shows as examples simulated emission patterns for two orientations of the transition dipole moment after excitation with the radial mode. The direction z is orthogonal to the substrate.

The mixing can be easily simulated with a computer program, and by comparing the computed patterns with the measured images one can determine the three-dimensional orientation of the transition dipole moment for excitation. Such simulated patterns are depicted in the bottom panels of Figure 1 together with a small coordinate system defining θ as the angle between the transition dipole moment and the surface normal. For an out-of-plane orientation of the dipole moment ($\theta = 0°$), a centrosymmetric spot will be observed as the transversal component does not contribute. For an in-plane orientation ($\theta = 90°$), a nice coffee bean like the one depicted in the right half of Figure 1b is observed. By comparison with calculated patterns, the peculiar shape of the particle image in the left part of Figure 1b can be explained by a dipole moment orientation of $\theta \approx 60°$.

After having presented results on SiO_2 NPs embedded in a thin PMMA polymer layer, we now want to turn to polystyrene (PS) as matrix material. At first, we would like to state that, in PS, dynamical effects seem more likely to occur than in PMMA. An example is given in Figure 2 that shows a series of images taken one after the other, all showing the same small section of $4.3 \times 4.3\ \mu m^2$ containing essentially only two SiO_2 NPs. The sample was excited with

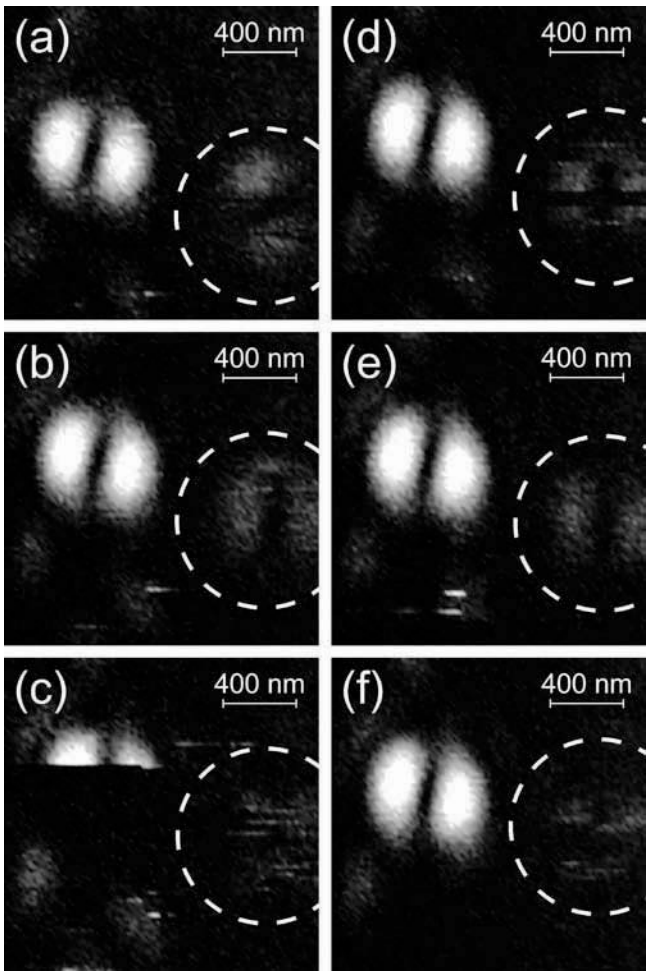

Figure 2. Images of SiO_2 NPs embedded in a polystyrene matrix and excited in an azimuthally polarized laser focus ($\lambda = 488$ nm). The images (a−f) reveal the same image section of a series of pictures recorded one after the other every 100 s. Each image essentially shows two NPs, one being represented by the bright coffee bean and a fainter one marked by the dashed circle. The following dynamical processes are observed: image c reveals fluorescence intermittency of the brighter NP (also called blinking). Blinking is also observed for the fainter NP in image d. In addition, we observe sudden flipping of the transition dipole moment of the fainter NP as can be seen by comparing images a and b as well as e and f.

azimuthally polarized laser beam, and the time between two consecutive samplings of the same nanoparticle was 100 s. Following the images from a−f, we observe a bright coffee bean in the left half of each image. In image c, this particle experiences fluorescence intermittency or blinking as manifested by the sudden quenching of PL being active for at least 24 s. In image d, the same NP appears bright again. Another interesting dynamical effect is demonstrated by the fainter coffee bean marked by the dashed circle. Comparing image a and b, we observe a sudden flipping of the orientation of the transition dipole moment. A similar change in dipole moment orientation for the fainter particle has occurred from image e to f. In picture c, the image of this NP is somewhat smeared out, indicating that the orientation of the transition dipole moment was not stable during the scan. It should be mentioned that a flipping of the transition dipole moment was observed rather rarely.

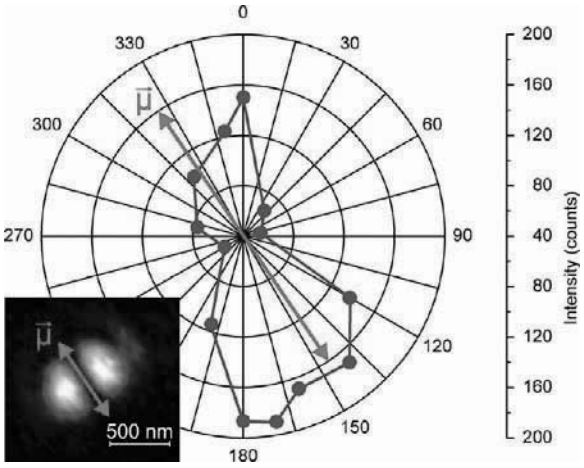

Figure 3. In the left corner, the fluorescence image of a SiO_2 NP in PMMA is shown. As the laser beam was azimuthally polarized, the transition dipole moment for excitation is oriented along the dark gap of the PL pattern. The emission of the same SiO_2 NP was observed through a linear polarizer and its intensity was recorded as a function of the rotation angle of the polarizer. The result presented in polar coordinates shows that the emission dipole moment has the same direction as the one for excitation.

Because of the presence of a one-dimensional transition dipole moment for excitation, the particle is expected to emit light possessing linear polarization. To confirm this assumption, the fluorescence of a single SiO_2 NP was investigated using a polarization analyzer in front of the photodetector. For each consecutive scan of the sample area, the analyzer was rotated by a distinct angle. The results of this experiment are presented in Figure 3. It shows in the inset an image of a single NP measured with azimuthally polarized laser beam. The transition dipole moment is indicated by the red arrow. The integrated fluorescence intensity of this NP was recorded as a function of the polarization analyzer orientation and plotted into a polar coordinate system. The fact that we measure two lobes demonstrates that the emission of a single SiO_2 NP is linearly polarized, and its orientation proves that the transition dipole moment for emission has the same direction as the one for excitation.

PL Spectra of Individual NPs. With the setup described in the Supporting Information, we have measured the PL spectra of various individual SiO_2 nanoparticles embedded both in PMMA and PS polymer matrices. Three examples are shown in Figure 4. The PL spectrum with the best signal-to-noise ratio has been measured in PMMA and is displayed in Figure 4a. Interestingly, it features a strong peak at smaller wavelength and two satellite peaks at longer wavelengths. As will be shown later, the first peak is the zero-phonon line while the other two peaks are attributed to phonon bands associated with the excitation of one or two quanta of vibrations in the SiO_2 network.

The other two PL spectra displayed in Figure 4b,c have been recorded from SiO_2 NPs embedded in PS. The inferior signal-to-noise ratio in conjunction with a two times smaller count rate is evident. In addition, the measured bands are clearly broader which also explains that the separation between the zero-phonon line and the first phonon band is less pronounced. Finally, the zero-phonon line of the

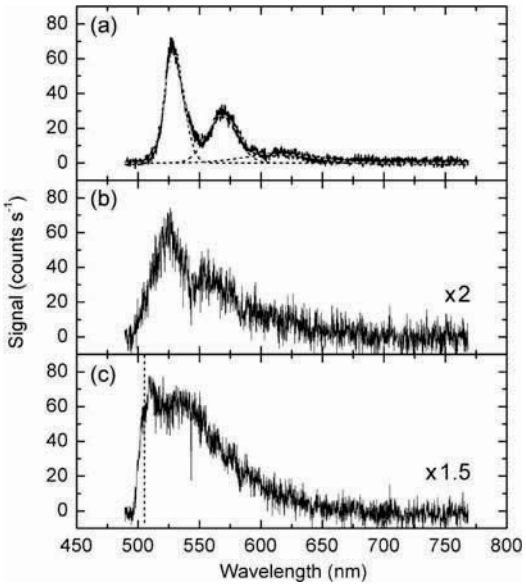

Figure 4. PL spectra of three individual SiO_2 nanoparticles embedded in PMMA (a) or PS (b and c). For a better comparison, the weaker PL spectra measured in PS have been multiplied by 2 or 1.5, respectively. The dashed line in panel (c) indicates the wavelength at which the long-wave pass filter transmits 50%. The uppermost spectrum has been fitted by three Gaussians also displayed in the figure.

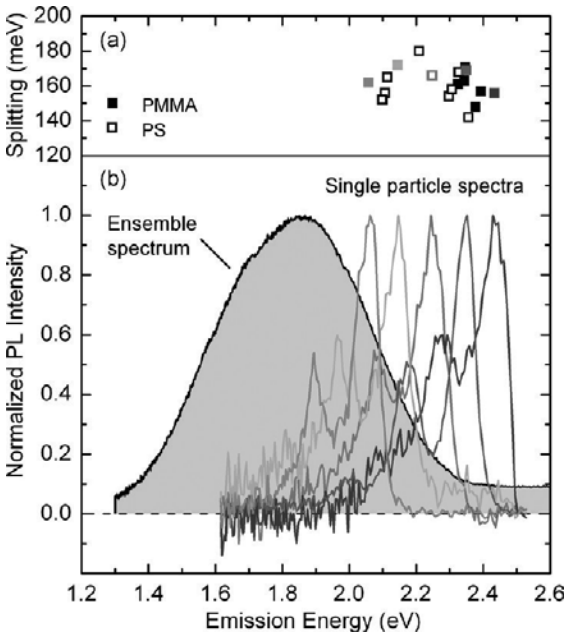

Figure 5. Panel b: Five PL spectra of individual SiO_2 nanoparticles embedded in PMMA or PS. Before plotting, the experimental data has been subjected to an averaging over six data points. For comparison, the broad PL spectrum obtained from an ensemble of SiO_2 NPs is shown as black curve. Panel (a) presents the splitting between zero-phonon line and first phonon band for all PL spectra measured in this study (except truncated spectra) as a function of zero-phonon line energy. Splitting values belonging to the PL spectra in panel b are plotted in the same color. Solid squares refer to PMMA and open symbols to PS matrices.

spectrum plotted in the bottom panel seems to be truncated at short wavelengths. This is caused by the long-wave pass filter that we had to use in order to block the straylight from the excitation laser. Assuming the same separation between zero-phonon line and first phonon band, we would extrapolate a peak position of the zero-phonon line in the region 500 ± 10 nm.

The PL spectra measured as a function of wavelength, $I_{PL}(\lambda)$, were transformed to energy spectra, $I_{PL}(E)$, taking into account the proper Jacobian and dividing the intensities by $dE/d\lambda$. As examples, we show five spectra of individual SiO_2 NPs in Figure 5. This set includes the spectrum with the lowest-energy zero-phonon line (red curve) as well as the one with the highest energy (dark-blue curve). PL spectra with truncated zero-phonon lines mentioned before were not considered here. The five single-particle spectra are compared with an ensemble spectrum taken from the same nanopowder from which the confocal microscopy samples were prepared. It should be mentioned that this ensemble spectrum was measured with a different setup that employed a low-repetition rate (20 Hz) pulsed Nd:YAG laser as excitation source (see Supporting Information). As a result, the fluorescence from excited states with long lifetimes was not discriminated against the short-lived fluorescence. Besides the fact that the ensemble spectrum is, as expected, much broader, it is noted that single-particle spectra could only be observed for energies above 2.0 eV. The smallest full width at half-maximum was observed for a NP embedded in PMMA (fwhm = 75 meV; blue curve). We have also analyzed the separation between the zero-phonon line and the first phonon peak for all measured spectra, except those with truncated zero-phonon line. The results are plotted in the upper panel (a) of Figure 5. Irrespective of the polymer matrix used, the splitting varies in the range 160 ± 20 meV.

Discussion. At first we would like to discuss the images of single SiO_2 NPs visualizing the orientation of the transition dipole moment (Figures 1−3). The fact that we are observing sharp coffee bean patterns proves that we are dealing with single NPs since the interaction of two and more NPs would produce blurry images. In most cases, the coffee bean pattern stays quite stable during the period of observation although the NP is excited many thousands of times. This suggests that we are exciting always the same luminescent center that gives rise to the PL photons that we observe. Other defects may be present but we are not sensitive to them as they cannot be accessed. The observation that the transition dipole moments for excitation and emission have the same direction further suggests that the PL photon arises from the same defect which was excited. Thus, we have the important result that charge carrier hopping between different defect states is not very likely to occur. The SiO_2 NP seems to behave like a molecule with stable linear transition dipole moment.

The use of radially polarized laser beams allowed us to visualize the transition dipole moment in space. Analyzing several hundred images, we found that there was no preferred direction with respect to the substrate surface suggesting that the dipole moments are randomly oriented. This is not surprising if one keeps in mind that the NPs are embedded in a ∼50 nm thick polymer matrix which keeps them far away from the substrate.

Despite the rather stable nature of the transition dipole moment, we are able to observe dynamical effects as, for example, fluorescence intermittency and flipping of the transition dipole moment. These phenomena can be explained by a redistribution of defect states caused by charge fluctuations in the surrounding of the NP. Transition dipole moment flipping results from the fact that another defect has become energetically more favorable to be accessed. As usual, fluorescence intermittency can be explained by electron trapping and nonradiative charge carrier recombination at the hole.

We have found that dynamical effects are more likely to occur when the SiO_2 NPs are embedded in the nonpolar PS ($[C_8H_8]_n$) matrix. In contrast, the defects involved in the excitation and photoemission process seem locally and energetically more stable if the NPs are surrounded by the polar PMMA ($[C_5O_2H_8]_n$) matrix. This is ascribed to the oxygen atoms surrounding the NPs and giving rise to a stronger fixation or localization of the defects involved in the process. The stabilized situation is also reflected by the better contrast of the excitation images.

The photoluminescence spectra of single SiO_2 NPs were found to exhibit, besides a narrow zero-phonon line, one or even two satellite peaks on the lower-energy side. The separation between the peaks is on the average 160 meV but may vary from 140 to 180 meV. This energy separation comes very close to the energy of the longitudinal optical mode (LO_3) of SiO_2 at 156 meV.[16] As a result, the lower-energy satellite peaks can be assigned to the excitation of one or two LO_3 phonon quanta in the SiO_2 NP being excited simultaneously with the radiative recombination of the charge carriers. Apparently, there is a strong coupling between the electronic transition and a collective vibration in the SiO_2 NP due to a sudden relaxation mechanism involving charges. Similar phonon couplings have been reported for other nanosized systems, as for example for CdSe NCs[17] and Si NCs.[18] Very recently, Martin et al.[10] observed strong electron−phonon coupling in single Si NCs involving LO_3 phonons in the surrounding SiO_2 shell. Interestingly, the spectra of Martin et al. are almost identical to the ones presented here. We will postpone the discussion of this amazing similarity to the end of this paper.

Comparing PL spectra of SiO_2 in PMMA with those obtained in PS, it is found that in general the quality of the SiO_2/PMMA spectra is higher. This is explained with the stronger fixation of the luminescent centers due to the presence of the polar ester groups in the PMMA matrix. The enhanced dynamics in PS is most likely related to a flipping of the loosely bound phenyl groups that are known to be responsible for considerable spectral dynamics and heterogeneity in single molecule spectroscopy.[19] As another point, we have observed that the spectra of SiO_2 NPs in PS appeared more often truncated than the ones in PMMA. This can also be explained with the presence of oxygen in PMMA. Because of the interaction between the defect state and the oxygen in the matrix, the energy of the defect state is lowered, thus giving rise to a red shift for the NPs embedded in PMMA compared to those in PS. Another explanation could be that a certain type of defect associated with higher energy is passivated by the presence of oxygen in PMMA while this is not the case in PS.

Another interesting point to be discussed is the big mismatch between the ensemble spectrum of SiO_2 NPs and the single particle spectra as shown in Figure 5. It is noticed that single particle spectra are only observed when the energy of the zero-phonon line is larger than 2 eV. The reason of this mismatch is probably related to differences in the PL efficiency for different NPs which may be emphasized by the different excitation sources used. In any case, it should be clearly stated here that single NP spectroscopy cannot be representative for the entire sample. Because of the low PL flux originating from an individual NP, single nanoparticle spectroscopy can only be applied to the brightest NPs. All NPs whose PL is below a certain threshold will be ignored. Thus, it appears that the SiO_2 NPs emitting photons at higher energy (2.0−2.5 eV) are brighter while the ones emitting at 1.8 eV are more abundant but less intense.

Now we want to discuss the origin of the PL observed in the present study. While there seems in general agreement to assign the PL maximum between 1.8 and 1.9 eV observed in the ensemble spectrum to nonbridging oxygen hole centers (NBOHCs; ≡Si−O•),[20,21] the situation is more complicated for the single particle spectra observed in the green between 2.0 and 2.5 eV. According to the work of Glinka et al.,[22] a broad PL band in the green extending from 1.8 to 2.8 eV with maximum at 2.35 eV, which has been observed for thermally untreated SiO_2 NPs with diameters of 7 and 15 nm, can be attributed to hydrogen-related species (≡Si−H and ≡Si−OH) on the surface of the nanoparticles. This broadband measured in ensemble spectra is an inhomogeneous composition of many different species each contributing with a slightly different energy mimicking small differences in the local environment of the defect. In single particle spectroscopy, this inhomogeneity is removed, and we can observe sharp zero-phonon lines characteristic for each individual NP.

As already mentioned, the fluorescence spectra of single SiO_2 NPs presented in Figure 5 are amazingly similar to the single particle spectra of Si nanocrystals measured by Martin et al.[10] This similarity refers to the entire shape of the PL spectra including the splitting into zero-phonon line and phonon band and the energy range in which single particle spectra could be recorded. Since the Si NCs are surrounded by a 1−2 nm thick layer of amorphous SiO_2 (ref 23), it could be possible that the PL observed in both systems (SiO_2 NPs and Si NCs) with single-particle spectroscopy have the same origin. To obtain more detailed information on this interesting issue, dedicated studies, including spectrally resolved lifetime measurements on single particles, will be carried out in the near future.

Finally, we would like to emphasize that the luminescent SiO_2 NPs presented in this study will be attractive candidates for fluorescence labeling and local heating centers in biological and medical applications.

Acknowledgment. This work was carried out within the European cooperation NANOLUM. F.H. and T.S. are

grateful for support by the Max Planck Society and the European Commission (Specific Targeted Project: BONSAI, Contract No. LSHB-CT-2006-037639). Financial support by the Forschungsschwerpunktprogramm Baden-Württemberg and from the European Commission through the Human Potential Program (Marie-Curie Research Training Network NANOMATCH, Contract No. MRTN-CT-2006-035884) is acknowledged. We thank Sebastian Bär and Holger Hintz for fruitful discussions.

Supporting Information Available: Details on synthesis of SiO_2 NPs, sample preparation for confocal microscopy, and experimental details on the confocal microscopy setups. This material is available free of charge via the Internet at http://pubs.acs.org.

References

(1) Canham, L. T. *Appl. Phys. Lett.* **1990**, *57*, 1046.
(2) Lehmann, V.; Gösele, U. *Appl. Phys. Lett.* **1991**, *58*, 856.
(3) Prokes, S. M. *Appl. Phys. Lett.* **1993**, *62*, 3244.
(4) Kanemitsu, Y.; Okamoto, S.; Otobe, M.; Ota, S. *Phys. Rev. B* **1997**, *55*, R7375.
(5) Cullis, A. G.; Canham, L. T.; Calcott, P. D. J. *J. Appl. Phys.* **1997**, *82*, 909.
(6) Godefroo, S.; Hayne, M.; Jivanescu, M.; Stesmans, A.; Zacharias, M.; Lebedev, O. I.; Van Tendeloo, G.; Moshchalkov, V. V. *Nat. Nanotechnol.* **2008**, *3*, 174.
(7) Gösele, U. *Nat. Nanotechnol.* **2008**, *3*, 134.
(8) Ledoux, G.; Gong, J.; Huisken, F.; Guillois, O.; Reynaud, C. *Appl. Phys. Lett.* **2002**, *80*, 4834.
(9) Wolkin, M. V.; Jorne, J.; Fauchet, P. M.; Allan, G.; Delerue, C. *Phys. Rev. Lett.* **1999**, *82*, 197.
(10) Martin, J.; Cichos, F.; Huisken, F.; von Borczyskowski, Chr. *Nano Lett.* **2008**, *8*, 656.
(11) Colder, A.; Huisken, F.; Trave, E.; Ledoux, G.; Guillois, O.; Reynaud, C.; Hofmeister, H.; Pippel, E. *Nanotechnology* **2004**, *15*, L1.
(12) Novotny, L.; Beversluis, M. R.; Youngworth, K. S.; Brown, T. G. *Phys. Rev. Lett.* **2001**, *86*, 5251.
(13) Dorn, R.; Quabis, S.; Leuchs, G. *Phys. Rev. Lett.* **2003**, *91*, 233901.
(14) Gutbrod, R.; Chizhik, A.; Chizhik, A.; Khoptyar, D.; Meixner, A. J. *Opt. Lett.* **2009**, *34*, 629.
(15) Failla, A. V.; Jäger, S.; Züchner, T.; Steiner, M.; Meixner, A. J. *Opt. Express* **2007**, *15*, 8532.
(16) Gourbilleau, F.; Portier, X.; Ternon, C.; Voivenel, P.; Madelon, R.; Rizk, R. *Appl. Phys. Lett.* **2001**, *78*, 3058.
(17) Empedocles, S. A.; Neuhauser, R.; Shimizu, K.; Bawendi, M. G. *Adv. Mater.* **1999**, *11*, 1243.
(18) Kovalev, D.; Heckler, H.; Ben-Chorin, M.; Polisski, G.; Schwartzkopff, M.; Koch, F. *Phys. Rev. Lett.* **1998**, *81*, 2803.
(19) Stracke, F.; Blum, C.; Becker, S.; Mullen, K.; Meixner, A. *J. Chem. Phys.* **2004**, *300*, 153.
(20) Munekuni, S.; Yamanaka, T.; Shimogaichi, Y.; Tohmon, R.; Ohki, Y.; Nagasawa, K.; Hama, Y. *J. Appl. Phys.* **1990**, *68*, 1212.
(21) Skuja, L. *J. Non-Cryst. Solids* **1994**, *179*, 51.
(22) Glinka, Y. D.; Lin, S.-H.; Chen, Y.-T. *Appl. Phys. Lett.* **1999**, *75*, 778.
(23) Hofmeister, H.; Huisken, F.; Kohn, B. *Europ. Phys. J. D* **1999**, *9*, 137.

NL901509K

SUPPORTING INFORMATION PARAGRAPH

Imaging and Spectroscopy of Defect Luminescence and Electron-Phonon Coupling in Single SiO_2 Nanoparticles

Experimental Methods

Synthesis of SiO_2 NPs

The synthesis of amorphous SiO_2 NPs from Si NCs, freshly prepared by CO_2 laser pyrolysis[1,2] was carried out according to the recipe of Colder et al.[3] The brownish Si nanopowder (~10 mg) collected on a filter at the exit of the flow reactor was dispersed in 1 cm^3 distilled water applying ultrasonic treatment for 10 min. The beige viscous solution was left for several days without any further treatment until the beige color had turned to a transparent appearance, a clear indication for complete oxidation of the Si NCs to SiO_2 NPs. Finally, the vial containing the transparent dispersion was covered by an aluminum foil and heated in a simple non-evacuated oven to 95 °C, in order to evaporate the water. In this way, a white powder was obtained which showed strong red-orange PL when it was illuminated with light from a simple laboratory UV lamp (λ = 254 nm).[3]

High-resolution transmission electron microscopy (HRTEM) studies, electron energy loss spectroscopy (EELS), as well as x-ray diffraction (XRD) measurements reveal the complete amorphous structure of the as-synthesized silica nanopowder. As reported by Colder et al.,[3] the processed powder may consist of silica shells (hollow SiO_2 NPs) having average inner and outer diameters of 9 and 18 nm, respectively, when the average size of the original Si NCs was 13 nm in diameter. The SiO_2 NPs used for the present study were mostly not hollow and had an average diameter of 21 nm. The reason, why the SiO_2 NPs are sometimes hollow and sometimes not, is not completely understood; but this property will not be important for the discussion of the present study as both powders exhibit strong red-orange

PL. Photoluminescence spectra of the silica nanopowder (ensemble spectra) were measured with a mini-spectrometer (Ocean Optics, model QE 65000) after excitation with the 4th harmonic (λ = 266 nm) of a pulsed Nd:YAG laser with 5 ns pulse width.

Sample preparation

Silicon dioxide NPs of the processed powder were embedded in very low concentration into a thin polymer film covering a quartz cover slide of 170 μm thickness. For this purpose, a small amount of the processed silica nanopowder was dispersed at low concentration in toluene and then mixed with a solution of poly(methyl methacrylate) (PMMA, $[C_5O_2H_8]_n$) or polystyrene (PS, $[C_8H_8]_n$). A droplet (10 μl) of this mixture was spin-coated on a quartz cover slide to obtain a 50 – 60 nm thick polymer film as determined by atomic force microscopy (AFM). The use of the two polymers PMMA and PS was motivated by the desire to obtain a polar (PMMA) and a non-polar (PS) matrix for the SiO_2 NPs. To make sure that samples don't contain impurities (e.g. dye molecules) a droplet of the polymer without dissolved silica nanopowder was spin-coated onto a quartz cover slide and spectroscopically verified.

Confocal microscopy setups

Two slightly different confocal microscopy setups were used in the present study. The optical measurements were performed with a modified inverted confocal microscope (Zeiss Axiovert 135 TV) using a high-numerical aperture oil immersion objective (Zeiss Plan Neofluar, 100/NA = 1.3). The term inverted refers to the fact that the polymer film with the SiO_2 NPs was on the opposite side of the cover slip with respect to the objective. An ultrafast laser system (Picoquant, model LDH-P-C470) operating at λ = 473 nm (2.62 eV) and providing pulses at a repetition rate of 10 MHz with a width of 300 ps served as excitation source for the measurements of fluorescence spectra. In order to discriminate against the straylight from the laser, the setup was equipped with a long-wave pass filter having its 50% transmission value at 510 nm. Fluorescence spectra were acquired with a spectrograph (Acton Research SpectraPro 300i) equipped with a CCD camera (Princeton Instruments, model LNCCD-1340/100-EB/1).

To investigate the three-dimensional orientation of the nanoparticles' transition dipole moment, we used a similar home-built confocal microscope setup additionally equipped with a mode conversion optical line for the generation of radially and azimuthally polarized laser beams.[4-7] The nanoparticles were excited at λ = 488 nm (2.54 eV) in the diffraction limited laser focus of NA = 1.25 immersion oil objective. The typical image size was 100 × 100 pixels distributed over 2 × 2 or 5 × 5 μm^2. For each pixel, the signal was integrated over 5 ms, resulting in a acquisition time of 50 s. Monodirectional scanning process doubles this time to the value of 100 s for one fluorescence image. When we recorded series of images, the next scan was started immediately after the previous had finished.

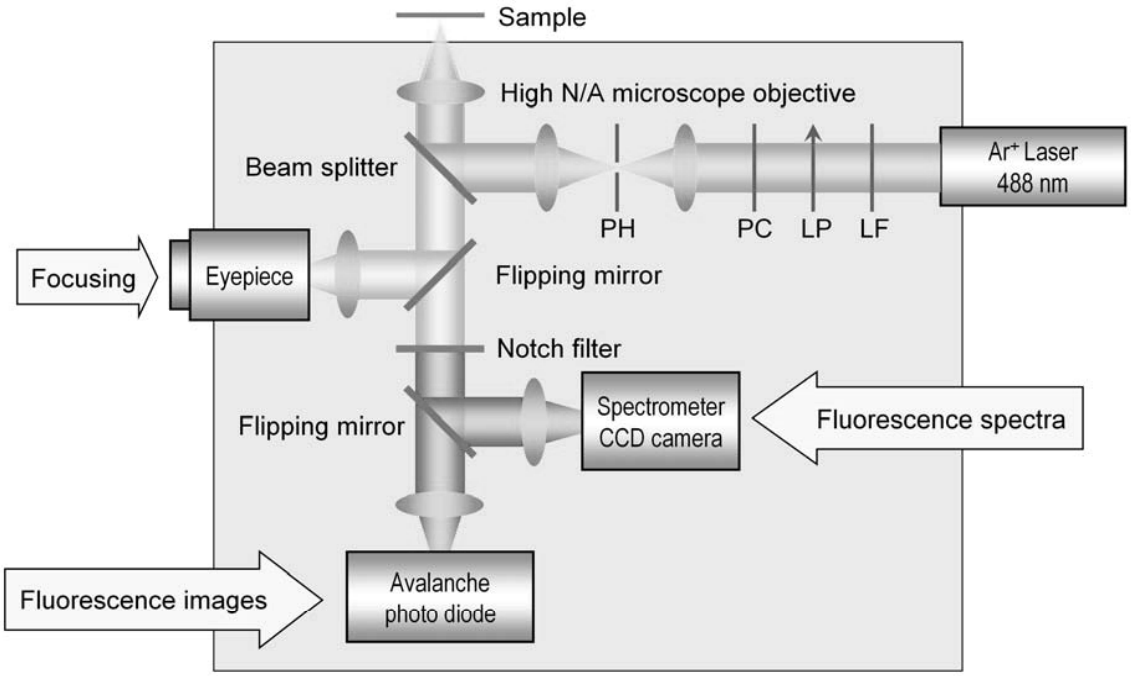

Figure S1. Combined schematic view of the two confocal microscope setups used in the present study. For visualization of the transition dipole moment, the Ar^+ laser with mode converter is employed (LF = laser line filter, LP = linear polarizer, PC = polarization converter, PH = pinhole). The fluorescence is then detected with an avalanche photodiode. For the measurement of fluorescence spectra, the Ar^+ laser is replaced by an ultrafast pulsed diode laser system emitting at 473 nm. PL spectra are recorded with a spectrometer backed by a CCD camera.

1. Huisken, F.; Hofmeister, H.; Kohn, B.; Laguna, M. A.; Paillard, V. *Appl. Surf. Sci.* **2000**, *154-155*, 305.

2. Huisken, F.; Ledoux, G.; Guillois, O.; Reynaud, C. *Adv. Mater.* **2002**, *14*, 1861.

3. Colder A.; Huisken, F.; Trave, E.; Ledoux, G.; Guillois, O.; Reynaud, C.; Hofmeister, H.; Pippel, E. *Nanotechnology* **2004**, *15*, L1.

4. Novotny, L.; Beversluis, M. R.; Youngworth, K. S.; Brown, T. G. *Phys. Rev. Lett.* **2001**, *86*, 5251.

5. Dorn, R.; Quabis, S.; Leuchs, G. *Phys. Rev. Lett.* **2003**, *91*, 233901.

6. Gutbrod, R.; Chizhik, A.; Chizhik, A.; Khoptyar, D.; Meixner, A. J. *Opt. Letters*, **2009**, *34*, 629.

7. Failla, A. V.; Jäger, S.; Züchner, T.; Steiner, M.; Meixner, A. J. *Opt. Express*, **2007**, *15*, 8532.

Chapter 7

Fluorescence imaging and spectroscopy of single Si and SiO_2 nanoparticles using confocal microscopy

In this chapter, we study single Si NCs and SiO_2 NPs using confocal laser scanning microscopy with the goal to compare both kinds of NPs and to determine to what extent quantum confinement or surface-related defect centers are responsible for the strong fluorescence of Si NCs. The single particle spectra of Si NCs and SiO_2 NPs are composed of a zero-phonon line and one or two phonon bands, which are associated with longitudinal optical phonons in SiO_2, and reveal in every detail an amazing similarity. Both systems reflect the same dynamical behavior (blinking and bleaching). Spectrally resolved fluorescence decay measurements yield the important result that the direct and the phonon-assisted recombination processes occur on the same nanosecond timescale (~4 ns). These experimental observations suggest that the photoluminescence of the Si NCs observed in this study is governed by defect luminescence.

This chapter is based on:

Chizhik, A.M., Chizhik, A.I., Meixner, A.J., Schmidt, T., Huisken, F. "Fluorescence imaging and spectroscopy of single Si and SiO_2 nanoparticles using confocal microscopy" *Bonsai Project Symposium: Breakthroughs in Nanoparticles for Bio-imaging, AIP Conf. Proc.* **2010***, 1275,* 63-70.

Fluorescence Imaging and Spectroscopy of Single Si and SiO_2 Nanoparticles Using Confocal Microscopy*

Anna M. Chizhik[a], Alexey I. Chizhik[a], Alfred J. Meixner[a], Torsten Schmidt[b], and Friedrich Huisken[b]

[a]*Institute of Physical and Theoretical Chemistry, University of Tübingen, Auf der Morgenstelle 8, D-72076 Tübingen, Germany*
[b]*Laboratory Astrophysics Group of the Max Planck Institute for Astronomy, Institute of Solid State Physics, University of Jena, Helmholtzweg 3, D-07743 Jena, Germany*

Abstract. Single silicon nanocrystals (Si NCs) and SiO_2 nanoparticles (SiO_2 NPs) have been studied by confocal laser scanning microscopy with the goal to compare both kinds of NPs and to determine to what extent quantum confinement or surface-related defect centers are responsible for the strong photoluminescence (PL) of Si NCs. Using special laser polarization techniques, the transition dipole moment (TDM) for the excitation of individual NPs (Si and SiO_2) could be shown to be stable and one-dimensional. The single particle spectra of Si NCs and SiO_2 NPs are composed of a zero-phonon line and one or two phonon bands, which are associated with LO_3 phonons in SiO_2, and reveal in every detail an amazing similarity. Both systems reflect the same dynamical behavior (blinking, bleaching, and TDM flipping). Spectrally resolved fluorescence decay measurements yield the important result that the direct and phonon-assisted recombination processes occur on the same nanosecond timescale (~4 ns). These experimental observations suggest that the PL of the Si NCs observed in this study is governed by defect luminescence.

Keywords: Silicon nanocrystals, silica nanoparticles, single particle spectroscopy, confocal laser scanning microscopy, electron-phonon coupling, defect luminescence, quantum confinement.
PACS: 87.64.mk, 78.55.Ap, 78.55.Qr, 78.67.Bf, 78.67.Hc

INTRODUCTION

Since more than two decades, there has been an ongoing discussion on whether the photoluminescence (PL) from nanostructured silicon originates from intergap transitions assisted by quantum confinement (QC) [1] or whether it is governed by surface-related defect centers (DCs) [2]. Very recently, it was shown [3] that it is possible to control the origin of the PL of silicon nanocrystals (Si NCs) and to switch between quantum confinement and defect-based PL by hydrogen passivation and UV irradiation, respectively. Investigations of naturally oxidized Si NCs selected in size (2.5 – 8 nm) revealed that the PL is caused by quantum confinement, with some slight devia-

*This paper comprises results of the oral contribution of Anna M. Chizhik (S3-10) and the poster presentation of Alexey I. Chizhik (P3-24).

CP1275, *BONSAI Project Symposium: Breakthroughs in Nanoparticles for Bio-Imaging,* edited by E. Borsella

tion occurring for small NCs (2 – 3 nm in diameter) [4]. This observation was confirmed by Wolkin *et al.* [5] who compared the PL of Si NCs passivated by hydrogen and oxygen with theoretical results. They concluded that defect PL via oxygen-related inner-gap states becomes dominant when quantum confinement causes the band gap to exceed a certain energy. Furthermore, Martin *et al.* [6] showed that the emission from Si NCs is governed by quantum confinement for the larger particles, while in smaller Si NCs defect-based luminescence is dominant. The defect PL in oxygen-passivated Si NCs originates from localized states in the SiO_2 shell surrounding the crystalline silicon core. Removing the entire Si core, for example by full oxidation, the same states should still be operative. Therefore, the question arises whether the same defect luminescence can also be observed in SiO_2 NPs which are prepared by intentional and complete oxidation of Si NCs. Strong visible luminescence observed from hollow SiO_2 NPs which had been obtained by full oxidation of Si NCs in water was reported by Colder *et al.* [7]. Surprisingly, the PL spectra of such SiO_2 nanopowder are very similar to the ones recorded from Si NCs, giving rise to the assumption that the origin of the PL can be attributed to the same operating mechanism, which would then obviously be related to defect PL. Thus, in spite of the extensive results on Si NCs, the origin of the emission is still under debate. The observations suggest that there is not a strict separation between quantum confinement-induced PL and defect PL but rather a gradual transition.

With the purpose to shed some new light on the origin of the PL in oxidized Si NCs, we have carried out a comparative study of the optical properties of single Si NCs and single SiO_2 NPs employing confocal laser scanning microscopy.

EXPERIMENTAL

Silicon nanocrystals (Si NCs) with diameters between 3 and 10 nm were produced by laser-induced pyrolysis of silane (SiH_4) in a gas flow reactor. The dissociation of the SiH_4 molecules is initiated by the radiation of a pulsed CO_2 laser providing very sharp temperature gradients in a wall-less environment. The decomposition is followed by the condensation of the nascent silicon atoms in the gas phase and the formation of liquid nanoparticles (NPs). Upon cooling in the carrier gas stream, the NPs crystallize to form Si NCs. Finally, the Si NCs are collected on a filter mounted into the exhaust line of the flow reactor. When the Si NCs are removed from the vacuum chamber and stored in the laboratory, they are oxidized and covered by a thin layer of SiO_2.

Amorphous SiO_2 NPs were prepared according to the recipe of Colder *et al.* [7]. About 20 mg of freshly prepared Si NCs are dispersed in 1 ml doubly distilled water applying ultrasonic treatment for 10 min. The beige viscous solution is stored at room temperature for several days without any further treatment until the yellowish color has turned into a transparent appearance, indicating that the crystalline Si NPs have been transformed to amorphous SiO_2 NPs. Finally, the water is evaporated in a simple non-evacuated oven at 95°C. The residue at the bottom of the vial is a white powder exhibiting strong red-orange PL under the illumination of a laboratory UV lamp.

For the investigation of single Si NCs (and single SiO_2 NPs) in the confocal laser scanning microscope, the particles are embedded in very low concentration into a thin

polymer film. To produce suitable samples, a small amount of the silicon nanocrystals (or the processed silica nanopowder) is dispersed in toluene and then mixed with a solution containing the polymer [poly(methyl methacrylate), PMMA or polystyrene, PS]. Then a droplet of the mixture is spin-coated onto a clean quartz cover slide. The thickness of the polymer film is 50 – 60 nm, as determined by atomic force microscopy (AFM) measurements.

For the present study, we have used two slightly different confocal microscopy setups (see Ref. [8] for details). The common scheme is shown in Figure 1a. The optical measurements were performed with a modified inverted confocal microscope (Zeiss Axiovert 135 TV) using a high-numerical aperture oil immersion objective (Zeiss Plan Neofluar, 100/NA = 1.3). The term inverted refers to the fact that the polymer film with the NPs was on the opposite side of the cover slide with respect to the objective. A pulsed diode laser (Picoquant, model LDH-P-C470) operating at $\lambda = 473$ nm (2.62 eV) and providing pulses at a repetition rate of 10 MHz with a width of 300 ps served as excitation source for the measurements of fluorescence spectra. In order to discriminate against the stray light from the laser, the setup was equipped with a long-wave pass filter having its 50% transmission value at 510 nm. Fluorescence spectra were acquired with the flipping mirror in the position indicated in Figure 1a, employing a spectrograph (Acton Research SpectraPro 300i) equipped with a CCD camera (Princeton Instruments, model LNCCD-1340/100-EB/1).

To investigate the three-dimensional orientation of the nanoparticles' transition dipole moment (TDM), we used a similar home-built confocal microscope setup additionally equipped with a mode conversion optical line for the generation of radially and azimuthally polarized laser beams [8]. The nanoparticles were excited at $\lambda = 488$ nm (2.54 eV) in the diffraction-limited laser focus of the NA = 1.25 immersion oil objective. The typical image size was 100 × 100 pixels distributed over 2 × 2 or 5 × 5 μm. For each pixel, the signal was integrated over 5 ms, resulting in an acquisition time of 50 s. Monodirectional scanning process doubles this time to the value of 100 s for one fluorescence image. When we recorded a series of images, the next scan was started immediately after the previous one was finished.

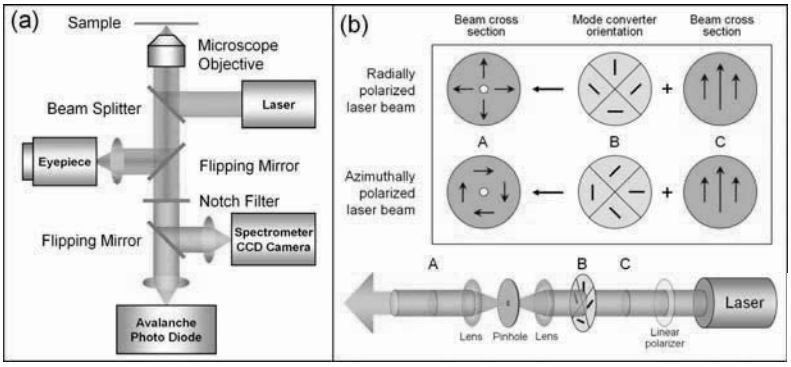

Figure 1. (a) The two versions of the confocal microscopy setup used in this study merged into one figure. Panel (b) explains the conversion of linearly polarized laser light to higher-order laser modes. In the present paper, we will concentrate on measurements using exclusively azimuthal polarization.

The measurements of the nanoparticles' TDM orientation were performed using azimuthally polarized laser beams. Figure 1b schematically shows the optical setup for the conversion of the linearly polarized Gaussian beam into a doughnut mode laser beam. A key element is the mode converter consisting of four $\lambda/2$ plates glued together as shown in the figure. Passing the linearly polarized Gaussian beam through the mode converter, we create a laser beam with either radial or azimuthal polarization. The collimated beam is reflected by a non-polarizing beam splitter and focused onto the sample through the microscope objective (see Figure 1a).

RESULTS

To compare the optical properties of single Si NCs with those of single SiO_2 NPs, we have investigated both nanoparticle systems employing the following techniques: (1) fluorescence imaging with higher-order laser modes, (2) monitoring the emission as a function of time, (3) spectral analysis of the fluorescence, and (4) spectrally resolved excited state lifetime measurements.

Fluorescence Imaging of Single Si NCs and SiO_2 NPs

The excitation of a single Si NC or SiO_2 NP by scanning the sample through the focal region of an azimuthally polarized laser beam with doughnut-shaped intensity profile (see Figure 1b), gives rise to an image consisting of two nearby bright spots of elliptical shape resembling a "coffee bean" [8]. An example of such image taken from a single SiO_2 NP is given in Figure 2a. The peculiar shape can be explained by the interaction of a linear transition dipole moment (TDM) of the NP with the polarized laser field. Assuming a parallel TDM, the dark gap of the coffee bean indicates the orientation of the projection of the TDM on the surface of the substrate to which the NP is attached.

The other images (b) – (d) of Figure 2 were obtained by scanning the same area of the substrate successively one after the other. The time needed to record one image was 100 s, *i.e.*, the entire observation time covered by Figure 2 was 400 s. As can be seen, the TDM stayed stable during all the time. A more careful look on the images, however, reveals some dark lines in images (b) and (c), indicating fluorescence inter-

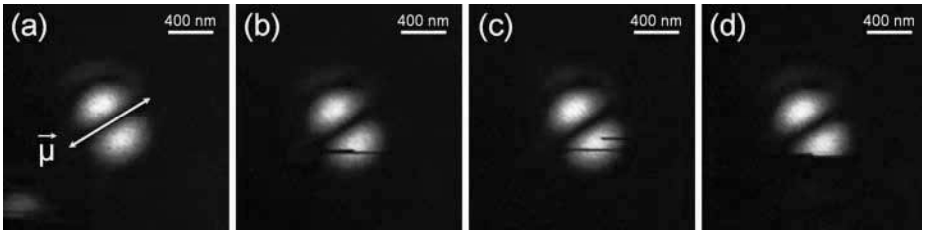

Figure 2. Successive scans of a sample area containing a single SiO_2 NP in PMMA through the focus of an azimuthally polarized laser beam. Dark lines are associated with fluorescence intermittence.

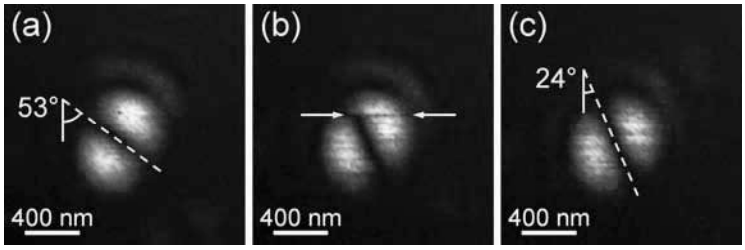

Figure 3. Series of three fluorescence excitation images recorded from a single Si NC embedded in PMMA. Note the sudden change (flipping) of the transition dipole moment in image (b).

mittence during that time. This phenomenon, also referred to as blinking, is quite common for single particle spectroscopy and is usually associated with an ionization of the NP. Figure 2d demonstrates another dynamical effect, namely the sudden cessation of the fluorescence, giving rise to the so-called bleaching. Qualitatively similar images were recorded for Si NCs. Comparing the images for Si NCs and SiO_2 NPs, actually no difference was found. This refers to the shape of the coffee beans, the level of fluorescence intensity, and the dynamical effects.

Figure 3 shows three successively scanned images of Si NCs in PMMA revealing a sudden orientational change (flipping) of the TDM from 53° to 24° (with respect to the *y*-axis) in image (b) [9]. It should be noted that such TDM flipping is observed quite rarely but equally often for Si NCs and SiO_2 NPs.

Time Traces and Blinking

In order to monitor the above-mentioned dynamical effects (blinking and bleaching) of Si NCs and SiO_2 NPs for spectroscopic issues, time traces were recorded with a linearly polarized Gaussian laser beam for excitation (λ_{exc} = 473 nm) [9]. Figure 4 shows a time trace acquired from a single Si NC with a dwell time of 100 ms. The transient signal features two-level transitions of the emission intensity between the background level (OFF state) to the ON state and backwards. This clearly demonstrates that the emission originates from a single quantum emitter. Similar time traces were recorded for SiO_2 NPs.

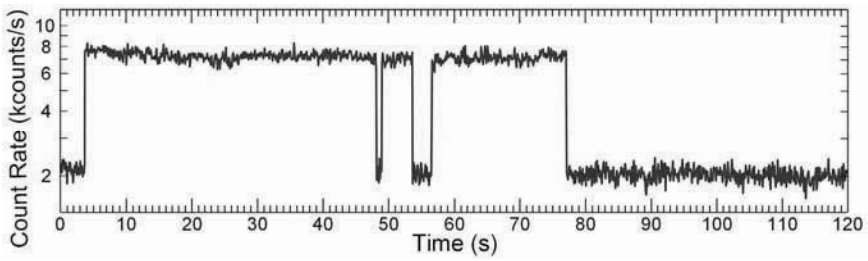

Figure 4. PL time trace obtained from a single Si NC embedded in PMMA revealing fluorescence intermittence (blinking) [9].

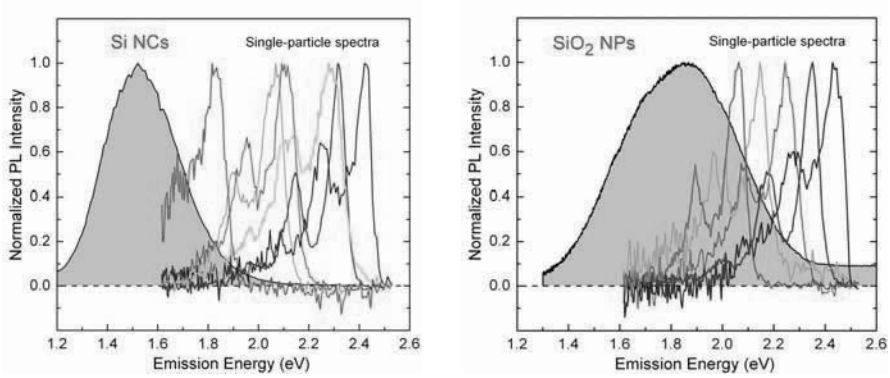

Figure 5. PL spectra of individual Si NCs (left) and SiO_2 NPs (right) are displayed in color. The broad spectra in gray are ensemble spectra taken from the Si and SiO_2 nanopowders, from which the samples for confocal microscopy were prepared [8,9].

PL Spectra

Detailed information on the spectroscopy of individual NPs is obtained by measuring their PL spectra. Using a fast diode laser (τ = 300 ps, ν = 10 MHz, λ = 473 nm) as excitation source, we obtained the PL spectra displayed in Figure 5 as colored curves. The left panel refers to Si NCs [9] while the right panel shows the results for SiO_2 NPs [8]. The broad gray spectra reflect the ensemble spectra measured from the same nanopowders, from which the confocal microscopy samples were prepared.

The single particle spectra are characterized by a zero-phonon line (peak with largest amplitude) and one or two satellite peaks with smaller amplitude at smaller energy. Interestingly, the spectra of Si NCs and SiO_2 NPs resemble each other so closely that no difference can be stated. The energy spacing between the main and satellite peaks varies between 140 and 180 meV. With this information, the satellite peak can be assigned to the excitation of longitudinal optical phonons in SiO_2. For SiO_2 NPs, the coupling with SiO_2 phonons can be easily understood. But the fact that the same pattern is also observed for Si NCs reveals that the PL in these NPs is dominated by the SiO_2 shell surrounding the crystalline Si core. In an earlier study on single Si NCs [6], this observation was interpreted as exciton-phonon coupling supported by charge carriers trapped at the interface. The fact that the Si NC spectra are identical with those of SiO_2 queries this interpretation and poses the question whether excitons are involved at all. It could also be that defect centers in the SiO_2 shell were responsible for the photon absorption.

PL Decay Lifetimes

We have also measured excited state lifetimes for single Si NCs and SiO_2 NPs [9]. The corresponding decay curves revealed single exponential decays yielding lifetimes from 1 to 13 ns with a maximum of the lifetime distribution at 4 ns. Analyzing 156

individual Si NCs and 43 SiO_2 NPs, no difference was found as far as the shape and slope of the decay curves are concerned. In addition, by using band pass filters in the fluorescence signal beam, we were able to measure the lifetimes for different emission wavelengths. Interestingly, the same lifetime was observed for all emission wavelengths monitored [9]. This observation demonstrates that there is no phonon-assisted effect.

DISCUSSION

We have performed a comparative study of the PL properties of single Si NCs and SiO_2 NPs using confocal laser scanning microscopy. The single particle character is evidenced by the following observations: (1) Using azimuthally polarized laser beams, the orientation of the transition dipole moment of single nanoparticles could be visualized. (2) PL time traces show the switching between ON and OFF states, characteristic for fluorescence intermittence in single nanoparticles. (3) PL spectra reveal narrow zero-phonon lines (< 100 meV) and well-separated phonon bands. Finally (4), in a semi-logarithmic representation, the measured decay curves can be fitted by straight lines, indicating that the excited state can be associated with a single lifetime.

In what follows, we will discuss the implications of the present study on the question whether the PL of the Si NCs is governed by quantum confinement (QC) or defect centers (DCs). The fluorescence study on single Si NCs using higher-order laser modes reveals that the transition dipole moment (TDM) for excitation is linear. In contrast, for exciton creation in spherical or nearly spherical semiconductor quantum dots, we would expect a 2-dimensional or 3-dimensional transition dipole moment [10]. Since this is not the case we can conclude that the PL results from another mechanism than recombination of charge carriers in a QC system. Although, in most cases, the TDM stays rather stable, we sometimes observe a sudden flipping of the TDM which is also not compatible with the QC picture. In contrast, TDM flipping can be understood if defect centers are responsible for the PL as it is very likely that several DCs exist in the shell of the same particle and may contribute to the PL. TDM flipping can then be explained by charge fluctuations in the environment of the NP affecting the energy levels of the DCs and thus favoring the activation of different DCs depending on the situation.

The typical PL spectrum observed in this study is composed of a zero-phonon line and up to two phonon bands at lower energy which can be associated with the excitation of longitudinal optical phonons in the SiO_2 shell. In the earlier study on single Si NCs [6], this observation was interpreted as exciton-phonon coupling supported by charge carriers trapped at the interface. The fact that identical PL spectra are observed from single SiO_2 NPs [8] queries this interpretation and suggests that DCs in the SiO_2 shell are responsible for the photon absorption.

In comparing Si NC and SiO_2 NP results, we found many close agreements: (1) The experiments visualizing the TDM for excitation deliver exactly the same results. (2) No difference is found as far as the activation of dynamical processes (TDM flipping, fluorescence intermittence, and bleaching) are concerned. (3) The shape of the spectra is identical; both are composed of a zero-phonon line and two phonon bands associ-

ated with the excitation of phonons in SiO_2. Finally (4), both Si NCs and SiO_2 NPs are characterized by the same rather short lifetime of approximately 4 ns.

Summarizing the experimental results, we found evidence that the PL of single Si NCs as prepared for this study is governed by defect luminescence. This conclusion is based on the close resemblance of Si NC and SiO_2 NP spectra, on the TDM images, and on the short lifetimes around 4 ns, incompatible with radiative recombination of charge carriers in a quantum-confined system. These findings, however, should not be generalized since the present technique is better adapted to processes with short lifetimes and may therefore overlook PL processes with long timescale. Thus, for example, the quantum-confined nature of the PL of larger size-selected Si NCs [4] is not questioned. In the near future, efforts should be undertaken to improve the signal-to-noise level in order to search for single Si NCs revealing QC PL with long lifetime.

ACKNOWLEDGMENTS

This work was carried out within the European cooperation NANOLUM. F. H. and T. S. are grateful for support by the Max Planck Society and the European Commission (Specific Targeted Project: BONSAI, Contract No. LSHB-CT-2006-037639). A. I. C., A. M. C., and A. J. M. acknowledge financial support by the Forschungsschwerpunktprogramm Baden-Württemberg and from the European Commission through the Human Potential Program (Marie-Curie Research Training Network NANOMATCH, Contract No. MRTN-CT-2006-035884).

REFERENCES

1. L. T. Canham, *Appl. Phys. Lett.* **57**, 1046-1048 (1990).
2. A. G. Cullis, L. T. Canham, and P. D. J. Calcott, *J. Appl. Phys.* **82**, 909-965 (1997).
3. S. Godefroo, M. Hayne, M. Jivanescu, A. Stesmans, M. Zacharias, O. I. Lebedev, G. van Tendeloo, and V. V. Moshchalkov, *Nature Nanotech.* **3**, 174-178 (2008).
4. G. Ledoux, J. Gong, F. Huisken, O. Guillois, and C. Reynaud, *Appl. Phys. Lett.* **80**, 4834-4836 (2002).
5. M. V. Wolkin, J. Jorne, P. M. Fauchet, G. Allan, and C. Delerue, *Phys. Rev. Lett.* **82**, 197-200 (1999).
6. J. Martin, F. Cichos, F. Huisken, and C. von Borczyskowski, *Nano Lett.* **8**, 656-660 (2008).
7. A. Colder, F. Huisken, E. Trave, G. Ledoux, O. Guillois, C. Reynaud, H. Hofmeister, and E. Pippel, *Nanotechnology* **15**, L1-L4 (2004).
8. A. M. Chizhik, A. I. Chizhik, R. Gutbrod, A. J. Meixner, T. Schmidt, J. Sommerfeld, and F. Huisken, *Nano Lett.* **9**, 3239-3244 (2009).
9. T. Schmidt, A. I. Chizhik, A. M. Chizhik, A. J. Meixner, and F. Huisken "Luminescence characteristics of individual Si nanocrystals studied by confocal microscopy" *Nano Lett.* submitted for publication (May 2010).
10. S. A. Empedocles, R. Neuhauser, M. G. Bawendi, *Nature* **339**, 126-129 (1999).

Chapter 8

Dynamical effects of defect photoluminescence from single SiO_2 and Si nanoparticles

In this chapter, we discuss details of fluorescence dynamics of single SiO_2 NPs and single Si NCs. A redistribution of energy of defect states caused by charge fluctuations in the surrounding of the embedded NP is investigated.

This chapter is based on:

Chizhik, A.I., Schmidt, T., Chizhik, A.M., Huisken, F., Meixner, A.J. "Dynamical effects of defect photoluminescence from single SiO_2 and Si nanoparticles" *Physics Procedia* **2011**, *13*, 28-32.

Available online at www.sciencedirect.com

ScienceDirect

Physics Procedia 13 (2011) 28–32

Physics Procedia

www.elsevier.com/locate/procedia

The 17th International Conference on Dynamical Processes in Excited States of Solids

Dynamical effects of defect photoluminescence from single SiO_2 and Si nanoparticles

Alexey I. Chizhik[a], Torsten Schmidt[b], Anna M. Chizhik[a], Friedrich Huisken[b], Alfred J. Meixner[a]*

[a]*Institute of Physical and Theoretical Chemistry, University of Tübingen, Auf der Morgenstelle 18, D-72076 Tübingen, Germany*
[b]*Laboratory Astrophysics Group of the Max Planck Institute for Astronomy, Institute of Solid State Physics, University of Jena, Helmholtzweg 3, D-07743 Jena, Germany*

Abstract

We present results of photoluminescence (PL) studies of single SiO_2 nanoparticles (SiO_2 NPs) and single Si nanocrystals (Si NCs). Single particle spectroscopy reveals almost identical PL spectra for both kinds of nanosized systems. The emission curves exhibit a zero-phonon line and one or two phonon bands, which can be assigned to longitudinal optical phonons in SiO_2. Using cylindrical vector beams for imaging the fluorescence of single particles we show that they possess a linear excitation transition dipole moment (TDM). Furthermore, the single particle fluorescence patterns demonstrate upon continuous excitation dynamical effects such as blinking, bleaching, and flipping of the TDM. The latter is related to a redistribution of defect states caused by charge fluctuations in the surrounding of the embedded NP. Excitation fluorescence images visualize the intermediate state resulting from the TDM flipping.

Keywords: Silicon nanocrystals; Silica nanoparticles; Defect luminescence; Single particle spectroscopy; Electron-phonon coupling; Transition dipole moment.

1. Introduction

Since the first observation of photoluminescence (PL) from porous silicon by Canham et al. [1], silicon-based nanostructures gained an increasing interest for the researchers. Being an outstanding electronic material, it is a poor light emitter due to an indirect bandgap. Improving the interface between silicon electronics and photonics would lead to a new breakthrough in information processing technology, moving towards entirely optical computers [2,3]. In spite of a growing volume of investigations, the PL origin from porous silicon [4] and silicon nanocrystals (Si NCs) embedded in an amorphous SiO_2 shell [5] is still under a long-running debate [6-10]. One possible origin is the radiative recombination of the quantum confined electron-hole pairs (excitons). According to the interpretation

* Corresponding author. Tel.: +49-7071-29-76903; fax: +49-7071-29-5490.
E-mail address: alfred.meixner@uni-tuebingen.de.

1875-3892 © 2011 Published by Elsevier B.V.
doi:10.1016/j.phpro.2011.02.007

of quantum confinement, reducing the size of the core-shell nanoparticle (NP) leads to an increase of the conduction band energy, while the valence band energy decreases. The barrier, standing on the way of tunability of the PL from Si NCs, arises from defects in the SiO_2 structure [11]. With decreasing size of the NP, the defects may appear as inner band gap states and drastically change the optical properties of the particle. Thus, fundamental knowledge of the defect-related PL mechanisms is very important for controlling optical characteristics of the quantum-confined systems. As has been shown in recent investigations, both SiO_2 NPs and Si NCs exhibit defect-based PL [12,13]. In this work we present new results on single nanoparticles PL dynamics.

2. Experimental

Silicon nanocrystals (Si NCs) with diameters between 3 and 10 nm were produced by laser-induced pyrolysis of silane (SiH_4) in a gas flow reactor according to the procedure, described elsewhere [14]. Amorphous SiO_2 NPs were prepared by full oxidation of freshly prepared Si NCs according to the recipe of Colder et al. [16]. Samples for single-particle PL measurements were prepared by spin coating. The polymer poly(methyl methacrylate) (PMMA) was used to immobilize the particles on the sample surface. For recording fluorescence excitation patterns the NPs were excited with an argon ion laser (λ_{exc} = 488 nm). A pulsed diode laser (Picoquant, LDH-P-C-470, λ_{exc} = 473 nm, repetition rate: 10 MHz, pulse width: 300 ps) was used for acquisition of single particle PL spectra and time traces. Further details about the home-built confocal microscope setup and sample preparation for single-particle PL measurements are describe elsewhere [12,13,15].

3. Results and discussion

Fig. 1 shows examples of two PL spectra acquired from one single Si NC (solid curve) and one SiO_2 NP (dashed curve) embedded in a PMMA matrix. The amazing similarity of the curves suggests for both spectra a common origin of the PL. The curves typically reveal two sharp bands. The separation between the peaks lies within the range 140 – 180 meV for all investigated particles [12,13]. Such energy separation is very close to the energy of the longitudinal optical mode of SiO_2 at 156 meV [17]. In some spectra the intensity was sufficient to distinguish a third feature at the red side of the spectrum. It is remarkable that the three bands turned out to be equidistant. This allows us to assign the satellite bands at the low-energy side to phonon- and double-phonon-assisted recombinations, respectively, while the most intensive band is related a to zero-phonon recombination. A large number of measured single particle PL spectra showed that the distribution of the zero-phonon band maxima of both types of NPs covers the range between 1.8 and 2.8 eV. According to Glinka et al. [18] we attribute the observed PL to hydrogen-related species (≡Si-H and ≡Si-OH) on the surface of the nanoparticles.

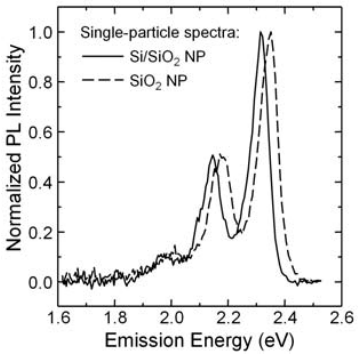

Figure 1. PL spectra of a single Si/SiO_2 core-shell nanoparticles (NP) (solid line) and a SiO_2 nanoparticle (NP) (dashed line) in PMMA matrix. The represented data are averaged over 6 data points.

Recent investigations of the excitation transition dipole moment (TDM) of single SiO_2 NPs using cylindrical vector beams (CVB, also known as higher-order laser modes [12,13,15,19]) revealed the presence of a one-dimensional TDM. Furthermore, we found that the TDM is randomly oriented with respect to the sample

surface. Fig. 2(a) demonstrates an example of an excitation fluorescence image of two individual SiO_2 NPs excited in the focus of a radially polarized laser beam. Simulated patterns, giving the best fit to the experimental (Fig. 2(b),(c)) data allow us to determine the three-dimensional orientation of the TDM. Remarkably, studies of the emission TDM using polarization microscopy [12] revealed that the TDM for excitation and emission have the same orientation. This result suggests that the PL photon arises from the same defect which was excited.

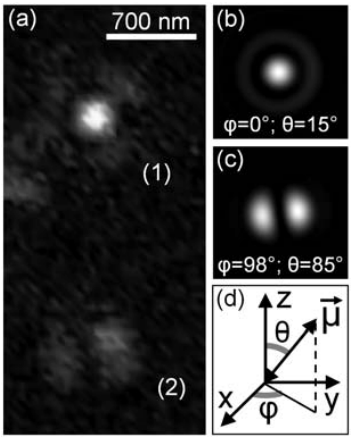

Figure 2. (a) Fluorescence excitation images of two SiO_2 NPs embedded in a PMMA matrix and excited in the focus of a radially polarized laser beam (λ_{exc} = 488 nm). Images (b) and (c) show simulated fluorescence patterns, giving the best fit to the experimental data. Angle values for the TDM orientations are given below the patterns according to the coordinate system (d).

The excitation of a single NP, possessing a linear TDM, by scanning it through the focal region of an azimuthally polarized laser beam (APLB) with doughnut-shaped intensity profile always gives rise to an image consisting of two nearby bright spots of elliptical shape resembling a “coffee bean” [12,13,15]. The projection of the transition dipole moment on the substrate is oriented along the dark gap between the two halves of the “coffee bean”. Fig. 3(a)-(c) shows a series of images, taken one after another and exhibiting the same Si NC immobilized in a PMMA matrix and excited with APLB. The time between two consecutive samplings of the area is 100 s. Images (a) and (c) show bright two-lobe patterns, demonstrating that the NP’s TDM flips from one orientation to another. This phenomenon can be explained by a redistribution of defect states caused by charge fluctuations in the surrounding of the NP such that another defect becomes energetically more favorable.. Image (b) shows an intermediate state without a definite orientation of the TDM. If the energy levels of the defects are very close, a very fast flipping of the TDM can occur, which can be seen in image 3(b). At the same time, as has been observed in the majority of cases [13], the particle, possessing a linear TDM, can exhibit fast switching from one defect to another.

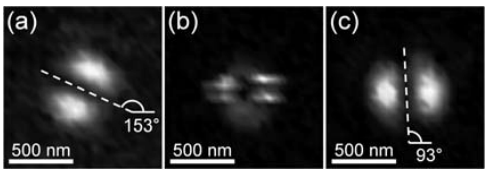

Figure 3. A set of excitation images obtained from one and the same single Si NC embedded in a PMMA matrix. As an azimuthally polarized laser beam was employed, the images reveal the projection of the TDM on the substrate. Images (a) and (c) show that the orientation of the TDM changes by 60°. In image (b), an intermediate state, reflected by the ring-like structure, is observed. It is caused by the overlapping of two “coffee bean” -like patterns arising from the first and last image.

Fig. 4 shows a time trace, acquired from a single SiO_2 NP embedded in PMMA by binning the photon counting events into 100 ms slots. The particle was excited with a linearly polarized Gaussian laser beam (λ_{exc} = 473 nm, repetition rate: 10 MHz, pulse width: 300 ps). The time trace shows two "on" states of the NP associated with an emission intensities near 11000 (active during 23.5 s) and 5500 (active during 5.2 s) counts per second. The background signal of 3500 counts per second originates from some weak fluorescence of the polymer matrix representing the "off" state. Although the curve exhibits two different optically active states, the transition between them occurs through the "off" state, which lasts 0.6 s (i.e., not related to the noise artifact). This shows that the two levels of the signal are not related to the overlap of the PL arising from two NPs, but can be attributed to the transition between different optically active defect-related states within one emitter. Since the particle was excited with the linearly polarized beam, the strong difference between the intensities of the two "on" states can be attributed to the states, possessing a different orientation of the TDM for excitation, and, hence, a different excitation efficiency.

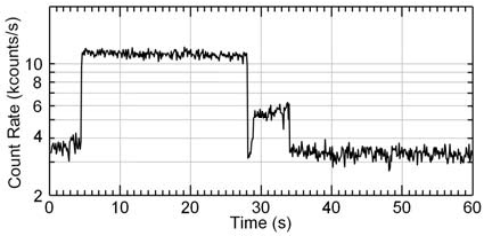

Figure 4. PL time trace obtained from a single SiO_2 NP embedded in PMMA. The NP was excited with a linearly polarized Gaussian laser beam (λ_{exc} = 473 nm). Two "on" states are characterized by count rates of nearly 11 and 5.5 kcounts/s. The background signal of ~3.5 kcounts/s is attributed to the polymer matrix.

4. Conclusions

Comparing single particle PL spectra, we have shown that the emission of SiO_2 NPs and Si NCs originates from defect states related to the silica structure. We observed that both types of the NPs exhibit flipping of the TDM. The phenomenon is related to a redistribution of defect states caused by charge fluctuations in the surrounding of the NP.

Acknowledgements

This work was carried out within the European cooperation NANOLUM. F. H. and T. S. are grateful for support by the Max Planck Society and the European Commission (Specific Targeted Project: BONSAI, Contract No. LSHB-CT-2006-037639). A.I.C., A.M.C. and A.J.M. acknowledge financial support by the Forschungsschwerpunktprogramm Baden-Württemberg and from the European Commission through the Human Potential Program (Marie-Curie Research Training Network NANOMATCH, Contract No. MRTN-CT-2006-035884).

References

[1] L.T. Canham, Appl. Phys. Lett. 57 (1990) 1046-1048.
[2] U. Gösele, Nature Nanotech. 3 (2008) 134-135.
[3] P. Ball, Nature 409 (2001) 974-976.
[4] M.V. Wolkin, J. Jorne, P.M. Fauchet, G. Allan, C. Delerue, Phys. Rev. Lett. 82 (1999) 197-200.
[5] J. Heitmann, F. Müller, M. Zacharias, U. Gösele, Adv. Mater. 17 (2005) 795-803.
[6] Y. Kanemitsu, H. Uto, Y. Masumoto, T. Matsumoto, T.Futagi, H. Mimura, Phys. Rev. B 48 (1993) 2827-2830.
[7] Y. Kanemitsu, T. Ogawa, K. Shiraishi, K. Takeda, Phys.Rev.B 48 (1993) 4883-4886.
[8] D. Kovalev, H. Heckler, G. Polisski, F. Koch, Phys. Stat. Sol. B 215 (1999) 871-932.
[9] F. Iacona, G. Franzo, C. Spinella, J. Appl. Phys. 87 (2000) 1295-1303.
[10] Z. Zhou, L. Brus, R. Friesner, Nano Lett. 3 (2003) 163-167.

[11] J. Martin, F. Cichos, F. Huisken, C. von Borczyskowski, Nano Lett. 8 (2008) 656-660.
[12] A. M. Chizhik, A. I. Chizhik, R. Gutbrod, A. J. Meixner, T. Schmidt, J. Sommerfeld, and F. Huisken, Nano Lett. 9 (2009) 3239-3244.
[13] T. Schmidt, A. I. Chizhik, A. M. Chizhik, A. J. Meixner, F. Huisken, Submitted for publication (October 2010).
[14] F. Huisken, G. Ledoux, O. Guillois, C. Reynaud, Adv. Mater. 14 (2002) 1861-1865.
[15] A.M. Chizhik, T. Schmidt, A.I. Chizhik, F. Huisken, A.J. Meixner, Proc. of SPIE 7393 (2009) 739305/1-11.
[16] A. Colder, F. Huisken, E. Trave, G. Ledoux, O. Guillois, C. Reynaud, H. Hofmeister, E. Pippel, Nanotech. 15 (2004) L1-L4.
[17] F. Gourbilleau, X. Portier, C. Ternon, P. Voivenel, R. Madelon, R. Rizk, Appl. Phys. Lett. 78 (2001) 3058-3060.
[18] Y.D. Glinka, S.-H. Lin, Y.-T. Chen, Appl. Phys. Lett. 75 (1999) 778-780.
[19] L. Novotny, M.R. Beversluis, K.S. Youngworth, T.G. Brown, Phys. Rev. Lett. 86 (2001) 5251-5254.

Chapter 9

Modification of electron-phonon coupling in single SiO_2 nanoparticles with a tunable optical subwavelength micro-resonator

In this chapter, using a tunable optical subwavelength microcavity, we demonstrate controlled modification of the electron-phonon coupling in a single SiO_2 nanoparticle. By varying the distance between the cavity mirrors we change the electromagnetic field mode structure around a single nanoparticle, which results in modification of probability of electron-phonon coupling in the particle. Experimentally, we demonstrate redistribution of the photoluminescence spectrum between zero-phonon and phonon-assisted bands and modification of excited state lifetime of the same individual SiO_2 particle measured at different cavity lengths. Mono-exponential character of the single-particle decay curves shows that zero phonon, phonon- and double phonon-assisted transitions occur from the same energy level but possess different transition probabilities, which are related to the probability of electron-phonon coupling.

This chapter is based on:

Chizhik, A.I., Chizhik, A.M., Schmidt, T., Huisken, F., Meixner, A.J. "Modification of electron-phonon coupling in single SiO_2 nanoparticles with a tunable optical subwavelength micro-resonator" in preparation.

Modification of Electron-Phonon Coupling in Single SiO_2 Nanoparticles with a Tunable Subwavelength Microcavity

Alexey I. Chizhik[1], Anna M. Chizhik[1], Torsten Schmidt[2], Friedrich Huisken[2], Alfred J. Meixner[1*]

[1]*Institute of Physical and Theoretical Chemistry, University of Tübingen, Auf der Morgenstelle 18, D-72076 Tübingen, Germany*
[2]*Laboratory Astrophysics Group of the Max Planck Institute for Astronomy, Institute of Solid State Physics, University of Jena, Helmholtzweg 3, D-07743 Jena, Germany*
**Corresponding author. E-mail address: alfred.meixner@uni-tuebingen.de*

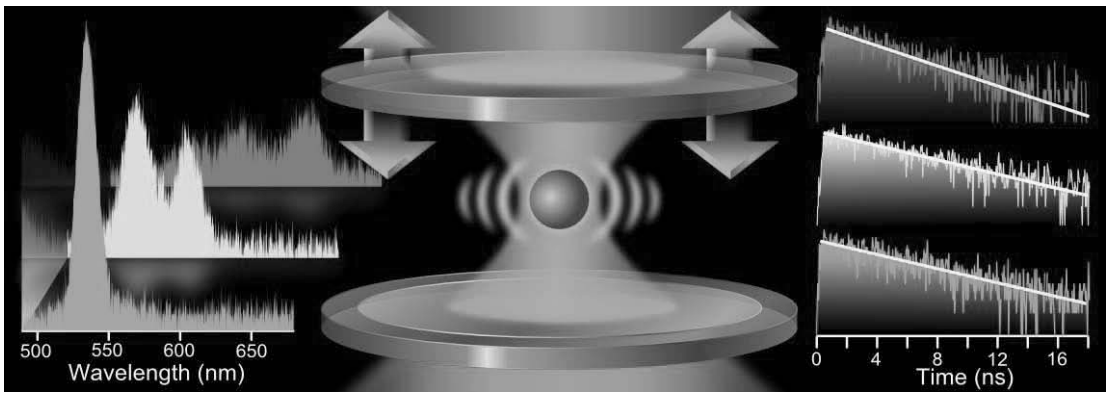

Abstract

Using a tunable optical subwavelength microcavity, we demonstrate controlled modification of the electron-phonon coupling in a single SiO_2 nanoparticle. By varying the distance between the cavity mirrors we change the electromagnetic field mode structure around a single nanoparticle, which results in modification of probability of electron-phonon coupling in the particle. Experimentally, we demonstrate redistribution of the photoluminescence spectrum between zero-phonon and phonon-assisted bands and modification of excited state lifetime of the same individual SiO_2 particle measured at different cavity lengths. Mono-exponential character of the single-particle decay curves shows that zero phonon, phonon- and double phonon-assisted transitions occur from the same energy level but possess different transition probabilities, which are related to the probability of electron-phonon coupling.

Keywords: Defect luminescence; electron-phonon coupling; microcavity; silica nanoparticle; single particle spectroscopy, radiative transitions.

Introduction

Photoluminescence (PL) of nanostructured silicon dioxide (SiO_2) has attracted a great deal of attention for its applications in microelectronics [Wilk-JApplPhys-2001], fabrication of fluorescent quantum dots [Huisken-PhysRevB-2000] and biological labeling [Lu-Nanolett-2007]. In the past decades, significant efforts have been devoted to

understanding fundamental mechanisms of the PL in SiO_2 [O'Reilly-PRB-1983, Kirk-PRB-1988, Glinka-APL-1999, Tohmon-PRB-1989, Munekumi-JApplPhys-1990, Godefroo-Nature, Goesele-Nature]. It has been shown, that defects in a silica bulk structure induce localized states in the band gap of SiO_2 which are possible sources of radiative recombination [Reilly-PRB-1983]. Although details are still unclear, a consensus has emerged that the PL from SiO_2 structures in the visible spectral range can be related to non-bridging oxygen centers [Skuja-1994, Munekuni-JApplPhys-1990], neutral oxygen vacancies [Tohmon-PRB-1989] and hydrogen-related species [Glinka-APL-1999]. Recently it has been shown that PL in single SiO_2 nanoparticles (NPs), which were obtained by full oxidation of silicon nanocrystals [Colder-Nanotech-2004], originates from localized states in the silica structure [SiO_2-Nanolett-2009]. Furthermore, the single particle PL measurements revealed a strong coupling between the electronic transition and a collective vibration in the SiO_2 NP due to a sudden relaxation mechanism involving charges [SiO_2-Nanolett-2009]. In particular, the PL spectra of single SiO_2 NP exhibit, besides a narrow zero-phonon line, one or even two satellite peaks on the lower-energy side, related to the excitation of one or two longitudinal optical (LO_3) phonon quanta in a SiO_2 NP [Goubrilleau-APL-2001] (Fig. 1(a)). As a result, the single SiO_2 NP emits the light in a broad range of wavelengths. One of the techniques which allow one to confine the PL of a quantum emitter to a narrow spectral range is embedding it inside an optical microcavity [Vahala-Nature-2003]. Placing an emitter within a confined geometry modifies its emission properties [Purcell], in particular, spectral and spatial distribution of the radiation. According to Fermi's golden rule, the density of modes of the electromagnetic field inside a cavity is changed with respect to the free space, and hence, the coupling of the dipole transition of an emitter to this field. Recently, extensive experimental studies of the cavity-controlled PL have been conducted for single quantum dots [Santori-Nature-2002, Englund-PRL-2005, Huisken-MatSciEng-2003, Huisken-JApplPhys-2004, Kazes-AdvMat-2002], molecules [Steiner-CPC-2005, Our-PRL-2009, Baer-ABC] and atoms [Aoki-2006-Nature].

In the present Letter we demonstrate the modification of the electron-phonon coupling in a single SiO_2 NP, embedded in a tunable subwavelength microcavity. By varying the distance between the cavity mirrors we change the electromagnetic field mode structure around the single NP, which results in a modification of the probability of electron-phonon coupling. This allows us for the first time to demonstrate a redistribution of the PL spectrum and modification of the excited state lifetime of the same individual SiO_2 NP measured at different cavity lengths. These findings is a new step forward in experimental quantum electrodynamics on individual emitters and are of fundamental importance for phonon-assisted chemical reactions [Schuster-2004-JACS, Utz-2008-Science], electron-defect scattering in plasmonic nanostructures [Link-1999-JPhysChemB] or in recombination processes where the assistance of a phonon changes the rate of the electron-hole recombination [Alivisatos-1996-JPhysChem] as well as for the development of a single SiO_2 particle tunable laser.

Results and discussions

Fig. 2(a) shows a schematic of the experimental setup with the tunable microcavity. The cavity mirrors were fabricated by placing thin silver layers (50 nm bottom and 100 nm

top) on a glass substrate [Steiner-CPC-2005, Chizhik-SPIEcavity-2009]. The bottom semi-transparent silver mirror was covered with a 30 nm SiO_2 layer which acts as a spacer between the NPs and the silver surface. The cavity length was adjusted with a piezo actuator and the width value was determined by measuring the white light transmission spectrum [Steiner-CPC-2005, Chizhik-PRL-2009, Chizhik-SPIEcavity-2009]. Between the top of the polymer layer and the top cavity mirror was air. SiO_2 NPs were obtained according to the recipe of Colder et al. [Colder-Nanotech-2004] by full oxidation of silicon nanocrystals, freshly synthesized by CO_2 laser pyrolysis [Huisken-AdvMat-2002, Huisken-ApplSurfSci-2000] and embedded in very low concentration into a 50 – 60 nm thick polymer film (as determined by atomic force microscopy, AFM). High-resolution transmission electron microscopy images, shown in fig. 2(c), reveal the complete amorphous structure of the as-synthesized silica nanopowder. Further details on the sample preparation and the confocal microscopy setup can be found in the experimental section.

The design of our tunable micro-resonator gives a cavity quality factor of Q=45, which allows us to fit an individual band of the single SiO_2 NP PL spectrum within a mode of the cavity. After selecting a single SiO_2 NP, we acquired PL spectra for the same particle at different cavity lengths. For each acquisition, the cavity length was adjusted in resonance with one of the spectral bands of the single particle spectrum. Since the cavity length is reduced down to the range of one half of the emission wavelength, there is only one resonator mode which overlaps with the emission spectrum of the particle. Therefore, the enclosed quantum object is forced to emit photons within a narrowed energy distribution, determined by the $\lambda/2$-resonator mode. This allows us to select those transitions, where the PL will mostly occur (Fig. 1(b)), which leads to a modification of the emission spectrum of a single SiO_2 NP. In total, we collected spectra for 14 particles. Fig. 3 shows three spectra (red curves) of the same individual SiO_2 NP, recorded at different cavity lengths. The spectra exhibit a clear modification upon tuning the local cavity mode. In particular, fig. 3(a) demonstrates an enhancement of the zero-phonon band, while the phonon-assisted transitions are inhibited. Adjusting the cavity mode in resonance with the spectral bands, originating from phonon-assisted transitions (fig. 3 (b) and (c)) results in their enhancement and suppression of the zero-phonon band. It should be noted, that the redistribution of the spectrum is exclusively determined by the coupling of the SiO_2 NP to the cavity mode, while plasmonic effects do not play a significant role, since the particles are separated from the surface of the bottom mirror with a spacer layer. For better comparison of the measured single particle spectra and a free space spectrum, the latter was shifted along the wavelength axis to fit the maxima of the cavity-controlled spectra. The position of the single SiO_2 NP PL spectrum in free space depends not only on the type of the defect, but also on its local environment in the SiO_2 structure, which can vary from one particle to another. Therefore, as has been recently observed [SiO_2-Nanolett-2009], the single SiO_2 NP PL exhibits a spectral shift, individual for each particle. The free space spectrum was arbitrarily normalized to obtain an equal area for the zero-phonon line with the spectrum shown in figure 3(b).

Whereas the long-wavelength side of all the spectra is determined by the cavity mode, spectra shown in fig. 3(b) and (c) feature blue-shifted emission with respect to the resonance wavelength. As the high NA objective lens was used for efficient light collection, some part of the off-axis emission is also collected, giving rise to a broadening

of the spectrum. This is a feature of the Fabry-Perot type microresonator [Our-SPIE-cavity], used in this study. A direct suppression of the off-axis emission requires a three-dimensional confinement, e.g., in photonic crystals [Campbell-Nature-2000].
Figures 3(d)-(f) show the photographs of the SiO_2 NPs ensemble PL taken through the eyepiece of the microscope at the respective cavity white light transmission profiles, visualizing the spectral modifications, shown in figures 3(a)-(c). It should be noted, that for this purpose the concentration of the NPs has been significantly increased with respect to the single particle level until an observation of the PL with the unaided eye was possible.

The spectral distribution of the PL of a single particle is related to its excited state lifetime, which can be acquired by time correlated single photon counting of an emitter. Let us consider transition of the electron from an initial excited state to a ground state of a quantum emitter. The number of the transition events dN from an initial level 1 to a final level 0 expected to occur within a time interval dt is proportional to the instantaneous population of the upper level N_1 and the transition probability λ_{10} [Istratov-RevScInst-1999, Enderlain-OptComm-1997]:

$$\frac{dN(t)}{dt} = -\lambda_{10} N_1 \qquad (1)$$

If the transition occurs from a level m to n cascading levels, Equation (1) can be rewritten as:

$$\frac{dN(t)}{dt} = -\sum_{i=1}^{n} \lambda_{mi} N_m \quad (2)$$

where N_m is the instantaneous population of the initial level and λ_i is the probability of the transition from a level m to a level i. The solution of Equation (2) is an exponential decay of the form:

$$N(t) = A \exp\left(-\sum_{i=1}^{n} \lambda t \right) + B \qquad (3)$$

Such monoexponential transients are typical for the PL of a single organic dye molecule, where different vibronic transitions occur from the lowest excited state. The situation becomes more complicated if we consider a scheme shown in Figure 1(a), where the transition may occur from different initial levels to a single ground level. Let us denote the instantaneous populations of the upper levels as N_1, N_2 and N_3 and respective transition probabilities as λ_{10}, λ_{20} and λ_{30}. Then we come to the following form of Equation (1):

$$\frac{dN_1(t)}{dt} + \frac{dN_2(t)}{dt} + \frac{dN_3(t)}{dt} = -\lambda_{10} N_1 - \lambda_{20} N_2 - \lambda_{30} N_3 \qquad (4)$$

which generally results in a multiexponential decay. Along with the single SiO_2 particle PL spectra we have recorded decay curves from the same individual NP which was used for measurements of the spectra. Figures 3(g)-(i) show the single particle transients acquired at the same cavity lengths as were selected for measurements of spectra (figures 3(a)-(c), respectively). The red curves indicated in the graphs represent the result of fitting the experimental data by a single-exponential decay function, yielding the excited state lifetime of the NP. We employed a bootstrap algorithm [Efron] for estimating the mean square deviation of the fitted lifetime obtained for each of the three cavity widths. Fitting 100 decay curves obtained by random selection of one of each ten points from the measured decay curve results in a probability density plot, shown in the column graphs in Figure 4(a)-(c) for the decays D1, D2 and D3, respectively. The distributions could be well fitted by a single Gaussian function, giving the mean square deviation of the single-particle lifetime values, which vary from 0.1 (decay curve D2) to 0.15 ns (decay curve D3).

The quality of the single-exponential fit has to be compared with fitting by higher orders of exponential decay. Figure 5 shows a plot of the relative residual obtained upon fitting the experimental data versus the order of the exponential decay used for the fitting procedure. For better comparison of the obtained values the relative residual function R_i is given by the following expression:

$$R_i = \frac{|D - F_1|}{|D - F_i|} * 100\% \qquad (5)$$

where i is the order of exponential fitting function, D is the experimental decay curve and F_i is the fitting function, respectively. According to this formula the residual in case of the single-exponential fit is equal to 100%, while the residuals obtained by the fits of higher orders are represented as its percentage. As depicted in Figure 5, the residuals, obtained upon fitting the experimental data with an exponential decay of second and third order turned out to be equal and varied between 98,0% and 99.9%. Thus fitting the measured single SiO_2 NP transients with exponential functions of orders higher than two does not decrease the residual. In other words, the quantum system does not exhibit more than two processes running on different time scales. The difference between the residuals, obtained upon fitting the experimental curves with exponents of first and second order of exponents does not exceed 2% and equals to 0.01% for the curve D2, which exhibits the highest signal to noise ratio. Hence, the quality of both fits is actually identical. This allows us to conclude that depopulation of all three levels of the quantum system at one particular cavity mode can be described by the same single-exponential function. Therefore, the excited-state lifetime for all three levels L_1, L_2 and L_3 is the same. According to formula (4), this means, that the instantaneous populations N_1, N_2 and N_3 are equal and related to the same energy level. Since recombinations P_I and P_{II} denote phonon-assisted recombinations (Figure 1(a)), they can be considered to occur from the level L_1 possessing a common instantaneous population N_1, while respective transition probabilities λ_{20} and λ_{30} describe the probability of electron-phonon and electron-double-phonon coupling.

In free space, different values of λ_{10}, λ_{20} and λ_{30} determine different intensities of the zero-phonon, phonon-assisted and double phonon-assisted band of the single SiO_2 NP

spectrum. However, when the particle is embedded in the microcavity, the transition probabilities, and hence, probability of the electron-phonon coupling is modified, which results in variation of single particle fluorescence lifetime and spectral distribution of the emission.

In summary, by placing the single SiO_2 NP in the tunable subwavelength microcavity we modified the probability of electron-phonon coupling in the particle by varying the cavity mode structure. Experimentally, we demonstrated a redistribution of the PL spectrum and modification of excited state lifetime of the same individual SiO_2 NP at different cavity lengths. Moreover, all measured decay curves could be well fitted by a single-exponential function, which proves that zero-phonon, phonon- and double phonon-assisted transitions occur from the same energy level but possess different transition probabilities, which are related to the probability of electron-phonon coupling. Modification of the electron-phonon coupling can be used for applications, where the control of the electron-phonon coupling is required, e.g. phonon-assisted chemical reactions [Schuster-2004-JACS, Utz-2008-Science], electron-defect scattering in plasmonic nanostructures [Link-1999-JPhysChemB] or in recombination processes where the assistance of a phonon modifies the rate of the electron-hole recombination [Alivisatos-1996-JPhysChem]. Modification of single-particle PL spectrum can be considered as a new step toward a single SiO_2 particle tunable laser, which can become an alternative way towards silicon optoelectronics [Ball-2001-Nature]. Combining the crystalline silicon, which possesses the exceptional electronic properties but is a poor light emitter due to an indirect band structure, with SiO_2 structure can allow for converting the electronic signal from silicon chip to the light and back.

Acknowledgements

This work was carried out within the European cooperation NANOLUM. F. H. and T. S. are grateful for support by the Max Planck Society and the European Commission (Specific Targeted Project: BONSAI, Contract No. LSHB-CT-2006- 037639). Financial support by the Forschungsschwerpunktprogramm Baden-Württemberg is also acknowledged.

Experimental Section (Goes to Supporting Information)

Cavity preparation: The bottom silver mirror and silica layer were prepared by vapor deposition onto commercially available and cleaned microscope glass coverslides (thickness 170 μm) using an electron beam source (EB3, Edwards) under high-vacuum conditions (≈ 10^{-6} mbar). The top silver layer was prepared by vapor deposition of silver on the surface of a plan-convex lens (focal length of 150 mm) under the same conditions. Film thickness was monitored during vapor deposition using an oscillating quartz unit (FTM7, Edwards) and verified by AFM measurements. The mirrors were fixed in a home-built aluminum holder, equipped with the piezo actuators (PSt 150/3.5×3.5/20, Piezomechanik GmbH) for adjusting cavity height. The white light transmission profiles acquired with a spectrograph (SpectraPro 300i, Acton Research) in combination with a CCD camera (LNCCD-1340/100-EB/1, Princeton Instruments)

Sample preparation: A small amount of the processed silica nanopowder was dispersed at subnanomolar concentration in toluene and then mixed with a 1% solution of poly(methyl methacrylate) (PMMA, $[C_5O_2H_8]_n$). A droplet (10 µl) of this mixture was spin coated on the SiO_2 surface covering the bottom mirror (rotation speed 8000 r/min). To obtain a reference spectrum of the PMMA-embedded SiO_2 NPs, a free space sample was prepared by spin coating a droplet of the same polymer-SiO_2-toluene mixture onto a glass cover slide. For all the single particle measurements, the background PL which includes the signal from the polymer and SiO_2 spacer layer was subtracted from the total signal.

All optical measurements were performed with a home-built confocal scanning microscope based on a Zeiss Axiovert 135 TV with fluorescence lifetime imaging extension (Picoharp 300, Picoquant GmbH, Berlin, Germany). Laser focusing and fluorescence light detection were done with the same high numerical aperture (NA) objective lens (Plan-Neofluar, 100×/N.A. = 1.25 oil immersion, Zeiss). Excitation light and fluorescence light were separated by a dichroic beam splitter (Zeiss FT500). For sample scanning, a feedback-controlled sample stage (PI, E-710.3CD) with nanometer positioning precision was employed. Fluorescence excitation was done with the light of a 473 nm pulsed diode laser (LDH-P-C-470, Picoquant GmbH, Berlin, Germany). Back-scattered excitation light was blocked with a long-pass filter (Semrock Razor Edge LP02-473RU-25). Fluorescence spectra were acquired with a spectrograph (SpectraPro 300i, Acton Research) in combination with a CCD camera (LNCCD- 1340/100-EB/1, Princeton Instruments). For each spectral measurement, the cavity length was adjusted via a defined voltage applied to the piezo actuator. For single-particle fluorescence lifetime imaging collected light was focused onto the active area of a spectrally integrating avalanche photo diode (APD) (SPCM 200, Perkin Elmer). Data acquisition was accomplished with a commercially available software package (SymPhoTime, Picoquant GmbH, Berlin, Germany).

References

[Wilk JApplPhys 2001] Wilk, G. D.; Wallace, R. M.; Anthony, J. M. *J. Appl. Phys.* **2001,** *89*, 5243-5275.

[Huisken PhysRevB 2000] Ledoux, G.; Guillois, O.; Porterat, D.; Reynaud, C.; Huisken, F.; Kohn, B.; Paillard, V. *Phys. Rev. B* **2000,** *62,* 15942-15951.

[Lu Nanolett 2007] Lu, C.-W.; Hung,Y.; Hsiao, J.-K.; Yao, M.; Chung, T.-H.; Lin,Y.-S.; Wu, S.-H.; Hsu, S.-C.; Liu, H.-M.; Mou, C.-Y.; Yang, C.-S. Huang, D.-M.; Chen, Y.-C. *Nano Lett.* **2007**, *7*, 149-154.

[Cullis 1997 JApplPhys] Cullis, A. G.; Canham, L. T.; Calcott, P. D. J. *J. Appl. Phys.* **1997**, *82*, 909-965.

[Godefroo Nature] Godefroo, S.; Hayne, M.; Jivanescu, M.; Stesmans, A.; Zacharias, M.; Lebedev, O. I.; Van Tendeloo, G.; Moshchalkov, V. V. *Nat. Nanotechnol.* **2008**, *3*, 174-178.

[Goesele Nature] Gösele, U. *Nat. Nanotechnol.* **2008**, *3*, 134-135.

[O'Reilly PRB 1983] O'Reilly, E.P.; Robertson, J. *Phys. Rev. B* **1983**, *27*, 3780-3795.

[Kirk PRB 1988] Kirk, C.T. *Phys. Rev. B* **1988**, *38*, 1255-1273.

[Glinka APL 1999] Glinka, Y. D.; Lin, S.-H.; Chen, Y.-T. *Appl. Phys. Lett.* **1999**, *75*, 778-780.

[Tohmon PRB 1989] Tohmon, R.; Mizuno, H.; Ohki, Y.; Sasagane, K.; Nagasawa, K.; Hama, Y. *Phys. Rev. B* **1989**, *39*, 1337-1345.

[Kamenitsu PRB 1993] Kanemitsu, Y.; Ogawa, T.; Shiraishi, K.; Takeda, K. *Phys. Rev. B* **1993**, *48*, 4883-4886.

[Skuja 1994] Skuja, L. *J. Non-Cryst. Solids* **1998**, *239*, 16-48.

[Munekuni J Appl Phys 1990] Munekuni, S.; Yamanaka, T.; Shimogaichi, Y.; Tohmon, R.; Ohki, Y.; Nagasawa, K.; Hama, Y. *J. Appl. Phys.* **1990**, *68*, 1212-1217.

[Colder Nanotech 2004] Colder, A.; Huisken, F.; Trave, E.; Ledoux, G.; Guillois, O.; Reynaud, C.; Hofmeister, H.; Pippel, E. *Nanotech.* **2004**, *15*, L1-L4.

[SiO_2 Nanolett 2009] Chizhik, A. M.; Chizhik, A. I.; Gutbrod, R.; Meixner, A. J.; Schmidt, T.; Sommerfeld, J.; Huisken, F. *Nano Lett.* **2009**, *9*, 3239-

[Goubrilleau APL 2001] Gourbilleau, F.; Portier, X.; Ternon, C.; Voivenel, P.; Madelon, R.; Rizk, R. *Appl. Phys. Lett.* **2001**, *78*, 3058-3060.

[Vahala Nature 2003] Vahala, K. J. *Nature* **2003**, *424*, 839-.

[Purcell] Purcell, E. M. *Phys. Rev.* **1946**, *69*, 681.

[Santori Nature 2002] Santori, C.; Fattal, D.; Vuckovic, J.; Solomon, G. S.; Yamamoto, Y. *Nature* **2002**, *419*, 594-597.

[Englund PRL 2005] Englund, D.; Fattal, D.; Waks, E.; Solomon, G.; Zhang, B.; Nakaoka, T.; Arakawa, T.; Yamamoto, Y.; Vuckovic, J. *Phys. Rev. Lett.* **2005**, *95*, 0139041-4.

[Huisken MatSciEng 2003] Amans, D.; Callard, S.; Gagnaire, A.; Joseph, J.; Ledoux, G.; Huisken, F. *Mater. Sci. Eng., B* **2003,** *101*, 305-308.

[Huisken JApplPhys 2004] Amans, D.; Callard, S.; Gagnaire, A, Joseph, J.; Huisken, F.; Ledoux, G. *J. Appl. Phys.* **2004**, *95*, 5010-5013.

[Kazes AdvMat 2002] Kazes M.; Lewis, D. Y.; Ebenstein, Y.; Mokari, T.; Banin U. *Adv. Mater.* **2002,** *14*, 317-321.

[Steiner CPC 2005] Steiner, M.; Schleifenbaum, F.; Stupperich, C.; Failla, A.V.; Hartschuh, A.; Meixner, A.J. *Chem. Phys. Chem.* **2005,** *6*, 2190-.
[Our PRL 2009] Chizhik, A.; Schleifenbaum, F.; Gutbrod, R.; Chizhik, A.; Khoptyar, D.; Meixner, A. J. *Phys. Rev. Lett.* **2009**, *102*, 073002-1.
[Our Cavity Submitted] Chizhik, A. I.; Chizhik, A. M.; Khoptyar, D.; Bär, S.; Meixner, A. J.; Enderlein , J. Submitted.
[Baer ABC 2010] Baer, S.; Chizhik, A.; Gutbrod, R.; Schleifenbaum, F.; Chizhik, A.; Meixner, A.J. *Anal. Bioanal. Chem.* **2010**, *396*, 3-.
[Aoki 2006 Nature] Aoki, T.; Dayan, B.; Wilcut, E.; Bowen, W.P.; Parkins, A.S.; Kippenberg, T. J.; Vahala, K. J.; Kimble, H. J. *Nature* **2006**, *443*, 671-674.
[Huisken AdvMat 2002] Huisken, F.; Ledoux, G.; Guillois, O.; Reynaud, C. *Adv. Mater.* **2002**, *14*, 1861-1865.
[Huisken ApplSurfSci 2000] Huisken, F.; Hofmeister, H.; Kohn, B.; Laguna, M. A.; Paillard, V. *Appl. Surf. Sci.* **2000**, *154*, 305-313.
[Our SPIE cavity] Chizhik, A.; Gutbrod, R.; Chizhik, A.; Baer, S.; Meixner, A. *SPIE Proc.* **2009,** *7396*, 73960F-1-9.
[Campbell Nature 2000] Campbell, M.; Sharp, D. N.; Harrison, M. T.; Denning, R. G.; Turberfield, A. J. *Nature* **2000**, *404*, 53-56.
[Enderlein OptComm 1997] Enderlein, J.; Erdmann, R. *Opt. Comm.* **1997**, *134*, 371-378.
[Istratov RevSciInstrum 1999] Istratov, A. A.; Vyvenko, O. F. *Rev. Sci. Instrum.* **1999**, *70*, 1233-1257.
[Efron] Efron, B. *Ann. Statt.* **1979**, *7*, 1-26.
[Schuster-2004-JACS] Liu, C.-S.; Hernandez, R.; Schuster, G. B. *JACS* **2004**, *126*, 2877-2884.
[Utz-2008-Science] Killelea, D. R.; Campbell, V. L.; Shuman, N. S.; Utz A. L. *Science* **2008**, *319*, 790-793.
[Link-1999-JPhysChemB] Link S.; El-Sayed, M. A.; *J. Phys. Chem. B* **1999**, *103*, 8410-8426.
[Alivisatos-1996-JPhysChem] Alivisatos, A.P. *J. Phys. Chem.* **1996**, *100*, 13226-13239.
[Ball-2001-Nature] Ball, P. *Nature* **2001,** *409*, 974-976.

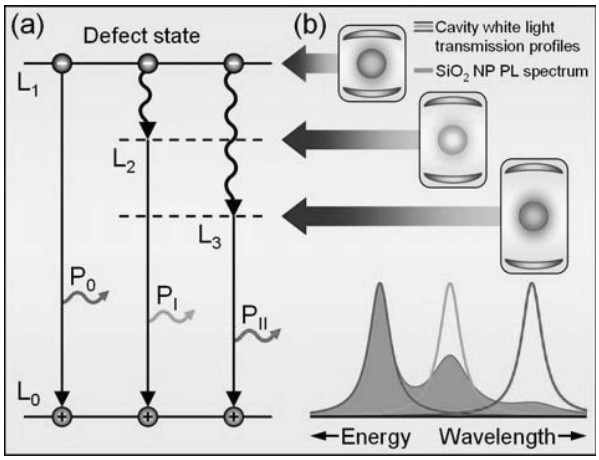

Fig. 1. (a). Diagram of zero-phonon (P_0), phonon- (P_I) and double-phonon- (P_{II}) assisted recombination on a defect state in the band gap of SiO_2. (b). Selecting those cavity modes, which are in resonance with a particular spectral band of the single SiO_2 nanoparticle, we can tune the spectral emission of the particle due to enhancement and suppression of zero-phonon and phonon-assisted transitions.

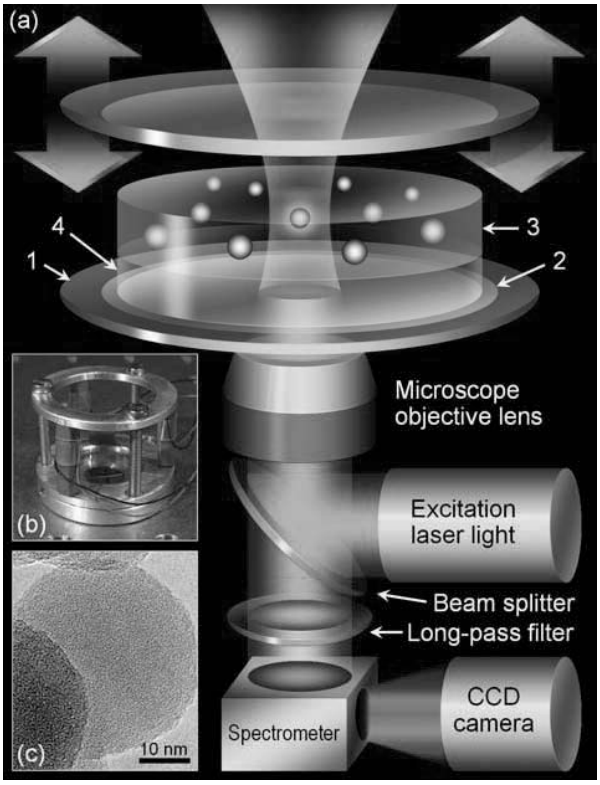

Fig. 2 (a). Scheme of the experimental setup. The tunable cavity consists of: Glass plates (1); silver layers (2); a polymer layer with SiO_2 nanoparticles inside it (3), spin coated on the surface of silica layer (4), acting as a spacer between the particles and the metallic surface. The longitudinal position of the upper mirror is adjusted with nanometer precision by a piezo actuator. The setup is equipped with an excitation laser source (@ 473 nm) and a spectrometer with CCD camera. (b). A photograph of the tunable microcavity. (c). The high-resolution electron microscopy image of a SiO_2 nanoparticle reveals the complete amorphous structure of the particle.

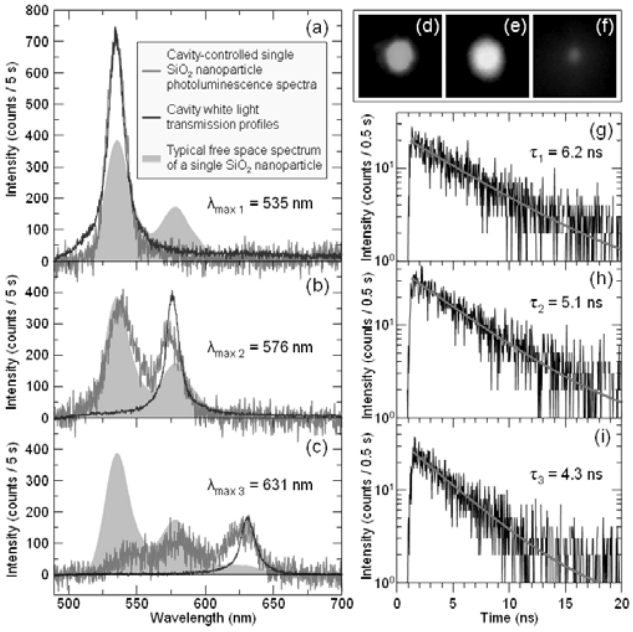

Fig. 3. (a)-(c): Measured photoluminescence spectra (red curve) of a single SiO_2 nanoparticle placed inside the micro-resonator at different cavity lengths. The blue curve shows the cavity white light transmission profile, normalized to the respective emission spectrum. The grey shaded area represents a typical photoluminescence spectrum of a free space single SiO_2 nanoparticle, shifted along the wavelength axis to fit the position of the cavity-controlled spectra. (d)-(f): Photographs of the emission of the SiO_2 particle ensemble at respective cavity lengths taken through the eyepiece of the microscope. (g)-(i): Transients (decay curves denoted in the main text as D1-D3, respectively) of the same single SiO_2 nanoparticle inside the micro-resonator as was used for recording the spectra measured at the. The decay curves (g)-(i) were acquired at the same cavity lengths, which were selected for measurements of single particle spectra shown in figures (a)-(c), respectively. All transients were fitted using a single-exponential decay function (red curves).

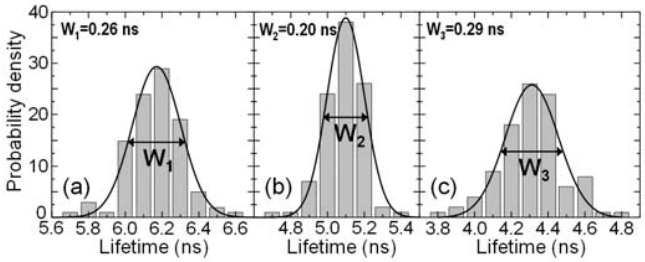

Figure 4. The column graphs (a)-(c) show a probability density distribution obtained using a bootstrap algorithm for the decay curves D_1, D_2 and D_3, respectively. The Gaussian fits (black curves) give a value of the mean square deviation of the single-particle lifetime, which varies from 0.1 (transient D2) to 0.15 ns (transient D3).

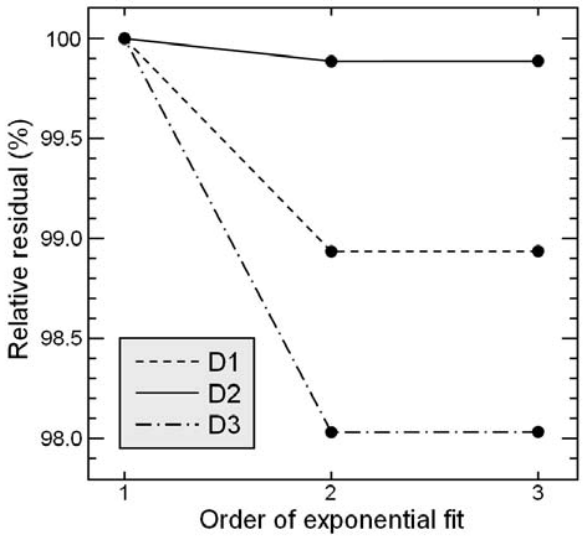

Figure 5. Relative residuals obtained upon fitting the decay curves D1, D2 and D3 with exponential decay functions of the first, second and third order. The relative residual values are determined as: $(|D-F_1|/|D-F_i|)*100\%$, where D and F_i are the experimental decay curve and the fitting exponential decay function of i^{th} order, respectively.

Instrumentation

Confocal microscope

The optical measurements were performed with a modified inverted confocal microscope (Zeiss Axiovert 135 TV) using a high-numerical aperture oil immersion objective (Zeiss Plan Neofluar, 100/NA = 1.3) (Figure S1). The term inverted refers to the fact that the polymer film with the SiO2 NPs was on the opposite side of the cover slip with respect to the objective. An ultrafast laser system (Picoquant, model LDH-P-C470) operating at λ = 473 nm (2.62 eV) and providing pulses at a repetition rate of 10 MHz with a width of 300 ps served as excitation source for the measurements of fluorescence spectra. In order to discriminate against the straylight from the laser, the setup was equipped with a long-wave pass filter having its 50% transmission value at 510 nm. Fluorescence spectra were acquired with a spectrograph (Acton Research SpectraPro 300i) equipped with a CCD camera (Princeton Instruments, model LNCCD-1340/100-EB/1).

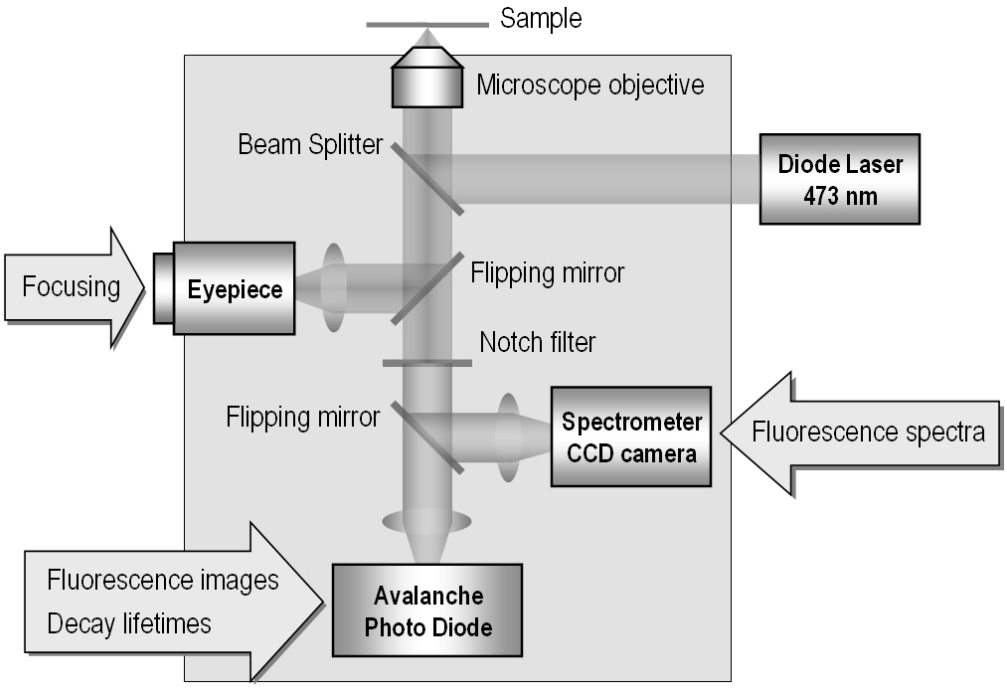

Figure S1. Schematic diagram of the experimental setup.

Preparation of cavity

The bottom silver mirror and silica layer were prepared by vapor deposition onto commercially available and cleaned microscope glass coverslides (thickness 170 µm) using an electron beam source (EB3, Edwards) under high-vacuum conditions (≈ 10^{-6} mbar). The top silver layer was prepared by vapor deposition of silver on the surface of a plan-convex lens (focal length of 150 mm) under the same conditions. Film thickness was monitored during vapor deposition using an oscillating quartz unit (FTM7, Edwards) and verified by atomic force microscopy (AFM) measurements. The mirrors were fixed in a home-built aluminum holder, equipped with the piezo actuators (PSt 150/3.5×3.5/20, Piezomechanik GmbH) for adjusting cavity height. The mirrors were fixed in a home-built aluminum holder, equipped with piezo actuators (Figure S2).

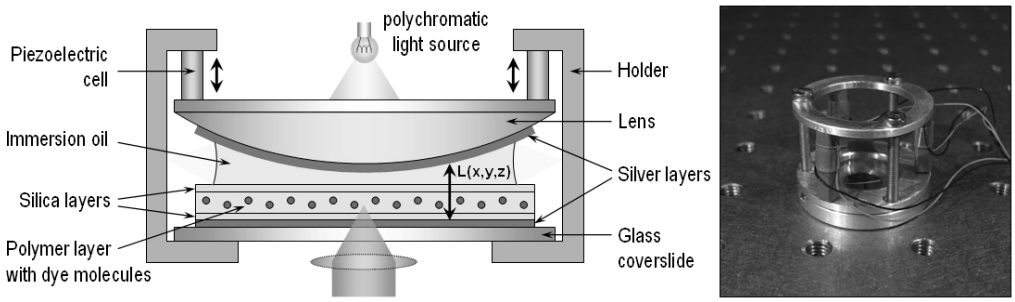

Figure S2. a) Scheme of the experimental setup. The tunable microcavity consists of: 1. Piezoelectric cell, 2. Immersion oil, 3. Silica layers, 4. Polymer (PMMA) layer with dye molecules, 5. Aluminum holder, 6. Lens, 7. Silver layers, 8. Glass coverslide. Inset (right): A photograph of the tunable microcavity.

Controlling the cavity geometry

The spherical shape of the upper mirror allows us to control the optical quality and the tuning capability of the micro-resonator by imaging the cavity white-light transmission patterns, see Figure S3(a). The Newton rings are a result of the different resonator lengths due to the curved surface of the top mirror. The central region of the micro-cavity (i.e., the region of minimum cavity length) remains dark, as no visible light is transmitted there. Moving of the upper cavity mirror leads to a shift of the transmission pattern.

The absolute values L of cavity length, see Figure S3(b), were determined using on-axis white light transmission profiles acquired with a spectrograph (SpectraPro 300i, Acton Research) in combination with a CCD camera (LNCCD-1340/100-EB/1, Princeton Instruments) and fitted by a Lorentzian line-shape function. We calculate the local cavity length (in particular thickness of air layer) by comparing the measured spectrum with a calculated spectrum using standard transfer-matrix method for plane waves passing through a stratified medium.

All fluorescence measurements were performed in the $\lambda/2$ region of the cavity, close to the center of the lens, where the horizontal displacement within the focal spot of our microscope objective (500 nm) results in a cavity length change ΔL of about 1 nm, which is of the order of the surface roughness of our silver mirrors. Therefore, our micro-resonator can be considered as a plane-parallel system.

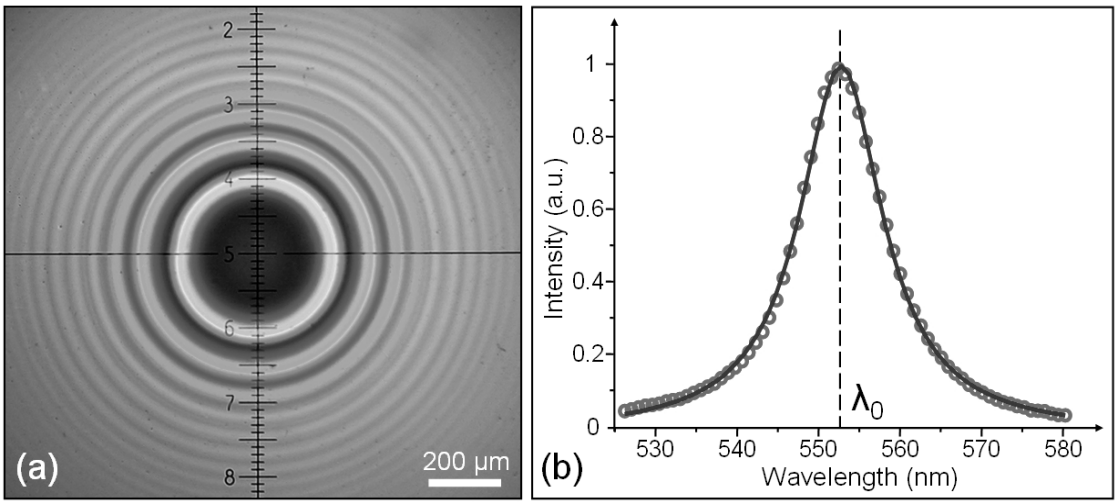

Figure S3. (a) White light transmission patterns (Newton rings) of the micro-cavity. The inner transmission ring shows the first order of interference. (b) Micro-cavity white light transmission spectrum (○) fitted by a Lorentzian function (–).

Preparation a sample with single dye molecule concentration

A 10 µl droplet of a 10^{-10} M solution of the perylene derivative N-(2,6-diisopropylphenyl)-perylene-3,4-dicarboxymid (abbreviated by PI in the following) in dichloromethane was spin-coated on the surface of the silica layer at

a rotation speed of 1000 rpm. After evaporation of the solvent, spatially separated molecules were covered with a layer of poly(methyl-methacrylate) (PMMA, [C5O2H8]*n*). A droplet (10 µl) of a 1% polymer solution in dichloromethane was spin-coated at rotation speed of 8000 rpm to deposit a 70 nm thick polymer film as was subsequently determined by AFM.

Preparation a sample with single SiO_2 nanoparticles

Silicon dioxide NPs of the processed powder were embedded in very low concentration into a thin polymer film covering a quartz cover slide of 170 µm thickness. For this purpose, a small amount of the processed silica nanopowder was dispersed at low concentration in toluene and then mixed with a solution of poly(methyl methacrylate) (PMMA, [C5O2H8]n) or polystyrene (PS, [C8H8]n). A droplet (10 µl) of this mixture was spin-coated on a quartz cover slide to obtain a 50 – 60 nm thick polymer film as determined by atomic force microscopy (AFM). The use of the two polymers PMMA and PS was motivated by the desire to obtain a polar (PMMA) and a non-polar (PS) matrix for the SiO_2 NPs. To make sure that samples don't contain impurities (e.g. dye molecules) a droplet of the polymer without dissolved silica nanopowder was spin-coated onto a quartz cover slide and spectroscopically verified.

Lifetime measurement

Fluorescence lifetime measurements were performed with a home-built confocal scanning microscope based on a Zeiss Axiovert 135 TV with fluorescence lifetime imaging extension (Picoharp 300, Picoquant GmbH, Berlin, Germany). Laser focusing and fluorescence light detection were done with the same objective (Plan-Neofluar, 100×/N.A. = 1.25 oil immersion, Zeiss). Excitation light and fluorescence light were separated by a dichroic beam splitter (Zeiss FT500). For sample scanning, a feedback-controlled sample stage (PI, E-710.3CD) with nanometer positioning precision was employed. Fluorescence excitation was done with the light of a 473 nm pulsed diode laser (LDH-P-C-470, Picoquant GmbH, Berlin, Germany). Within the detection path, a steep edge filter (LP02-473RU-25

Semrock) was used to block back-reflected or elastically scattered light. Collected fluorescence was focused onto the active area of a spectrally integrating avalanche photo diode (APD) (SPCM 200, Perkin Elmer). Data acquisition was accomplished with a commercially available software package (SymPhoTime, Picoquant GmbH, Berlin, Germany). Fluorescence decay curves were fitted using a mono-exponential function, $A \exp(-t/\tau + B)$, convoluted with the instrument response function, which was recorded under comparable experimental conditions. All fluorescence transients were recorded with an integration time of five seconds.

List of the Abbreviations

AFM – atomic force microscopy

APD – avalanche photo diode

APLB – azimuthally polarized laser beam

CCD – charge-coupled device

DC – defect centre

DCM – dichlormethan

HRTEM – high resolution transmission electron microscopy

NA – numerical aperture

NC – nanocrystal

NP – nanoparticle

PI – perylene derivative N-(2,6-diisopropylphenyl)-perylene-3,4-dicarboxymide

PL – photoluminescence

PMMA – poly(methyl-methacrylate)

PS – polystyrene

PVA – polyvinyl alcohol

R6G – rhodamine 6G

TEM – transmission electron microscopy

QC – quantum confinement

QY – quantum yield

Publication list

1. Chizhik, A.I., Schleifenbaum, F., Gutbrod, R., Chizhik, A.M., Khoptyar, D., Meixner, A.J., Enderlein, J. “Tuning the Fluorescence Emission Spectra of a Single Molecule with a Variable Optical Sub-wavelength Metal Microcavity" *Phys. Rev. Lett.* **2009**, *102,* 073002-1-4.

2. Chizhik, A.M., Chizhik, A.I., Gutbrod, R., Meixner, A.J., Schmidt, T., Sommerfeld, J., Huisken, F. “Imaging and Spectroscopy of Defect Luminescence and Electron-Phonon Coupling in Single SiO_2 Nanoparticles” *Nano Lett.* **2009**, *9*, 3239-3244.

3. Chizhik, A.I., Chizhik, A.M., Khoptyar, D., Bär, S.; Meixner A.J. “Excitation isotropy of single CdSe/ZnS nanocrystals” *Nano Lett.* **2011**, *11*, 1131-1135.

4. Chizhik, A.I., Chizhik, A.M., Khoptyar, D., Bär, S., Meixner, A.J., Enderlein, J. “Probing the radiative transition of single molecules with a tunable micro-resonator” *Nano Lett.* **2011**, *11*, 1700-1703.

5. Gutbrod, R., Khoptyar, D., Steiner, M., Chizhik, A.M., Chizhik, A.I., Bär, S., Meixner, A.J. “Three-Dimensional Orientation of Single Molecules in a Tunable Optical lambda/2 Microresonator” *Nano Lett.* **2010**, *10*, 504-508.

6. Chizhik, A.M., Berger, R., Chizhik, A.I., Lyubimtsev, A., Viani, L., Cornil, J., Bär, S., Hanack, M., Hulliger, J., Meixner, A. J., Egelhaaf, H.-J., Gierschner, J. “Polarized Fluorescence from Single Stopcock Molecules at Channel Entrances of an All-Organic Host-Guest Compound” *Chem. Mater.* **2011**, *23*, 1088-1090.

7. Chizhik, A.M., Jäger, R., Chizhik, A.I., Bär, S., Mack, H.-G., Sackrow, M., Stanciu, C., Lyubimtsev, A., Hanack, M., Meixner, A.J. "Optical imaging of

excited-state tautomerization in single molecules" *Phys. Chem. Chem. Phys.* ***2011***, *13*, 1722-1733.

8. Tsyganenko, A.A., Chizhik, A.M., Chizhik, A.I. “A FTIR search for linkage isomerism of CN- ions on oxides and zeolites” *Phys. Chem. Chem. Phys.* **2010,** *12*, 6387-6395.

9. Bär S., Chizhik, A.I., Gutbrod, R., Schleifenbaum, F., Chizhik, A.M., Meixner, A.J. “Microcavities: tailoring the optical properties of single quantum emitters” *Anal. Bioanal. Chem.* **2010**, *396*, 3-14.

10. Gutbrod, R., Chizhik, A.I., Chizhik, A.M., Khoptyar, D., Meixner, A.J. “Longitudinal localization of a fluorescent bead in a tunable microcavity with an accuracy of λ/60” *Opt. Lett.* **2009**, *34*, 629-631.

11. Chizhik, A.I., Chizhik, A.M., Schmidt, T., Huisken, F., Meixner, A.J. “Modification of electron-phonon coupling in single SiO_2 nanoparticles with a tunable optical subwavelength micro-resonator” in preparation.

12. Schmidt, T., Chizhik, A.I., Chizhik, A.M., Meixner, A.J., Huisken, F. “Luminescence Characteristics of Individual Si Nanocrystals Studied by Confocal Microscopy” in preparation.

13. Chizhik, A.I., Schmidt, T., Chizhik, A.M., Huisken, F., Meixner, A.J. “Dynamical effects of defect photoluminescence from single SiO_2 and Si nanoparticles” *Physics Procedia* **2011**, *13*, 28-32.

14. Chizhik, A.M., Schmidt, T., Chizhik, A.I., Huisken, F., Meixner, A.J. “Confocal microscopy and spectroscopy of defect photoluminescence in single SiO_2 nanoparticles” *Proc. SPIE* **2009**, *7393*, 739305. doi:10.1117/12.825288.

15. Chizhik, A.I., Gutbrod, R., Chizhik, A.M., Bär, S., Meixner, A.J. “Controlling the optical properties of single molecules by optical confinement in a tunable microcavity” *Proc. SPIE 2009*, 7396, 73960F. doi:10.1117/12.825278.

16. Chizhik, A.M., Chizhik, A.I., Meixner, A.J., Schmidt, T., Huisken, F. “Fluorescence imaging and spectroscopy of single Si and SiO_2 nanoparticles using confocal microscopy” *Bonsai Project Symposium: Breakthroughs in Nanoparticles for Bio-imaging, AIP Conf. Proc.* **2010***, 1275,* 63-70.

17. Gutbrod, R., Chizhik, A.I., Chizhik, A.M., Khoptyar, D., Steiner, M., Bär, S., Meixner, A.J. “Controlling the optical properties of single quantum emitters by optical confinement in a tunable microresonator” *SPIE Proc.* **2010***, 7712,* 77120Q.

18. Chizhik, A.I., Chizhik, A.M., Huss, A., Jäger, R., Meixner, A.J. “Nanoscale probing of dielectric interfaces with a radially polarized illumination” in preparation.

Acknowledgement

I would like to thank:

● my supervisor **Prof. Dr. Alfred J. Meixner** (University of Tübingen) for giving me the great opportunity to work in Tübingen nano-optics group, invaluable support and showing me the right way in the world of science.

● **Prof. Dr. Jörg Enderlein** (University of Göttingen) and **Prof. Dr. Friendrich Huisken** (University of Jena) for exceptionally fruitful collaboration and brilliant advices.

● my dear wife and colleague **Dr. Anna Chizhik** (University of Tübingen) for her priceless support, stimulating discussions and wise advices.

● **Dr. Wolfgang Langer** (University of Tübingen) and **Juliette Ruddy** (University of Tübingen) for an endless help with solving administrative and bureaucratic problems.

● **Dr. Dmitry Khoptryar** and **Dr. Raphael Gutbrod** (University of Tübingen) for the invaluable support and fruitful cooperation.

● **Dipl. Phys. Torsten Schmidt**, **Dipl. Phys. Karsten Potrick** and **Dipl. Phys. Jana Sommerfeld** (University of Jena) for very fruitful collaboration, interesting discussions and providing the samples of Si nanocrystals and SiO_2 nanoparticles.

● **Dipl. Chem. Regina Jäger** and **Sebastian Jäger** (University of Tübingen) for the great help with numerous problems.

● **Dr. Frank Schleifenbaum**, **Dr. Kirstin Elgass** and **Dipl. Chem. Sebastien Peter** for valuable advises and technical support.

● **Anja Huss** (University of Tübingen) for the amazing friendly atmosphere and continuous support.

● All members of the **Nano-optics group, University of Tübingen** for fruitful discussions and the team work.